

Effects of salt precipitation during evaporation on porosity and permeability of porous media

von der Fakultät Bau- und Umweltingenieurwissenschaften der Universität Stuttgart und
dem Stuttgarter Zentrum für Simulationswissenschaft zur Erlangung der Würde eines
Doktor-Ingenieurs (Dr.-Ing.) genehmigte Abhandlung

vorgelegt von

Joseph Piotrowski

aus Darmstadt

Hauptberichter: Prof. Dr. J.A. (Sander) Huisman

Mitberichter: Prof. Dr. Holger Steeb

Mitberichter: apl. Prof. Dr.-Ing. Holger Class

Mitberichter: Prof. Dr. Alex Furman

Tag der mündlichen Prüfung 07.07.2022

Institut für Wasser- und Umweltsystemmodellierung (IWS) der Universität Stuttgart
2022

Declaration of authorship

I, Joseph Piotrowski, declare that this thesis titled, “Effect of salt precipitation during evaporation on porosity and permeability of porous media” and the work presented in it are my own. Due acknowledgement has been made in the text to all the other works and materials that were used.

Hiermit erkläre ich, Joseph Piotrowski, dass diese Arbeit nur meine Originalarbeit umfasst und dass ich die vorliegende Dissertation “Effect of salt precipitation during evaporation on porosity and permeability of porous media” unabhängig geschrieben habe. Alle anderen verwendeten Quellen und Materialien wurden im Text entsprechend anerkannt.

Signature: _____

Date: _____

Acknowledgements

The work presented in this thesis was part of the research project C05 "Process-dependent porosity-permeability relations for fluid-solid reactions in porous media" within the collaborative research center 1313 "Interface-driven multi-field processes in porous media – flow, transport and deformation" at the University of Stuttgart funded by the German Research Foundation (DFG) – Project Number 327154368. My work was organized at the Institute of Bio- and Geoscience, IBG-3: Agrosphere, Forschungszentrum Jülich GmbH as a host institute in collaboration with the Institute of Applied Mechanics, MIB and the Institute for Modelling Hydraulic and Environmental Systems, IWS at the University of Stuttgart.

First, I would like to thank my supervisor Prof. Dr. Johan Alexander (Sander) Huisman for his continuous guidance, encouragement, and patience over the last years, while leaving a suitable degree of individuality. Sander supported me in all processes that are involved to obtain the doctorate and always found the time for discussions. I am grateful for his supervision and for the opportunity to work closely together with him. Second, I would like to express my gratitude to Prof. Dr. Holger Steeb for his constant support and supervision with many administrative challenges, the chance to use his laboratories and equipment, for his encouragement in inspiring discussions, and for examining my thesis. Third, I would like to thank Dr. Andreas Pohlmeier for his essential support and knowledge on nuclear magnetic resonance, for his suggestions and feedback in scientific context, and for the opportunity and time to discuss puzzling results.

I also would like to thank Prof. Dr. Holger Class for fruitful discussions, for his help on administrative concerns regarding the CRC 1313, and for his review of this thesis. Further, I would like to thank Prof. Dr. Alex Furman for being willing to examine my thesis. I would further like to extend my sincere thanks to Prof. Dr. Harry Vereecken for his support and interest during the PhD report discussions and PhD seminars. I also would like to thank Prof. Dr. Jan Vanderborght for his comments that improved my understanding of the subject. Further, I would like to thank Prof. Dr. Rainer Heling for interesting and stimulative discussions and for extending my knowledge on porous media. I also very much appreciate the collaboration with Dr. Uri Nachshon, who inspired me to develop the methodology of my first paper.

I thank my colleagues at the Forschungszentrum Jülich Odilia Esser, Dr. Franz-Hubert Hegel, Dr. Alexander Graf, Bernd Schilling, Ansgar Weuthen, Ferdinand Engels, Normen Hermes, Dr. Michael Herbst, Dr. Lutz Weihermüller, Daniel Dolfus, Dr. Jenna Poonoosamy, and the

IBG-3 workshop for supporting me with experimental challenges and providing quick solutions. I would also like to thank Gaby Pillert, Sandy Schnober, and Dr. Katrin Vermöhlen for their support on administrative aspects, and Thomas Schuster and Tobias Korf for providing extensive IT hardware and support. Many thanks to my fellow PhD students, Dr. Cosimo Brogi, Dr. Magdalena Landl, Lukas Strebel, Tobias Selzner, Theresa Boas, Dr. Satoshi Izumoto, Dr. Anne Klosterhalfen, and to my office mates Tarig Bukhary, Olga Dombrowski, Haoran (Henry) Wang, Yafei Huang, David Mengen, and all the others for the happy lunch breaks and for the nice time at the institute.

I would also like to thank my colleagues Dongwon Lee, Matthias Ruf, Dr. Nikolaos Karadimitriou at the MIB in Stuttgart for the fundamental assistance with XRCT measurements and data analysis. Further, I would like to thank Felix Weinhardt and Dr. Johannes Hommel for the continuous collaboration despite the long distance to Stuttgart. I also would like to thank Stefanie Siegert and Beate Spinner for the help with bureaucracy, and all the other colleagues at the University of Stuttgart and at the CRC 1313 for the warm atmosphere during my stays in Stuttgart.

Finally, I want to thank my friends, my family, and my girlfriend Janine for supporting me over the years and for always being there.

Abstract

Salt precipitation from evaporation is a key factor for soil degradation due to salinization in arid and semi-arid regions. It also plays a key role in porous construction material deterioration due to salt weathering. Evaporation-induced water movement transports dissolved salt ions to the surface of the porous medium where they accumulate. When the solubility limit is reached, salt starts to precipitate and forms crusts on top (efflorescence) or inside (subflorescence) of the porous medium depending on the type of solute in solution. For the development of strategies to treat salt-affected porous media and to prevent precipitation, it is important to understand the formation and the impact of the salt crusts on water flow during evaporation. Salt crust formation depends on ambient factors such as temperature, relative humidity, and wind speed over the porous medium, and also on solution properties, such as the type of dissolved ions and viscosity. However, it is not known how the hydraulic properties of the porous medium such as porosity, permeability, and water retention affect evaporation and crust formation in detail. In this context, the overall aim of this thesis is to improve understanding of the impact of salt crusts on evaporation with a focus on the porosity, the intrinsic permeability, and the spatial and temporal development of salt crusts.

In a first step, the evaporation of sodium chloride (NaCl), magnesium sulfate (MgSO₄), and sodium sulfate (Na₂SO₄) solutions from sand was investigated and the permeability of the salt crusts was determined. Samples with subflorescent MgSO₄ crusts were resaturated and the crust permeability was determined using liquid flow measurements. These measurements were found to be prone to air entrapment during resaturation. In addition, unknown liquid properties (i.e., concentration and viscosity) due to mixing during resaturation may have led to partial dissolution of the salt crusts. Both aspects shed doubt on the liquid flow determination of the intrinsic permeability of the salt crusts from low initial concentration. To avoid the uncertainties using liquid flow measurements, a novel approach to determine the intrinsic crust permeability using a gas permeameter set-up was developed. Evaporation and salt crust formation of NaCl, MgSO₄, and Na₂SO₄ solution initially at 33% of the solubility limit from sand were investigated next. It was found that the initial evaporation rate of the different salt solutions varied, which was attributed to the presence of the different solutes that affected the vapor pressure directly over the surface. During the experiment, the evaporation rate of the samples with NaCl and Na₂SO₄ solution stayed above the one of the samples with MgSO₄ solution, which was related

to the different crust formation for the three types of solutes. Using the novel approach, it was found that the intrinsic crust permeability of the separated dried crusts was similar for the different types of solutes. This could explain the reduction of the evaporation rate due to an efflorescent barrier in the case of NaCl, which was found in previous studies that also reported a similar permeability of crusts from high initial NaCl concentration. However, the low evaporation rate in the case of MgSO₄ was not consistent with the relatively high crust permeability. It was concluded that the permeability of efflorescent NaCl crusts affect evaporation mostly independent of the properties of the porous medium and the initial solute concentration. At the same time, the type of salt and the properties of the porous medium play a significant role for the permeability of subflorescent crusts, which affect evaporation to a different extent.

In a second step, the intrinsic permeability and the porosity of subflorescent MgSO₄ crusts from varying initial concentration in sand were determined using the newly developed gas permeameter and non-invasive micro-X-ray computed tomography (μ XRCT) to establish a porosity-permeability relationship. For this, sand samples with MgSO₄ solution with an initial concentration of 0.32 mol/L, 0.64 mol/L, and 0.96 mol/L were evaporated until 40%, 30%, or 20% water saturation in each sample was reached. This provided subflorescent MgSO₄ crusts formed from varying initial concentration and different duration of evaporation. The intrinsic permeability of these crusts was again determined using the gas permeameter set-up. The volume fractions of void, salt, and sand and the thickness of each separated crust were obtained non-invasively using μ XRCT. The results showed that the permeability decreased with increasing initial concentration and increasing time of evaporation (i.e. decreasing saturation). This was expected due to more salt precipitation from higher initial concentration and longer evaporation, which was partly also reflected in thicker crusts. However, the crusts from high initial concentration showed a relatively constant thickness despite a substantially reduced permeability. The intrinsic crust permeability was found to be one order of magnitude lower than in the previous experiment, which was attributed to the higher air flow velocity and associated higher evaporation rate in this experiment. Importantly, it was found that all crusts deformed during precipitation by at least 20% after only one cycle of saturation and drying, which has not been reported before. Therefore, a porosity-permeability relationship that assumes a rigid porous matrix was not established. It is concluded that the deformation of unconsolidated porous media needs to be taken into account to better understand the impact of subflorescent crusts on evaporation.

In a third step, the development of subflorescent MgSO₄ crusts was monitored non-invasively using μ XRCT to investigate changes in the pore space and single-sided unilateral nuclear magnetic resonance (NMR) to determine high-resolution near-surface water content profiles during evaporation. For this, sand samples with deionized water and MgSO₄ solution with an initial

concentration of 0.96 mol/L were evaporated. It was found that void, brine, salt, and sand could not be segmented because of limited contrast between the brine and the salt phase. However, a downward movement of the evaporation front was observed involving salt precipitation, which deformed the top of the sand. To avoid deformation, cylindrical bodies of porous sintered glass with similar porosity, intrinsic permeability, and internal surface area were prepared with the same solutions. It was found that evaporation of deionized water was similar for sand and sintered glass, which was related to the similar evaporation conditions and properties of the porous media. In contrast, evaporation of saline solution and salt crust formation differed in both porous media. The delayed crust formation in sintered glass was attributed to the smooth surface and to the highly supersaturated magnesium sulfate solution, which reduced nucleation and thus hindered crust formation. μ XRCT measurements on the sintered glass sample showed that salt crystals grew into the void space that was not occupied with liquid before. This suggests that film flow may have supported crystal growth, which needs to be analysed in more detail in future studies. It is concluded that the surface properties of the porous medium and properties (i.e., viscosity) of the highly supersaturated solution significantly affect evaporation of MgSO_4 solution and the formation of subflorescent MgSO_4 crusts.

In conclusion, this thesis provides important insights on how salt precipitation affects evaporation. It was shown that efflorescent sodium chloride crusts reduce evaporation by forming a barrier, of which the permeability is mostly independent of the properties of the porous medium. In contrast, it is known that subflorescent salt crust formation and thus the permeability of the subflorescent salt crusts significantly depends on the properties of the porous medium. In particular, it was shown in this thesis that the formation of subflorescent MgSO_4 crusts strongly depends on the surface properties of the porous medium so that a different intrinsic crust permeability results from varying initial concentrations. Thus, evaporation is impacted by the type of solute and associated crust formation. Further, the properties of the supersaturated saline solution (i.e., viscosity and nucleation properties) are important for the liquid supply to the surface during evaporation. In addition, unconsolidated porous media deform due to subflorescent salt precipitation, which needs to be considered to understand the impact of subflorescent salt crusts on evaporation.

Zusammenfassung

Die Ausfällung von Salzen durch die Verdunstung von Wasser stellt einen Schlüsselfaktor bei der Degradierung von Böden in ariden und semi-ariden Regionen auf Grund von Versalzung dar, sowie beim Verfall von porösen Baumaterialien. Die Verdunstung von Wasser führt zum Transport von gelösten Salzionen an die Oberfläche des porösen Mediums, wo sie sich ansammeln. Sobald die Löslichkeitsgrenze überschritten wird, beginnt Salz auszufallen. In Abhängigkeit der gelösten Ionen bilden sich Salzkrusten entweder auf (Effloreszenz) oder im (Subfloreszenz) porösen Medium. Um Strategien zur Behandlung oder Vermeidung von Salzaufällung zu entwickeln, ist es wichtig, die Bildung und die Auswirkung von Salzkrusten während der Verdunstung zu verstehen. Die Salzkrustenbildung hängt von äußeren Faktoren wie Temperatur, relativer Feuchte und Windgeschwindigkeit über dem Medium ab, sowie von der Art der gelösten Ionen und der Viskosität der Lösung. Der genaue Einfluss der hydraulischen Eigenschaften des porösen Mediums, wie Porosität, Permeabilität oder Wasserretention ist jedoch weitestgehend unbekannt. Daher das Hauptziel dieser Doktorarbeit in der Verbesserung des Verständnisses über die Auswirkungen von Salzkrusten auf die Verdunstung mit Fokus auf Porosität, Permeabilität, sowie zeitliche und örtliche Entwicklung der Salzkrusten.

In einem ersten Schritt wurde die Verdunstung von Natriumchlorid (NaCl), Magnesiumsulfat (MgSO_4) und Natriumsulfat (Na_2SO_4) Lösung aus Sand untersucht und die Permeabilität der Salzkrusten bestimmt. Proben mit MgSO_4 Kruste wurde wiederaufgesättigt und die Krustenpermeabilität wurde mit Hilfe von Durchflussmessungen bestimmt. Die Bestimmung der Permeabilität von Magnesiumsulfatkrusten mittels Flüssigkeitsdurchflussmessungen erwies sich als anfällig gegenüber Lufteinschlüssen. Zudem führten unbekannte Flüssigkeitseigenschaften (u.a. Konzentration und Viskosität) durch die Wiederauf sättigung womöglich zu teilweiser Auflösung der Krusten. Beide Aspekte wecken Zweifel an der Permeabilitätsbestimmung von Salzkrusten aus niedriger Initialkonzentration mittels den Flüssigkeitsdurchflussmessungen. Um die Ungenauigkeiten im Zusammenhang mit Flüssigkeitsdurchflussmessungen zu vermeiden, wurde ein neuartiger Ansatz zur Bestimmung der intrinsischen Krustenpermeabilität mit Hilfe von Gasflussmessungen entwickelt. Daraufhin wurden Krusten durch die Verdunstung von NaCl , MgSO_4 und Na_2SO_4 Lösungen mit Initialkonzentrationen von 33% der jeweiligen Löslichkeitsgrenze aus Sand untersucht. Zu Beginn des Experiments, unterschied sich die Verdunstungsrate der verschiedenen Salzlösungen, was auf die unterschiedlichen gelösten Ionen und deren Ein-

fluss auf den Dampfdruck über der Probenoberfläche zurück geführt wurde. Im Verlauf des Experiments blieb die Verdunstungsrate der NaCl und Na₂SO₄ Lösungen über derjenigen der MgSO₄ Lösung, was auf die unterschiedliche Krustenbildung zurückgeführt wurde. Die intrinsische Permeabilität der separierten und getrockneten Krusten wurde mit Hilfe des neuartigen Ansatzes bestimmt und war für alle Krusten ähnlich. Die Reduktion der Verdunstungsrate im Falle von NaCl konnte auf die effloreszente Barriere zurückgeführt werden, wie bereits frühere Studien zeigten, die ebenfalls eine ähnliche Krustenpermeabilität fanden. Die niedrige Verdunstung im Falle von MgSO₄ war jedoch nicht konsistent mit der relativ hoher Permeabilität der Kruste. Die Ergebnisse deuten darauf hin, dass die effloreszente NaCl Kruste die Verdunstung weitgehend unabhängig vom porösen Medium und von der Initialkonzentration beeinflusst. Im Gegensatz dazu wird die Permeabilität von subfloreszenten Krusten stark vom vorliegenden Salztyp und von den Eigenschaften des porösen Mediums bestimmt, was die Verdunstung unterschiedlich beeinflusst.

In einem zweiten Schritt wurde die Porosität und die Permeabilität von subfloreszenten MgSO₄-Krusten aus unterschiedlichen Initialkonzentrationen in Sand mit Hilfe des neuentwickelten Gaspermeameters und von Mikro-Röntgen Computertomographie (μ XRCT) bestimmt, um eine Porositäts-Permeabilitätsbeziehung zu ermitteln. Dafür verdunsteten Sandproben mit 0.32 mol/L, 0.64 mol/L und 0.96 mol/L Initialkonzentration, bis 40%, 30% oder 20% Flüssigkeits-sättigung in der jeweiligen Probe erreicht wurden. Die Permeabilität der einzelnen subfloreszente MgSO₄-Krusten von verschiedener Initialkonzentration und unterschiedlicher Verdunstungsdauer wurde nach der Krustenseparierung und -trocknung mit Hilfe des Gaspermeameters bestimmt. Anschließend lieferten nicht invasive Messungen mit μ XRCT die Volumenanteile von Porenleerraum, Salz und Sand und die Krustendicke. Die Permeabilität nahm mit höherer Initialkonzentration und längerer Verdunstungsdauer ab, was der höheren Menge an ausgefallenem Salz zugeschrieben wurde. Die Krustendicke nahm mit steigender Salzausfällung zu, außer im Fall von hoher Initialkonzentration, wo eine gleichbleibende Krustendicke beobachtet wurde, obwohl die Permeabilität signifikant abnahm. Die intrinsische Permeabilität lag eine Größenordnung unter derjenigen aus dem vorigen Experiment, was auf höhere Luftflüsse und die damit einhergehende höhere Verdunstungsrate in diesem Experiment zurückgeführt wurde. Von großer Bedeutung ist, dass der Volumenanteil der Sandphase aller Krusten um mindestens 20% im Vergleich zum Initialzustand nach nur einem Zyklus von Sättigung und Trocknung abnahm, woraus erstmalig eine signifikante Deformation aller Krusten abgeleitet wurde. Daher war es nicht möglich, eine Porositäts-Permeabilitätsbeziehung zu ermitteln, da diese auf der Annahme einer unverformbaren porösen Matrix beruht. Es gilt zu beachten, dass die Deformation von unkonsolidierten porösen Medien durch Salzausfällung berücksichtigt wird, um den Einfluss von subfloreszenten Krusten auf die Verdunstung besser zu verstehen.

In einem dritten Schritt wurde die Entwicklung von subfloreszenten MgSO₄-Krusten auf der

Porenskala mit Hilfe von μ XRCT beobachtet und Wassergehaltsprofile mittels magnetischer Resonanztomographie (NMR) während der Verdunstung bestimmt. Dafür verdunsteten Sandproben mit voll entsalztem Wasser und mit MgSO_4 -Lösung mit 0.96 mol/L Initialkonzentration. Die vier Phasen Porenleerraum, Salz, Flüssigkeit und Sand konnten auf Grund von unzureichendem Kontrast zwischen Salz und Flüssigkeit nicht segmentiert werden. Die Abwärtsbewegung der Verdunstungsfront wurde jedoch beobachtet, was Salzausfällung und eine Deformation des Sandes einschloss. Um die Deformation zu vermeiden, wurden zylindrische Körpern aus gesintertem, porösen Glas mit ähnlicher Porosität, intrinsischer Permeabilität und innerer Oberfläche mit denselben Lösungen vorbereitet. Die Verdunstung von deionisiertem Wasser aus Sand und gesintertem Glas war vergleichbar, was auf ähnliche Verdunstungsbedingungen und Eigenschaften der porösen Medien zurückgeführt wurde. Im Gegensatz dazu unterschied sich die Verdunstung und Salzkrustenbildung in beiden Medien voneinander, wobei die Krustenbildung im gesinterten Glas im Vergleich zum Sand erheblich verzögert wurde. Dies konnte mit der glatten Oberfläche und der stark übersättigten MgSO_4 -Lösung erklärt werden, welche die Keimbildung und damit die Krustenbildung reduzierten. μ XRCT Messungen zeigten, dass Salzkristalle in der Porenleerraum des gesinterten Glases hineinwuchsen, obwohl sich dort zuvor keine Flüssigkeit befunden hatte. Dies legt nahe, dass Flüssigkeitsfilme das Kristallwachstum begünstigten, was in zukünftigen Studien näher untersucht werden sollte. An dieser Stelle wird festgestellt, dass die Oberflächeneigenschaften des porösen Mediums und die Eigenschaften (u.a. Viskosität) der stark übersättigten MgSO_4 -Lösung die Verdunstung und die Krustenbildung erheblich beeinflussen.

Insgesamt liefert diese Arbeit wichtige Erkenntnisse zum Effekt von Salzausfällung auf die Verdunstung. Die effloreszente NaCl Krustenbildung reduziert die Verdunstung durch die Bildung einer Barriere, deren Permeabilität weitestgehend unabhängig von den Eigenschaften des porösen Mediums ist. Im Gegensatz dazu ist bekannt, dass die subfloreszente MgSO_4 -Krustenbildung und die Permeabilität der subfloreszenten Krusten stark von den Eigenschaften des porösen Mediums abhängt. Diese Arbeit zeigt, dass die subfloreszente MgSO_4 -Krustenbildung in besonderem Maße von den Oberflächeneigenschaften des porösen Mediums abhängt, was eine unterschiedliche Permeabilität von Krusten verschiedener Initialkonzentration bewirkt. Daraus lässt sich ableiten, dass die Verdunstung substanziell vom Typ des gelösten Salzes und der damit verbundenen Krustenbildung beeinflusst wird. Weiterhin sind die Eigenschaften der übersättigten Lösung (u.a. Viskosität und Keimbildung) von Bedeutung für die Versorgung der Probenoberfläche mit Flüssigkeit während der Verdunstung. Zusätzlich gilt, dass die Deformation von nicht konsolidierten porösen Materialien durch subfloreszente Salzausfällung berücksichtigt werden sollte, um den Einfluss von subfloreszenten Salzkrusten auf die Verdunstung besser zu verstehen.

Contents

Declaration of authorship	i
Acknowledgements	iii
Abstract	v
Zusammenfassung	ix
Contents	xiii
List of figures	xvii
List of tables	xxi
List of abbreviations	xxiii
List of symbols	xxv
1. Introduction	1
1.1. Motivation	1
1.2. Evaporation from porous media	2
1.2.1. Evaporation of water without consideration of solutes	2
1.2.2. Evaporation of saline water and efflorescent salt crust formation	4
1.2.3. Subflorescent salt crust formation	6
1.2.4. Porosity and permeability of salt crusts	7
1.3. Aims and structure of the thesis	9
2. Theory and Background	11
2.1. Theoretical concepts and definitions	11
2.1.1. Porous media at different scales	11
2.1.2. Definitions at the macro-scale	13
2.1.3. Flow in porous media	13
2.1.4. Contact angle and capillary pressure	15

2.2.	Evaporation and salt precipitation	16
2.2.1.	Stages of evaporation of deionized and saline water	16
2.2.2.	Evaporation in mathematical models	18
2.2.3.	Modelling salt precipitation during evaporation	19
2.2.4.	Phase diagrams of salt solutions	21
2.2.5.	Supersaturation and nucleation	23
2.3.	Background for used experimental methods	25
2.3.1.	Determination of the intrinsic permeability of porous media	25
2.3.2.	Basics of micro-X-ray computed tomography	28
2.3.3.	Principles of nuclear magnetic resonance	31
3.	Evaporation and crust formation from solutions of different salt types	37
3.1.	Introduction	37
3.2.	Materials and methods	38
3.2.1.	Preparation of samples with different types of salt solution	38
3.2.2.	Salt crust permeability from liquid flow measurements	42
3.2.3.	Permeability determination using gas flow	43
3.3.	Results and discussion	46
3.3.1.	Samples for liquid flow permeability determination	46
3.3.2.	Evaporation of different types of salt solution from sand	50
3.3.3.	Permeability of crusts from different salts	53
3.4.	Conclusions	57
4.	Porosity and permeability of subflorescent magnesium sulfate crusts	59
4.1.	Introduction	59
4.2.	Materials and methods	60
4.2.1.	Samples with varying initial concentrations	60
4.2.2.	Micro-X-ray computed tomography hardware and projections	61
4.2.3.	Reconstruction and post-processing of μ XRCT measurements	62
4.2.4.	Segmentation and analysis of processed imaging data	65
4.3.	Results	66
4.3.1.	Evaporation of salt solutions with varying initial concentration	66
4.3.2.	Thickness and intrinsic permeability of separated crusts	67
4.3.3.	Segmented image data of separated salt crusts	70
4.3.4.	Relating volume fractions and crust permeability	72
4.4.	Discussion	74
4.5.	Conclusions	76

5. Non-invasive monitoring of subflorescent magnesium sulfate crust formation	79
5.1. Introduction	79
5.2. Materials and methods	80
5.2.1. Evaporation from sand and from sintered glass samples	80
5.2.2. Micro-X-ray computed tomography during evaporation	82
5.2.3. Water content profiles from unilateral nuclear magnetic resonance	84
5.3. Results and discussion	87
5.3.1. Evaporation from sand and from sintered glass	87
5.3.2. Water content profiles in sand and sintered glass samples	89
5.3.3. Pore-scale imaging of the salt crust developed in sand	91
5.3.4. Registration of time-dependent imaging data	93
5.3.5. Segmentation using the sintered glass phase mask	95
5.3.6. Phase volume fractions from μ XRCT measurements	96
5.3.7. Depth profiles of segmented phases in sintered glass	98
5.3.8. Differences in crust formation in sintered glass and sand	101
5.4. Conclusions	103
6. Conclusions and outlook	105
6.1. Conclusions	105
6.2. Outlook	108
References	115
A. Supplementary material Chapter 3	127
A.1. Thickness of crusts from different salts	127
A.2. Pressure measurements of crusts from different salts	129
B. Supplementary material Chapter 4	131
B.1. Surface data and thickness distribution of separated crusts	131
B.2. Pressure measurements of separated crusts	135
C. Supplementary material Chapter 5	139

List of figures

1.1. Efflorescent and subflorescent salt crusts separated from sand.	5
2.1. Schematic picture of pore and REV-scale in porous media and volume dependency.	12
2.2. Contact angle on flat surface and capillarity between sand grains.	16
2.3. Schematic illustration of the cumulative mass loss and evaporation rate during the evaporation of deionized and saline water from porous media.	18
2.4. Phase diagram of aqueous NaCl solution as a function of water activity a_w and temperature T	22
2.5. Phase diagram of aqueous MgSO ₄ solution as a function of water activity a_w and temperature T	23
2.6. Phase diagram of aqueous Na ₂ SO ₄ solution as a function of water activity a_w and temperature T	24
2.7. Constant head permeameter set-up to determine the hydraulic conductivity of a sample.	26
2.8. Set-up to determine the air permeability of a sample.	28
2.9. Schematic set-up and optical parameters of micro-X-ray computed tomography.	30
2.10. Exemplary results obtained from μ XRCT measurements.	31
2.11. Precession of spins in magnetic field.	32
2.12. Precession and excitation of macroscopic magnetization in external field.	33
2.13. Pulse sequence of Hahn echo and dephasing of magnetization.	35
2.14. Echo train from multiple 180° pulses.	36
3.1. Picture of sand samples in steel column.	39
3.2. Picture of sand sample in PMMA sample holder.	40
3.3. Sketch of falling head set-up to determine the hydraulic conductivity.	43
3.4. Sketch of the gas permeameter set-up and exemplary results for permeability determination of a dry P3 filter plate.	44
3.5. Cumulative mass loss and evaporation rate of 1 mol/L MgSO ₄ initial concentra- tion from sand in steel columns.	47
3.6. Results for the determination of hydraulic conductivity and permeability in sand columns with and without salt crusts.	48

3.7. Evaporation of samples with deionized water, NaCl, MgSO ₄ , and Na ₂ SO ₄ solution from F32 quartz sand.	50
3.8. Photos of sample surface at different times.	52
3.9. Pressure difference as a function of gas flow rate for two selected salt crusts at the highest flow rate of 300 mL/min.	54
3.10. Permeability of sand and of crusts formed from evaporation of NaCl, MgSO ₄ , and Na ₂ SO ₄ solution.	55
4.1. Sample holder with field-of-view (FOV) of μ XRCT measurements used to characterize the separated salt crust.	60
4.2. Photo of the modular μ XRCT set-up.	62
4.3. Evaporation rate of samples with deionized water and varying initial MgSO ₄ concentrations from sand.	67
4.4. Surface and thickness distribution of salt crust.	68
4.5. Thickness of salt crusts from varying initial MgSO ₄ concentration as a function of saturation.	69
4.6. Intrinsic permeability of crusts formed from 0.32 mol/L, 0.64 mol/L, and 0.96 mol/L initial MgSO ₄ concentration at 40%, 30%, and 20% saturation.	69
4.7. Filtered and segmented side view of crust formed from 0.64 mol/L initial concentration at 20% saturation.	70
4.8. Depth profiles and axial slices from segmented μ XRCT data of the crust formed from 0.64 mol/L initial concentration at 20% saturation.	71
4.9. Mean volume fractions of all crusts obtained from segmented μ XRCT data. . . .	72
4.10. Relationship between void fraction and crust permeability.	73
5.1. Photo of sintered glass sample covered at the lateral surface with a shrinking tube. . .	81
5.2. Schematic set-up of the unilateral NMR-MOUSE and selected measurements. . . .	85
5.3. Cumulative mass loss and evaporation rate of deionized water and 0.96 mol/L MgSO ₄ solution from sand and from sintered glass.	88
5.4. Surface pictures of sand and sintered glass sample with 0.96 mol/L MgSO ₄ solution. . .	89
5.5. Water content profiles from NMR of the sand and sintered glass sample.	90
5.6. Side view, depth profiles of phases, and histogram from time-lapsed μ XRCT data of subfluorescent magnesium sulfate crust in sand.	92
5.7. Registered subareas and side view of μ XRCT data from sintered glass sample at initial dry state and after 3.8 days (60% saturation).	94
5.8. Filtered data, mask data, and corresponding histograms from a subarea of μ XRCT data of sintered glass at the dry state and at 21% saturation.	96

5.9. Segmented and overlaid subareas 0.8 mm below the surface at 60% and 21% saturation.	97
5.10. Depth profiles of segmented phases obtained from μ XRCT data of the sintered glass sample at 100%, 90%, 60%, and 21% saturation.	99
5.11. Depth profiles from NMR and μ XRCT data of the sintered glass sample.	100
6.1. Segmented 3D void space from μ XRCT data of separated crust in sand.	109
A.1. Pressure difference over gas flow rate of all sand samples.	128
A.2. Pressure difference over gas flow rate of all dried salt crusts.	129
A.3. Pressure difference over gas flow rate of all wet salt crusts.	130
B.1. Surface data and thickness distribution of separated crusts from 0.32 mol/L initial concentration.	132
B.2. Surface data and thickness distribution of separated crusts from 0.64 mol/L initial concentration.	133
B.3. Surface data and thickness distribution of separated crusts from 0.96 mol/L initial concentration.	134
B.4. Pressure measurements of separated and dried crusts from 0.32 mol/L, 0.96 mol/L, and 0.96 mol/L initial concentration.	135
B.5. Pressure measurements of separated, wet crusts from 0.32 mol/L, 0.96 mol/L, and 0.96 mol/L initial concentration.	136
B.6. Pressure measurements of sand samples.	137

List of tables

3.1.	Physical properties and particle size distribution of F32 quartz sand.	38
3.2.	Physical properties of solutions used to prepare samples in steel columns and for the determination of the hydraulic conductivity.	39
3.3.	Properties of the substances for sample preparation and permeability determination at 20 °C in PMMA sample holders.	41
3.4.	Normalized ratios of initial evaporation rate and initial vapor pressure difference for the samples with different salt solutions.	51
4.1.	Technical specifications of the μ XRCT set-up.	62
4.2.	Details of the reconstruction and the filtering software to process μ XRCT measurements.	63
4.3.	Reconstruction parameters for μ XRCT measurements on separated salt crusts.	63
4.4.	Filtering parameters used on reconstructed μ XRCT imaging data of separated salt crusts.	64
4.5.	Segmentation steps, methods and parameters used to process μ XRCT imaging data.	65
4.6.	Additional procedures, methods and parameters used to process segmented μ XRCT imaging data.	66
5.1.	Registration steps, methods, and parameters used on filtered μ XRCT data of the sintered glass sample.	83
5.2.	Parameters for measurements on sintered glass, sand, and calibration using the NMR-MOUSE.	86
A.1.	Measured distance from top and bottom of the sample holder to the crust.	127
B.1.	Arithmetic and harmonic mean of the thickness distribution of the crust segments obtained from μ XRCT data.	131
C.1.	Measurement depths on sintered glass and marker solution using the NMR-MOUSE.	139

List of abbreviations

ANOVA	Analysis of Variance	NMR	Nuclear magnetic resonance
AMNLM	Adaptive manifold non-local mean	PMMA	Polymethyl methacrylat
Cl/Cl ⁻	Chloride	PT	Pressure transducer
CPMG	Carr-Prucell-Meiboom-Gill	REV	Representative elementary volume
FBP	Filter back projection	rf	Radio frequency (coil)
FC	Flow controller	RX	Receiver
FID	Free induction decay	SDD	Source detector distance
FOV	Field-of-view	SOD	Source object distance
F32	Quartz sand	TX	Transmitter
GUI	Graphical user interface	XRCT	X-ray computed tomography
¹ H	Hydrogen	1D	One-dimensional
H ₂ O	Water	2D	Two-dimensional
LBM	Lattice Boltzmann modelling	3D	Three-dimensional
MgSO ₄	Magnesium sulfate		
MOUSE	Mobile universal surface explorer		
μXRCT	Micro-X-ray computed tomography		
Na/Na ⁺	Sodium		
NaCl	Sodium chloride		
Na ₂ SO ₄	Sodium sulfate		

List of symbols

Greek

α	Flip angle [rad]	b	Exponential fitting parameter [-]
α'	Empirical pressure parameter [-]	\mathbf{B}_0	External magnetic field [T]
γ	Surface energy [J/m ²]	\mathbf{B}_1	Oscillating magnetic field [T]
θ	Water content [m ³ /m ³]	d	Diameter [m]
λ	Local linear attenuation coefficient [-]	E	Energy state [-]
μ	Dynamic viscosity [Pa.s]	f	Geometric magnification [-]
ν	Frequency [Hz]	Fo	Forchheimer number [-]
ρ	Density [kg/m ³]	\mathbf{g}	Gravitational acceleration vector [m/s ²]
τ	Tortuosity [-]	g	Gravitational acceleration [m/s ²]
ϕ	Porosity [-]	H	Total potential/hydraulic head [m]
φ	Contact angle [°]	h	Sample length [m]
Φ_S	Sphericity [-]	h_w	Matric potential head [m]
χ	Saturation [-]	I	X-ray beam intensity [W/m ²]
ψ	Potential [m]	j	Ray path [-]
ω	Precession frequency [rad/s]	K	Hydraulic conductivity [m/s]

Latin

A	Area (cross-sectional) [m ²]	\mathbf{k}	Intrinsic permeability tensor [m ²]
a_w	Water activity [-]	k	Intrinsic permeability [m ²]
		L	Liquid level [m]

Latin

l	Sample holder length [m]	t_E	Echo time [s]
\mathbf{M}	Macroscopic Magnetization [A/m]	t_P	Pulse duration [s]
m	Empirical shape parameter [-]	t_R	Repetition time [s]
n	Number of quantity [-]	u_0	Superficial velocity [m/s]
n'	Empirical shape parameter [-]	V	Volume [m ³]
p	Pressure [Pa]	x	Mole fraction [-]
p_c	Capillary pressure [Pa]	z	Vertical coordinate [m]
Q	Volumetric flow rate [m ³ /s]	Superscripts	
\mathbf{q}	Flux density vector [m/s]	s	Salt
q	Flux density [m/s]	sol	Solution phase
Ra	Surface roughness [-]	Subscripts	
Re	Reynolds number [-]	air	Air phase
RH	Relative humidity [-]	amb	Ambient
r_p	Precipitation rate constant [1/s]	α	Phase substitute
S	Signal intensity [-]	b	Burette/reservior
s	Thickness [m]	b	Bulk
T	Temperature [°C]	corr	Corrected
T_1	Longitudinal relaxation time [s]	crust	Salt crust
T_2	Transversal relaxation time [s]	depth	Measurement depth
T_2^*	T_2 in inhomogeneous fields [s]	e	Effective quantity
t	Time [s]	g	Gas phase
t_{acq}	Acquisition time [s]	h	Pressure head
t_d	Dead time [s]	i	Inlet

Subscripts

l	Liquid phase	s	Solid phase
lr	Residual liquid	sat	Saturated
lift	Lift position	sens	Sensitive
max	Maximum	sg	Sintered glass
mol	Molar	spec	Specific
nw	Non-wetting	ssc	Sand in steel columns
o	Outlet	total	Total quantity
o	Osmotic head	void	Void space
p	Particle	w	Wetting
r	Relative	z	Gravitational head
ref	Reference	0	Initial State
rf	Radio frequency	\uparrow	Up
S	Saturation	\downarrow	Down
s	Sample		

Constants

γ_{H}	Gyromagnetic constant (^1H)	42.58 [MHz/T]
k_{B}	Boltzmann constant	1.380649×10^{-23} [J/K]
\hbar	Planck's constant	$1.054\,571\,817 \times 10^{-34}$ [J s]

Chapter 1

Introduction

1.1. Motivation

Soil salinization in arid and semi-arid areas is one of the key factors that control soil degradation (Nkonya and Anderson, 2015). About 932.2 Mha of soil are estimated to be affected by salinization globally (Daliakopoulos et al., 2016). More than 20% of irrigated land has been or still is affected by unsustainable agricultural and farming practices that have caused problematic salinization of arable soil (Pitman and Läubli, 2002; Schofield and Kirkby, 2003). The potential threat of this salinization for global food supply is obvious as about 40% of agricultural production is obtained from irrigated land (Vereecken et al., 2009). At the same time, many parts of the world suffer from shortage of irrigation water with sufficient quality (i.e., low salinity) (Icekson-Tal et al., 2003; Bortolini et al., 2018). It is well known that high solute content in soil water affects photosynthesis, root water uptake, and plant growth (Chaves et al., 2009), and may thus lead to reduced crop yields (Oster, 1994).

Evaporation from soil is a key factor that determines soil salinization (Gupta et al., 2008; Artiola et al., 2019). Dissolved ions accumulate at the soil surface due to the upward movement of water by evaporation (Jambhekar et al., 2015; Grünberger et al., 2008). When the solubility limit for a given salt is reached, salt precipitation is initiated (Driessen and Schoorl, 1973; Dowuona et al., 1992). The precipitation of salt on top of a porous medium is called efflorescence (e.g., sodium chloride (NaCl), (Driessen and Schoorl, 1973; Nachshon et al., 2011a; Eloukabi et al., 2013)), while salt precipitation inside of a porous medium is called subflorescence (e.g., sodium sulfate (Na₂SO₄) or magnesium sulfate (MgSO₄), (Tsui et al., 2003; Espinosa-Marzal and Scherer, 2010; Flatt et al., 2014)). Both types of salt crusts will affect flow and transport near the soil surface due to changes in porosity, water retention, and permeability, which in turn may have an impact on evaporation and water infiltration. Enhanced surface runoff due to salt crust formation can then promote erosion and land loss (Smoot et al., 1994). Understanding of how salt precipitation affects the porosity, permeability, and water retention of the top soil is

essential for prediction and remediation of salt-affected soils (*Liao et al.*, 2019).

Salinization is not only important in an agricultural context. For example, salt accumulation associated with evaporation may also lead to structural deterioration of porous building materials and monuments, which is known as salt weathering (*Steiger et al.*, 2011a; *Flatt et al.*, 2014). Upward flow of saline water allows the evaporation of water over the vertical interface of the wall above the ground, which leads to salt precipitation and crust formation at the base of buildings (*Scherer*, 2004; *Steiger et al.*, 2011a). The growing salt crystals during salt precipitation induce a pressure on the matrix of bricks and stones, which promotes corrosive processes such as deformation or even destruction of the porous structure (*Flatt and Scherer*, 2002; *Tsui et al.*, 2003; *Espinosa-Marzal and Scherer*, 2013). As in the case of soil salinization, understanding how salt precipitation affects water flow and solute transport is important for the preservation of cultural heritage, where salt weathering represents a critical degradation process (*Bertolin*, 2019).

1.2. Evaporation from porous media

1.2.1. Evaporation of water without consideration of solutes

Evaporation from porous media depends on the ambient atmospheric conditions, mainly the temperature, relative humidity, and the speed and direction of air flow over the surface (*Scherer*, 1990; *Shokri et al.*, 2008; *Assouline et al.*, 2013). At the same time, the properties of the porous medium affect liquid and vapor flow to the surface and thus will also control evaporation (*Lehmann et al.*, 2008; *Or et al.*, 2013). If the ambient conditions are constant, the potential evaporation (i.e., the evaporation of deionized water from a liquid surface at the same atmospheric conditions) is higher than the evaporation from porous media (*Shokri et al.*, 2008). This lower evaporation is due to the reduced area due to the presence of the solid phase (*Or et al.*, 2013). This indicates that the pore geometry and the transport properties of the porous medium play an important role for evaporation. A high evaporative demand of the atmosphere results in a high evaporation rate from porous media and vice versa. This condition continues as long as a capillary liquid connection to the surface is present through partially saturated pores where water flows along thin films at the surface of the solid phase (*Yiotis et al.*, 2004). Evaporation in these conditions is often referred to as stage I evaporation (*Lehmann et al.*, 2008; *Shokri et al.*, 2008; *Or et al.*, 2013). When the liquid flow by capillarity is not able to provide a connection to the surface of the porous medium anymore, pores are entirely invaded by air and the evaporation rate decreases significantly as the evaporation front moves into the porous medium. Vapor diffusion from the evaporation front to the surface now is the main transport mechanism of water (*Lehmann et al.*, 2008; *Or et al.*, 2013), and this is often referred

to as stage II evaporation. Using non-invasive unilateral nuclear magnetic resonance (NMR) and magnetic resonance imaging (MRI) measurements, near-surface soil moisture profiles were determined during stage I and stage II evaporation (*Merz et al.*, 2014). Approximately uniform water content profiles were observed during stage I evaporation, whereas a dry surface layer developed during stage II evaporation indicating the downward movement of the evaporation front. With continuing stage II evaporation, this evaporation front receded downward into the soil.

Texture is known to be a key control factor on the evaporation of porous media because it determines pore size and the spatial separation between actively evaporating pores (*Or et al.*, 2013). It has been shown that the evaporation rate from columns with fine sand is higher than the evaporation rate from columns with coarse sand during stage I evaporation when the atmospheric demand is low (*Lehmann et al.*, 2008). This was related to the higher amount of isolated active pores that were present on a given surface area and provided capillary liquid supply in the case of fine sand. Additionally, it was shown that the higher capillary pressure in the case of small pores (i.e., fine sand) provided liquid to the surface for a longer time than large pores (i.e., coarse sand), which resulted in a delayed transition from stage I to stage II (*Lehmann et al.*, 2008). Numerical simulations suggested that the vapor pressure field over the isolated active pores led to non-linear diffusive fluxes across the boundary layer, which explains the decreasing evaporation rate at high evaporative demand during stage I evaporation (*Shahraeeni and Or*, 2012a,b; *Or et al.*, 2013).

In field applications, soil with heterogeneous flow and transport properties are the rule rather than the exception. Therefore, there is a need to consider evaporation from heterogeneous porous media. Evaporation experiments with sharp vertical textural interfaces between coarse and fine sand showed that the coarse-textured region dried out first, while the capillary liquid connection was still present in the fine-textured region (*Lehmann and Or*, 2009). This was associated with horizontal flow from the coarse to fine sand that provided liquid to the fine textured medium, which is expected to result in sharp contrasts in water content. Evaporation experiments monitored with electrical resistivity tomography measurements at a larger scale confirmed the horizontal flow and the sharp contrast in water content (*Bechtold et al.*, 2012). It is important to note that averaging the properties of both media cannot be used to estimate the evaporative loss because of this hydraulic coupling between the two domains (*Or et al.*, 2013). In the case of fully saturated porous media, evaporation experiments from heterogeneous sand columns showed that solutes redistributed from fine to coarse regions at the surface (*Bechtold et al.*, 2011). This suggests that solute transport may be largely decoupled from the evaporation process at full liquid saturation, and it was proposed that the saturated hydraulic conductivity and molecular diffusion were the key factors determining solute transport. In this same context, the evaporation of horizontally layered porous media with varying texture was also strongly

dependent on the hydraulic coupling of the layers in the porous media during stage I evaporation (*Shokri et al.*, 2010). Fine-textured media were found to be wet, although air already invaded the coarse medium below. Hence, the transition from stage I to stage II of evaporation varied substantially depending on the layering. From this short overview, it is clear that the properties of the porous medium strongly affect evaporation.

1.2.2. Evaporation of saline water and efflorescent salt crust formation

In natural systems, dissolved ions are usually present in water so that salt may accumulate near the surface during evaporation from porous media as described above. The chemical composition of soil water in arid and semi-arid regions is commonly dominated by dissolved Na^+ and Cl^- ions (*Artiola et al.*, 2019). Consequently, salt crusts that include sodium chloride (NaCl) precipitation are generally observed in the field (*Smoot et al.*, 1994). Thus, NaCl precipitation due to evaporation on sand columns has been investigated in a range of studies. It is important to note that NaCl precipitates on top of porous medium, which is called efflorescence (see Figure 1.1a) and that efflorescent NaCl precipitation generates a new porous medium on top of the soil with its own hydraulic properties in terms of porosity, water retention, and permeability (*Nachshon et al.*, 2011b,a; *Eloukabi et al.*, 2013; *Shokri-Kuehni et al.*, 2017). It was observed that the evaporation of the same NaCl solution led to an earlier crust development for coarse sand than for fine sand (*Rad et al.*, 2015). In addition, the appearance of the crust was more patchy and a thicker crust was formed in case of the coarse sand (*Rad et al.*, 2015). This was attributed to the limited amount of fine pores at the surface of the coarse sand that acted as active pores and preferred locations for nucleation. In contrast, fine sand promoted crusty salt precipitation (closed crust) due to the higher amount of active pores and the dense distribution of nucleation sites (*Rad et al.*, 2015). The patchy formation of NaCl crust on coarse grained porous media was confirmed by evaporation experiments on glass beads and it was found that a patchy crust enhanced evaporation compared to a closed crust (*Veran-Tissoires and Prat*, 2014). This was attributed to the narrow pores of the closed crust that affected the flow of water. The evaporation of NaCl solution from porous media consisting of glass beads with regular shape and sand grains with irregular particle shape was compared by *Rad and Shokri* (2014). They observed a delayed crust formation for the sand samples, which was attributed to a higher amount of active pores present in the sand compared to a lower amount of active pores in the porous medium with glass beads. This lower amount of active pores was confirmed using pore size distributions obtained from X-ray computed tomography (XRCT) images (*Rad and Shokri*, 2014). Again, the lower amount of evaporation sites for glass beads resulted in a more patchy crust formation than in the case of sand (*Rad and Shokri*, 2014).

In the case of heterogeneous columns with sharp vertical textural interfaces of both coarse

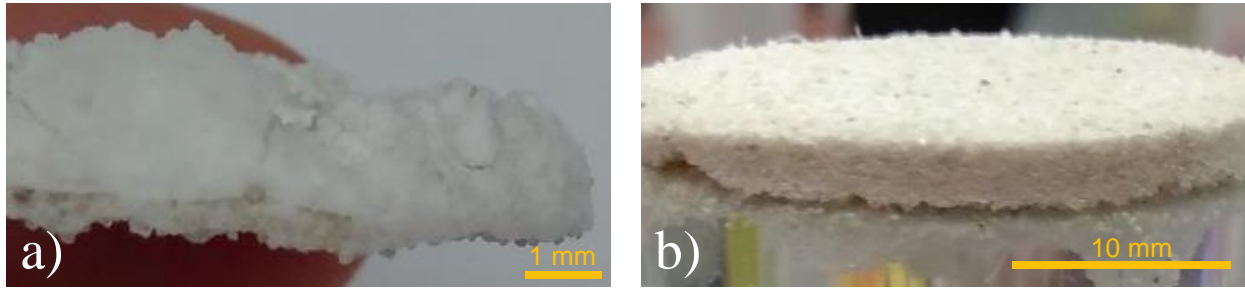


Figure 1.1: (a) Efflorescent NaCl crust and (b) subflorescent MgSO₄ crust separated from sand.

and fine sand, the evaporation of NaCl solution at the solubility limit formed precipitates preferably on the fine sand and the crust formation on the coarse sand was delayed (*Nachshon et al.*, 2011b,a; *Bergstad et al.*, 2017). This was attributed to the preferential evaporation from the fine-textured porous medium, which leads to the earlier formation of a salt crust if the solubility limit is already reached at all locations. In contrast, it was found that evaporation of NaCl solution with low initial concentration from a similar set-up resulted in preferential crust development on the regions with coarse sand (*Bergstad et al.*, 2017). This was again attributed to the limited amount of local active pores in the coarse domain compared to the fine domain, which acted as preferred location for nucleation as described above (*Rad et al.*, 2015). Thus, the supersaturation was reached earlier in the fewer pores of the coarse domain, which resulted in the earlier start of crust formation on coarse sand (*Bergstad et al.*, 2017). At the same time, the regions with fine sand were still wet and the solution was not yet close to the solubility limit. It is important to note that the difference in crust formation depended on the initial concentration of the NaCl solution. This suggests that the evaporation and subsequent crust formation of other type of salt solutions may also be affected by varying initial concentration, which has not been investigated yet.

Although extensive knowledge on efflorescence at the macro-scale is available, the time-dependent development of salt crusts and the related pore-scale processes have been investigated in less detail. *Shokri-Kuehni et al.* (2017) showed that NaCl crusts on sand remained wet during the formation process using infrared radiation measurements of surface temperature. They suggested that the observed temperature fluctuations indicated the alternation of local evaporation (temperature decrease) and salt precipitation (temperature increase). They concluded that the water content of the salt crust is important for the liquid supply to the active pores. To understand the formation of the three-dimensional (3D) structure of efflorescent NaCl crusts, non-invasive images of the developing salt crust were obtained in situ using XRCT (*Nachshon et al.*, 2018). They found that the new porous NaCl structure initially formed an efflorescent layer on the surface of a sample as expected. However, they observed that a detached dome-shaped formation of salt crystals was formed with limited contact to the sample surface at a

few locations ("pillars") only with continued salt precipitation. Again, this was attributed to the reduced amount of active pores in the newly formed efflorescent layer and the properties of the NaCl solution and crystals (e.g. surface tension, hygroscopicity) (*Nachshon et al.*, 2018). This also suggests that evaporation may occur in the gaps between the sample surface and the detached salt crust, which further complicates interpretation. From the results of previous studies on the development of salt crusts, it is clear that the water content in and near the crust is important to understand evaporation as well as salt crust formation processes. Near-surface water content profiles obtained with XRCT of samples with NaCl solution showed a liquid connection to the surface shortly after the start of the evaporation (*Rad and Shokri*, 2014). They found that the water content quickly decreased at the surface and stayed close to saturation in the lower regions of the porous media.

Most research on efflorescent precipitation from evaporation of saline solutions has been focused on NaCl crust formation. The development of salt crusts from other types of salt has not been investigated so far. Other salts that occasionally precipitate on top of porous media (e.g. sodium sulfate (Na_2SO_4)) have mainly been studied with respect to their destructive subflorescent salt crust formation inside of porous media. Subflorescent precipitation is reviewed in more detail below.

1.2.3. Subflorescent salt crust formation

The occurrence of efflorescent or subflorescent salt crust formation depends on the type of salt and the ambient conditions. Whereas NaCl forms efflorescent crusts, magnesium sulfate (MgSO_4) is known to precipitate subflorescently (i.e., inside of the porous medium, see Figure 1.1b) (*Balboni et al.*, 2011; *Espinosa-Marzal and Scherer*, 2013). In the case of Na_2SO_4 , the ambient conditions mostly determine whether subflorescent or efflorescent precipitation occurs (*Scherer*, 2004; *Espinosa-Marzal et al.*, 2008; *Flatt et al.*, 2014). However, it is not generally known under which conditions (e.g., relative humidity, temperature, wind speed as well as properties of the surface and the pore space) subflorescence of Na_2SO_4 will occur (*Espinosa-Marzal and Scherer*, 2010). It should be noted that the crystal formation of both MgSO_4 and Na_2SO_4 involves different possible hydration states, which further complicates investigations of subflorescent salt precipitation.

Evaporation experiments with limestone samples suggested that pore clogging from Na_2SO_4 precipitation occurred preferably in small pores, which was determined by measuring the capillary uptake of decan of the dried sample (*Espinosa-Marzal and Scherer*, 2013). It was suggested that repeated hydration and dehydration of the crystals in response to changing ambient conditions might re-open the pore system. This allowed further evaporation and a further recession of the evaporation front into the porous medium, which may have enhanced subflorescent precipi-

tation (*Espinosa-Marzal and Scherer, 2013*). The destructive character of Na_2SO_4 precipitation inside building materials has been reported to depend strongly on the occurrence of multiple cycles of drying and re-wetting (*Flatt and Scherer, 2002; Tsui et al., 2003*). The resistance of a porous material to subflorescent salt precipitation can be determined with standardized tests of the tensile strength (*Flatt et al., 2014*). However, it was not investigated how the development of the subflorescent salt precipitation at the pore-scale affected evaporation, which is important to improve the fundamental understanding of the involved processes.

In the case of evaporation of MgSO_4 solution, a dense layer of salt formed at the surface of limestone samples, which reduced evaporation strongly (*Espinosa-Marzal and Scherer, 2013*). It was suggested that the high viscosity of the supersaturated MgSO_4 solution result in slow liquid flow to the surface and subflorescent crust formation (*Espinosa-Marzal and Scherer, 2010, 2013*). Also, the evaporation rate seemed to play an important role for the formation of MgSO_4 crusts (*Espinosa-Marzal et al., 2008; Espinosa-Marzal and Scherer, 2010, 2013*). It was suggested that more precise information on the location of the precipitates in the pores is needed to predict damage from subflorescent salt precipitation (*Espinosa-Marzal and Scherer, 2013*). In contrast to these results for building materials, it was reported that the evaporation of MgSO_4 solution at the solubility limit from sand columns was enhanced by the formation of a subflorescent crust (*Nachshon and Weisbrod, 2015*). This was attributed to the capillary liquid connection that was still provided during crust formation. The different findings concerning the flow and transport inside subflorescent MgSO_4 crusts (i.e., denser layer vs. enhanced evaporation) suggest that the transport properties of the evolving crust are closely related to the properties of the porous medium. However, it is not known under which conditions a crust from MgSO_4 solution enhances or reduces evaporation.

Available knowledge of the impact of subflorescent salt precipitation on evaporation is sparse, as most studies investigated efflorescent crust formation. However, the different location of the precipitates compared to efflorescence suggests that flow and transport properties of subflorescent crusts depend strongly on the porous medium. This suggests that the properties of subflorescent crusts need to be investigated in more detail with a focus on improving our understanding of water movement inside such crusts as well as salt crust formation.

1.2.4. Porosity and permeability of salt crusts

The partly contradictory observations described above suggest that the hydraulic properties of salt crusts, such as porosity, permeability, and water retention properties, are important to understand the evaporation from salt-affected porous media. Despite the wide range of studies on evaporation of saline solutions from porous media, the hydraulic properties of salt crusts have rarely been investigated. *Weisbrod et al. (2014)* performed micro-X-ray computed to-

mography (μ XRCT) measurements of pure sand and the associated salt crust developed from NaCl solution. After segmentation, they estimated the intrinsic permeability ($1.73 \cdot 10^{-11} \text{ m}^2$) of the packed sand using Lattice-Boltzmann modelling. The porosity of the sand was determined directly from the segmented μ XRCT data. After salt crust formation, the analysis of the segmented μ XRCT data using Lattice-Boltzmann modelling suggested a reduced porosity and permeability ($3.7 \cdot 10^{-12} \text{ m}^2$). Only the part of the sample consisting of sand with salt precipitation was investigated. The complicated structure of the efflorescent part of the NaCl crusts that is expected to have a major impact on evaporation (*Nachshon et al.*, 2018) was not analysed by *Weisbrod et al.* (2014). Clearly, it is of interest to determine the permeability of the entire NaCl crust including the complicated efflorescent structure because this will provide additional insights on how the crust permeability affects evaporation.

In a follow-up study on the permeability of salt crusts, evaporation experiments were performed using sand columns either saturated with deionized water, NaCl solution, or MgSO_4 solution at the solubility limit (*Nachshon and Weisbrod*, 2015). The permeability of all sand columns ($2 \cdot 10^{-10} \text{ m}^2$) prior to evaporation was determined using a constant head permeameter set-up. After evaporation and crust formation, the samples with crusts were resaturated using the corresponding saline solutions and the intrinsic permeability of the samples with salt crusts was determined again and used to estimate the permeability of the salt crusts itself. It was found that the mean intrinsic permeability of the crust from NaCl was $4 \cdot 10^{-12} \text{ m}^2$, which is one order of magnitude below the mean intrinsic permeability of the crusts from MgSO_4 ($3 \cdot 10^{-11} \text{ m}^2$). Both types of salt crust reduced the initial permeability of the sand, however to a different extent. This was also reflected in the evaporation, which decreased significantly due to the presence of the efflorescent NaCl crust. As already discussed, the subflorescent MgSO_4 crust seemed to enhance evaporation. In the presented approach using liquid flow to determine the intrinsic permeability of salt crusts, it is assumed that the permeability of the sand below the crust before and after evaporation and resaturation remains the same. However, it is well established that resaturation of a partially saturated porous sample with a liquid may lead to air entrapment and associated changes in flow and transport properties (*Jelinkova et al.*, 2011). As the intrinsic permeability of the resaturated reference sample with deionized water was not determined by *Nachshon and Weisbrod* (2015), it is not known to which extent air entrapment affected the measurements procedure using the constant head permeameter. Therefore, the presented crust permeability estimates need to be verified using independent methods. Additionally, the permeability of crusts from low initial solute concentration has not yet been investigated. This is of particular importance, as crust formation was found to be different for crusts that developed from a varying initial solute concentration (*Bergstad et al.*, 2017). In this context, there also is a need to provide more data on the permeability of subflorescent salt crusts for a better understanding of the flow and transport processes during

evaporation of saline water (*Espinosa-Marzal and Scherer, 2013*).

1.3. Aims and structure of the thesis

The literature review provided above suggests that there is a range of open research questions revolving around incomplete understanding of how salt precipitation affects evaporation. Thus, the overall aim of this thesis is to improve understanding of the impact of salt crusts on evaporation with a focus on the porosity, intrinsic permeability, and the spatial and temporal development of salt crusts. Three sub-objectives are defined to achieve this overall aim.

1. Compare the impact of different salt solutions on the evaporation from sand and analyse the role of the permeability of efflorescent and subflorescent salt crusts.
2. Establish a porosity-permeability relationship for subflorescent precipitation formed from evaporation of solutions with varying initial concentration.
3. Monitor the time-dependent development of subflorescent salt crust formation to improve understanding of how pore-scale processes affect evaporation.

The remainder of the thesis is organized as follows. Chapter 2 provides an overview of the theoretical concepts of evaporation from porous media and the experimental methods used to assess flow and transport in this thesis. First, flow in porous media is described and the stages of evaporation are presented, as well as specific properties of saline solutions and modelling concepts of multiphase flow. Then, experimental methods to determine the permeability of porous media are explained and non-invasive measurements techniques to determine the geometry of the pore space and the water content in porous media are introduced. Chapter 3 will address sub-objective 1. The evaporation and crust formation of NaCl, MgSO₄, and Na₂SO₄ solutions at 33% of the corresponding solubility limit will be investigated. A novel gas permeameter is presented that is used to determine the permeability of separated salt crusts. Liquid and gas flow measurements on the salt crusts will be performed and the obtained permeability of the crusts from both methods will be compared. Then, evaporation and permeability of the crusts from the different salt solutions will be analysed. Chapter 4 will address sub-objective 2. The porosity and the permeability of subflorescent MgSO₄ crusts formed from varying initial concentration will be determined. The permeability will be determined with the gas permeameter set-up introduced in Chapter 3 and the porosity will be obtained from μ XRCT data. The insights from the μ XRCT data will be related to the crust permeability, and the feasibility of establishing a porosity-permeability relationship for subflorescent MgSO₄ precipitation will be determined. Chapter 5 will address sub-objective 3. The time-dependent formation of subflorescent MgSO₄ crusts will be investigated using both sand and sintered glass samples. The pore

space will be analysed using registered μ XRCT data obtained after different times of evaporation. Additionally, the water content will be monitored using single-sided unilateral nuclear magnetic resonance (NMR) during evaporation. The experimental results will be interpreted to obtain insights on the dynamics of crust formation in both types of porous material. The thesis concludes with Chapter 6, which provides a synthesis of the findings and an outlook for future research.

Chapter 2

Theory and Background

This chapter consists of the three parts. In the first part, relevant theoretical concepts and definitions regarding porous media will be described in general. This will include scales, properties of porous media on the macro-scale, flow in porous media, and capillarity. In addition, differences in terminology and definitions from engineering and geosciences will be highlighted and explained.

In the second part, a detailed overview of theoretical concepts describing evaporation from porous media and the associated salt precipitation will be provided. To highlight the governing processes, mathematical modelling of evaporation and salt precipitation on the macro-scale will be described. Then, equilibrium and dynamic crystallization processes in saline solutions will be presented, which is important for understanding salt precipitation in porous media.

In the third and final part, established experimental methods to determine the hydraulic conductivity and permeability of porous media using liquid and gas flow will be briefly described. Finally, the basics of micro-X-ray computed tomography (μ XRCT) and nuclear magnetic resonance (NMR) measurements used for the non-invasive investigation of salt precipitation and water content distribution will be introduced.

2.1. Theoretical concepts and definitions

2.1.1. Porous media at different scales

Materials that consist of a solid matrix and pore structures are called porous media. The pore space is mostly filled with one or multiple fluids (liquid, gas, or both). In many engineering and scientific fields, it is important to consider the properties of a porous medium at different scales. Imaging techniques with a high spatial resolution such as X-ray computed tomography can provide helpful insights on the relevant processes on the micro- or pore-scale (*Wildenschild and Sheppard, 2013; Cnudde and Boone, 2013*) (Figure 2.1a). Many relevant porous media properties are prone to oscillate with changing volume at this micro-scale (*Class,*

2001) (Figure 2.1b). When the volume increases, this oscillation decreases. The smallest volume that does not show an oscillation of the property is called the representative elementary volume (REV) (Figure 2.1b). This bulk volume V_b indicates the transition from the micro- to the macro-scale. Most relevant applications that include measuring and modelling evaporation are described on REV- or macro-scale (Figure 2.1a). If the REV is chosen too small, the microscopic variability may still affect the averaged quantity (Figure 2.1b). It should be noted that the porosity and other averaged quantities such as permeability or phase volume fractions may show different REV's for the same porous medium. Therefore, the size of the REV must be chosen such that each relevant property is not affected by increasing or decreasing scale anymore (*Helmig, 1997*).

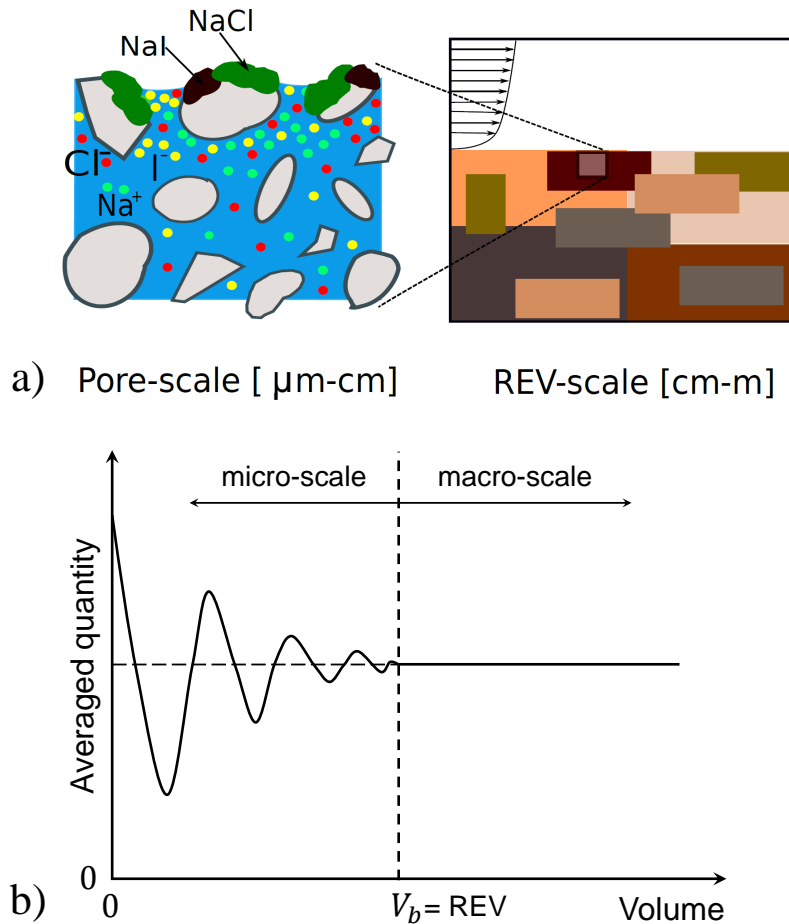


Figure 2.1: (a) Schematic picture of pore and REV-scale in porous media coupled with free-flow (modified from *Jambhekar (2017)*). The shown solutes are sodium (Na^+), chloride (Cl^-), and iodide (I^-), which occur on the molecular scale. The precipitates are sodium chloride (NaCl) and sodium iodide (NaI). (b) Definition of macro- and micro-scale with the help of a representative elementary volume (REV) (modified from *Class (2001); Bear (1972)*).

2.1.2. Definitions at the macro-scale

A porous medium consists of pores (voids) and a solid matrix so that the porosity ϕ in a REV of the porous medium is defined as

$$\phi = \frac{V_{\text{void}}}{V_b}, \quad (2.1)$$

where V_{void} is the volume of the void space and V_b is the bulk volume of the REV (*Helmig, 1997*). In this thesis, two phases are considered in the void space (i.e., gas (g) and liquid (l)). The saturation of these phases is defined as

$$\chi_\alpha = \frac{V_\alpha}{V_{\text{void}}} \quad \forall \alpha \in \{l, g\}, \quad (2.2)$$

where V_α is the volume of the respective phase and V_{void} is the volume of the void space in the corresponding REV. By definition, the sum of the saturation of the gas phase χ_g and the saturation of the liquid phase χ_l is equal to one:

$$\chi_g + \chi_l = 1. \quad (2.3)$$

It should be noted that from now on "saturation" refers to liquid saturation if not indicated differently. The volumetric water content of a bulk volume is defined as

$$\theta = \frac{V_l}{V_b}. \quad (2.4)$$

2.1.3. Flow in porous media

Flow in saturated porous media is described with a generalized form of Darcy's law, which is valid when the flow velocity is sufficiently low to ensure laminar flow conditions (*Whitaker, 1986*):

$$\mathbf{q} = -\frac{\mathbf{k}}{\mu} [\nabla p - \rho \mathbf{g}], \quad (2.5)$$

where \mathbf{q} [m/s] is the flux density, \mathbf{k} [m²] is the intrinsic permeability tensor, μ [Pa·s] is the fluid viscosity, ∇p [Pa/m] is the pressure gradient in three dimensions, ρ [kg/m³] is the fluid density, and \mathbf{g} [m/s²] is the gravitational acceleration vector. One-dimensional isotropic flow is considered from now so that only the vertical component of the flux density (q [m/s]), the gravitational acceleration vector (g [m/s²]), and the intrinsic permeability (k [m²]) remain. It should be noted that the intrinsic permeability is a macroscopic property of the porous medium only (*Hillel, 2003*).

If multiple fluids are present, Darcy's law for multiple phases is used to describe flow in porous media:

$$q_\alpha = -\frac{k_{r\alpha}}{\mu_\alpha} k [\nabla p_\alpha - \rho_\alpha g] \quad \forall \alpha \in \{l, g\}, \quad (2.6)$$

where $k_{r\alpha}$, μ_α , p_α , and ρ_α are the relative permeability, the viscosity, the pressure, and the density of phase α , respectively, k [m²] is the intrinsic permeability in vertical direction and g [m/s²] is the gravitational acceleration in vertical direction. The use of Equation 2.6 requires the specification of constitutive relationships for water retention and relative permeability, and the approach of *Van Genuchten* (1980) and *Mualem* (1976) is widely used for this. In this approach, the relative permeability is described by (*Mualem*, 1976):

$$k_{rl} = \sqrt{\chi_e} \left[1 - \left(1 - \chi_e^{\frac{1}{m}} \right)^m \right]^2, \quad (2.7)$$

for liquid and

$$k_{rg} = (1 - \chi_e)^{\frac{1}{3}} \left[1 - \chi_e^{\frac{1}{m}} \right]^{2m}, \quad (2.8)$$

for gas, where m [-] is the shape parameter from the water retention function (see below). The effective phase saturation χ_e is defined as

$$\chi_e = \frac{\chi_l - \chi_{lr}}{1 - \chi_{lr}}, \quad (2.9)$$

where χ_{lr} is the residual liquid saturation (*Jambhekar et al.*, 2015). The water retention of a porous medium is described by (*Van Genuchten*, 1980)

$$\theta = \theta_{lr} + \frac{\theta_{\text{sat}} - \theta_{lr}}{(1 + (\alpha' p)^{n'})^m}, \quad (2.10)$$

where θ_{lr} is the residual water content (i.e., amount of water that remains in the void space at high tension), θ_{sat} is the saturated water content (i.e., porosity ϕ). α' is inversely related to the air-entry pressure, and n' and $m = 1 - 1/n'$ are empirical shape parameters.

The above formulations use pressure with the dimension of [Pa], which results from the use of a potential on the basis of volume. In soil physics and hydrogeology, a potential definition on the basis of weight is preferably used (*Hillel*, 2003), which is then sometimes called head. With this potential definition, water flows along the gradient of the total potential head or hydraulic head H , which is described with the convenient unit of [m] (*Hillel*, 2003). In another definition of the total potential ψ , energy is related to mass with the dimension of [J/kg], which is equivalent to the hydraulic head $H = \psi/g$ via the gravitational acceleration. In this thesis, the total potential head H is assumed to consist of the gravitational potential ψ_z , the pressure potential

ψ_h and the osmotic potential ψ_o (i.e., $H = (\psi_z + \psi_h + \psi_o)/g$). The gravitational potential ψ_z results from the vertical level of the soil water in the gravitational field. A positive pressure potential ψ_h is called hydrostatic potential, whereas a negative pressure potential (i.e., suction) is called matric potential. The osmotic potential ψ_o results from the presence of solutes in the soil water. In this formulation, water flow through soil in vertical direction z can be described using the original relationship provided by Henry Darcy (*Darcy*, 1856):

$$q = -K_S(h_w) \frac{dH}{dz}, \quad (2.11)$$

where K_S is the hydraulic conductivity that depends on the matric potential head $h_w = \psi_h/g$ and thus on the properties of both the porous medium and the fluid. The hydraulic conductivity of saturated porous media K_S can be converted into the intrinsic permeability k of the sample using (e.g. *Kasenow* (2002))

$$k = \frac{K_S \mu}{\rho g}. \quad (2.12)$$

2.1.4. Contact angle and capillary pressure

The gas and the liquid phase will be considered as two fluids. The gas phase is treated as one (pseudo) component that consists of air and water vapor. The liquid phase consists of water that can contain solutes. The amount of gas dissolved in water is neglected. The spatial distribution of the two fluid phases in a porous medium depends on the wetting properties of the fluids with respect to the matrix, which is determined by the contact angle. If a drop of liquid is considered on a solid surface in the presence of a gas phase in equilibrium (Figure 2.2a), the liquid, the gas phase, and the solid phase form a force balance at the contact line between the phases (e.g. *Green and Perry* (2008a)):

$$\frac{\gamma_{sg} - \gamma_{sl}}{\gamma_{lg}} = \cos \varphi, \quad (2.13)$$

where γ_{sg} [J/m²] is the surface energy of the solid-gas interface, γ_{sl} [J/m²] is the surface energy of the solid-liquid interface, and γ_{lg} [J/m²] is the surface energy of the liquid-gas interface (i.e., the surface tension of the liquid [N/m = J/m²]). The so-called contact angle φ is formed at the three-phase contact line (Figure 2.2a). The attraction of water molecules to each other (cohesion) is stronger than the attraction between air and water molecules (adhesion), which causes the curved surface.

Typically, the liquid is the wetting (w) phase and the gas phase is the non-wetting (nw) phase. Therefore, the contact angle of the wetting liquid commonly is smaller than 90° (Figure 2.2a). The attraction of the wetting phase to the (solid) surface is the source of the so-called capillary

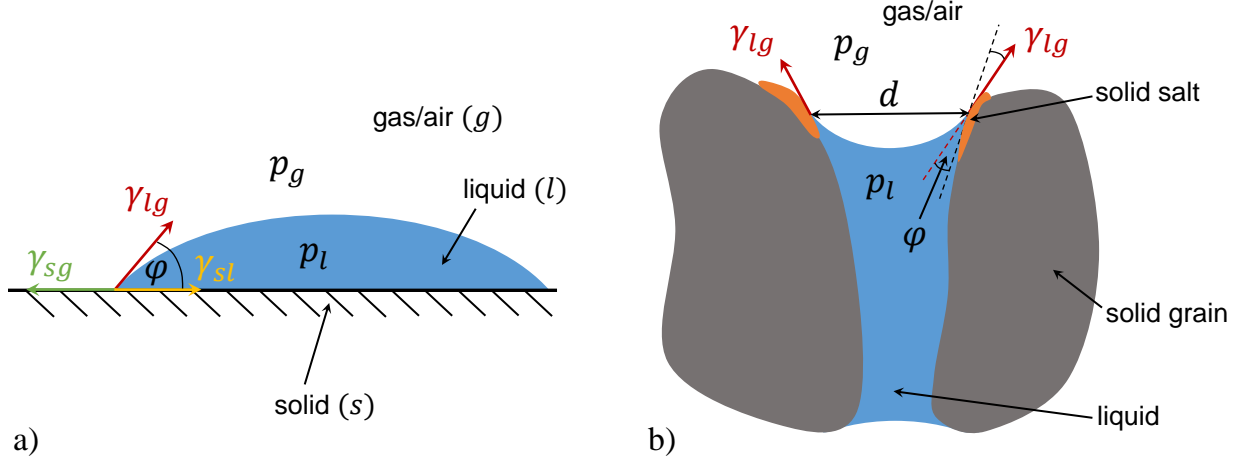


Figure 2.2: (a) Illustration of the contact angle of a wetting liquid on a solid surface with air as non-wetting phase. γ is the surface energy of the interface between solid-gas (sg), solid-liquid (sl), and liquid-gas (lg). (b) Capillary pressure $p_c = p_g - p_l$ as difference between the pressure of the gas and the liquid phase in a pore between sand grains (modified from *Jambhekar (2017)*).

pressure that occurs for example in a capillary with a small diameter. The capillary pressure p_c is defined as the difference in pressure between the gas (g) and the liquid (l) phase (*Green and Perry, 2008a*). If (nearly) cylindrical pores are assumed, this pressure difference is equal to the pore diameter d , the contact angle φ , and the surface tension γ_{lg} (i.e., the Young-Laplace equation, e.g. *Green and Perry (2008b)*):

$$p_c = p_g - p_l \approx \frac{4\gamma_{lg} \cos \varphi}{d}. \quad (2.14)$$

It should be noted that in a porous medium, the capillarity allows the filling of pores with liquid above the actual liquid level against the force of gravity. Figure 2.2b illustrates the interactions at the interface of all phases in a pore. If salt precipitation is present inside the porous medium, it is important to note that the contact angle changes with the interfacial properties of the (precipitating) solid. Additionally, the reduced pore diameter due to precipitation affects the capillary pressure (see Equation (2.14)). This affects the transport of water molecules from the liquid to the gas phase. Other mechanisms that affect evaporation are described below.

2.2. Evaporation and salt precipitation

2.2.1. Stages of evaporation of deionized and saline water

The evaporation of deionized water from natural porous media can be divided into two stages that were already briefly introduced in Chapter 1 (stage I and II, see Figure 2.3b) (*Lehmann*

et al., 2008; *Or et al.*, 2013). In stage I, liquid is provided to the surface through capillary connections, where it evaporates at a high rate to meet the atmospheric demand of water vapor. This demand is the driving force of evaporation and can be expressed by

$$e \propto p_{\text{sat}}^{\text{H}_2\text{O}}(T) - p_{\text{amb}}^{\text{H}_2\text{O}}, \quad (2.15)$$

which shows that the evaporation rate e is proportional to the difference of the saturation vapor pressure of water directly above the surface $p_{\text{sat}}^{\text{H}_2\text{O}}(T)$ and the vapor pressure of water in the ambient air $p_{\text{amb}}^{\text{H}_2\text{O}}$ (*Scherer*, 1990). The saturation vapor pressure depends on the local temperature T and the water vapor pressure of the ambient air is related to the relative humidity defined as $RH = p_{\text{amb}}^{\text{H}_2\text{O}}/p_{\text{sat,air}}^{\text{H}_2\text{O}}(T)$. The pressure $p_{\text{sat,air}}^{\text{H}_2\text{O}}(T)$ is the saturation vapor pressure of the ambient air that might be different from the saturation vapor pressure at the surface $p_{\text{sat}}^{\text{H}_2\text{O}}(T)$ due to non-isothermal effects during evaporation at the micro-scale. Previous studies have shown that the evaporation rate during stage I is relatively high but not necessarily constant (*Lehmann et al.*, 2008; *Shahraeeni and Or*, 2012a,b; *An et al.*, 2018). This is related to the non-linear relation between the vapor pressure field above actively evaporating pores and the reduced number of actively evaporating pores with time due to progressing invasion by air (*Lehmann et al.*, 2008; *Or et al.*, 2013). Stage I of evaporation continues as long as capillary forces provide a liquid connection to the surface of the porous medium. When the capillary pressure increases due to a decreasing liquid pressure from evaporation (Equation (2.29)), the gas phase pressure exceeds the liquid pressure and pores are invaded with air (*Lehmann and Or*, 2009). The air invasion first occurs in the large pores, as their air-entry pressure is smaller compared to small pores (*Lehmann and Or*, 2009). In this case, the evaporation front (better evaporation zone, i.e., the location of the transition of water from liquid to gas) moves down into the porous medium. Small pores still provide liquid to the surface supporting the relatively high evaporation rate (*Lehmann et al.*, 2008; *Or et al.*, 2013). When capillarity is not able to provide a liquid connection to the surface anymore, the evaporation rate drops sharply. This indicates the transition to stage II of evaporation (Figure 2.3b). The evaporation front is now disconnected from the surface and moves further down into the porous medium. In stage II, the limiting water transport mechanism responsible for the much lower evaporation rate is vapor diffusion from the evaporation front to the surface of the porous medium.

In the absence of a continuous liquid supply from below, the evaporation of saline water from porous media can be separated in three stages (SS1, SS2, and SS3) (*Nachshon et al.*, 2011b,a; *Jambhekar et al.*, 2015). Again, these stages are defined using the cumulative mass loss and the evaporation rate (see Figure 2.3). However, the relevant processes are partly different from the processes determining the evaporation of deionized water. In stage SS1, the initial evaporation rate of saline water is lower than that of deionized water due to the reduced

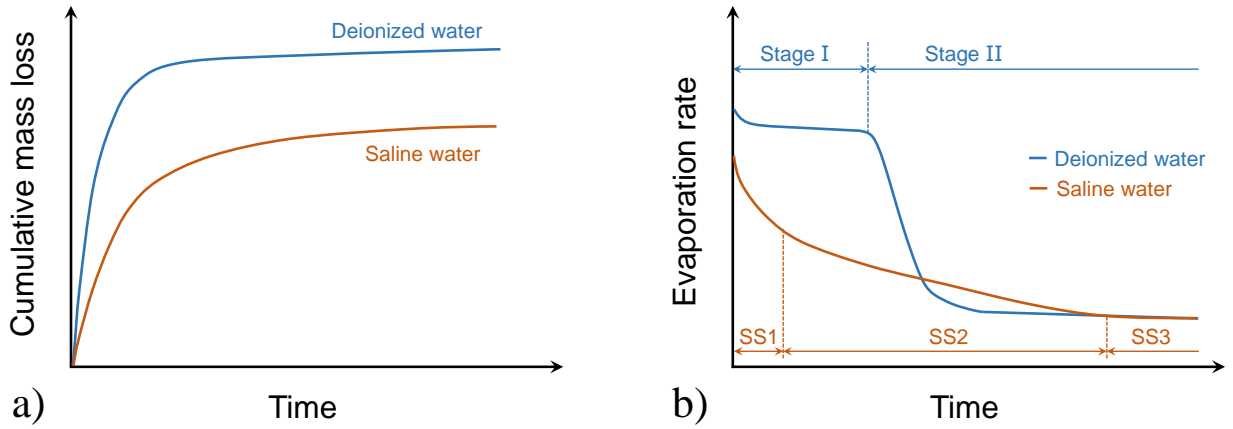


Figure 2.3: Schematic illustration of the temporal development of the (a) cumulative mass loss and (b) evaporation rate during the evaporation of deionized and saline water from porous media. The different stages for the evaporation of deionized water (I, II) and saline water (SS1-SS3) are also indicated.

saturation pressure of the saline solution ($p_{\text{sat}}^{\text{sol}} < p_{\text{sat}}^{\text{H}_2\text{O}}$, see Equation (2.15)) (Rad and Shokri, 2012; Jambhekar et al., 2015, 2016). With progressing evaporation in stage SS1, this saturation pressure further decreases because salt ions accumulate in the solution at the surface while water evaporates, which further reduces the evaporation rate. The transition to stage SS2 occurs when the local limit for the ion concentration of the liquid is reached and salt crystals start to form. The formation of salt crystals further reduces evaporation by reducing the available pore space, although capillarity may still provide a liquid connection to the surface (Veran-Tissoires and Prat, 2014; Shokri-Kuehni et al., 2017). With progressing evaporation, stage SS3 is reached. This stage is characterized by a low evaporation rate, which originates either from the disconnection of the capillary connection to the surface or from the crust that builds a barrier for water transport at the surface (Nachshon et al., 2011b; Jambhekar et al., 2015). It should be noted that salt precipitation during stage SS2 and SS3 changes the structure of the pore space and therewith the flow and transport properties (i.e., capillary pressure, see Figure 2.2b) (Espinosa-Marzal et al., 2008), which results in complex interactions between solution and porous medium properties on the micro- and macro-scale.

2.2.2. Evaporation in mathematical models

modelling evaporation of deionized water from porous media on the REV-scale provides knowledge of mass and energy fluxes across the interface between the ambient air and the porous medium and allows predictions of evaporation rates and water content profiles. This helps to understand the underlying processes and, therefore, concepts to model evaporation from porous media are presented in the following. Different modelling concepts to describe heat and water

transport in porous media and at the surface of the porous medium on the REV-scale were reviewed by *Vanderborght et al.* (2017). The effects of the simplifying assumptions in these modelling concepts were discussed using numerical examples by *Fetzer et al.* (2017). The most advanced modelling concepts consider two fluid phases (gas and liquid) and two components (dry air and water) and use Fickian or Maxwell diffusion as well as multi-phase Darcy flow in non-isothermal conditions. Simplified models using one component (water) in the liquid and diffusive fluxes in the gas phase (dry air and water) are also available, and have been used in non-isothermal as well as isothermal conditions. The most simplified model concept relies on the assumption that only one phase (liquid) and one component (water) is flowing, which is affected by the presence of air and is modeled by the Richard's equation. The free-flow domain (i.e., the air above the porous medium) is usually described using the mass balance, the Reynolds-averaged Navier-Stokes-equations, or component and energy balances in one-dimensional (1D) steady-state (*Vanderborght et al.*, 2017). The coupling of free-flow domain to the porous media domain includes heat, mass, and momentum transfer which are modeled assuming thermal, chemical, and mechanical equilibrium, respectively. Different (semi-)empirical and theoretical coupling conditions are available, and the interested reader is referred to literature (*Beavers and Joseph*, 1967; *Eggenweiler and Rybak*, 2021) for more information. Often, the use of a simplified one-dimensional flow and transport description is justified for homogeneous porous media with a sufficiently large surface because lateral variation in the free-flow domain is small (*Vanderborght et al.*, 2017). However, (lateral) vapor transport in the porous medium becomes important when an evaporation front develops (i.e., during stage II) (*Fetzer et al.*, 2017), which shows that advanced modelling concepts are necessary to describe the evaporation process in detail for dry conditions. In addition, lateral vapor transport was found to be important for heterogeneous porous media and especially for the coupling conditions of the porous to the free-flow domain (*Vanderborght et al.*, 2017).

2.2.3. Modelling salt precipitation during evaporation

The mathematical description of salt precipitation during evaporation from porous media at the REV-scale is useful to understand how changes in porosity and permeability affect evaporation. Models were formulated based on concepts of modelling deionized water evaporation in previous studies (*Jambhekar et al.*, 2015, 2016; *Jambhekar*, 2017; *Mejri et al.*, 2017, 2020). A fully coupled non-isothermal multi-phase model that consists of a porous media domain below a free-flow domain and that considers salt precipitation was presented by *Jambhekar et al.* (2015). It showed good agreement with experimental data during the early stage and late stage of evaporation. The remaining differences between measured and simulated evaporation were attributed to the simplified representation of the effect of salt precipitation on the porosity and

permeability of the porous media, which will be discussed in more detail below. In a follow-up study, the model of *Jambhekar et al.* (2015) was extended to consider the precipitation of multiple types of salt ions using a kinetic approach proposed by *Mayer et al.* (2002) (*Jambhekar et al.*, 2016; *Jambhekar*, 2017). This kinetic approach to describe salt precipitation was further extended to heterogeneous porous media by *Mejri et al.* (2017). It was found that heterogeneity in porous media properties significantly affected the spatial and temporal development of salt precipitation (e.g. precipitation along sharp vertical textural interfaces). The extended model was able to reasonably describe evaporation and salinization data from field measurements (*Mejri et al.*, 2020).

A key aspect of modelling salt precipitation is the potential feedback with the hydraulic properties. The precipitation of solid salt (superscript s) is commonly modeled as a source/sink in the mass balance equation (*Jambhekar et al.*, 2015, 2016; *Jambhekar*, 2017):

$$\frac{\partial(\phi_s^s \rho_{\text{mol},s}^s)}{\partial t} = r_p \phi \rho_{\text{mol},l} \chi_l (x_l^s - x_{l,\text{max}}^s), \quad (2.16)$$

where ϕ_s^s [-] is the volume fraction of solid salt, ρ_{mol}^s [mol/m³] is the molar density of salt (superscript s) and liquid brine (subscript l), respectively, χ_l [-] is the liquid saturation, r_p [1/s] is the precipitation rate constant, and x_l^s is the mole fraction of salt in liquid. The solubility limit of the salt is represented by $x_{l,\text{max}}^s$ (*van Duijn and Pop*, 2004). The reduction in porosity due to precipitation is taken into account using

$$\phi = \phi_0 - \phi_s^s, \quad (2.17)$$

where ϕ_0 is the initial porosity of the REV. The reduction in porosity due to salt precipitation affects the intrinsic permeability of porous media. So-called porosity-permeability relationships are widely used on the REV-scale to estimate the impact of the decrease in porosity on the intrinsic permeability. One prominent porosity-permeability relationship is the Kozeny-Carman relationship (*Kozeny*, 1927; *Carman*, 1937) that can be written as (*Hommel et al.*, 2018):

$$k = \frac{\Phi_S^2 d_p^2}{180} \frac{\phi^3}{(1 - \phi)^2}, \quad (2.18)$$

where Φ_S is a dimensionless particle geometry parameter (i.e., sphericity) and d_p is the characteristic particle diameter. Equation (2.18) was derived for single phase flow through spherical, packed sand particles with similar grain surface and radius (*Kozeny*, 1927; *Carman*, 1937; *Hommel et al.*, 2018). It was assumed that the matrix does not change in shape and composition during flow and only a reduction in pore space due to precipitation is considered. Reformulating Equation (2.18) using more relevant parameters for natural porous media leads to

$$k = \frac{\phi^3}{\tau(1 - \phi)^2 A_{\text{spec}}^2}, \quad (2.19)$$

where τ is the tortuosity and A_{spec} [m^2/m^3] is the specific surface area (*MacQuarrie and Mayer, 2005*). In studies dealing with changes in the pore space due to dissolution and precipitation, the permeability is often related to an initial reference condition of the porous medium (*Jambhekar, 2017*):

$$k = k_0 \left(\frac{\phi}{\phi_0} \right)^3 \left(\frac{1 - \phi_0}{1 - \phi} \right)^2, \quad (2.20)$$

where k_0 is the unaltered intrinsic permeability of the porous medium.

Despite their widespread use in reactive transport modelling, it is important to realize that there are a range of strong simplifying assumptions when using porosity-permeability relationships. First, it is important to consider that the use of Equation (2.20) or other porosity-permeability relationships relies on the assumption that the porous matrix is not altered by precipitation (*Hommel et al., 2018*). Second, the assumptions of the Kozeny-Carman relationships are simplified with respect to heterogeneous porous media. Third, the Kozeny-Carman model often significantly underestimates the reduction in permeability because the change of the pore geometry due to chemical reactions is not considered (*MacQuarrie and Mayer, 2005*). Thus, it is clear that the position of the precipitation in the pore space is of importance for flow and transport and for more reliable predictions using porosity-permeability relationships (*Hommel et al., 2018*). This was illustrated by *Ghezzehei (2012)*, who showed that the shape and distribution of the salt crystals in the pore space have a significant impact on the permeability at the REV-scale. *Ghezzehei (2012)* also emphasized that the impact of hydrodynamics on the precipitation process was not yet considered, and that this would require a multiscale-multiphysics modelling approach combined with experimental parameter estimation. Therefore, it is of interest to investigate if porosity-permeability relations that are used in modelling approaches can be validated using experimental measurements.

2.2.4. Phase diagrams of salt solutions

During evaporation of water from saline solutions, the formation of salt crystals represent a phase transition. Phase diagrams of different types of salts can be used to describe the transition from a dissolved to a solid (crystal) state at equilibrium conditions. Figure 2.4 shows the phase diagram of aqueous NaCl solution. The water activity a_w is defined as the ratio of the (reduced) saturation vapor pressure of a saline solution to the saturation vapor pressure of deionized water at the same conditions. This should not be confused with the relative humidity, which is the ratio of the partial pressure of water in the gas phase and the saturation vapor

pressure of deionized water. In the temperature range relevant for this study (20 °C to 30 °C), NaCl precipitates in the form of halite (i.e., the classical NaCl crystal) from aqueous solution. Thus, only one morphological form of the NaCl crystal is expected to be present in the NaCl salt crusts investigated in this study.

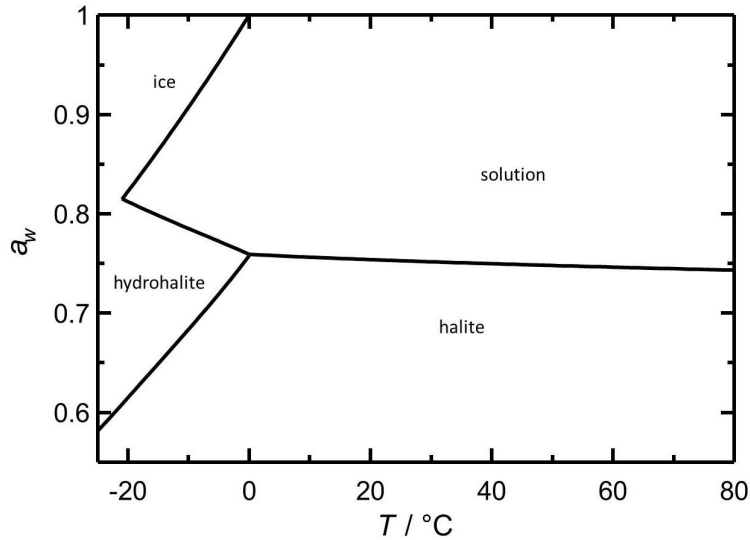


Figure 2.4: Phase diagram of aqueous NaCl solution as a function of water activity a_w and temperature T (from Steiger *et al.* (2008)).

In contrast to NaCl, multiple hydrated MgSO_4 crystals may form depending on the ambient conditions (Steiger *et al.*, 2011b). In most non-equilibrium conditions, $\text{MgSO}_4 \cdot 6\text{H}_2\text{O}$ and $\text{MgSO}_4 \cdot 7\text{H}_2\text{O}$ precipitate directly from aqueous solution (Balboni *et al.*, 2011), which may transform into hydrated crystals that include less H_2O molecules if the conditions approach equilibrium. At laboratory conditions ($T = 25^\circ\text{C}$, $RH = 30\text{-}40\%$) and assuming equilibrium, the dominant crystal is expected to be $\text{MgSO}_4 \cdot 4\text{H}_2\text{O}$ (Steiger and Asmussen, 2008; Steiger *et al.*, 2011b), with a density of 2.01 g/cm^3 (Baur, 1964) (see Figure 2.5).

In the case of Na_2SO_4 , five anhydrous polymorphous phases exist (I-V), of which phase I, II, and IV are known to occur at high temperatures only (Steiger and Asmussen, 2008). The stable phase V forms preferably at lower temperatures. Phase III is metastable, but has been found during evaporation experiments from porous media (Steiger and Asmussen, 2008). Additionally, two hydrated crystals occur, $\text{Na}_2\text{SO}_4 \cdot 7\text{H}_2\text{O}$ and $\text{Na}_2\text{SO}_4 \cdot 10\text{H}_2\text{O}$, of which the latter is the dominant form at room temperature and relative humidity below 60% at equilibrium (see Figure 2.6). However, evaporation experiments performed at room temperature and relative humidity below 40% confirmed that $\text{Na}_2\text{SO}_4(\text{V})$ and $\text{Na}_2\text{SO}_4(\text{III})$ precipitated directly from supersaturated solution (Rodriguez-Navarro *et al.*, 2000).

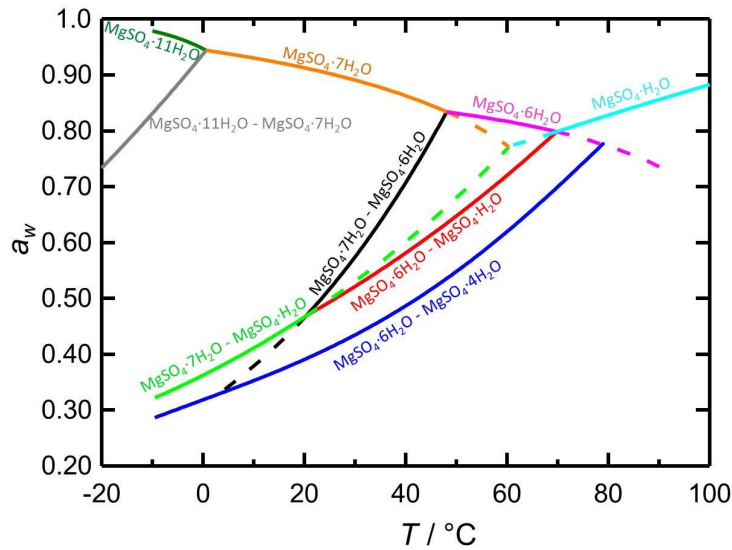


Figure 2.5: Phase diagram of aqueous MgSO_4 solution as a function of water activity a_w and temperature T (from Steiger *et al.* (2011b)).

2.2.5. Supersaturation and nucleation

The phase diagrams of different salt solutions (Figure 2.4, Figure 2.5, and Figure 2.6) describe the solubility limit depending on temperature and water activity in equilibrium. It is important to note that this equilibrium is not reached instantaneously. In fact, as long as water evaporates at a high rate from the porous medium, the accumulation of ions will continue even if the solubility limit is locally reached. This results in a supersaturated liquid in a meta-stable state where the ion concentration is higher than the solubility limit of the solution (Green and Perry, 2008c). This supersaturation is necessary for both the nucleation and the growth of crystals. Nucleation is the formation of very small salt crystals that provide the starting point for crystal growth. Nucleation that occurs out of the solution without external impact is called homogeneous or primary nucleation. Heterogeneous or secondary nucleation results from nucleation seeds (e.g. particles, gas bubbles), surface charge, or the geometry of the domain (e.g. surface roughness, contact of grains). For example, a smooth surface may reduce heterogeneous nucleation (Scherer, 2004). Surface charge of hydrophilic or hydrophobic materials may govern attractive or repulsive interaction between the brine phase and grain surface, which also affects heterogeneous nucleation (Scherer, 2004; Espinosa-Marzal and Scherer, 2010).

The growth of crystals also depends on the presence of supersaturated solution, which provides solutes that are incorporated into the crystal structure (Scherer, 2004). Therefore, a liquid connection to the active pores is crucial for evaporation and salt crust formation. The supply

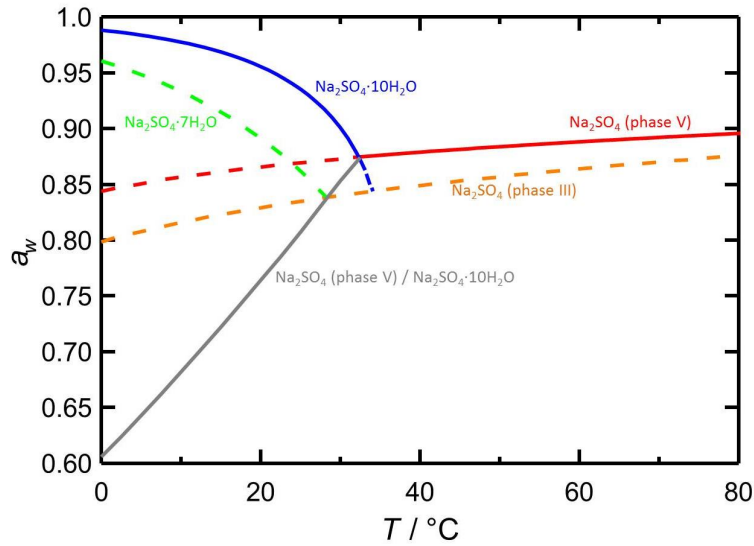


Figure 2.6: Phase diagram of aqueous Na_2SO_4 solution as a function of water activity a_w and temperature T (from *Steiger and Asmussen* (2008)).

of liquid to the surface is affected by the fluid properties of the supersaturated salt solution, such as the viscosity, surface tension, and vapor pressure (*Rodriguez-Navarro and Doehne*, 1999). Therefore, the type of solute and the resulting salt crystal have a significant impact on nucleation and crystal growth, which is also reflected in the formation of efflorescent and subflorescent salt crusts (*Espinosa-Marzal et al.*, 2008). Furthermore, the extent to which supersaturation can occur for a given solute can affect the nucleation rate (*Espinosa-Marzal and Scherer*, 2010).

It was shown that evaporation of MgSO_4 solution resulted in precipitates inside of dolomitic limestones (i.e., subflorescent precipitation) (*Balboni et al.*, 2011). The occurrence of subflorescent precipitation was mainly attributed to the high viscosity of the supersaturated MgSO_4 solution that retarded the capillary flux to the evaporation sites at the surface. Additionally, the high viscosity of the supersaturated solution also resulted in a decrease of the nucleation rate (*Espinosa-Marzal and Scherer*, 2010), which further hindered the start of precipitation from aqueous solution. After the start of salt precipitation, pores near the surface were clogged by crystal formation and evaporation was reduced. If the liquid supply was disconnected from the salt crystals, pore clogging could have led to a decreased hydration or to deliquescence (i.e., the dissolution of the crystal within the incorporated water due to changes in ambient conditions) of the crystals that were already formed (*Espinosa-Marzal and Scherer*, 2013). It was suggested that deliquescence may lead to reopening of clogged pores and an associated increase of evaporation (*Espinosa-Marzal and Scherer*, 2010). However, detailed pore-scale

investigations on such re-opening have not been performed yet.

In the case of Na_2SO_4 , it was found that the evaporation rate showed a major impact on the type of salt crust (efflorescent or subflorescent) that is formed (*Rodriguez-Navarro and Doehne, 1999*). Na_2SO_4 is known to be one of the most damaging salts in concrete, stones, and bricks and standardized tests are used to investigate the destructive impact of subflorescent salt precipitation (*Flatt et al., 2014*). The major cause of damage from Na_2SO_4 precipitation in porous materials arises during cycles of drying and re-wetting of Na_2SO_4 crystals (*Flatt and Scherer, 2002; Tsui et al., 2003*). This is again related to the (meta-stable) precipitation of Na_2SO_4 (III and V) directly from aqueous solution. The dissolution of Na_2SO_4 (III and V) creates a high over saturation with respect to $\text{Na}_2\text{SO}_4 \cdot 10\text{H}_2\text{O}$, and the subsequent precipitation of $\text{Na}_2\text{SO}_4 \cdot 10\text{H}_2\text{O}$ generates stresses.

2.3. Background for used experimental methods

2.3.1. Determination of the intrinsic permeability of porous media

Knowledge of the intrinsic permeability is necessary to describe flow and transport in porous media in the context of evaporation and salt precipitation. The intrinsic permeability can be determined experimentally using established liquid flow measurement techniques (*Reynolds and Elrick, 2002a; Hillel, 2003*). Figure 2.7 shows a sketch of the experimental set-up for the widely used constant-head method (i.e., a constant head permeameter). A reservoir with a constant water level provides liquid that flows upwards through a sample with cross-sectional area A . The flow rate Q is obtained from the volume of outflow in a given amount of time after saturation has been reached. The amount of outflow can be determined volumetrically or gravimetrically. Using Equation (2.11), the difference of the hydraulic head ΔH over the sample length h provides the saturated hydraulic conductivity:

$$K_S = \frac{Q}{A} \frac{h}{\Delta H}. \quad (2.21)$$

This hydraulic conductivity K_S can be converted to the intrinsic permeability of the sample k using Equation (2.12).

The intrinsic permeability of porous media with efflorescent or subflorescent salt crusts can be determined using the procedure proposed by *Nachshon and Weisbrod (2015)*. In this procedure, samples without crust are prepared and the hydraulic conductivity K_S is determined using a constant-head permeameter set-up. Next, the samples are allowed to evaporate to form a salt crust. After the formation of a salt crust, the samples are resaturated and the hydraulic conductivity of the entire sample including the crust is determined again. The unknown per-

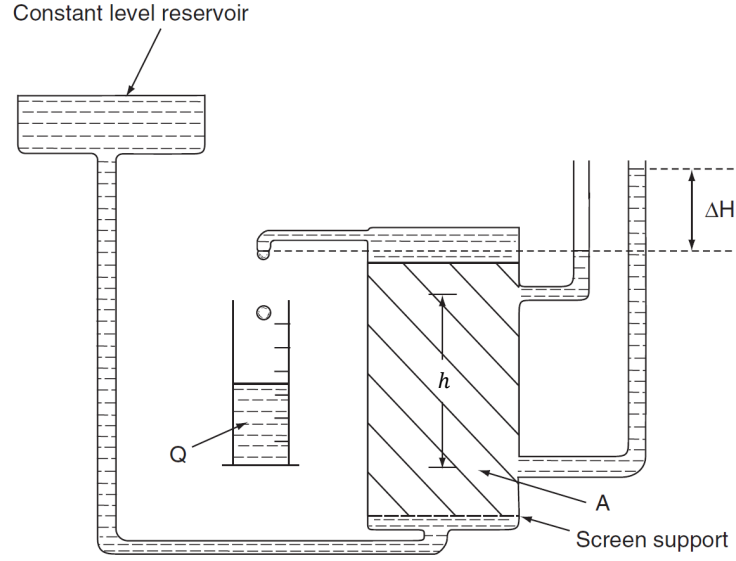


Figure 2.7: Constant head set-up to determine the hydraulic conductivity of a sample by measuring the upward flow (from *Hillel* (2003)). Q is the flow rate, A is the cross-sectional area of the sample and ΔH is the difference of the hydraulic head over the sample length h .

meability of the salt crust k_{crust} can then be calculated assuming a connection in series (*Hillel*, 2003; *Nachshon and Weisbrod*, 2015):

$$k_{\text{crust}} = \frac{s_{\text{crust}}}{\frac{h_{\text{total}}}{k_{\text{total}}} - \frac{h_0}{k_0}}, \quad (2.22)$$

where s_{crust} is the thickness of the crust, h_{total} is the length of the entire sample with crust, k_{total} is the permeability of the entire sample with crust, and h_0 and k_0 are the length and the permeability of the initial sample without crust, respectively.

The use of Equation (2.11) and (2.21) is only valid for laminar (Darcy) flow conditions that occur for sufficiently low flow velocities. These conditions are described by the Reynolds number, which is defined as the ratio of the inertial forces to the viscous forces in liquids (*Reynolds*, 1894). *Chilton and Colburn* (1931) proposed the following definition for the Reynolds number Re for flow through a tube with packed particles:

$$Re = \frac{\rho u_0 d_p}{\mu}, \quad (2.23)$$

where d_p is the mean particle diameter (i.e., characteristic length of the particle) and u_0 is the superficial velocity of the fluid that equals the volumetric flow rate per area Q/A (i.e., the flux density q). Non-viscous/non-Darcy flow in porous media can be expected when Re exceeds 40. It was shown that Equation (2.23) also applies to loosely consolidated sand (*Zeng*

and Grigg, 2006). A simple calculation example illustrates that Darcy flow can be expected for most constant-head flow experiments. *Nachshon and Weisbrod* (2015) used sand with a particle diameter of 384 μm and obtained a flux density of $4.35 \cdot 10^{-5}$ m/s. If the density (1000 kg/m^3) and the viscosity (1 mPas) of water are used, a Reynolds number of $Re = 0.015$ is obtained using Equation (2.23). This is well below the critical threshold of $Re = 40$, and Darcy flow conditions can thus safely be assumed. A limitation of the constant head approach shown in Figure 2.7 is the possibility of (sand) sample deformation during flow, especially when using higher flow velocities or in the presence of a salt crust with lower intrinsic permeability at or near the sample surface (*Nachshon and Weisbrod*, 2015).

The determination of the intrinsic permeability of salt crusts using liquid flow can be prone to uncertainty due to air entrapment during resaturation of the sample. To avoid this, a simple laboratory set-up using gas flow can be used instead (*Ball and Schjønnning*, 2002; *Takeuchi et al.*, 2008). Figure 2.8 shows a general gas permeameter set-up that relies on the flow of pressurized air (or another inert gas) through a sample. A differential pressure transducer is used to measure the pressure difference Δp across the sample. In this particular set-up, it is assumed that the outlet pressure is equal to the ambient pressure. When the gravitational impact of the gas phase on the pressure is neglected, the intrinsic permeability k can be calculated from a rearranged form of Equation (2.5).

$$k = \mu \frac{h}{A} \frac{1}{\frac{\Delta p}{Q}}, \quad (2.24)$$

where A is the cross-sectional surface area of the sample and h the length of the sample. Gas flow will obviously be affected by remaining liquid in the pores of a sample. Thus, only the relative air permeability can be determined using this set-up if the sample contains liquid. However, if the sample is dry, the relative permeability of gas is equal to the intrinsic permeability.

It is important to note that laminar (Darcy) flow conditions need to be ensured to determine the permeability of a sample using gas flow with the approach outlined above. The laminar flow conditions for incompressible fluids can be determined using the Reynolds number obtained from Equation (2.23). However, gas that flows through porous media is prone to be compressed at high pressure differences or flow rates. Compressible flow in porous media can be described using the quadratic Forchheimer equation (*Forchheimer*, 1901), which can be written as (*Rust and Cashman*, 2004):

$$\frac{p_i^2 - p_o^2}{2 p h} = \frac{\mu}{k_{\text{viscous}}} u_0 + \frac{\rho}{k_{\text{inertial}}} u_0^2, \quad (2.25)$$

where p_i is the fluid pressure at the inlet, p_o is the fluid pressure at the outlet, h is the sample length, k_{viscous} is the viscous (Darcy) permeability and k_{inertial} is the inertial (non-Darcy)

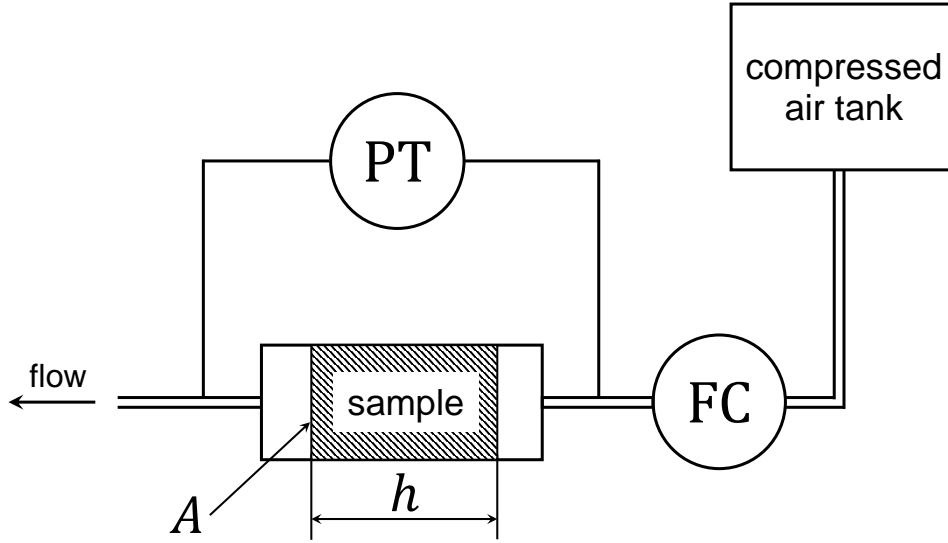


Figure 2.8: Air permeability set-up after *Ball and Schjønning* (2002). The pressurized air flows via the controller FC through the sample with cross-sectional area A and length h . The pressure drop over the sample is monitored by the pressure transducer PT.

permeability. The viscosity μ , the density ρ , and the velocity u_0 of the fluid are determined at the pressure p . When inertial effects can be neglected, Equation (2.25) can be rearranged to Equation (2.5) (Darcy's law, u_0 is equal to q). The Forchheimer number describes the flow conditions in porous media with respect to compressibility:

$$Fo = \frac{\rho u_0}{\mu} \left[\frac{k_{\text{viscous}}}{k_{\text{inertial}}} \right]. \quad (2.26)$$

A $Fo < 1$ indicates a viscous (Darcy) flow regime for consolidated sand (*Zeng and Grigg, 2006*), which also is required for the accurate determination of the intrinsic permeability of a porous medium using the approach outlined above.

2.3.2. Basics of micro-X-ray computed tomography

The geometry of the pore space (e.g. pore size, grain angularity) plays an important role for evaporation and salt crust formation in porous media, in particular for subflorescent salt precipitation. Images of the pore space provide a possibility to understand the mechanisms of liquid transport and formation of solids at the micro-scale (*Wildenschild and Sheppard, 2013*). In this context, micro-X-ray computed tomography (μ XRCT) is an interesting method to visualize the interior of a sample without destroying the structure of the object using X-rays (*Withers et al., 2021*). The underlying principle is based on the attenuation of X-ray radiation

that penetrates the investigated material, which results in a decrease of the intensity of the transmitted radiation (*Cnudde and Boone, 2013*). The transmitted intensity I is described by Beer's law:

$$I = I_0 e^{-\int \lambda(j) dj}, \quad (2.27)$$

where I_0 is the incident beam intensity, λ is the local linear attenuation coefficient, and j is the raypath. This equation is valid for a monochromatic source and a straight raypath. The linear attenuation coefficient mostly depends on the density of the material (i.e., denser material leads to more attenuation) and on the atomic number of the material (*Cnudde and Boone, 2013*). The intensity of the attenuated radiation can be measured using a two-dimensional (2D) projection, which is already useful in medical applications. For example, bone fractures can often easily be visualized using such a simple 2D X-ray projection. To obtain a 3D image, multiple 2D projections need to be acquired with different object orientations. Figure 2.9a shows a schematic set-up of a μ XRCT measurement device to determine the 3D structure of a sample. The X-ray source emits radiation, which penetrates the object (sample). After passing the sample, radiation hits a detector that records the intensity of the radiation. This provides a 2D projection of the sample at the present position. Then, the sample is rotated and the next projection is obtained. When the sample has made a full rotation, the 3D image can be determined from all projections using image reconstruction. The rotation axis of the sample and the center of the X-ray beam have to be aligned to provide an acceptable reconstruction result. During reconstruction, the intensity of each voxel in the 3D image is estimated based on the 2D projections, the amount of rotations, the geometric magnification, and the detector specifications using filter back projection (details in Chapter 4). Post-processing such as denoising and filtering is required to obtain a 3D image that can be segmented into the expected physical phases (i.e., assigning each voxel to a phase). Advanced segmentation methods were used in two steps in this thesis, which will be described in detail in Chapter 4.

The resolution of the voxels of the investigated volume is determined by the geometric magnification. As illustrated in Figure 2.9b, the geometric magnification of the sample can be obtained using (*Withers et al., 2021*):

$$f = \frac{\text{SDD}}{\text{SOD}}, \quad (2.28)$$

where f is the geometric magnification factor, SDD is the source-detector-distance that usually stays constant, and SOD is the source-object-distance that can be changed. The geometric magnification decreases when the sample is moved away from the source (Figure 2.9b) and the width of the projection reduces accordingly. Moving the sample closer to the source increases the geometric magnification (Figure 2.9d). The size of the detector is now the limiting factor to

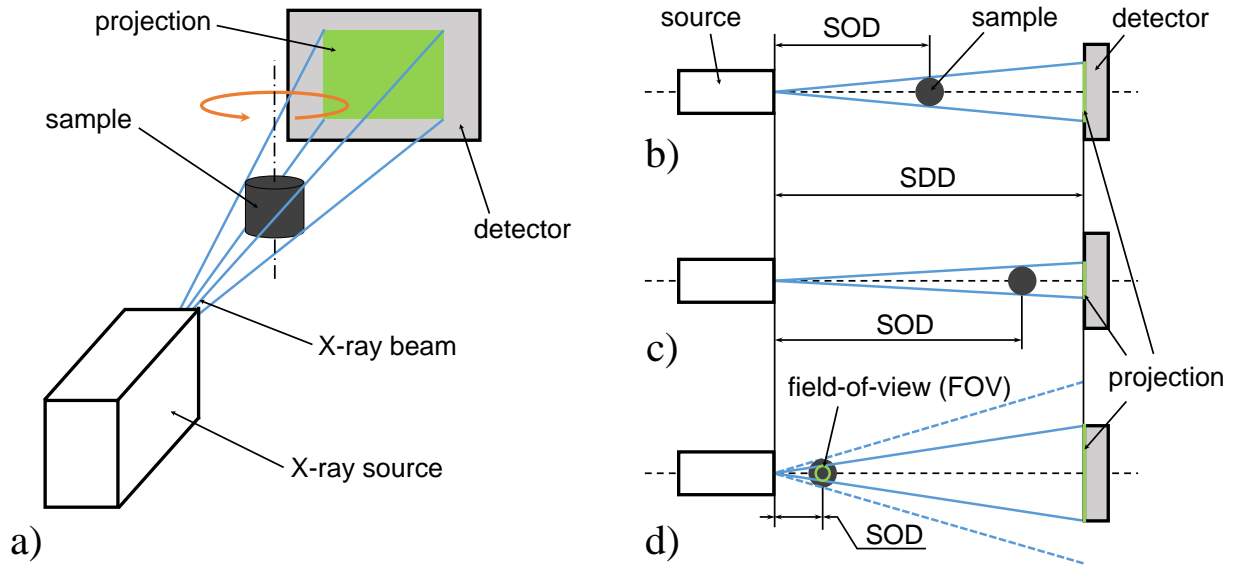


Figure 2.9: (a) Schematic set-up for micro-X-ray computed tomography (μ XRCT) measurements. The X-ray beam hits the sample and the attenuated radiation is recorded as a 2D projection using a detector. Multiple projections are acquired during the rotation of the sample. (b) Top view of set-up. SOD is the source-object-distance that can be adjusted. SDD is the source-detector-distance that normally stays constant. (c) Low geometric magnification. (d) High geometric magnification. The field-of-view (FOV) that can be obtained is smaller than the sample because of the size of the detector.

capture a projection of the entire sample. The obtained projection corresponds to the circular field-of-view (FOV) in the center of the sample (green circle in Figure 2.9d). The resolution of a projection is determined by the pixel size of the detector divided by the geometric magnification. Figure 2.10a shows a (vertical) projection of a sintered glass sample obtained with the μ XRCT device used in this thesis (more information in Chapter 4). The geometric magnification was 12.375 and the detector pixel size 0.0495 mm, which resulted in a resolution of 4 μ m. The contours of the glass grains can roughly be recognized at the surface of the sample and in the dark area below the surface, but a distinction between the grains is hardly possible by eye. This is attributed to fact that the X-ray beam passes through the entire sample and the 3D structure is mapped on the 2D projection plane. There are many grains and voids on the optical axis of one specific detector pixel, which all contribute to the acquired intensity (i.e., grey value) of this pixel in the corresponding projection. As mentioned above, a reconstruction algorithm was used to obtain the 3D structure of the sample from all projections. Figure 2.10b shows an example of a reconstructed (horizontal) axial slice of the sintered glass sample. The glass grains appear in light grey and can be visually distinguished from the voids in dark grey. The reconstructed data need to be further processed using filtering and segmentation algorithms.

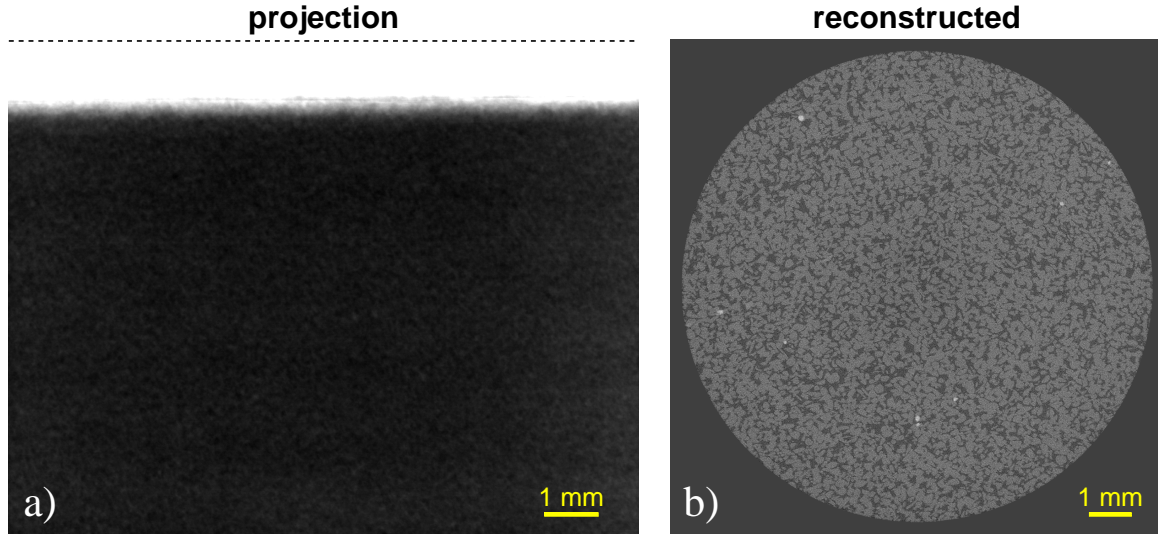


Figure 2.10: Exemplary results obtained from μ XRCT measurements of a sintered glass sample. (a) Projection that corresponds to Figure 2.9d. The bright part at the top represents air and the dashed black line indicates the maximum height of the FOV. The sample was larger than the width of the FOV at the left, the right, and the bottom of the projection. (b) Reconstructed axial slice (top view of the sample). The circular FOV results from the rotation of the sample during the scan. In the FOV, the dark grey areas are voids, the light grey areas are glass, and the white spots indicate impurities in the glass with a high density.

2.3.3. Principles of nuclear magnetic resonance

In the context of geosciences, nuclear magnetic resonance (NMR) measurements are widely used for the non-invasive characterization of porous media, including the characterization of natural soil (*Pohlmeier et al.*, 2009), the determination of soil moisture (*Hall et al.*, 1997), and the investigation of drying porous media (*Van der Heijden et al.*, 2009; *Faure and Coussot*, 2010). Depending on the used system and samples size, a resolution in the micrometer scale can be obtained. The non-invasive measurement principle relies on a property of many atomic nuclei called spin. An analog of this quantum mechanical property in classical physics is a rotation around its own axis linked to an intrinsic angular momentum. This is described by a spin quantum number that is $1/2$ in the case of ^1H (hydrogen/proton). The spin of atomic nuclei provides a microscopic magnetization, which interacts with external magnetic fields. Two distinct energy states E_{\uparrow} and E_{\downarrow} exist in the case of ^1H . The relative number of spins at each energy level n_{\uparrow} and n_{\downarrow} in an ensemble of spins follows the Boltzmann distribution:

$$\frac{n_{\downarrow}}{n_{\uparrow}} = e^{-\frac{E_{\downarrow} - E_{\uparrow}}{k_{\text{B}} T}}, \quad (2.29)$$

where k_{B} is the Boltzmann constant (1.380649×10^{-23} J/K) and T is the temperature [K]

(Blumich *et al.*, 2014). It is important to note that Equation (2.29) depends on the external magnetic field \mathbf{B}_0 :

$$\Delta E = \hbar\gamma_{\text{H}}\mathbf{B}_0, \quad (2.30)$$

where \hbar is Planck's constant ($1.054\,571\,817 \times 10^{-34}$ J s) and γ_{H} is the gyromagnetic constant, which is 42.58 MHz/T for ^1H (Blumich *et al.*, 2014; McRobbie *et al.*, 2017). Figure 2.11 schematically illustrates a classical physics analog for the spin in the magnetic field \mathbf{B}_0 . The resulting macroscopic magnetization \mathbf{M} of a large number of spins in a system can be treated as a classical magnet. Only the magnetic components of the spins that point in the direction of \mathbf{B}_0 add up to the macroscopic magnetization \mathbf{M} .

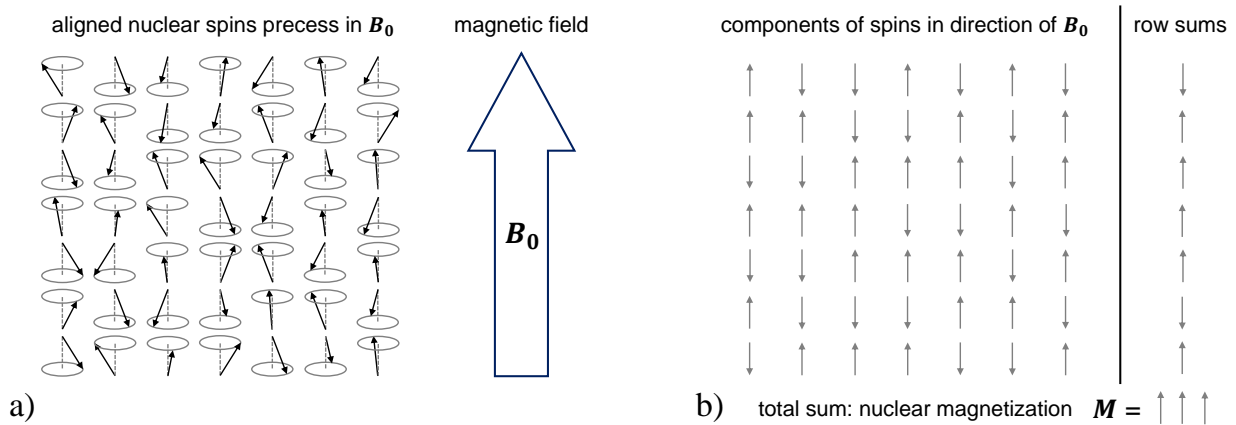


Figure 2.11: (a) 49 exemplary spins out of 10^{23} spins performing a precession movement in the direction of the magnetic field \mathbf{B}_0 (modified after Blumich *et al.* (2014)). (b) Nuclear magnetization \mathbf{M} as total sum of the components of the magnetization of the spins that are aligned in the direction of \mathbf{B}_0 (modified after Blumich *et al.* (2014)).

During a measurement, a sample is positioned near or inside of a radio frequency (rf) coil and the ensemble is placed in the magnetic field \mathbf{B}_0 . An electromagnetic excitation pulse transmitted by the rf-coil (transmitter) produces an oscillating magnetic field \mathbf{B}_1 . If this induced magnetic field is perpendicular to the homogeneous \mathbf{B}_0 field, it deflects the nuclei from the initial state if the frequency of the pulse ω_{rf} matches the spin precession frequency ν_0 (McRobbie *et al.*, 2017) (see Figure 2.12a). The flip angle α

$$\alpha = \gamma_{\text{H}} B_1 t_p, \quad (2.31)$$

depends on the amplitude B_1 and the duration of the rf-pulse t_p and is 90° in many cases. After excitation, the magnetization starts to precess around the axis of \mathbf{B}_0 towards the initial state (Figure 2.12a), which induces a local magnetic field (Fukushima and Roeder, 1981). This

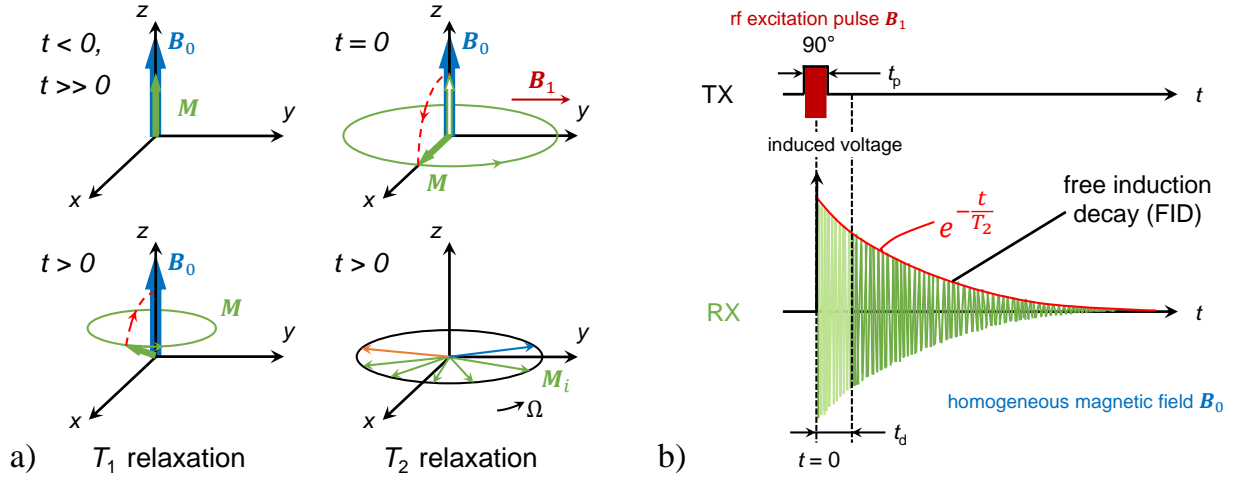


Figure 2.12: Precession and excitation of macroscopic magnetization in an external field (modified after *Blumich et al. (2014)*). (a) Magnetization M in an homogeneous magnetic field B_0 at time $t < 0$ and $t \gg 0$. At time $t = 0$, the magnetization M is flipped 90° around the y -axis by the pulsed magnetic field B_1 . Then, M precesses around the z -axis until the direction aligns with B_0 , which is called T_1 relaxation. The dephasing of the magnetization in the x - y -plane is called T_2 relaxation with the component precession frequency Ω . (b) The exponential decay of the dephasing of M with the time constant T_2 in a homogeneous magnetic field is called free induction decay (FID). The signal right after the excitation (pale green) cannot be accessed due to the dead time of the system t_d .

field induces a current in the rf-coil that serves as receiver now. The precession frequency ν_0 is proportional to the strength of B_0 :

$$\nu_0 = \frac{\omega_0}{2\pi} = \frac{\gamma_H B_0}{2\pi}, \quad (2.32)$$

where ω_0 is the circular precession frequency [rad/s]. The precession decays exponentially with two relaxation mechanisms until the orientation of the magnetization aligns with the direction of B_0 . The first relaxation mechanism is the re-establishment of the thermal equilibrium, the so-called spin-lattice, longitudinal, or T_1 relaxation (*Blumich et al., 2014*). The re-establishment of the thermal equilibrium can be described by

$$S(t) = S_0 \left(1 - e^{-\frac{t}{T_1}} \right), \quad (2.33)$$

where S is the measured signal, which is proportional to the precessing magnetization and the induced current in the surrounding detector coil, and S_0 is the signal intensity that is proportional to the spin density (*Blumich et al., 2014*). The recovery of the system (i.e., the time to reach the initial state) depends on the motion in the domain and all magnetic interactions. The second relaxation mechanism is related to the interaction between the molecules and with the

magnetic environment in the x - y -plane, which is called spin-spin relaxation, also T_2 relaxation (see Figure 2.12a) (*Fukushima and Roeder, 1981; McRobbie et al., 2017*). The phase angle of all components of the magnetization dephase in the x - y -plane with the component frequency Ω (Figure 2.12a). This results in a decrease of the magnitude of the macroscopic magnetization \mathbf{M} . The decay time constant is called T_2 if \mathbf{B}_0 is homogeneous (see Figure 2.12b). The exponential regression to the signal amplitude of a single pulse provides T_2 for a single-phase system and is called the free induction decay (FID) (*McRobbie et al., 2017; Blumich et al., 2014*):

$$S(t) = S_0 e^{\frac{-t}{T_2}}, \quad (2.34)$$

where $S(t)$ is the measured signal, and S_0 is the signal intensity at time $t = 0$ that is proportional to the spin density. The signal cannot be measured during and directly after the excitation pulse (i.e., for the dead time t_d). The dead time occurs because the rf-coil first serves as transmitter and then as receiver. Thus, the signal intensity at $t = 0$ is determined from extrapolation of Equation (2.34) (see Figure 2.12b).

Inhomogeneity in the applied magnetic field occurs for every magnetic set-up to a slight extent because of imperfections in the magnet itself or because of the geometric orientation (i.e., single sided magnets, intended magnetic gradients). In an inhomogeneous \mathbf{B}_0 field, the decay is faster than in a homogeneous field because the inhomogeneities affect the spin precession. The related decay constant T_2^* includes all imperfections of \mathbf{B}_0 and the spin-spin relaxation. For highly inhomogeneous magnetic fields (e.g. in stray-field NMR), the FID is very short so that T_2^* can hardly be obtained (see Figure 2.13a). The magnetization of each spin dephases differently in the x - y -plane during the decay to the initial state due to relaxation processes, which is illustrated in Figure 2.13. The dephasing can be refocused using a so-called 180° pulse that flips the magnetization around the x -axis (see Figure 2.13b). After a specific time, a signal can be detected with the rf-coil (receiver), which results from the refocusing of the magnetization of each component \mathbf{M}_i within the x - y -plane. This signal is called the Hahn echo (*Hahn, 1950*). The time between the excitation pulse and the detected echo signal is the echo time t_E and the 180° pulse is applied at $t_E/2$. If the refocusing with a 180° pulse is repeated for the acquisition time t_{acq} , a so-called echo train (Carr-Purcell-Meiboom-Gill, CPMG) can be obtained (see Figure 2.14). The exponential function that envelopes the maxima of the obtained echos provides the system-specific time constant T_2 and the signal intensity $S(t = 0) = S_0$ is again obtained by fitting Equation (2.34) to the measured signal intensities.

Multiple excitations are usually performed, each of which results in an echo train. The measured signal is averaged over all acquisitions (i.e., excitations). The time between two excitation pulses is called repetition time t_R and should be chosen between three and five times the longitudinal relaxation time T_1 . Shorter repetition times may result in an underestimation of the time

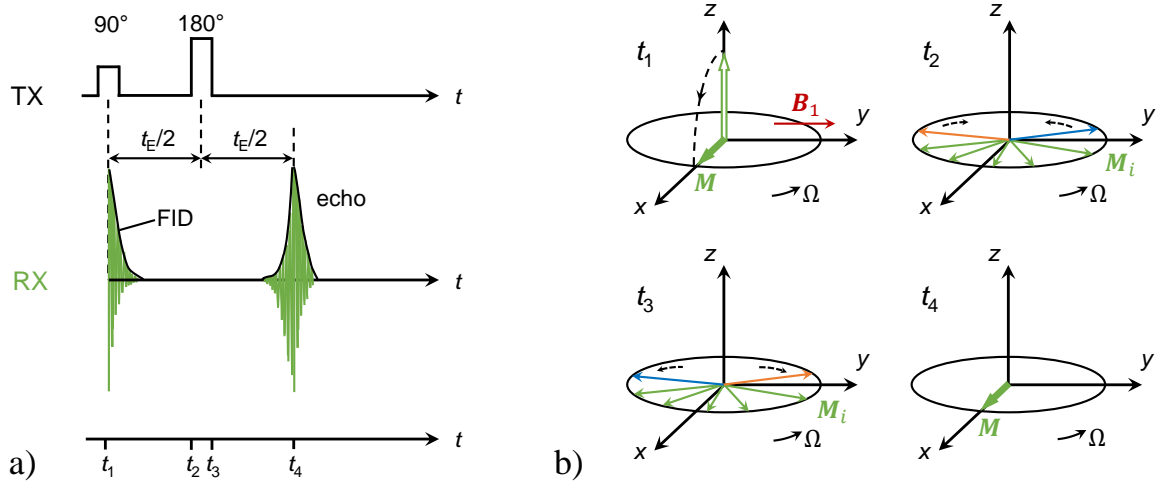


Figure 2.13: Pulse sequence of Hahn echo and dephasing of magnetization (modified after *Blumich et al. (2014)*). (a) TX is the transmitter pulse and RX is the receiver signal. The signal right after the 90° pulse cannot be measured with the receiver because of the dead time. The Hahn echo is obtained after the echo time t_E . (b) The times t_1 to t_4 correspond to the bottom time axis in (a). Ω is the component precession frequency, which is different for each magnetization component M_i .

needed for recovery from the excitation. The underestimation can be corrected by determining the deviation from unity of the term in parenthesis in Equation (2.33). If the deviation is small (i.e., $t_R > 3T_1$), the measured signal intensity $S(t)$ is equal to the true signal intensity S_0 . If the deviation is larger (i.e., $t_R < 3T_1$), the measured signal intensity $S(t)$ is smaller than the true signal intensity S_0 . The true signal intensity S_0 can be determined from $S(t)$ and T_1 by rearranging Equation (2.33).

The signal intensity S_0 at time $t = 0$ is proportional to the spin density and thus the water content of the excited volume. As the signal intensity depends on the B_0 field, the intensity is only a relative measure for the water content. A reference marker solution with known $^1\text{H}_2\text{O}$ content is needed as calibration to determine the water content of a sample. If the signal intensity of the marker solution is determined with the same experimental parameters as used to investigate the sample, the volumetric water content of the sample θ can be obtained by

$$\theta = \frac{\theta_{\text{ref}}}{S_{\text{ref}}} S_0, \quad (2.35)$$

where θ_{ref} is the volumetric water content of the reference marker solution, S_0 is the extrapolated signal intensity of the sample that is proportional to the spin density, and S_{ref} is the extrapolated signal intensity of the reference that is proportional to the spin density of the marker solution (*Merz et al., 2014*). The (axial) dimensions of the container with the reference marker solution need to be identical to the dimensions of the sample (*Blumich et al., 2014*). If this is not the

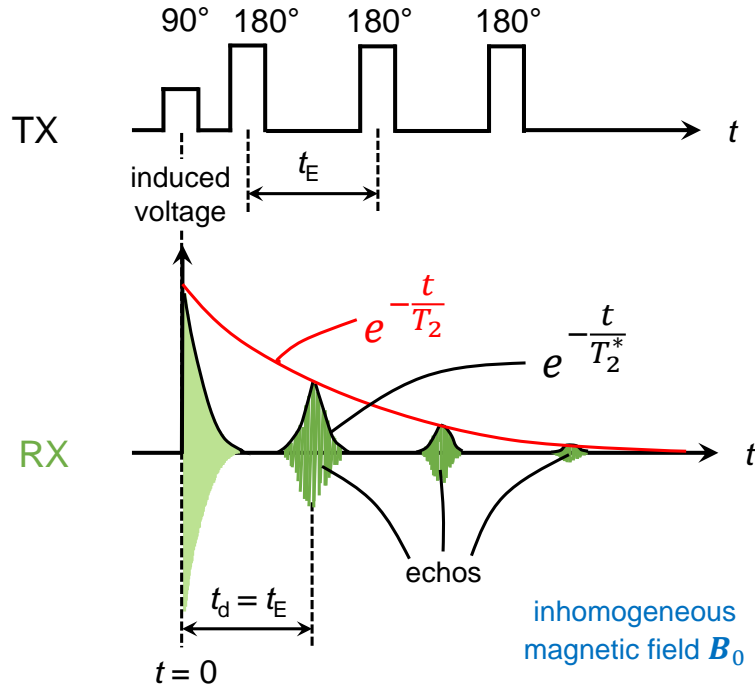


Figure 2.14: Echo train from multiple 180° pulses (modified after *Blumich et al. (2014)*). The pale green signal after the induced voltage by the transmitter (TX) cannot be assessed with the receiver (RX). The exponential fit to the envelope of the echo train provides T_2 and S_0 using Equation (2.34). The decay of each echo is very short so that T_2^* cannot be determined using the CPMG pulse sequence.

case, the reference signal intensity can be corrected using

$$S_{\text{ref,corr}} = \frac{A_{\text{sample}}}{A_{\text{ref}}} S_{\text{ref}}, \quad (2.36)$$

where $S_{\text{ref,corr}}$ is the corrected reference signal intensity, A_{sample} is the cross-sectional area of the sample, and A_{ref} is the cross-sectional area of the marker container. Previous studies have shown that reasonable measurement results can be obtained for a water content above $0.03 \text{ cm}^3/\text{cm}^3$ for a portable unilateral NMR device (*Merz et al., 2014*). For lower water contents, measurements may be affected by measurement uncertainties that arise from the scattering of the measured echo amplitude.

Chapter 3

Evaporation and crust formation from solutions of different salt types

3.1. Introduction

In this chapter¹, evaporation and crust formation of different salt solutions from sand will be investigated. The evaporation rate will be obtained from mass loss measurements of sand columns. To understand the impact of the permeability of salt crusts on evaporation, the intrinsic crust permeability will be determined using both liquid and gas flow methods.

Two objectives will be addressed in this chapter. First, the permeability of MgSO_4 crusts obtained from liquid flow measurements methods will be compared to the crust permeability from gas flow measurements. It will be shown that liquid flow measurements are prone to air entrapment and crust dissolution, while gas flow measurements seemed to be less affected by experimental uncertainties. Second, the permeability of salt crusts developed from NaCl , MgSO_4 , and Na_2SO_4 solutions will be investigated using a novel gas permeameter set-up. It will be shown that the crusts from different salt solutions affected evaporation differently, although the intrinsic crust permeability was similar.

The remainder of this chapter is organized as follows. First, the sample preparation for liquid and gas flow measurements of the intrinsic crust permeability will be described and both measurement set-ups will be presented. Then, the results and limitations of evaporation and crust permeability determination using liquid flow will be discussed. In addition, evaporation and crust formation from solutions of different types of salts will be presented and the determination of the intrinsic crust permeability using gas flow will be elaborated. Further, the permeability obtained from liquid and gas flow measurements of crust from MgSO_4 will be compared.

¹This chapter is partly based on a journal article published as: Piotrowski, J., J.A. Huisman, U. Nachshon, A. Pohlmeier, and H. Vereecken (2020), Gas permeability of salt crusts formed by evaporation from porous media, *Geosciences*, 10(11), 423, doi:10.3390/geosciences10110423.

3.2. Materials and methods

3.2.1. Preparation of samples with different types of salt solution

For the experiments focused on liquid flow determination of the intrinsic crust permeability, six steel columns with an inner diameter of 85 mm were prepared with 1 mol/L magnesium sulfate (MgSO_4) solution and quartz sand. An additional six steel columns were prepared with deionized water (see Table 3.1 and 3.2). First, a column was filled to about one-third with liquid through a perforated bottom plate (see Figure 3.1). Then, 800 g of F32 quartz sand (mean grain diameter 240 μm , density 2.65 g/cm^3 , Quartzwerke Frechen, Frechen, Germany, see Table 3.1) was added gradually while ensuring that a liquid layer was always maintained at the sample surface. A cloth between the sand and the perforated plate was used to prevent clogging of the plate. When all sand was filled into the sample holder, the steel column was shaken and tapped to obtain an even sand surface. Excess liquid was drained through the perforated bottom plate so that the pressure at the bottom of the sand column was equal to the ambient pressure. After drainage, the bottom was closed and the distance of the sample surface to the edge of the steel column was determined at four equidistant positions at the perimeter of the sample. The averaged distance of the sample surface to the edge of the steel column was subtracted from the overall length of the steel column to obtain the sample height, which varied between 84 mm and 87 mm. This height was used to obtain the total volume and the porosity ϕ of each sample, which was 0.37 for all samples. At the end, the sample was covered to prevent evaporation until the actual start of the evaporation experiment.

Table 3.1: Physical properties and particle size distribution of F32 quartz sand (Quartzwerke Frechen, Frechen, Germany).

Particle density	Particle size	Mass fraction	Mean particle size
[g/cm^3]	[mm]	[%]	[μm]
2.65	> 0.335	5	240
	0.250 - 0.355	28	
	0.180 - 0.250	49	
	0.125 - 0.180	16	
	0.090 - 0.125	2	
	< 0.090	-	

The air-entry pressure [mm] of the sand was estimated to be -300 mm using Equation (2.14) and assuming a contact angle of 0° (complete wetting). The required average pore size of the sand packing (100 μm) was estimated from a packing of sintered glass beads with the same grain size (*Glover and Walker, 2009*). As this air-entry pressure is well below the matric potential at

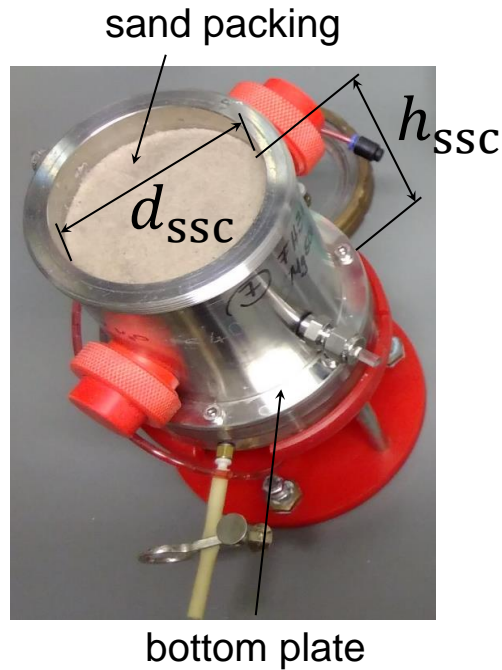


Figure 3.1: Picture of steel column filled with sand and liquid (sand steel column, ssc). The height of the sand packing h_{ssc} varied between 84 mm to 87 mm and the diameter d_{ssc} was 85 mm.

the sample surface after drainage to steady-state conditions (-87 mm to -84 mm), it is assumed that all samples were initially fully saturated with liquid.

Table 3.2: Physical properties of solutions used to prepare samples in steel columns and for the determination of the hydraulic conductivity at 20 °C (Müller, 1939; Weingärtner et al., 2016; Rumble, 2019). $\text{MgSO}_4 \cdot 7\text{H}_2\text{O}$ was obtained from Th. Geyer, Renningen, Germany.

Substance	Molar mass	Concentration	Viscosity	Density
	[g/mol]	[mol/L]	[Pa s]	[g/cm ³]
H ₂ O	18.01	-	1.002	0.9982
		2.88 (limit)	8.066	1.296
MgSO ₄ · 7H ₂ O	246.48	2.50	6.336	1.267
		1.00	1.946	1.113

After sample preparation, the hydraulic conductivity of each sample was determined using a falling-head method (for details see below). Then, evaporation was initiated by removing the cover of each column. The mass loss of each sample was measured daily with a balance for 31 days (CP 4202 S, Satorius AG, Göttingen, Germany). The temperature (20 °C - 21 °C) and relative humidity (20% - 50%) were also determined daily (NC7004-675, FreeTec

PEARL.GmbH, Buggingen, Germany). The columns with deionized water evaporated entirely and the columns with MgSO_4 solution reached a final saturation between 27% and 33%. For the experiments focused on gas flow determination of the intrinsic crust permeability, saturated sand columns were prepared in triplicates with solutions of NaCl , MgSO_4 , and Na_2SO_4 (see Table 3.3 for details). The initial concentration of each solution was set to 33% of the maximum solubility following previous studies (*Shokri-Kuehni et al., 2017; Bergstad et al., 2017*). Additionally, three samples with deionized water were prepared as a reference. Custom-made sample holders made of polymethylmethacrylat (PMMA, plexiglass) with an inner diameter of $d = 31$ mm, a total length of $l = 140$ mm, and a maximum filling height $h_{\text{max}} = 100$ mm were used for the evaporation experiments (see Figure 3.2). A filter plate (P3, Robu, Hattert, Germany) was fixed inside the sample holder with a removable plug in order to hold the sample material in place.

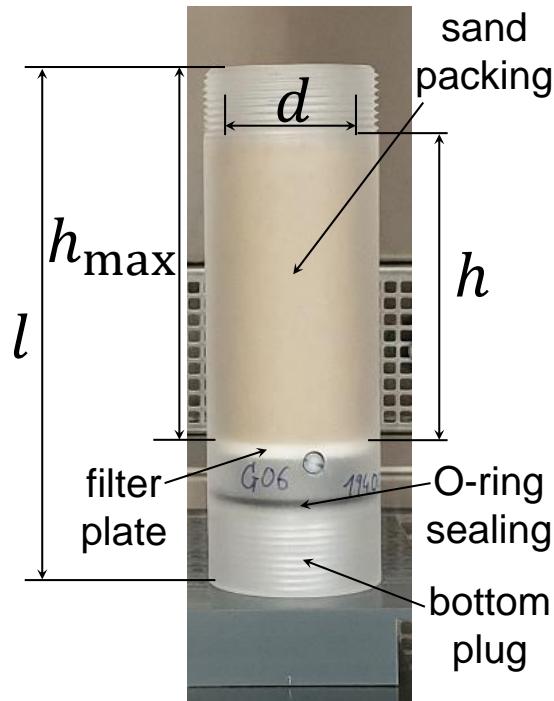


Figure 3.2: Picture of the PMMA sample holder filled with sand and liquid. The height was $h = 80 \pm 1$ mm, diameter $d = 31$ mm, the maximum possible filling height $h_{\text{max}} = 100$ mm, and the overall length of the sample holder l was 140 mm.

F32 quartz sand (Quarzwerke Frechen, Frechen, Germany) was again used for all evaporation experiments. To prepare samples, the sample holder was first filled with saline solution (or water). Next, 100 g of F32 quartz sand was dispersed in the liquid at once. Subsequently, tapping on the outside of the sample holder resulted in slight consolidation of the sand. This resulted in a sample height of $h = 80$ mm (see Figure 3.4). In a next step, excessive solution

was allowed to drain out through an opening in the bottom plug that was closed after drainage. No liquid was supplied from the bottom during evaporation. As discussed above, the air-entry pressure of the sand and the filter plate were roughly estimated with Equation (2.14) to be -300 mm and -750 mm, respectively. The required maximum pore size of the filter plates (40 μm) was provided by the manufacturer. As these air-entry pressures are well below the matric potential at the sample surface after drainage to steady-state conditions (-80 mm), it is assumed that all samples were initially fully saturated with liquid. After sample preparation, the initial height and volume of each sample was determined by measuring the distance from the edge of the sample holder to the sample surface at four equidistant positions along the sample holder wall. The porosity ϕ of each sample was then determined from the total volume and the known weight and particle density of the sand (density $\rho = 2.65 \text{ g/cm}^3$, Table 3.1), and was found to be $\phi = 0.37 \pm 0.01$. More information on the initial sample properties can be found in the published data set (*Piotrowski and Huisman, 2021*).

Table 3.3: Properties of the substances for sample preparation and permeability determination at 20 °C in PMMA sample holders. The density of the solutions and the vapor pressures are interpolated from *Westphal et al. (2010)* and *Clarke (1985)* for NaCl, from *Müller (1939)* and *Guendouzi et al. (2003)* for MgSO₄, and from *Guendouzi et al. (2003)* and *Plessen (2000)* for Na₂SO₄. The vapor pressure of H₂O corresponds to fully saturated wet air (*Weingärtner et al., 2016*). The properties of nitrogen (N₂) are taken from *Böcker et al. (2013)*.

Substance	Physical properties			Solution prepared for evaporation		
	Molar mass [g/mol]	Viscosity [mPa s]	Maximum solubility [mol/L]	Initial concentration [mol/L]	Density [g/cm ³]	Initial vapor pressure [kPa] at 25 °C
NaCl	58.44	-	6.13	2.04	1.079	2.935
MgSO ₄ · 7 H ₂ O	246.48	-	2.88	0.96	1.107	3.111
				0.64	1.073	3.131
				0.32	1.036	3.147
Na ₂ SO ₄	142.04	-	1.41	0.47	1.058	3.111
H ₂ O	18.01	1.002	-	-	0.9982	3.169
N ₂	28.01	0.0176	-	-	(1.162 · 10 ⁻³)	-

In an attempt to ensure similar evaporation conditions for all samples, they were placed beneath fans (Tristar Europe B.V., Tilburg, The Netherlands) with four samples at defined position below each fan. Temperature and relative humidity were automatically recorded every hour using a multi-purpose measuring device (FHAD 46-C2, ALMEMO® D06, Ahlborn, Holzkirchen, Germany). The temperature during evaporation was 25 °C \pm 1 °C and the relative humidity varied between 20-40%. Evaporation was determined from mass loss by measuring the mass of

each sample with a scale (accuracy ± 0.01 g, EX2202, Ohaus Cooperation, Parsippany, USA) two times per day during the first five days. After this, the mass was measured one time per day. After 13 days of evaporation, the mass was measured once every two days in order to ensure a mass loss greater than 0.1 g, which was the smallest amount that could be reliably measured with the scale. Subsequent to weighing, the position of each sample was changed randomly to avoid that one sample experienced the same ventilation conditions for a longer period of time. The water saturation of each sample was obtained from the mass loss and the known initial water content.

3.2.2. Salt crust permeability from liquid flow measurements

The procedure for crust permeability determination using liquid flow with a constant head permeameter was already used in previous studies (*Nachshon and Weisbrod, 2015*). In this study, a falling head set-up was used to determine the hydraulic conductivity and the permeability (Figure 3.3). A liquid supply (i.e., burette) was connected to the bottom of a sample, while the water table of the burette was higher than the outlet at the top of the sample. As soon as the valve that closes the outlet at the top was opened, liquid flowed through the sample from bottom to top. The hydraulic conductivity was determined from the change in water level height in the burette L_i and the associated time t_i using

$$K_S = \left(\frac{d_b}{d_s} \right)^2 \frac{h}{t_{i+1} - t_i} \ln \left(\frac{L_i}{L_{i+1}} \right), \quad (3.1)$$

where d_b is the diameter of the burette, d_s the diameter of the sample, h the length of the sample, and L_i and L_{i+1} are the water levels in the supply reservoir at times t_i and t_{i+1} , respectively (*Reynolds and Elrick, 2002b*). The permeability of the sample can then be determined using Equation (2.12).

After evaporation was terminated, the samples prepared with deionized water were resaturated with deionized water and the samples with salt crust formation were resaturated with MgSO_4 solution at the solubility limit (see Table 3.2 and 3.3). After this, the hydraulic conductivity of all samples was determined again using the falling head set-up. The thickness of the consolidated part of the crusts was measured with a caliper by destructively removing the crust from the sample. The permeability of the entire sample with salt crust was again obtained using Equation (2.12). Then, the permeability of each salt crust was determined using Equation 2.22, the length of the sample h , the thickness of the salt crust s (see Figure 3.3), and the initial length and permeability of the sample obtained before salt crust formation.

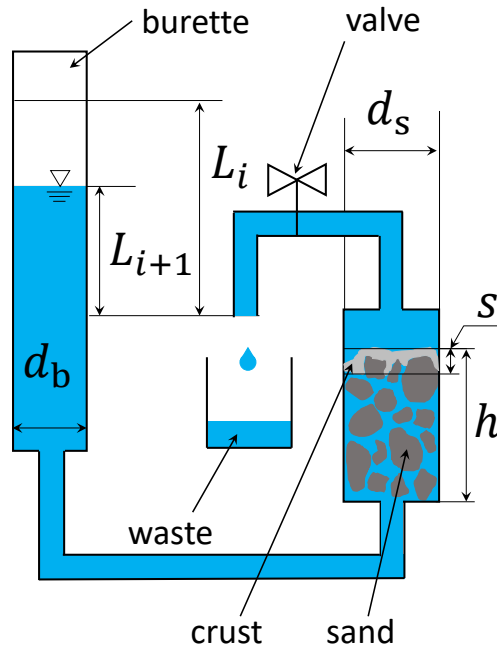


Figure 3.3: Sketch of the falling head permeameter set-up used to determine the hydraulic conductivity of a sample (not to scale, after *Hillel (2003)*). h is the length of the sample, s the thickness of the salt crust, d_s the diameter of the sample, and d_b the diameter of the burette. L_i and L_{i+1} are the levels of the liquid supply at the times t_i and t_{i+1} , respectively, after opening the valve to allow upwards liquid flow through the sample (see text for details).

3.2.3. Permeability determination using gas flow

The evaporation of the samples with NaCl and Na₂SO₄ solution was stopped when the water saturation inside the column reached 20% after 9-17 days. In contrast, the evaporation of samples with MgSO₄ solution was stopped when 30% water saturation inside the column was reached after 60 days of evaporation (see Subsection 3.3.2 for details). To separate the crust, the bottom plug, the filter plate, and the sand below the crust were removed carefully while leaving the crust attached to the wall inside the sample holder (see Figure 3.4a). A similar approach was used to study the migration of a crust along the wall of a Hele-Shaw cell (*Licsandru et al., 2019*). Next, the mass of the removed sand and the crust was determined. The removed sand was found to be wet throughout the whole length of the sample. To determine the crust thickness, the distance of the crust to the top and bottom of the sample holder was measured with a caliper at four positions along the perimeter of the salt crust close to the wall (see Table A.1 in Appendix A). Afterwards, the bottom plug was inserted again and the permeability of the wet crust was determined using the gas permeameter set-up described below. After this initial permeability determination, the removed sand and the crust were dried at 60 °C for 96 hours.

This relatively low temperature prevented morphological changes in the crystal structure of $\text{MgSO}_4 \cdot 7\text{H}_2\text{O}$ (Balboni *et al.*, 2011). The measured water loss was used to determine the saturation of the sand and the crust after evaporation. It also served as a check of the water balance, where a maximum underestimation of 4% compared to the initial water content was found for all samples. After drying, the crust permeability of each sample was determined again.

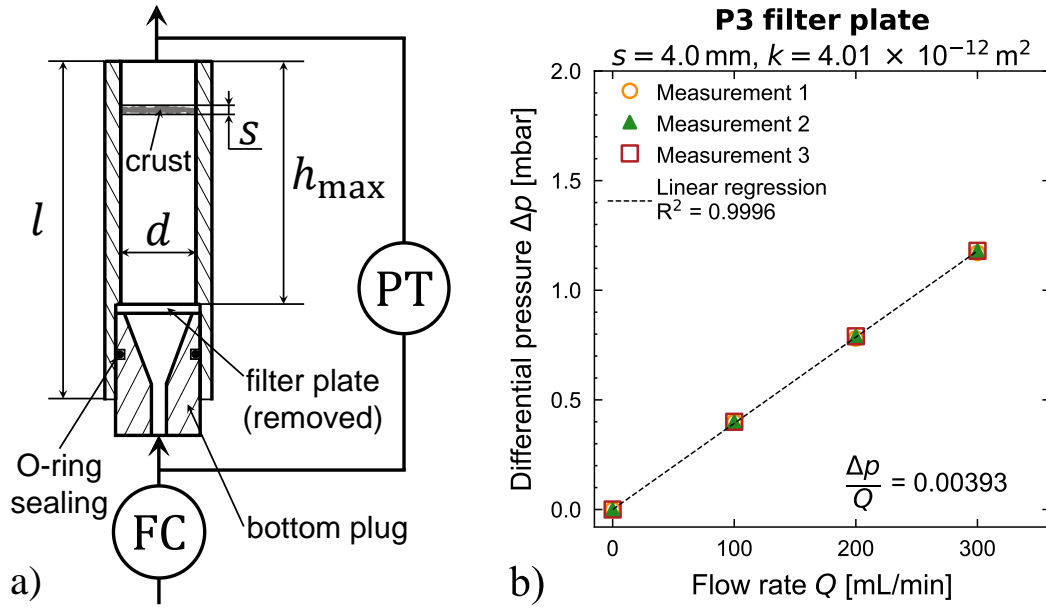


Figure 3.4: (a) Sketch of a separated crust attached inside of the sample holder. The maximum filling height was $h_{\max} = 100$ mm, the overall length of the sample holder l was 140 mm, and the crust thickness s varied between 1 mm and 4 mm. The flow controller FC and the pressure transducer PT were connected to the reinserted bottom plug. (b) Exemplary results for permeability determination of a dry P3 filter plate. The filter plate was fixed as indicated in the sketch in panel (a) and no crust was present during these test measurements.

A known gas flux of dry nitrogen gas (density $\rho = 1.162 \cdot 10^{-3} \text{g/cm}^3$ and viscosity $\mu = 0.0176 \text{mPas}$ at 20°C , Table 3.3) was introduced into the sample holder using a flow controller (High-Tech BV, Bronkhorst, Ruurlo, Netherlands), which induced a pressure difference across the salt crust. The upstream pressure was measured by a differential pressure transducer. Here, two types of pressure transducers that could easily be exchanged were used. The first type measured in the range of 0-10 mbar (accuracy ± 0.01 mbar, DPS 300, BD-Sensors, Thierstein, Germany) and the second type measured in the range from 0-1000 mbar (accuracy ± 1 mbar, DP2 Series, Ramco National Featuring Panasonic Sensors, West Des Moines, Iowa, USA). Both the downstream outlet of the sample holder and the outlet port of the differential pressure transducer were assumed to be at ambient pressure. The crust permeability was then determined using Equation (2.24).

Three measurement series at four flow rates (0, 100, 200, and 300 mL/min) were performed for all salt crusts. To ensure steady state conditions, each flow rate was applied until no changes in pressure were observed anymore. It was found that the measured pressure differences were linearly related to the flow rate, as expected for laminar/Darcy flow conditions. Therefore, a linear regression between pressure difference and flow rate was performed and the resulting slope was used to calculate the crust permeability using Equation (2.24).

To evaluate flow conditions in the gas permeameter set-up, the Reynolds number Re was determined using Equation (2.23) (Zeng and Grigg, 2006). Using this definition that considers the particle diameter as characteristic length, non-Darcy flow in porous media is expected when Re exceeds 40 (Chilton and Colburn, 1931; Zeng and Grigg, 2006). The Reynolds number for gas flow in the F32 quartz sand samples was calculated using $d_p = 240 \mu\text{m}$ and the fluid properties of nitrogen at 20°C ($\rho = 1.162 \cdot 10^{-3} \text{g/cm}^3$, $\mu = 0.0176 \text{mPas}$). It was found to be $Re = 0.105$ for the highest gas flow rate of 300 mL/min used in this study, which is substantially lower than the threshold of $Re = 40$ (Chilton and Colburn, 1931; Zeng and Grigg, 2006). Thus, Darcy (laminar) flow conditions in the sand samples can likely be assumed based on the estimations using Equation (2.23).

In the case of flow inside tubes, it is well known that the transition from laminar to turbulent flow occurs above $Re = 2300$ (Chilton and Colburn, 1931; Schlichting and Gersten, 2017) when the diameter of the tube is used as the characteristic length in Equation (2.23). To evaluate the flow conditions inside the empty sample holder (i.e., a series of tubes), a superficial fluid velocity of 300 mL/min, the fluid properties of gaseous nitrogen, and the tube diameter d instead of the particle diameter d_p were used (Schlichting and Gersten, 2017). The resulting Reynolds number for the smallest tube diameter ($d = 2 \text{mm}$) of the gas permeameter set-up was found to be $Re = 195$. Test measurements with the empty sample holder using the highest flow rate of 300 mL/min showed a pressure loss due to laminar flow resistance of only 0.02 mbar, which was taken into account for all measurements. Overall, it was concluded that laminar/Darcy flow conditions in the sample holder were maintained in all experimental conditions and that the use of Equation (2.24) is thus justified.

The permeability determination with the gas permeameter set-up was further tested using 25 filter plates (VitraPOR P3 (16-40 μm), ROBU, Hattert, Germany) with known dimensions. The filter plates were positioned above the bottom plug as indicated in Figure 3.4a. The particle diameter was estimated to be three times the pore size, e.g. $d_p = 120 \mu\text{m}$. This resulted in a Reynolds number of $Re = 0.052$ using Equation (2.23). Figure 3.4b shows three differential pressure measurements at four different flow rates (0 mL/min, 100 mL/min, 200 mL/min, and 300 mL/min) on an exemplary filter plate, which showed a strong linear relationship ($R^2 = 0.9996$). This again confirms that laminar/Darcy flow conditions can safely be assumed for the filter plates at given experimental conditions. The thickness of each filter

plate was determined with a caliper. Then, Equation (2.24) was applied to calculate the permeability of every filter plate (*Piotrowski and Huisman, 2021*). The mean permeability of the P3 filter plates was $5.30 \cdot 10^{-12} \text{ m}^2$ ($3.39\text{-}7.64 \cdot 10^{-12} \text{ m}^2$) and deviated only 16% from the permeability of $6.32 \cdot 10^{-12} \text{ m}^2$ reported by the manufacturer.

The mass loss of the sand samples prepared with deionized water was also monitored and the samples were dried at 60°C after the evaporation experiment. The permeability of the entire sample including filter plate was determined using the gas permeability set-up, as the filter plate that kept the dried sand in position could not be removed (see Figure 3.2 and Figure 3.4a). Equation (2.22) was used to calculate the permeability of the sand only with the permeability ($3.39\text{-}7.64 \cdot 10^{-12} \text{ m}^2$) and thickness (3.8-4.2 mm) of each individual filter plate obtained before the start of the experiment as described above.

3.3. Results and discussion

3.3.1. Samples for liquid flow permeability determination

Figure 3.5a shows the averaged cumulative mass loss of the samples with deionized water and MgSO_4 solution. As expected, the mass loss of the samples with deionized water was always higher than the mass loss of the samples with MgSO_4 solution, which can be attributed to the lower saturation vapor pressure of the saline MgSO_4 solution and the formation of the salt crust. The impact of the lower saturation vapor pressure (see Equation (2.15)) can also be seen in Figure 3.5b, where the mean initial evaporation rate of the samples with MgSO_4 solution (3.3 mm/day) was below the mean initial evaporation rate of the samples with deionized water (4.0 mm/day). For deionized water, stage I evaporation continued until day nine followed by a steep drop of the evaporation rate that indicated the start of stage II evaporation. After day 15, water evaporated with a relatively low rate below 0.4 mm/day. Thus, the sand samples with deionized water showed the typical two-stage evaporation process reported in previous studies (*Lehmann et al., 2008; Shokri and Or, 2011; Or et al., 2013*) (see Figure 2.3).

In the case of the samples with MgSO_4 solution, the evaporation rate decreased during stage SS1 and crust formation was observed after two days. This indicated the start of stage SS2, which continued until day 26. The mass loss of the samples with MgSO_4 solution was low after day 28, where the samples showed a saturation of $30\% \pm 3\%$ (Figure 3.5a). It can be seen that the evaporation rate of the samples with MgSO_4 solution was higher than the evaporation rate of the samples with deionized water after day 13. This suggests that a liquid connection to the surface of the samples with MgSO_4 solution was still provided. The relatively low evaporation rate can be attributed to the presence of the MgSO_4 crust that may have blocked pores, which was reported in previous studies (*Espinosa-Marzal and Scherer, 2013*). A detailed investigation

on the liquid content profiles during evaporation can be found in Chapter 5.

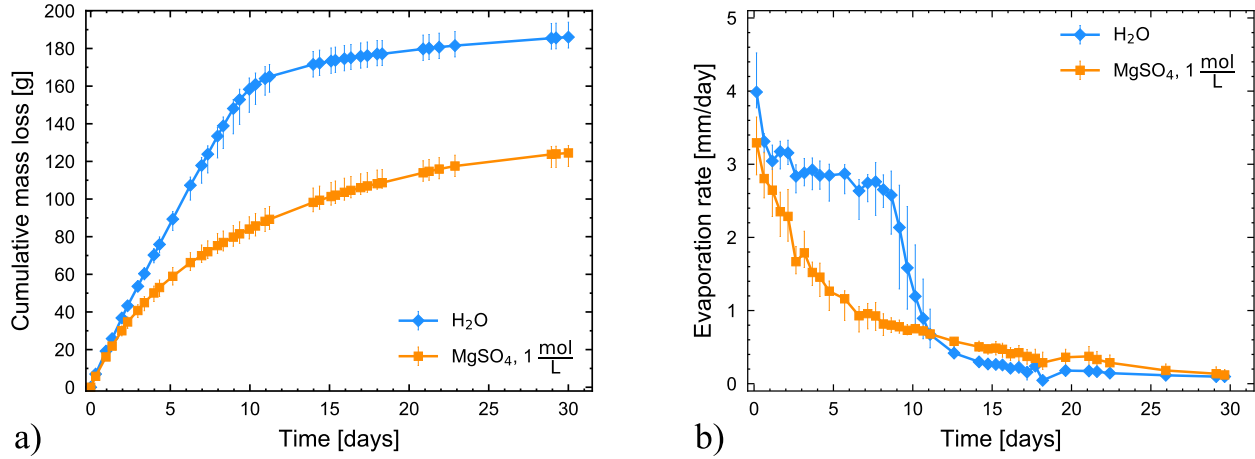


Figure 3.5: (a) Cumulative mass loss over time of deionized water and 1 mol/L MgSO₄ initial concentration from sand in steel columns. The evaporation of all samples was stopped after 30 days, where the samples with deionized water reached 0% saturation and the samples with MgSO₄ solution reached 30%±3% saturation. (b) Evaporation rate over time of deionized water and 1 mol/L MgSO₄ initial concentration from sand in steel columns.

In contrast to the results presented here, *Nachshon and Weisbrod (2015)* reported that the cumulative evaporation from sand samples with MgSO₄ solution at the solubility limit was found to be equal or even larger than the cumulative evaporation of deionized water. This difference may be related to the different sands that were used (mean grain size 384 μm in (*Nachshon and Weisbrod, 2015*) and 240 μm in this study). *Nachshon and Weisbrod (2015)* suggested that the reduction of the hydraulic conductivity due to subflorescent salt precipitation was not sufficient to suppress evaporation, as the crust was wet and provided liquid to the surface. This indicates that the hydraulic properties of the porous matrix show a strong impact on evaporation and crust formation, which was also reported in previous studies (*Espinosa-Marzal and Scherer, 2010; Bergstad et al., 2017*). Thus, future studies should focus on the impact of the grain size on subflorescent salt precipitation.

The measured hydraulic conductivity and permeability of six sand samples with deionized water before evaporation and after resaturation is shown in Figure 3.6. The mean hydraulic conductivity of the sand before evaporation was $7.80 \cdot 10^{-5}$ m/s with a small range between $7 \cdot 10^{-5}$ m/s and $9 \cdot 10^{-5}$ m/s. This mean hydraulic conductivity is one order of magnitude lower compared to *Nachshon and Weisbrod (2015)*, which is attributed to the smaller grain size of the sand that was used in this study ($d_p = 384 \mu\text{m}$ in *Nachshon and Weisbrod (2015)* and $d_p = 240 \mu\text{m}$ here). The relatively low range of hydraulic conductivity indicates that the packing procedure provides reproducible results.

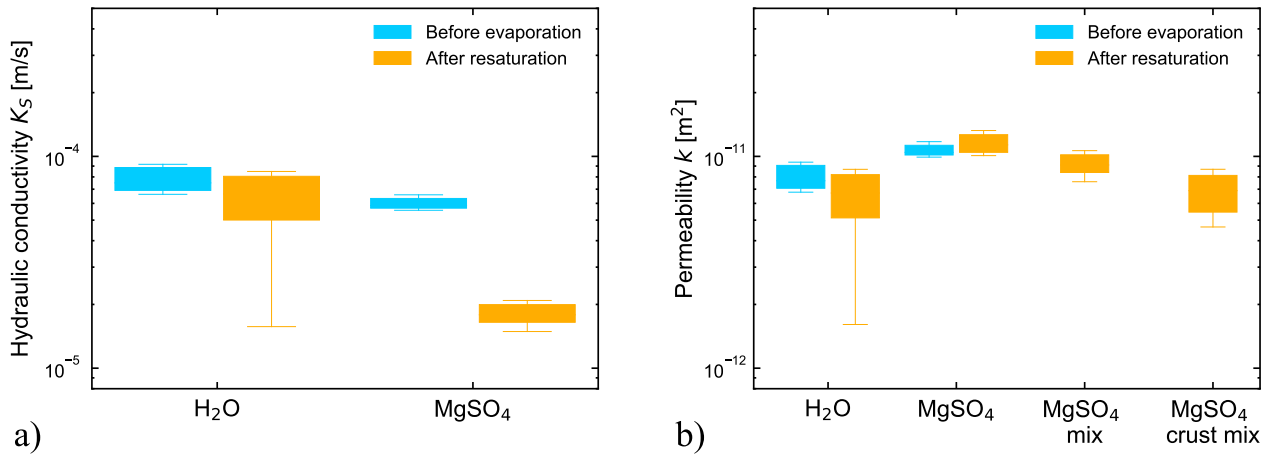


Figure 3.6: (a) Hydraulic conductivity and (b) permeability before evaporation and after crust formation and resaturation of sand used for permeability determination using liquid flow. "MgSO₄ mix" indicates the bulk permeability that was determined with an estimated mixed concentration (2.50 mol/L) after resaturation using Equation (2.12). "MgSO₄ crust mix" indicates the permeability of the crust that was determined with the "mixed" permeability and Equation (2.22).

The hydraulic conductivity of the samples prepared with deionized water after resaturation was consistently lower than before evaporation (Figure 3.6a). The majority of the measured hydraulic conductivity values fell between $5 \cdot 10^{-5}$ m/s and $8 \cdot 10^{-5}$ m/s, but one sample showed a hydraulic conductivity of only $1.5 \cdot 10^{-5}$ m/s. These results clearly show that the hydraulic conductivity of the sand was different before evaporation and after resaturation. This is most likely due to air entrapment during resaturation that reduced the area for liquid flow and thus the hydraulic conductivity. In addition, the wider spread of the hydraulic conductivity after resaturation indicates that the extent of air entrapment is quite variable between individual columns. It is important to realize that this observed decrease in hydraulic conductivity for the samples without salt crust formation sheds considerable doubt on the procedure of *Nachshon and Weisbrod* (2015) to obtain salt crust permeability. If reductions in bulk hydraulic conductivity are inadvertently attributed to the hydraulic conductivity of the crust instead of a reduction of the hydraulic conductivity of bulk porous medium due to air entrapment, this may lead to an underestimation of the hydraulic conductivity of the crust.

The hydraulic conductivity of the six columns initially saturated with 1 mol/L MgSO₄ solution showed a significant decrease before evaporation and after resaturation (Figure 3.6a). However, this is at least partly due to the different liquid properties since saturated 2.88 mol/L MgSO₄ solution was used to resaturate the samples to avoid that the crust would dissolve after resaturation. These differences in liquid properties have been accounted for in case of the permeability calculation (Figure 3.6b). It can be seen that the mean permeability of the samples saturated

with 1 mol/L MgSO_4 solution ($1.07 \cdot 10^{-11} \text{ m}^2$) before evaporation was higher than that of the samples saturated with deionized water ($7.99 \cdot 10^{-12} \text{ m}^2$). This is attributed to differences in liquid density and viscosity that likely affected sample preparation. After resaturation, the mean permeability slightly increased when the liquid properties of the saturated 2.88 mol/L MgSO_4 solution were used to calculate permeability. Since it is known that MgSO_4 leads to subflorescent crust formation where salt precipitation reduces the porosity, such an increase in bulk permeability is physically implausible. This apparent increase in permeability is attributed to the lower solute concentration of the residual liquid in the sand below the salt crust. This concentration most likely shows a gradient from the bottom ($\geq 1 \text{ mol/L}$) to the top of the sample ($\leq 2.88 \text{ mol/L}$) before resaturation, since the column did not evaporate completely. A conservative estimate of the solute concentration of the solution below the salt crust after resaturation can be obtained by assuming complete mixing. This results in a concentration of 2.50 mol/L ($0.2 \cdot 1 \text{ mol/L} + 0.8 \cdot 2.88 \text{ mol/L}$). If the density and viscosity at this estimated concentration are used, the bulk permeability after resaturation was lower than that of sand and the resulting mean crust permeability obtained with Equation (2.22) was $6.77 \cdot 10^{-12} \text{ m}^2$. The results from previous studies showed comparable reductions of the permeability from $1 \cdot 10^{-10} \text{ m}^2$ for the pure sand to $4 \cdot 10^{-11} \text{ m}^2$ for the MgSO_4 crust (*Nachshon and Weisbrod, 2015*). It is important to emphasize that the assumptions on the concentration made above are highly simplified and that there will be a gradient in concentration in reality after resaturation. In addition, the liquid with a concentration below the solubility limit will partly dissolve the crust. This can only be avoided if a saturated salt solution is used for the evaporation experiments, as was done by *Nachshon and Weisbrod (2015)*. However, the initial concentration of saline solutions has a significant impact on crust formation during evaporation. *Shokri-Kuehni et al. (2017)* showed that the crust development on samples with high initial concentration of NaCl started earlier than on samples with low initial concentration. Additionally, the cumulated mass loss after 10 days, i.e., the total amount of evaporated water was lower for the samples with higher initial concentration. *Bergstad et al. (2017)* found that crusts from samples with low initial concentration of NaCl built up faster on coarse sand than on fine sand, whereas for solutions at the solubility limit it was the other way around. These findings suggest that the hydraulic properties of crusts may be different for samples with low or high initial concentration. The results presented in this section suggest that there are significant uncertainties with liquid permeability determination of salt crusts from unsaturated saline solutions, and highlight the need for alternative methods to investigate crust permeability.

3.3.2. Evaporation of different types of salt solution from sand

Figure 3.7 presents the mean cumulative mass loss and the evaporation rate for the triplicate samples saturated with deionized water, NaCl, MgSO₄, and Na₂SO₄ solution. The samples saturated with deionized water were evaporated entirely after eight days with a 1-2 day differences between the samples (see Figure 3.7a). The samples with NaCl and Na₂SO₄ solution reached 20% water saturation after 9-17 days of evaporation. The evaporation rate of the samples with MgSO₄ solution was very low after 6 days of evaporation, and even after 60 days of evaporation the saturation was still above 20%. Therefore, the crust permeability of the MgSO₄ samples was determined when 30% saturation was reached after 60 days. This already suggests that the MgSO₄ crust had a substantial effect on the evaporation and almost sealed the surface of the porous medium in this study, which was not reported in previous studies (*Nachshon and Weisbrod, 2015*). This finding will be further elaborated when the results of the crust permeability determination are discussed.

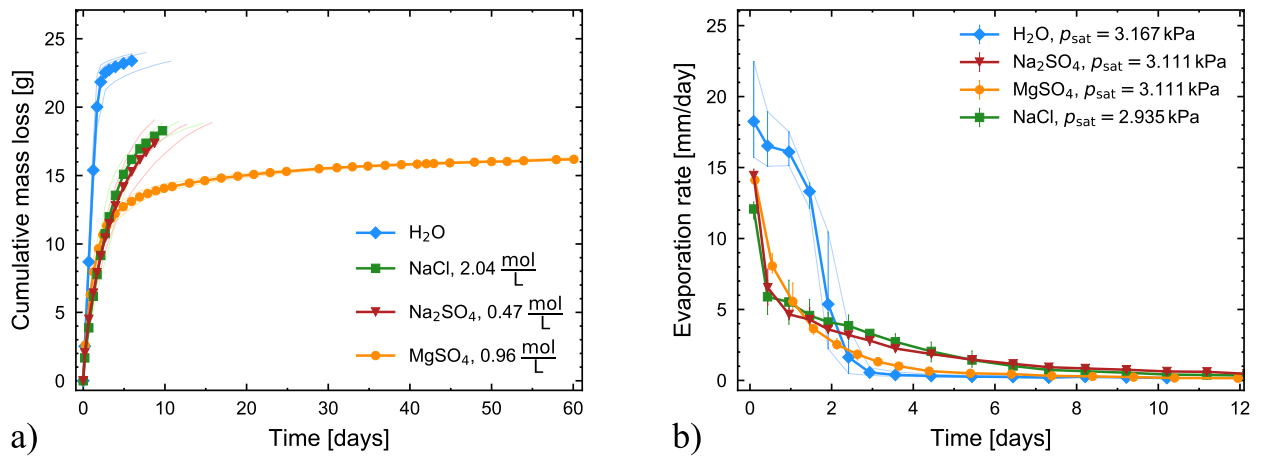


Figure 3.7: (a) Cumulative mass loss of samples with deionized water, NaCl, MgSO₄, and Na₂SO₄ solution from F32 quartz sand as a function of time. The light colored lines and the error bars show the measured mass loss of the individual samples. (b) Evaporation rate as a function of time. The evaporation rate is shown until day 12 only to provide a detailed view of the initial evaporation conditions.

The evaporation rate of all samples is shown in Figure 3.7b. The samples with deionized water consistently showed the highest mean initial evaporation rate of 18.3 mm/day at day 0. The mean initial evaporation rate was 14.4 mm/day for the samples with Na₂SO₄ solution and 14.1 mm/day for the samples with MgSO₄ solution. The mean initial evaporation rate of the samples with NaCl solution was the lowest with 12.1 mm/day. The order of the initial evaporation rates corresponds qualitatively to the initial saturation pressure of the solutions (see Table 3.3). Table 3.4 shows the ratio of the initial evaporation rate of samples with salt solution

and deionized water. Additionally, the vapor pressure difference of the initial saline solutions is normalized with the vapor pressure difference of deionized water according to Equation (2.15). It can be seen that the ratios of the initial evaporation rates are lower compared to the normalized vapor pressure difference estimated from the solution concentration at the start of the experiment. This is attributed to the relatively low temporal resolution used to determine the "initial" evaporation rate (i.e., determination of weight at the start and after 0.25 days of evaporation). In this time period, ions already accumulated at the surface and reduced the saturation vapor pressure of the liquids. Despite the lack of a quantitative agreement, the consistent order of the initial evaporation rate provides confidence that the method of sample preparation and the evaporation conditions in the laboratory provide meaningful results that are consistent with the general understanding of evaporation from porous media.

Table 3.4: Normalized ratios of initial evaporation rate and initial vapor pressure difference for the samples with different salt solutions. The ambient vapor pressure $p_{\text{amb}}^{\text{H}_2\text{O}} = 0.950 \text{ kPa}$ was determined at $25 \text{ }^\circ\text{C}$ and 30% relative humidity and the vapor pressure difference was obtained from Equation (2.15).

Solution	Initial evaporation rate	Initial evaporation rate normalized	Vapor pressure difference	Vapor pressure difference normalized
	[mm/day]	[-]	[kPa]	[-]
NaCl	12.1	0.66	1.985	0.89
MgSO ₄ · 7 H ₂ O	14.1	0.77	2.161	0.97
Na ₂ SO ₄	14.4	0.79	2.161	0.97
H ₂ O	18.3	1	2.217	1

In the case of the samples with deionized water, stage I evaporation occurred until day 1.5 (see Figure 3.7b). After 1.5 days, the evaporation rate dropped considerably indicating that stage II was reached. The slightly decreasing evaporation rate during stage I is attributed to the high evaporation rate ($\approx 15 \text{ mm/day}$). This is in agreement with previous studies, where it was also reported that the evaporation rate in stage I is not necessarily constant for rates higher than 5 mm/day (*Or et al.*, 2013; *An et al.*, 2018).

The evaporation rate of the saline samples decreased substantially within the first day. This is attributed to the accumulation of ions in the top layer during evaporation of water and the resulting decrease of the saturation pressure, which is characteristic for stage SS1 evaporation of saline solutions. Crust formation was visually monitored for all saline samples (Figure 3.8). The samples with NaCl solution developed a white efflorescent crust on top of the sand surface within the first two days (Figure 3.8b). For the samples with MgSO₄ solution, almost no change of the surface was visible besides some differences in color that were attributed to differences

in saturation (Figure 3.8e). The crusts of the samples with Na_2SO_4 solution appeared glassy with white patches on top after two days (Figure 3.8h), which is consistent with observations in previous studies (Nield *et al.*, 2016). In combination with the evaporation rates, these crust observations suggest that the impact of the crust on evaporation and thus the transition to stage SS2 evaporation already occurred between day 1 and day 2 for all saline samples.

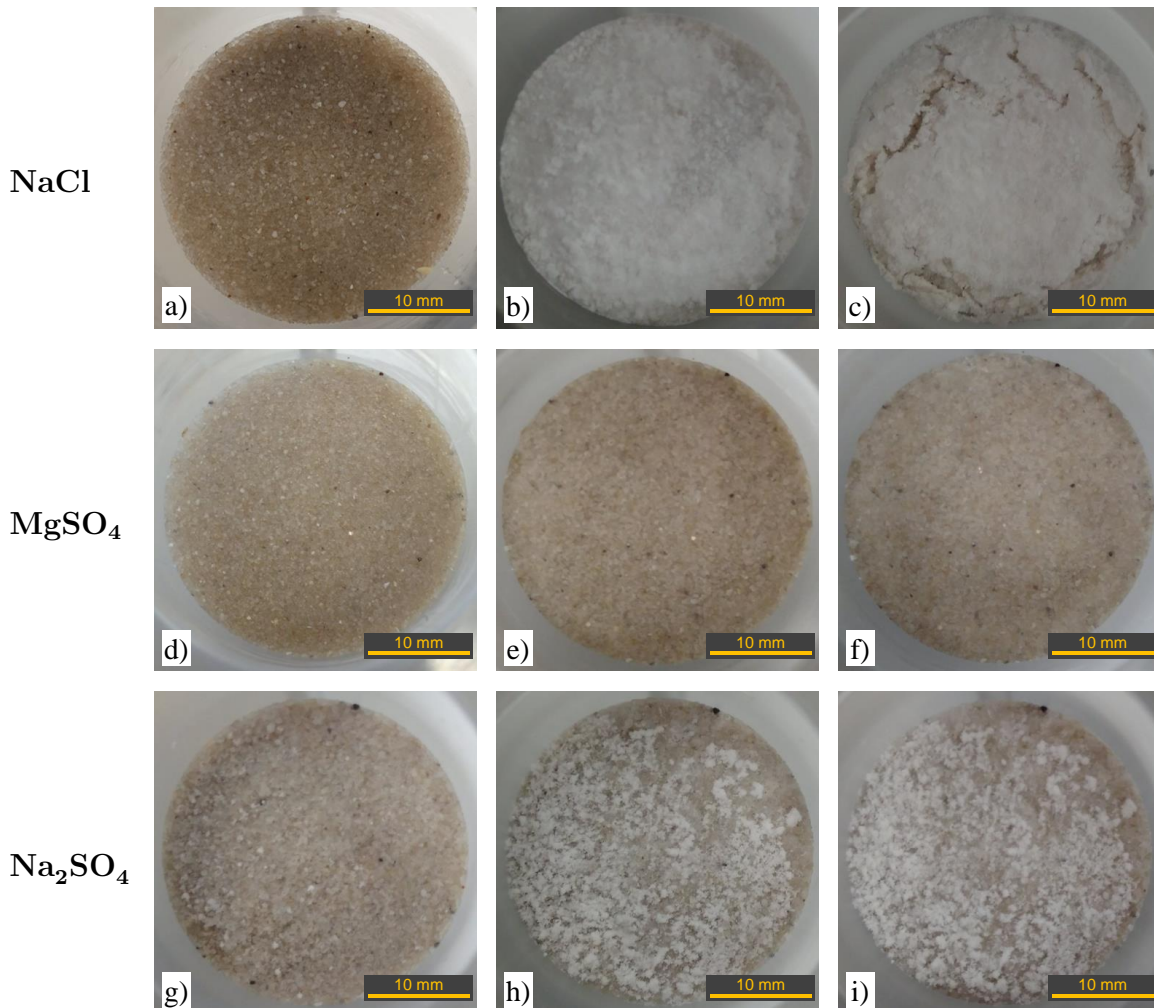


Figure 3.8: Photos of sample surface at different times (first column: after sample preparation; second column: after two days of evaporation; third column: before crust separation). (a,b,c) NaCl . (d,e,f) MgSO_4 . (g,h,i) Na_2SO_4 .

Shortly after the start of evaporation stage SS2, the evaporation rate of the samples with MgSO_4 solution decreased below that of the samples with NaCl and Na_2SO_4 solution and dropped below 0.1 mm/day after six days (Figure 3.7b). At that time, only half of the initial amount of water was evaporated (≈ 12 mL of 23 mL). Therefore, it seems likely that capillary liquid paths were still connected to the sample surface. At the end of the evaporation experiment (60 days), the sand below the MgSO_4 crusts was found to be wet throughout each column,

which further supports the assumption of a liquid connection to the surface. Additionally, the crusts themselves were wet after separation (see below). The low evaporation rate is thus attributed to the presence of the subflorescent crust that may have partly closed the pore space. Additionally, the high viscosity of the supersaturated MgSO_4 solution most likely reduced the speed of supplying liquid to the surface. Clearly, knowledge of the complex interaction between pore space reduction (i.e., higher capillary pressure, Equation (2.14)) and decreasing viscosity of the supersaturated MgSO_4 solution is needed. Thus, the pore space of subflorescent MgSO_4 crusts will be investigated in Chapter 4 using μXRCT image data on the micro-scale and the water content during evaporation will be monitored in Chapter 5 using μXRCT and unilateral NMR.

For the samples with NaCl solution, the evaporation rate remained between 4.1 and 2.7 mm/day from day 2 to day 3. This plateau in the evaporation rate during stage SS2 was also reported during the formation of the efflorescent NaCl crust in previous studies (*Shokri-Kuehni et al.*, 2017). The evaporation rate of the samples with NaCl and Na_2SO_4 solutions fell below 1 mm/day at day 9, shortly before the crust separation for the individual samples (see Figure 3.7b). As the removed sand below the crusts was wet and the crusts themselves contained water (see below), it is likely that a liquid capillary connection to the surface was present until the separation of the crust. In Chapter 5, the water content will be determined using NMR during subflorescent MgSO_4 precipitation, however, future studies should monitor the liquid content during evaporation for other salt types such as NaCl and Na_2SO_4 .

3.3.3. Permeability of crusts from different salts

Exemplary results for the crust permeability determination are shown in Figure 3.9 for two selected crusts. In Figure 3.9a, the measured pressure differences for the Na_2SO_4 crust were low and relatively close to the accuracy of the pressure transducer (0.01 mbar) for the low gas flow rates. Nevertheless, a strong linear relationship between pressure difference and gas flow rate was observed ($R^2 = 0.9884$). In case of the MgSO_4 crust (Figure 3.9b), the relationship between pressure difference and gas flow rate was also strongly linear ($R^2 = 0.9916$). To test the flow conditions during the measurements, the two examples shown in Figure 3.9 were selected because they represent the lowest and highest measured pressure differences at the highest flow rate of 300 mL/min for all crusts. The analysis of the measurement with the highest pressure difference using the Forchheimer equation that accounts for gas compressibility showed an almost identical Darcy permeability (i.e., $k_{\text{viscous}} = 1.00 \cdot 10^{-14} \text{ m}^2$ for Equation (2.25) and $k = 1.03 \cdot 10^{-14} \text{ m}^2$ for Darcy's law, Equation (2.5)) (*Rust and Cashman*, 2004; *Takeuchi et al.*, 2008). Additionally, the Forchheimer number $Fo = 0.1$ was one order of magnitude below the threshold value of the transition from Darcy to non-Darcy flow ($Fo = 1$) (*Zeng and Grigg*,

2006). This indicates that gas compressibility can be neglected for the experimental conditions used in this study. The measurements of all salt crusts resulted in linear regression equations with R^2 above 0.9804 (Figure A.2 in Appendix A). This clearly indicates that the assumption of laminar flow conditions and incompressible gas were valid for all measurements performed in this study. The results of the crust thickness determination are listed in Table A.1 in Appendix A. In the case of NaCl crusts, the dome-shaped structures filled with air were not considered for the crust thickness determination.

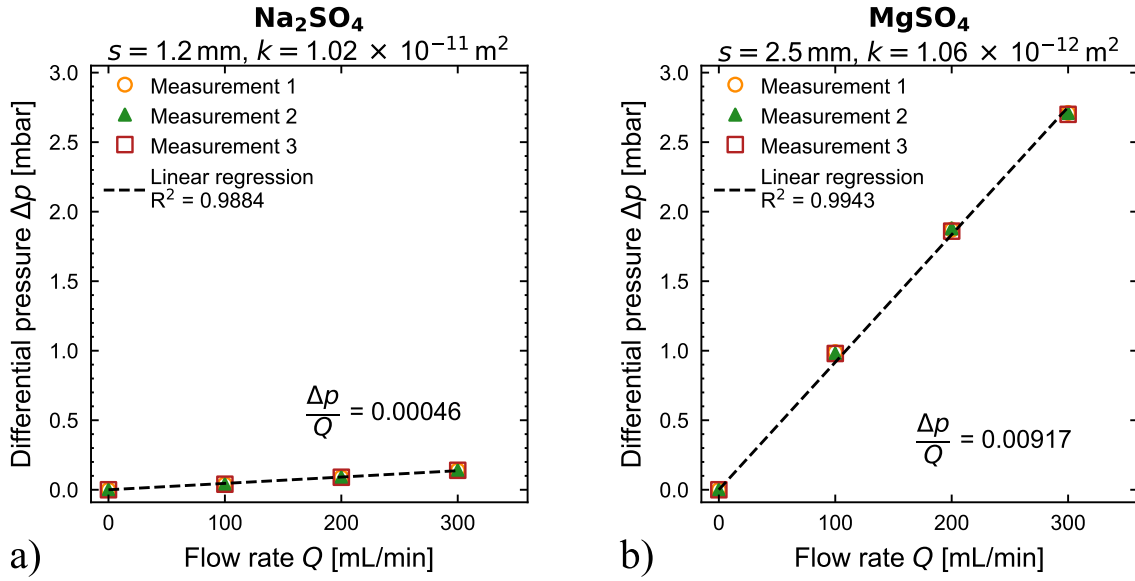


Figure 3.9: Pressure difference as a function of gas flow rate for two selected salt crusts at the highest flow rate of 300 mL/min. (a) Lowest measured pressure difference of all dried crusts. (b) Highest measured pressure difference of all dried crusts.

Figure 3.10 shows the gas permeability of the separated crusts from different salt types directly after evaporation (Figure 3.10b) and after further drying (Figure 3.10a). It should be noted that some additional salt precipitation likely occurred within the crust due to the oven drying, which may have affected the obtained crust permeability. The mean permeability of the sand columns is also provided ($2.10 \cdot 10^{-11} \text{ m}^2$) and serves as a reference for the permeability of the different salt crusts. The mean permeability of the sand and both the wet (probability = 0.0001) and the dry crusts (probability = 0.0002) were significantly different according to a one-way analysis of variance (ANOVA). Obviously, only the intrinsic permeability of the salt crusts determined in the dry state can be compared to previously reported estimates of (intrinsic) permeability obtained using liquids. The mean permeability of the dry NaCl crusts was $4.77 \cdot 10^{-12} \text{ m}^2$ in this study (Figure 3.10a). This value is similar to the NaCl crust permeability found in previous studies ($3.7 \cdot 10^{-12} \text{ m}^2$ Weisbrod *et al.* (2014) and $4 \cdot 10^{-12} \text{ m}^2$ Nachshon and Weisbrod (2015)) although the initial concentration of the evaporating solutions was different (0.89 mol/L Weis-

brod et al. (2014), 2.04 mol/L in this study, and 6.13 mol/L *Nachshon and Weisbrod* (2015)). It is known that NaCl crusts build an efflorescent layer on top of the surface, which can be considered as a new porous medium with its own transport properties. The consistency of our results with previous studies suggests that the initial concentration of the NaCl solution affects the intrinsic permeability of the efflorescent NaCl crusts to a minor extent. Nevertheless, the speed of crust formation and the appearance of the crust depend substantially on the initial concentration, as already reported in previous studies (*Bergstad et al.*, 2017).

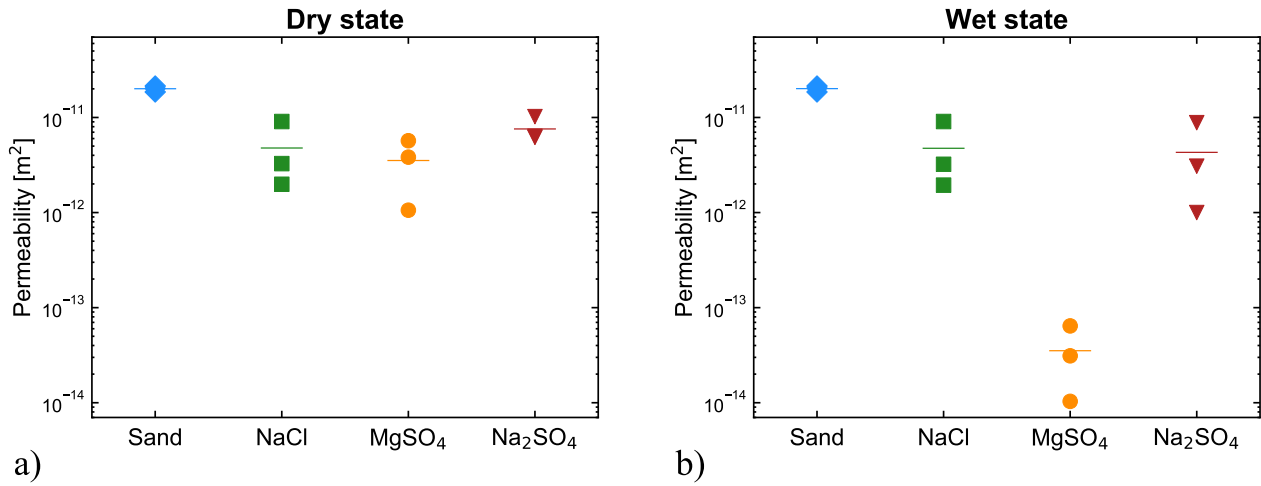


Figure 3.10: Permeability of sand and of crusts formed from evaporation of NaCl, MgSO₄, and Na₂SO₄ solution. (a) Intrinsic permeability after drying at 60 °C for 96 hours (dry state). (b) Permeability directly after evaporation (wet state). The label "Sand" indicates the samples with deionized water. The horizontal colored bar represents the arithmetic mean value.

The mean intrinsic permeability of the MgSO₄ crusts ($3.53 \cdot 10^{-12} \text{ m}^2$) was similar to the mean permeability of the NaCl crusts ($4.77 \cdot 10^{-12} \text{ m}^2$) (Figure 3.10a). This finding is not in agreement with previously reported results, where the permeability of the MgSO₄ crusts ($3 \cdot 10^{-11} \text{ m}^2$) was almost one order of magnitude higher than the permeability of the NaCl crusts ($4 \cdot 10^{-12} \text{ m}^2$) (*Nachshon and Weisbrod*, 2015). This is at least partly attributed to the difference in permeability of the sand used for the evaporation experiments ($5 \cdot 10^{-10} \text{ m}^2$ in *Nachshon and Weisbrod* (2015) and $2.10 \cdot 10^{-11} \text{ m}^2$ in this study). Clearly, the permeability of subflorescent MgSO₄ crusts depends strongly on the properties of the porous medium. In addition, fully saturated salt solutions were used and the samples were allowed to evaporate for 80 hours only in *Nachshon and Weisbrod* (2015). In this study, the samples with MgSO₄ solution were allowed to evaporate for a much longer time (60 days). This may have led to a denser crust despite the use of a lower initial salt concentration. Therefore, the differences in permeability of the MgSO₄ crusts may also be due to the different experimental conditions and especially to differences in the time of evaporation. The dependence of the permeability of MgSO₄ crusts on initial concentration and

the temporal crust development will be investigated in more detail in Chapter 4 and Chapter 5, respectively.

The mean intrinsic permeability of the subflorescent Na_2SO_4 crusts is also reported in Figure 3.10a. It was found to be $7.57 \cdot 10^{-12} \text{ m}^2$, which was slightly higher than that of the MgSO_4 crusts. This is the first time that the permeability of a subflorescent Na_2SO_4 crust was determined. It is interesting to note the differences in crust permeability before and after drying in Figure 3.10. In the case of the NaCl crusts, a considerable mass loss of 20% was observed upon drying of the crust, but the permeability before and after drying was nevertheless similar (see Figure 3.10). It was already reported that NaCl crusts were wet during evaporation (*Shokri-Kuehni et al.*, 2017). Additionally, it was shown that efflorescent NaCl crusts partly detach from the surface of the sample and create dome-shaped structures with air between loosely connected "pillars" on the surface (*Nachshon et al.*, 2018). Similar structures were observed in this study (Figure 3.8c). The small difference in permeability before and after drying suggests that the remaining water in the crust was located in pore spaces that do not effectively contribute to gas flow, which may be related to the complicated structure of NaCl crusts (*Nachshon et al.*, 2018). In contrast, the mean intrinsic permeability of the MgSO_4 crusts in the dry state ($3.53 \cdot 10^{-12} \text{ m}^2$) was two orders of magnitude higher than the mean relative gas permeability in the wet state ($3.52 \cdot 10^{-14} \text{ m}^2$) (see Figure 3.10). This increase in permeability was associated with a mass loss of 30% during drying. In the case of the Na_2SO_4 crusts, the intrinsic gas permeability in the dry state ($7.57 \cdot 10^{-12} \text{ m}^2$) was also substantially higher than the relative permeability in the wet state ($4.30 \cdot 10^{-12} \text{ m}^2$) and the associated mass loss after drying was 19%. Clearly, the remaining liquid inside the pores of these subflorescent crusts partly blocked the pores and reduced the permeability for gas in the wet state.

The results presented above suggest that the intrinsic permeability of salt crusts formed by evaporation of unsaturated saline solutions can be reliably determined with the proposed gas permeameter set-up. For the given experimental conditions, it was found that the NaCl and MgSO_4 crusts showed a comparable permeability in the dry state, whereas the mean gas permeability of Na_2SO_4 was slightly higher. However, all crusts were found to be wet during the entire evaporation process indicating that the intrinsic crust permeability alone is not sufficient to explain the evaporation of the samples with salt crust formation. This is highlighted by the relatively high intrinsic permeability of the MgSO_4 crusts that was associated with a very low evaporation rate. Therefore, the relative permeability of the crust also needs to be considered to improve understanding of evaporation processes in the presence of salt crusts. In particular, it is of interest to investigate the location of the evaporation front in evaporating samples with crust formation in order to determine if liquid capillarity or gas diffusion governs water transport through the crust.

In this study, the mean intrinsic permeability of the MgSO_4 crusts determined using liquid flow

($6.77 \times 10^{-12} \text{ m}^2$) was higher than the mean intrinsic permeability of the dry MgSO_4 crusts that was obtained from gas flow measurements ($3.53 \times 10^{-12} \text{ m}^2$). However, the mean permeability of the samples without crust that was determined using liquid flow ($7.99 \times 10^{-12} \text{ m}^2$) was lower than the mean permeability of the samples without crust using gas flow ($2.10 \times 10^{-11} \text{ m}^2$). Hence, the decrease in permeability due to crust formation was found to be higher for the samples used for gas permeability determination. This difference was attributed to three uncertainties that were elaborated above. First, the samples measured with gas flow evaporated for 60 days. In contrast, the samples for liquid flow measurements evaporated for 30 days only. Hence, a denser crust with a lower permeability may have formed in the samples that were measured using gas flow. The second uncertainty is related to the estimated density and viscosity of the MgSO_4 solution inside the resaturated samples that were used for liquid flow measurements. For example, a small decrease in the concentration of the MgSO_4 solution from 2.88 mol/L to 2.50 mol/L would result in a substantial decrease in the viscosity (8.066 mPa.s to 6.336 mPa.s) and an associated linear decrease in permeability according to Equation (2.12). The third substantial uncertainty results from air entrapment after resaturation, which affected the liquid flow. In the case of the permeability determination on dry separated crusts using gas flow, the amount of assumptions is considerably reduced. Therefore, the results from permeability determination using gas flow are deemed to be more reliable than the results from permeability determination using liquid flow.

3.4. Conclusions

Uncertainties in liquid flow measurements for the determination of the intrinsic crust permeability (i.e air entrapment and crust dissolution) were avoided by using the novel gas permeameter set-up. The presented results suggest that an easy and more accurate determination of the permeability of salt crusts was possible for crusts formed from low initial concentration. The novel approach using gas flow measurements allowed the analysis of the permeability of separated salt crusts that formed during the evaporation of unsaturated NaCl , MgSO_4 , and Na_2SO_4 solutions from sand columns. The intrinsic permeability of the efflorescent NaCl crusts was found to be comparable to previously reported values. The intrinsic permeability of the subflorescent MgSO_4 crusts was lower than previously reported values, which was attributed to the different properties of the used porous medium and to differences in the time of evaporation.

The impact of the intrinsic permeability of the salt crust on the evaporation differed for the three types of salt. In the case of the efflorescent NaCl crust, the formation of a crust with a lower intrinsic permeability than the underlying porous medium seemed to have reduced the evaporation rate, which was also reported in previous studies (*Nachshon and Weisbrod, 2015*).

The low evaporation rate of the samples with MgSO_4 solution could not be explained by the relatively high intrinsic permeability of the subflorescent MgSO_4 crusts. The similar evaporation and slightly higher crust permeability of the samples with Na_2SO_4 solution compared to the samples with NaCl solution indicated a similar impact on evaporation.

Since it was found that the initial concentration has a substantial impact on efflorescent NaCl crust formation (*Bergstad et al.*, 2017), it is important to study the effect of varying initial concentration for salt types that form subflorescent precipitation. In addition, knowledge of the available pore space within the crusts obtained from micro X-Ray computed tomography (μXRCT) may provide insights on the relationship between porosity and permeability, which can be used to model evaporation and subflorescent salt precipitation. This will be addressed in Chapter 4.

The large differences in (relative) gas permeability of the subflorescent salt crusts between the wet state and the dry state observed in this study suggest that the distribution of water in the salt crust in unsaturated conditions may have an underestimated impact on evaporation. Thus, future studies should also focus on unsaturated flow properties of salt crusts. In particular, the investigation of the water retention properties and the liquid distribution in the crust may provide information on how the unsaturated conditions inside the crust affect evaporation. In this context, it is of interest to investigate the time dependency of the crust formation and the resulting effects on the liquid distribution using μXRCT and unilateral NMR to explore the dynamic effects on evaporation. Furthermore, it would be interesting to monitor the location of the evaporation front and the dynamics of salt precipitation in the pore space to obtain a deeper understanding of the processes that control the low evaporation in the presence of a subflorescent MgSO_4 crust. These topics will be investigated in Chapter 5.

Chapter 4

Porosity and permeability of subflorescent magnesium sulfate crusts

4.1. Introduction

In this chapter¹, the permeability of subflorescent magnesium sulfate crusts determined using gas flow will be related to properties of the crusts obtained from μ XRCT at the micro-scale. These investigations are motivated by the findings in Chapter 3, where it was argued that changes in pore structure significantly affect evaporation. For this, sand samples with MgSO_4 solution of varying initial concentration will be allowed to evaporate until 40%, 30%, or 20% saturation is reached. Then, the crust will be separated from the sand and the permeability of the separated crusts will be determined following the procedures developed in Chapter 3. The separated crusts will then be measured using μ XRCT to obtain 3D imaging data at the micro-scale and advanced post-processing methods will be used to provide the segmented 3D imaging data to analyse the pore structure. The results will be combined to obtain a porosity-permeability relationship for subflorescent MgSO_4 crusts from varying initial concentration, which is the second sub-objective of this thesis.

The remainder of this chapter is organized as follows. First, the sample preparation and the experimental crust permeability determination introduced in Chapter 3 will be recapitulated. Then, details of the μ XRCT measurements and the post-processing of the obtained imaging data will be provided. In a next step, the results from evaporation, crust permeability, and the XRCT-based pore-scale analysis will be presented. Finally, the experimental results will be put into context in an overall discussion.

¹This chapter is adapted from a journal article in preparation: Piotrowski, J., Lee, D., Pohlmeier, A., Vereecken, H., Steeb, H., and Huisman, J.A., Porosity and permeability of subflorescent salt crusts formed by evaporation from porous media.

4.2. Materials and methods

4.2.1. Samples with varying initial concentrations

The custom-made sample holders with an inner diameter of 31 mm made from polymethylmethacrylat (PMMA) that were presented in Chapter 3 were also used for the experiments presented in this chapter (Figure 3.2 and Figure 4.1). Evaporation and salt crust formation of triplicate samples with four different concentrations of MgSO_4 solution were investigated (0.00, 0.32, 0.64 and 0.96 mol/L MgSO_4 , Th. Geyer, Renningen, Germany). Samples were prepared by filling the sample holders with solution and adding 100 g of F32 quartz sand with a particle density of 2.65 g/cm^3 and a mean grain diameter of $240 \text{ }\mu\text{m}$ (Quarzwerte Frechen, Frechen, Germany). The resulting height h of each sample was $80 \pm 1 \text{ mm}$. After sample preparation, excess liquid was drained through an opening in the bottom plug that was closed afterwards. The liquid content of every sample was determined gravimetrically using the sample dimensions and the mass and density of the sand. The porosity of each sample was assumed to be equal to this initial liquid content and was $0.38 \pm 0.006 \text{ cm}^3/\text{cm}^3$. Subsequently, the twelve samples were grouped in batches of four samples and each batch was placed below a fan (WFB1212M, Delta Electronics, Taipei, Taiwan) to initiate evaporation. The temperature and the relative humidity were recorded with a data logger (FHAD 46-C2, ALMEMO[®] D06, Ahlborn, Holzkirchen, Germany) and varied in the range of $26 \pm 4 \text{ }^\circ\text{C}$ and 24% to 48%, respectively. Initially, the mass of every evaporating sample was determined twice a day with a

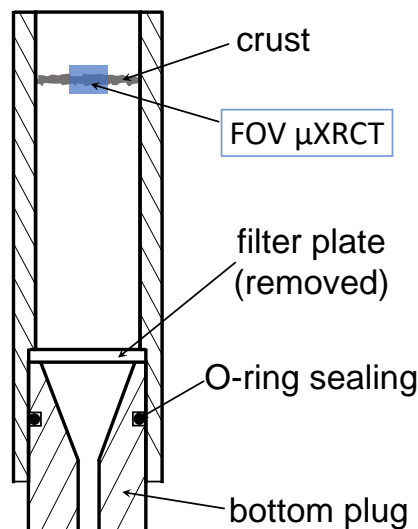


Figure 4.1: Sample holder with field-of-view (FOV, blue) of μXRCT measurements used to characterize the separated salt crust. The dimensions of the FOV are $11.76 \text{ mm} \times 11.76 \text{ mm} \times 9 \text{ mm}$.

balance (accuracy ± 0.02 g, EX2202, Ohaus Cooperation, Parsippany, USA), which was used to calculate the evaporation rate and the corresponding saturation of each sample. After five days, the mass loss was measured once per day and after 18 days once every two days. The increased time interval allowed a reliable mass loss determination despite the lower evaporation rate.

Evaporation of the nine samples with saline solution was stopped at three levels of saturation in the respective sample (40%, 30%, and 20%) so that one sample (crust) from each initial concentration at each level of saturation was obtained. The sand below the crust was removed and collected. The removed sand as well as the crust that was tightly attached to the sample holder were dried for 96 hours at 60 °C. The mass balance after oven-drying showed a maximum deviation of 4% from the known amount of initially added water. The crust thickness, which is necessary for the calculation of the intrinsic permeability, was obtained from μ XRCT data (see below). After drying, the intrinsic permeability of each crust was determined using the gas permeameter approach already tested and used in Chapter 3 (see Figure 3.4a and Table 3.3). This provided the intrinsic permeability of all nine crusts formed from solutions with different initial concentration and evaporation duration. Additionally, the samples prepared with deionized water were dried and the intrinsic permeability of the remaining pure sand was determined. For this, the permeability of the sand was calculated by considering the permeability of the filter plate and assuming a connection in series (*Nachshon and Weisbrod, 2015*). More information about these experiments can be found in the published data set (*Piotrowski and Huisman, 2021*).

4.2.2. Micro-X-ray computed tomography hardware and projections

A modular and flexible μ XRCT set-up was used for all scans (*Ruf and Steeb, 2020*) (Figure 4.2). A source current of 130 μ A and a source voltage of 130 kV were used, which resulted in a source power of 16.3 W to record each projection (see Table 4.1). The exposure time (i.e., the time of X-ray emission to acquire one projection) was 1500 ms. The geometric magnification of 12.375 was obtained from the source-detector-distance (SDD) of 1011.11 mm and the source-object-distance (SOD) of 81.706 mm using Equation (2.28). With the used detector (see Table 4.1), this resulted in a resolution of $4 \mu\text{m} \times 4 \mu\text{m} \times 4 \mu\text{m}$ per voxel and a corresponding field-of-view (FOV) of $11.76 \text{ mm} \times 11.76 \text{ mm} \times 9 \text{ mm}$. After acquiring one projection, the sample was rotated by 0.2° and the next projection was taken until a total amount of 1800 projections were recorded (i.e., a full rotation of 360°). This procedure was repeated five times in total with shifted detector position (i.e., 14 pixels up, down, left, and right with respect to the initial detector position). The resulting five images were merged using the stitching procedure by *Ruf and Steeb* (2020) to exclude dead pixels that originate from manufacturing imperfections in the

detector.

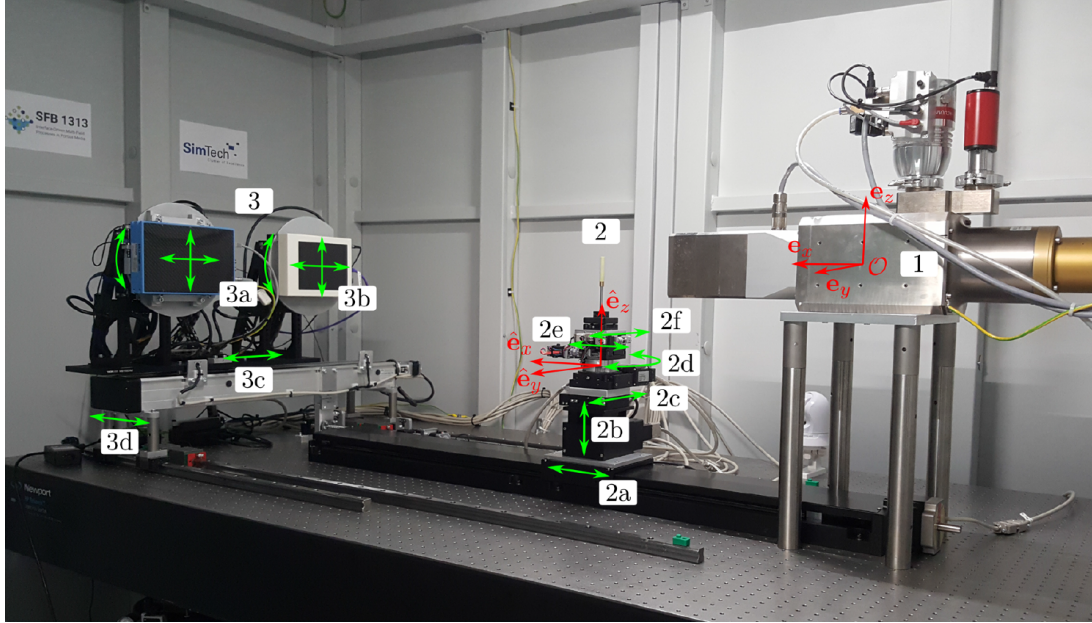


Figure 4.2: Photo of the modular μ XRCT set-up that was used to investigate salt precipitation on the pore-scale (from *Ruf and Steeb* (2020)). The source (1) was fixed, the position of the sample (2) can be adjusted using the stages (2a-2f). The rotation of the sample was performed with the rotation table (2d). The position of the used detector (3b) was only changed according to the scan procedure (3a was not used, and stages 3c,d were not changed).

Table 4.1: Technical specifications of the μ XRCT set-up (*Ruf and Steeb*, 2020).

Device	Name	Company	Location	Details
X-ray source	FORE 180.01C TT	Finetec Technologies GmbH	Garbsen, Germany	Tungsten transmission target
Detector	Shad-o-Box 6K HS	Teledyne DALSA Inc.	Waterloo, Ontario, Canada	CsI scintillator, pixel size 0.0495 mm

4.2.3. Reconstruction and post-processing of μ XRCT measurements

To obtain a 3D image from the μ XRCT measurements, cone beam reconstruction of the merged projections was performed with Octopus Reconstruction using the filtered back projection (FBP) option (Table 4.2). A list of all reconstruction parameters is provided in Table 4.3. During reconstruction, the projections were normalized and sinograms (i.e., an intermediate step for the conversion from 2D projections to slices in perpendicular direction) were created. During the creation of the sinograms, the intensity value of each detector pixel was inverted so

that pixels that recorded a high X-ray attenuation (i.e., low intensity) appear darker than pixels that recorded a low X-ray attenuation (i.e., high intensity). Then, the Fourier filter option "region of interest" and the quality mode "bi-linear interpolation" were enabled to enhance the image quality. The settings were applied on the entire stack and the result was stored in the form of axial slices in 8-bit grey-scale 2D images in the .tif-file format. The thickness of each slice (4 μm) was equal to the voxel size of the image data.

Table 4.2: Details of the reconstruction and the filtering software to process μXRCT measurements (*Ruf and Steeb, 2020*).

Process	Method	Company		Location	Details
Reconstruction	Filter back projection	-		Ghent, Belgium	Octopus Reconstruction (<i>Vlassenbroeck et al., 2007</i>), Version 8.9.4.9
Filtering	3D adaptive non-local manifold filter	Thermo Scientific	Fisher	Waltham, MA, USA	AVIZO [®] , Version 2019

Table 4.3: Reconstruction parameters for μXRCT measurements using Octopus Reconstruction (Table 4.2). The published data sets are available in *Ruf et al. (2021a,b,c)*.

Group	Parameter	Setting/Value
Geometry	Mode	Cone beam
	Last angle	360°
	Pixel size	0.0495 mm
	Centre of rotation ^a	1479.5
	Source object distance	81.706 mm
	Source detector distance	1011.11 mm
	Direction of rotation	Clockwise
	Vertical centre ^a	1152
	Horizontal centre ^a	1470
	Tilt	0°
	Skew	0°
Quality	Voxel size	0.00399 mm
	Noise filter	0
	Filter type	Region of interest
	Quality	Bi-linear interpolation
	Beam hardening correction method	No bhc
	Scatter correction value	0
	Zero clipping value	0.001
	Vertical smoothing	false

^a varied for different scans

Table 4.3: Continued.

Group	Parameter	Setting/Value
Ring filter settings		
	Maximum ring size	15
	Minimum arc length	270°
	Lower limit intensity	-0.446494
	Upper limit intensity	5.8715
	Maximum ring intensity	3.15899
Output	Offset angle	0
	Output type	8 bit
	Scaling mode	After reconstruction
	Minimum grey value ^a	-1.01153
	Maximum grey value ^a	6.52393
	Region	false
Range	Start position ^a	700
	End position ^a	1469
	Step	1

^a varied for different scans

The reconstructed image stack was filtered to reduce inherent noise in the measurements and noise from the reconstruction process. The adaptive manifold non-local mean filter was applied in 3D on the stack using AVIZO[®] (Schlüter *et al.*, 2014) (Table 4.2). Default settings were used for the spatial standard deviation (5), the intensity standard deviation (0.2), the search window (10 px), and the local neighborhood (3 px) (Table 4.4). The resulting filtered 3D stack was saved in 2D axial slices in 16-bit grey-scale .tif-format.

Table 4.4: Filtering parameters used on reconstructed μ XRCT imaging data using AVIZO[®] (Thermo Fisher Scientific, Waltham, MA, USA). The published data sets are available in Ruf *et al.* (2021a,b,c).

Filter	Parameter	Setting/Value
3D adaptive manifold non-local mean (AMNLM)	Mode	GPU adaptive manifold
	Interpretation	3D
	Spatial standard deviation	5
	Intensity standard deviation	0.2
	Search window	10 px
	Local neighborhood	3 px
	CUDA Device	GeForce GTX 780, 3072 MB

4.2.4. Segmentation and analysis of processed imaging data

The segmentation of the filtered data into outside, void, salt, and sand voxels was performed slice-by-slice in three steps. First, the solid phase (salt + sand) was roughly estimated using the MATLAB[®]-functions "multithresh" and "imquantize" (Table 4.5). In the second step, the output of the first step served as input for the MATLAB[®]-function "active contour" (Table 4.5), where the exact contour of the solid phase was determined. The binarized contour output data was used to determine the combined area of void space and outside in the filtered data. This provided the input for the third step, where salt and sand were segmented using the MATLAB[®]-function "k-means clustering" (Table 4.5). Combining the results of the second and third step provided the segmented data, which consisted of the three phases void/outside, salt, and sand. The outside of each horizontal axial slice was removed by cropping using a circular mask, which provided the void space in every axial slice. The removal of the outside area in vertical direction (i.e., above and below the surface of the crust) is described below.

Table 4.5: Segmentation steps, methods and parameters used to process filtered μ XRCT imaging data using MATLAB[®] (Image processing toolbox, Version 2019b, The Mathworks Inc., Natick, MA, USA). More information is available in the published data sets (*Ruf et al.*, 2021a,b,c).

Step	Method	Parameter	Setting/Value	Details
1.	Multithresh	Threshold	3	<i>Otsu</i> (1979)
	Imquantize	Levels	Output multithresh	
2.	Active contour	Mask	Output imquantize	Salt and sand phase only <i>Chan and Vese</i> (2001)
		Method	Chan-Vese	
		SmoothFactor	1.1	
3.	K-means clustering	Clusters	3	<i>MacQueen</i> (1967)
		Distance	Cityblock	

To determine the top and bottom surface of each crust segment from the 3D imaging data, the maximum and the minimum voxel position with solid phase in vertical direction were determined. The topmost voxels with solid phase describe the top surface of the salt crust and the lowermost voxels with solid phase describe the bottom surface. Before determining the crust thickness distribution by subtraction, both surfaces were smoothed using a median filter (window size of 31 px \times 31 px, see Table 4.6). The window size was chosen as small as possible while still removing outlier pixels. The selected window size is substantially smaller than the mean grain size (≈ 60 px \times 60 px). The average crust thickness was determined by calculating the arithmetic mean of the thickness distribution. After obtaining the top and bottom surface, they were used to remove the outside phase above and below the crust from the segmented 3D image. Finally, the volume fractions of void, salt, and sand were determined between the

top and the bottom surface using the MATLAB[®]-function "regionprops" for each axial slice of the masked 3D image (Table 4.6). The phase volume fractions for the entire crust were obtained by dividing the total amount of void, salt, and sand phase voxels by the total amount of voxels in the crust. The reconstructed and segmented μ XRCT imaging data sets for the nine crusts formed from varying initial concentration have been published as data sets (*Ruf et al.*, 2021a,b,c). The published data sets provide the axial slices of both the reconstructed and the segmented μ XRCT data in .tif-file format together with the processing parameters used to obtain these results.

Table 4.6: Additional procedures, methods and parameters used to process segmented μ XRCT imaging data using MATLAB[®] (Image processing toolbox, Version 2019b, The Mathworks Inc., Natick, MA, USA).

Procedure	Method	Parameter	Setting/Value	Details
Surface filtering	Medfilt2	Window size	31 px	Top and bottom surface of crust segment
Volume fractions	Regionprops	Masked 3D image	Area	Analysis 2D slice-by-slice

4.3. Results

4.3.1. Evaporation of salt solutions with varying initial concentration

Figure 4.3 shows the mean evaporation rate of all samples until day 13. The initial evaporation rate of the reference samples with deionized water was 30.5 mm/day. In contrast, the initial evaporation rate of the samples with deionized water was 18.3 mm/day in Chapter 3, where the same preparation methods were used. The higher initial evaporation rate is attributed to the use of fans with a higher air flow velocity in this chapter. The transition from stage I to stage II of evaporation occurred between day 1 and day 2 in this study, as indicated by the significant drop of the evaporation rate. It is known that the evaporation rate is not necessarily constant in stage I for high evaporative demands (*Or et al.*, 2013; *An et al.*, 2018), and this was also found here.

The mean initial evaporation rate of the samples with MgSO_4 solution was lower than the initial evaporation rate of the samples with deionized water. This is attributed to the difference of the saturation vapor pressure at the surface and the vapor pressure of the ambient air, which is higher in the case of deionized water. During day 1, the evaporation rate of the samples with saline solution decreased, as the solutes accumulated at the surface and reduced evaporation (stage SS1). It was found that the evaporation rate of all samples with saline solution was

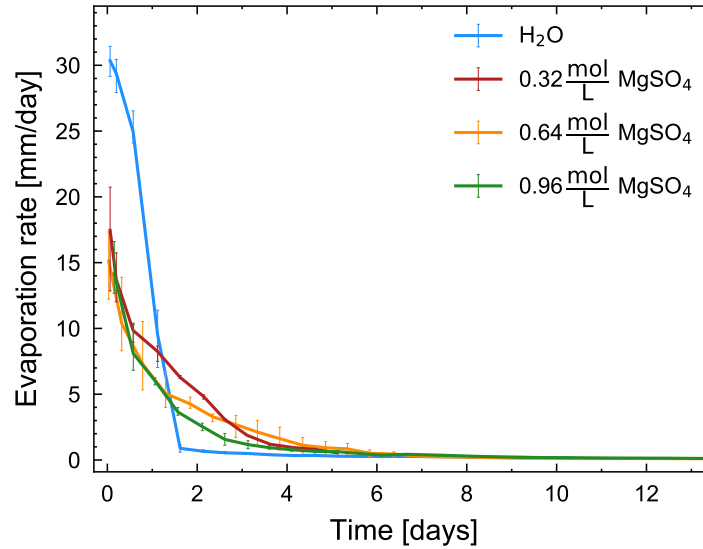


Figure 4.3: Evaporation rate of samples with deionized water and varying initial MgSO_4 concentrations from sand. The error bars indicate the variation in the evaporation rate of the remaining samples. After day 13, the evaporation rate was below 0.1 mm/day for all remaining samples.

similar during stage SS1. This suggests that the impact of the varying initial concentration of MgSO_4 solution is minor during stage SS1, which was also found in previous studies investigating the evaporation of NaCl solutions with various initial concentration (*Bergstad et al., 2017*).

Between day 1 and day 5, the mean evaporation rate of the samples with saline solution diverged with the highest rate for the samples with the lowest initial concentration and the lowest rate for the samples with the highest initial concentration. The mean evaporation rate of all samples converged again after day 5 at a relatively low evaporation rate less than 0.3 mm/day. Initial crust development was observed for all samples between day 1 and day 5 indicating the start of stage SS2 of evaporation. During stage SS2, the crust formation from different initial concentrations obviously affected evaporation. It was observed that a higher initial concentration led to a lower evaporation rate. After day 5, the remaining crusts that formed from the different initial concentrations had a similar impact on the evaporation rate, which stayed below 0.05 mm/day until the end of the experiment.

4.3.2. Thickness and intrinsic permeability of separated crusts

Figure 4.4 shows the top and bottom surface of a crust formed from 0.64 mol/L initial concentration at 20% saturation determined from μXRCT data. Figure 4.4a shows that this sample had a flat top surface and minor variations at the left side of the bottom surface. The roughness

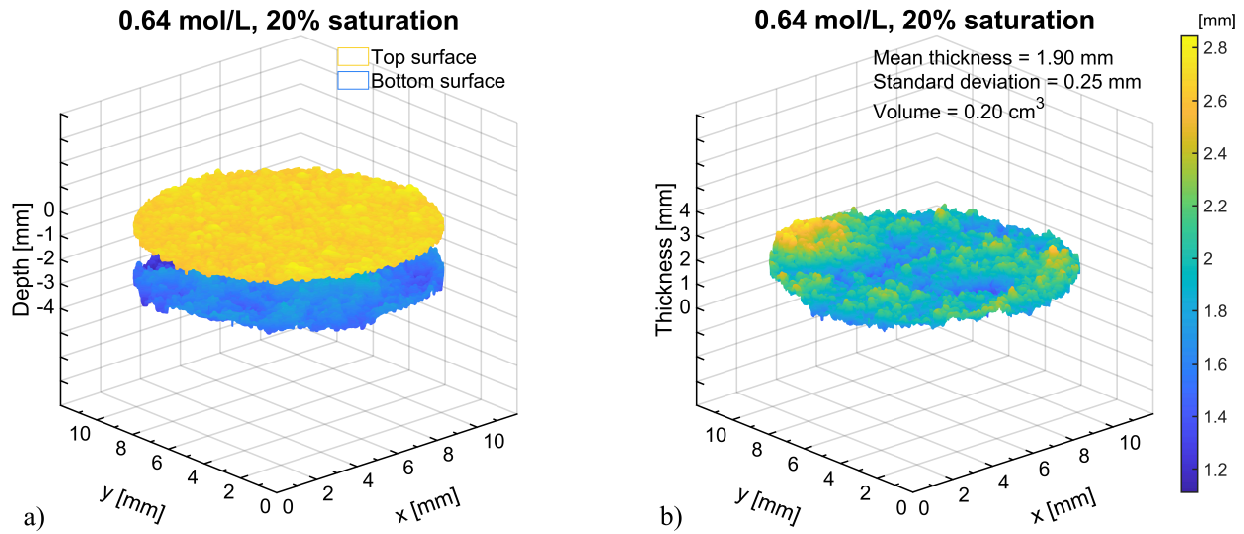


Figure 4.4: (a) Surface data and (b) thickness distribution of the salt crust formed from 0.64 mol/L initial concentration at 20% saturation.

of the top and bottom surface was quantified using the average deviation from the arithmetic mean of each surface (*Butler, 2008*), and was found to be $Ra_{\text{top}} = 65.5 \mu\text{m}$ for the top surface and $Ra_{\text{bottom}} = 185.4 \mu\text{m}$ for the bottom surface. This roughness falls within the range of the average grain size ($240 \mu\text{m}$). The mean crust thickness was 1.9 mm with a standard deviation of 0.25 mm and showed a continuous thickness distribution without macro-pores (see Figure 4.4b). The surface data and the thickness distribution of all crusts is provided in Figures B.1 to B.3 in Appendix B.

Figure 4.5 shows the thickness of all crust segments as a function of final bulk water saturation of the sample. The crust thickness increased with longer evaporation time (i.e., lower degree of saturation) for the crusts formed from low and medium initial concentration. This was attributed to the increasing amount of precipitates with time. The crust thickness of the samples formed from an initial concentration of 0.96 mol/L was similar for all levels of saturation. The thickness of the crust formed from 0.64 mol/L initial concentration at 30% saturation was an outlier. The results suggest that the thickness of the crusts formed from different initial concentrations converged with longer evaporation time. It should be noted that the sample with 0.96 mol/L initial concentration was terminated at 25% instead of 20% saturation after it evaporated for about 120 days at a very low evaporation rate ($< 0.03 \text{ mm/day}$).

Figure 4.6 shows the intrinsic permeability of the dried reference sand samples and the salt crusts formed from varying initial concentrations at different levels of saturation. The mean permeability of the pure sand was $1.97 \times 10^{-11} \text{ m}^2$, which corresponds well to the permeability

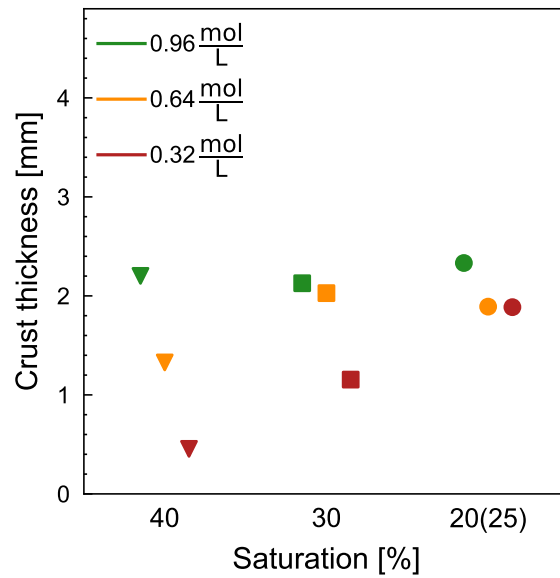


Figure 4.5: Thickness of salt crusts from varying initial MgSO_4 concentration as a function of saturation (lower saturation corresponds with longer time of evaporation). The thickness of the crust formed from 0.96 mol/L initial concentration was determined at 25% saturation.

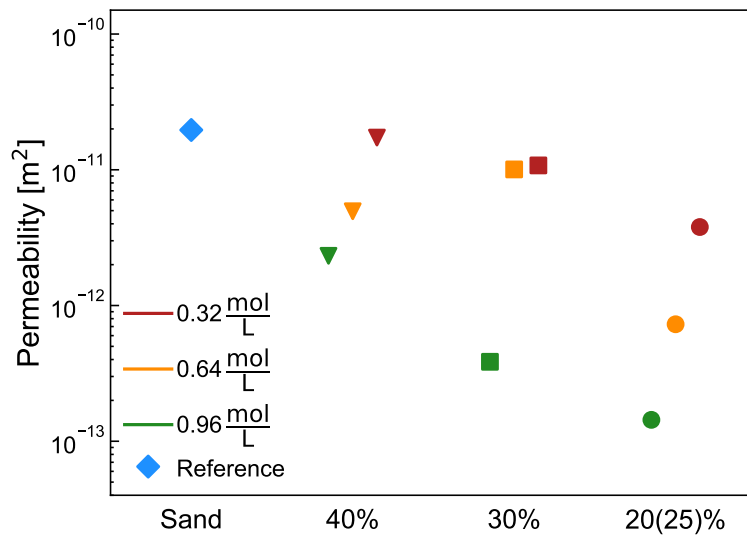


Figure 4.6: Intrinsic permeability of crusts formed from 0.32 mol/L , 0.64 mol/L , and 0.96 mol/L initial MgSO_4 concentration at 40%, 30%, and 20% saturation. The samples with deionized water are indicated with the label "Sand". The intrinsic permeability of the crust from 0.96 mol/L initial concentration was obtained at 25% saturation.

for F32 sand found in Chapter 3 ($2.10 \times 10^{-11} \text{ m}^2$). The mean porosity of these samples was 0.38 ± 0.006 , which is also close to the values presented in Chapter 3 (0.37 ± 0.01). The intrinsic permeability of the salt crusts generally decreased with increasing initial concentration and longer time of evaporation (i.e., decreasing saturation), except for the crust formed from 0.64 mol/L initial concentration at 30% saturation (Figure 4.6). This is not surprising given the increased amount of precipitation, which resulted from both the increased amount of salt ions at higher initial concentration and the reduced amount of liquid at lower saturation.

4.3.3. Segmented image data of separated salt crusts

Figure 4.7 shows a side view of a salt crust segment formed from 0.64 mol/L solution at 20% saturation. Comparing the filtered grey-scale image in Figure 4.7a to the segmented image in Figure 4.7b suggests that most features of the void, salt, and sand were captured by the segmentation procedure. The upper sample surface was slightly inclined from left to right, with a height difference in the range of a single grain size. At the bottom of the crust, the surface was rougher due to the removal of the sand. The separated crust showed a relatively homogeneous distribution of sand and the subflorescent salt precipitation was more dominant in the vertical center region of the crust. In addition, the void space seems to provide a continuous connection between the bottom and the top of the crust.

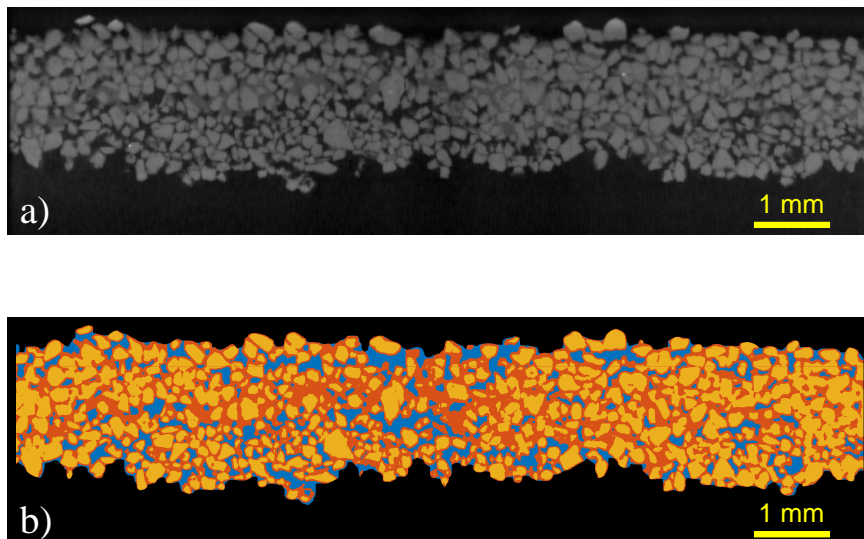


Figure 4.7: Side view of crust formed from 0.64 mol/L initial concentration at 20% saturation. (a) Filtered data. Light grey is the sand, dark grey is the salt, and black is the air phase. (b) Segmented data. Yellow, blue, and red represent the sand, salt, and void phase, respectively. Black is the outside area.

Figure 4.8 shows the depth profiles and segmented axial slices from the segmented μ XRCT imaging data of the crust formed from 0.64 mol/L initial concentration at 20% saturation. The depth profile shows a dense area at -1 mm with a void fraction of 0.05 only (Figure 4.8c), which may have controlled flow through the crust. Except for the regions below -2.5 mm and above -0.4 mm, the sand fraction in Figure 4.8a was consistently smaller than the reference sand fraction (0.62). This is an important finding because it illustrates that the evaporation-induced salt precipitation deformed the unconsolidated sand sample. It is likely that stress was induced on the sand grains by the precipitated salt crystals. Individual grains were displaced and the

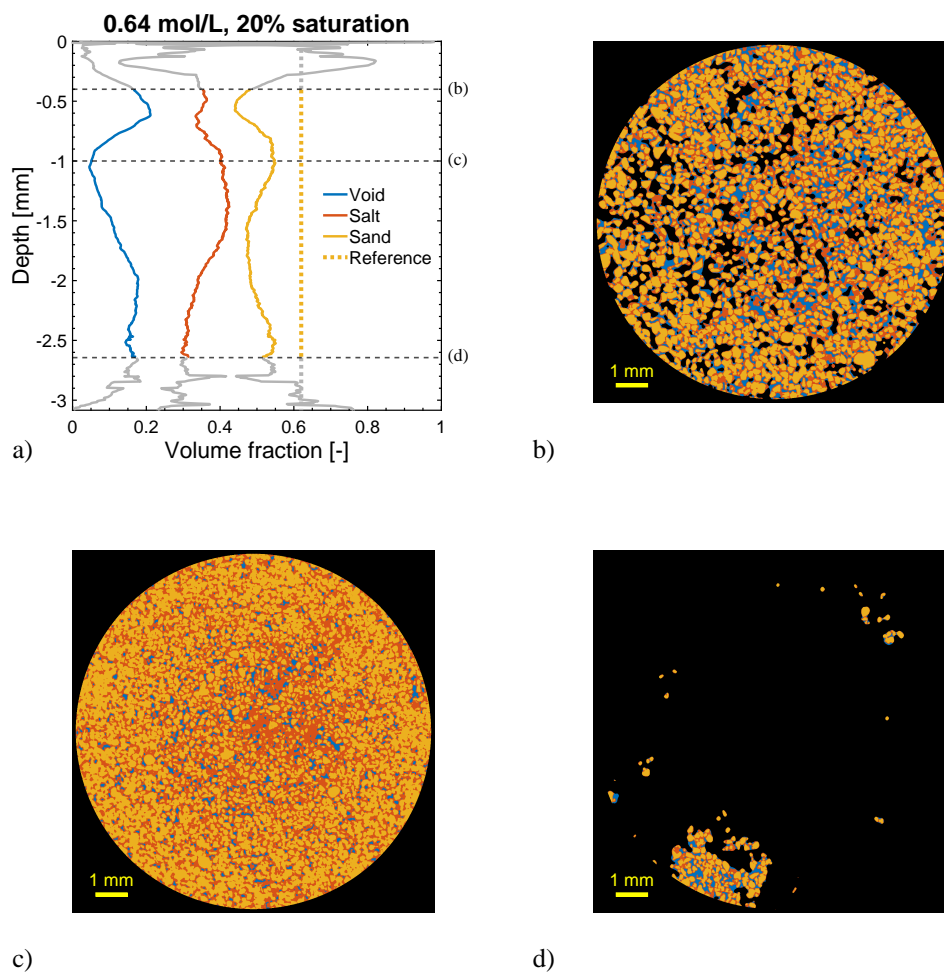


Figure 4.8: Depth profiles and axial slices from segmented μ XRCT data of the crust formed from 0.64 mol/L initial concentration at 20% saturation. (a) Depth profiles of the volume fractions of sand, salt, and void. The gravimetrically determined average reference sand fraction (0.62) is indicated by the vertical yellow dotted line. (b,c,d) Axial slices for the positions indicated in panel (a). The colors of the phases correspond to panel (a). For the determination of the volume fractions, the outside area was not considered.

amount of sand in the observed area was reduced. Above -0.4 mm and below -2.5 mm, the volume fractions were more uncertain because the total amount of voxels of sand, salt, and void in the area of interest decreased (Figure 4.8b,d). Additionally, the surface pores were excluded in the segmentation procedure to determine the top and the bottom of the crust, which may have affected the volume fractions in this regions too. Thus, the depth profiles above -0.4 mm and below -2.5 mm were not further interpreted.

4.3.4. Relating volume fractions and crust permeability

Figure 4.9 shows the mean volume fractions of all crust segments determined from μ XRCT. The mean sand fraction of all crust segments was consistently lower than the reference sand fraction (0.62) for all samples (Figure 4.9a). A one-way analysis of variance (ANOVA) (Davis, 1986) indicated a significant difference (probability = 0.0092) between the mean sand fraction of the crusts from varying initial concentrations and the reference sand fraction. It unambiguously shows the deformation of the parent porous medium (sand) by the subflorescent precipitation of the salt crystals in the original pore space. Figure 4.9b shows the salt fraction of all crusts, which increased with higher initial concentration and lower saturation. This increase in the salt fraction is plausible because more water evaporated at lower saturation, which led to a higher amount of precipitation. Figure 4.9c shows the void fraction of all crusts, which decreased consistently with decreasing saturation. Again, this is attributed to the larger amount of precipitation with increased time of evaporation. Only the crust formed from 0.96 mol/L initial concentration at 40% saturation did not fit into this pattern and showed a lower void fraction than the other crusts formed from 0.96 mol/L initial concentration. It is interesting to note that the void fraction of the crusts formed from high initial concentration generally was higher

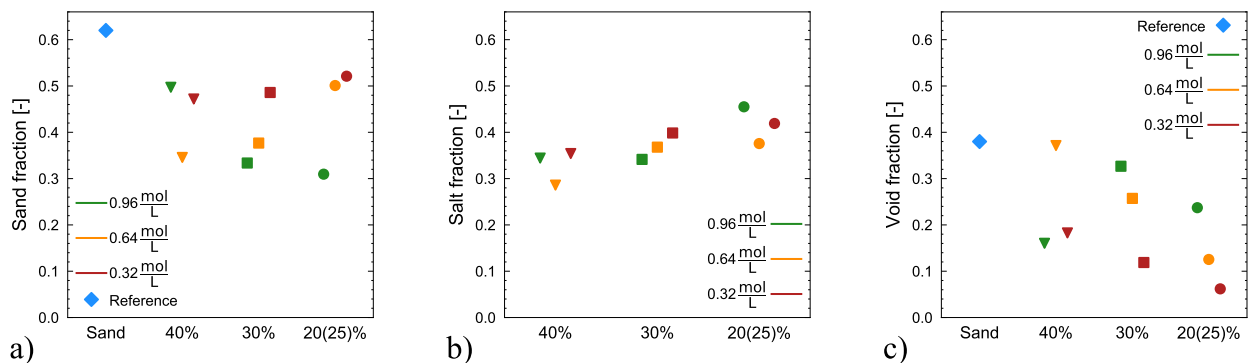


Figure 4.9: Mean volume fractions of all crust obtained from segmented μ XRCT data of (a) sand, (b) salt, and (c) void as a function of saturation. The crust from 0.96 mol/L initial concentration was analysed at 25% saturation. The reference mean sand and void fractions were determined gravimetrically.

than the void fraction of the crusts formed from lower initial concentration. This can partly be related to the formation of a horizontal gap at the top of the crusts from 0.64 mol/L at 40% saturation and at 30% saturation, and the crust from 0.96 mol/L at 30% saturation. During this gap formation, the upper sand grains were lifted up by about 0.25 mm. However, the void fraction of the crusts at 20(25)% saturation also decreased with decreasing initial concentration, although no gap formation was observed.

Figure 4.10a shows the relationship between the intrinsic permeability and the void fraction for all crusts (i.e., the porosity-permeability relationship). For all samples, the permeability and void fraction after salt precipitation were lower than the permeability and void fraction of the reference sand sample. In general, lower initial concentration (red symbols) seemed to be associated with higher permeability and lower void fraction, whereas higher initial concentration (green symbols) resulted in crusts with low permeability and relatively high void fraction. However, no consistent relation between the intrinsic permeability and the void fraction was obtained. This is not unexpected given the observed deformation of the crusts and the porous matrices. It can be argued that the intrinsic permeability of the crust is largely determined by the layer with the lowest void fraction. Therefore, it was also investigated whether a less ambiguous relation is obtained when the minimum void fraction of each crust was considered (Figure 4.10b). The minimum void fraction ranged between 0.05 and 0.2. Again, no clear porosity-permeability relationship was obtained.

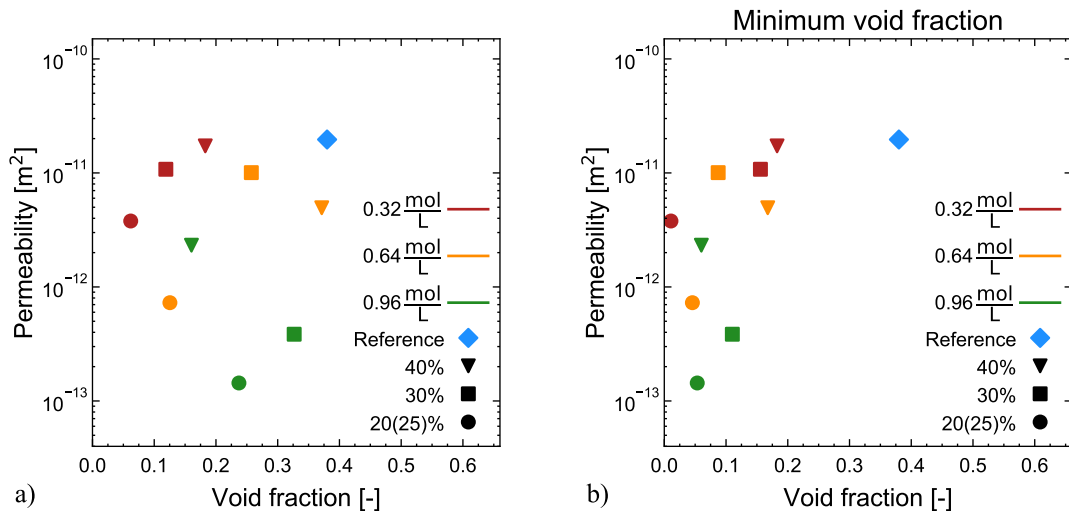


Figure 4.10: (a) Relationship between void fraction and crust permeability (i.e., the porosity-permeability relationship). (b) Relationship between minimum void fraction and crust permeability.

4.4. Discussion

The precipitation of MgSO_4 hydrates is known to generate high crystallization pressures that can destroy consolidated porous media during multiple cycles of wetting and drying (*Scherer, 2004; Espinosa-Marzal and Scherer, 2013; Flatt et al., 2014*). However, the present study is the first to report the deformation of unconsolidated porous media due to subflorescent salt precipitation after only one cycle of drying. This observed deformation sheds considerable doubt on the assumption of a rigid porous medium in modelling subflorescent salt precipitation in unconsolidated sand. In contrast, efflorescent salt precipitation as observed for NaCl showed very little deformation of the porous sand matrix due to the mostly disconnected salt crust that formed above the surface (*Nachshon et al., 2018*), which suggests that the assumption of a rigid porous medium might be valid for efflorescent salt precipitation. However, modelling liquid and/or gas flow in a newly developed porous media (i.e., the efflorescent NaCl crusts) also poses significant challenges to REV-scale modelling (*Shokri-Kuehni et al., 2020*).

The observed deformation resulted in a reduction of the sand fraction by more than 20%, which likely explains why no consistent porosity-permeability relationship was found for MgSO_4 precipitation. The deformation is in conflict with the assumptions of the Kozeny-Carman equation that is widely used to estimate the change in intrinsic permeability due a change in the void space. In the derivation, it is assumed that the porous matrix does not change during salt precipitation. Alternatively, the lack of a consistent relationship can be attributed to experimental limitations that resulted in uncertainty in the porosity and permeability estimates. However, this is considered to be unlikely as discussed in detail in the following.

A first possible source of uncertainty that influences the permeability determination is the potential formation of multiple hydrated forms of $\text{MgSO}_4 \cdot n\text{H}_2\text{O}$ ($n = 1,2,4,5,6,7,10,11,\dots$). According to *Steiger et al. (2011b)*, the dominant form was $\text{MgSO}_4 \cdot 4\text{H}_2\text{O}$ for the ambient conditions of both the evaporation of the samples and the drying of the separated crusts. However, all crusts were not completely dry at the time of crust separation so that other hydrated forms of MgSO_4 could have been present. Therefore, the drying of the separated crusts could have led to additional salt precipitation prior to the intrinsic permeability determination. Since the same drying procedure was applied to all crusts, the additional precipitation most likely affected all crusts in a similar way. Hence, it seems reasonable to assume that the intrinsic permeability of the dry crusts obtained from the gas permeameter is representative for the permeability of the crusts before drying.

A second possible source of uncertainty is related to the different volumes investigated for the permeability determination and the μXRCT measurements, which may have affected the relationship between porosity and permeability. However, the subflorescent crusts appeared uniform in the area investigated with μXRCT , and only showed thicker parts close to the wall

of the sample holder due to edge effects. Therefore, it is assumed that the scanned part of the crust is representative in terms of crust thickness and volume fraction.

A third possible source of uncertainty results from the correct determination of a representative crust thickness to determine the intrinsic crust permeability. It can be debated whether a representative crust thickness should be obtained using the harmonic or the arithmetic mean of the crust thickness distribution. In the case of the crust formed from 0.64 mol/L at 20% saturation, the arithmetic mean was 1.90 mm and the harmonic mean was 1.87 mm. Since the harmonic mean is mostly used to average fluxes and the difference between the harmonic and arithmetic mean of the crust thickness distribution was small (deviation of 1.6%), the arithmetic mean was used to calculate the intrinsic crust permeability. A comparison of the arithmetic and harmonic mean thickness of all crusts is provided in Table B.1 in Appendix B, which shows that the harmonic mean thickness was always smaller or equal to the arithmetic mean thickness. The maximum deviation was 17.8% for the sample with the lowest intrinsic permeability. The general decreasing trend of the intrinsic crust permeability with increasing precipitation was not affected by this uncertainty in the determination of the crust thickness.

A fourth possible source of uncertainty is related to inaccurate estimates of the intrinsic crust permeability that may have occurred for very thin crusts (see Figure 4.5), as discontinuities (e.g. macro-pores) may dominate flow for such crusts. Additionally, some of the measured pressure differences over the crust were small and close to the accuracy of the pressure measurements, which may have affected the determination of the intrinsic crust permeability. The sample with the lowest initial concentration (0.32 mol/L) and the highest saturation (40%) was expected to show the lowest amount of salt precipitation. Nevertheless, the μ XRCT images showed a continuous crust (see Figure B.1 in Appendix B). However, the measured pressure difference was only 3 Pa, which is close to the reported accuracy of the pressure transducer of 1 Pa (*Piotrowski and Huisman, 2021*). The estimated intrinsic permeability ($1.08 \times 10^{-11} \text{ m}^2$, $R^2=0.414$) showed a large uncertainty but was still below the reference permeability of pure sand ($1.97 \times 10^{-11} \text{ m}^2$, $R^2=0.999$). All other crusts were also continuous and the measured pressure differences were higher than 12 Pa for the highest flow rate. Additionally, the uncertainty of the linear regression used to determine the intrinsic permeability was above $R^2 = 0.952$ for all crusts (Figure B.4). This suggests that the intrinsic crust permeability was accurately determined even in the case of thin crusts. In general, the discussed uncertainties in the determination of porosity and intrinsic permeability of the crusts suggest that the inconsistency in the porosity-permeability relationship for the sand–MgSO₄ system cannot be attributed to experimental limitations.

It is interesting to note that the intrinsic permeability of the crust developed from 0.96 mol/L solution at 30% saturation was about one order of magnitude lower than in Chapter 3, although the same sand was used and the temperature and the relative humidity of the experiments were similar ($T = 25 \text{ }^\circ\text{C}$ and $RH = 20 - 40\%$ in Chapter 3 and $T = 26 \text{ }^\circ\text{C}$ and $RH = 24 - 30\%$

here). However, the experiments were performed with different air flow velocity, which resulted in different initial evaporation rates (18.3 mm/day in Chapter 3 and 30.5 mm/day here). This suggests that the evaporation rate has a significant impact on the formation of subflorescent salt crusts, which was already reported in previous studies (*Espinosa-Marzal and Scherer, 2010*) and needs to be systematically investigated in future studies.

As it is not known to which extent precipitated salt was removed during crust separation, future studies should also consider in situ investigation of salt precipitation below the consolidated crust. This was not possible here due to the selected procedure for crust permeability determination. In Chapter 5, time-lapse imaging and water content monitoring during salt crust formation will be used to investigate the liquid distribution and the precipitation below the consolidated salt crust.

The complex relation between precipitation, deformation and crust permeability is further illustrated by the observation that some crusts showed a different intrinsic permeability despite a similar crust thickness (see Figure 4.5 and Figure 4.6). This is most likely related to differences in the network of voids that formed during salt precipitation from varying initial concentrations (see Figure 4.7). In this context, it is interesting to note that the void fraction of the crust formed from 0.96 mol/L initial concentration at 20(25)% saturation was higher than the void fraction of samples with lower initial concentration, although no horizontal gap formation was observed (see Figure 4.9c). This may be related to the higher amount of deformation for the sample with 0.96 mol/L initial concentration, which is indicated by a smaller sand fraction in the crust (see Figure 4.9a). In future studies, Stokes-flow simulations on the pore structure of the crusts could help to provide a better understanding of the impact of the crusts on the flow and transport of liquid and vapor and of the role of the pore connectivity. Knowledge of time-lapse salt crust formation and the related pore space evolution may also help to better understand the impact of salt precipitation process on evaporation, which will be addressed in Chapter 5.

4.5. Conclusions

The intrinsic permeability of subflorescent MgSO_4 crusts from evaporation of solution with varying initial concentration was linked to pore space properties from μXRCT imaging data. The permeability was found to be one order of magnitude below previously reported values for similar conditions, which was attributed to the speed of the air flow above the sample surface. This suggests that the evaporation rate plays a major role in the formation of subflorescent salt crusts, which should be investigated in more detail. Furthermore, it was observed that salt precipitation deformed the unconsolidated sand samples. The deformation occurred for all

crusts, independent of initial concentration and saturation. It is obvious that the deformation of the porous matrix challenges the assumption of a rigid porous matrix, which provides the basis for porosity-permeability relationships such as the Kozeny-Carman relationship that is used for modelling evaporation and precipitation on the REV-scale. It is concluded that a porosity-permeability relationship for the investigated sand–MgSO₄ system will be hard to find, particularly by taking into account the deformation of the subflorescent salt crust.

Future work should focus on the time-dependent formation of the crust using non-invasive time-lapse imaging, which can provide insights into both the formation process of the solid crust and the liquid distribution within the pore space. The wet crusts observed in this and previous studies suggests that the water content of (subflorescent) crusts plays a significant role for salt precipitation and thus affects evaporation. Assessing the location of the evaporation front could shed light on how fluid and solutes are transported in the pore space during evaporation. Analyzing the movement of single particles in unconsolidated porous materials in response to salt precipitation will provide information on the deformation process and the resulting effects on flow and transport through subflorescent crusts. Finally, to make progress with the validation of numerical simulation models describing evaporation using experimental data, deformation due to salt precipitation needs to be avoided. Chapter 5 will address the non-invasive time-lapse imaging of salt crust formation on the pore-scale and the monitoring of the water content of the crusts during evaporation to improve the understanding of the subflorescent crust formation process in unconsolidated and rigid porous media. The analysis of particle displacements due to salt precipitation and validation of numerical evaporation models is beyond the scope of this thesis.

Chapter 5

Non-invasive monitoring of subflorescent magnesium sulfate crust formation

5.1. Introduction

In this chapter, the temporal development of the formation of subflorescent MgSO_4 crusts will be studied to shed light on how salt precipitation affects evaporation during the formation process. For this, it is important to monitor changes in the void, liquid, and solid phase in the sample during salt crust formation. Additionally, since it was shown in Chapter 4 that subflorescent MgSO_4 salt precipitation deformed the unconsolidated sand sample, rigid porous media will be used to investigate the impact of salt precipitation on evaporation in the absence of this confounding factor. Non-invasive imaging methods will be used to provide the distribution of the phases mentioned above. In particular, μXRCT will be used to obtain pore-scale information with a resolution of micrometers. In addition, unilateral single-sided NMR will be used to obtain measurements of the liquid volume fraction over the entire cross section of the sample independent from μXRCT . The evaporation rate of each sample will be determined from mass loss measurements again.

Two types of porous media will be investigated, one is the unconsolidated F32 sand already used in Chapter 3 and Chapter 4 and the other is a sintered porous borosilicate glass. It will be shown that the segmentation of the solid sand phase obtained from μXRCT does not agree with gravimetric measurements in case of sand. Image processing using masks could not be used to resolve this, since salt precipitation deformed the porous matrix during evaporation (see Chapter 4). Therefore, rigid sintered glass samples will additionally be investigated. In particular, the initial μXRCT data of the dry sintered glass samples will be used as a mask for the μXRCT data at later stages of evaporation to provide an improved distinction between solid glass phase and the remaining phases.

The remainder of this chapter is organized as follows. First, the methods used to prepare the

sand and the sintered glass samples will be presented and in situ measurement procedures using non-invasive unilateral single-sided NMR and μ XRCT will be described in detail. Then, the results obtained from evaporation, NMR, and μ XRCT measurements will be presented and discussed.

5.2. Materials and methods

5.2.1. Evaporation from sand and from sintered glass samples

In a first step, one sample was prepared with F32 sand and 0.96 mol/L MgSO_4 solution and one sample was prepared with F32 sand and deionized water using the PMMA sample holders, materials, and preparation procedure described in Chapter 3. The maximum filling height of the sample holder h_{max} was 83 mm and the sample height h was 80 mm (Figure 3.2). Both samples had a porosity of 0.37. After preparation, the samples evaporated below a fan (WFB1212H-F00, Delta Electronics Inc., Bangwua, Thailand) and the temperature ($24^\circ\text{C}\pm 2^\circ\text{C}$) and relative humidity (27%-40%) were recorded with a data logger (FHAD 46-C2, ALMEMO[®] D06, Ahlborn, Holzkirchen, Germany). The mass loss was determined every twelve hours using a balance (accuracy ± 0.02 g, EX2202, Ohaus Cooperation, Parsippany, USA) to ensure a reliable determination of the evaporation rate. The saturation of each sample was obtained from the initial water content, the mass loss, and the dimensions of the sample.

In a second step, two custom-made samples of sintered porous borosilicate glass (VitraPOR P2, Robu, Hattert, Germany, density 2.23 g/cm^3) with a height of 80 mm and a diameter of 30 mm were coated with a shrinking tube and the mass of the dry samples was determined using a balance (accuracy ± 0.02 g, EX2202, Ohaus Cooperation, Parsippany, USA) (see Figure 5.1). As for the sand samples, one sample was saturated with a solution of 0.96 mol/L MgSO_4 and the other sample was saturated with deionized water. To saturate the sintered glass samples, they were placed vertically in a beaker filled with the respective liquid so that the water table was 5 cm below the surface of the sample. Then, the beaker with sample was put in a desiccator and a vacuum pump (TRIVAC D2.5E, Leybold GmbH, Köln, Germany) was used to generate a negative pressure of 32 mbar for at least 30 min to evacuate the air and to saturate the sample with liquid. After this, the mass of the saturated sample was determined and the top and bottom of the sample were covered with a flexible wax film cover (parafilm) to prevent evaporation. The porosity of both samples was determined from the difference in mass before and after saturation using the density of the liquid (Table 3.3) and the sample dimensions. It was found that the porosity of the sample saturated with deionized water was $\phi = 0.36 \pm 0.005$, whereas the porosity of the sample saturated with MgSO_4 solution was $\phi = 0.37 \pm 0.005$. There is some uncertainty in these porosity estimates, because it is possible that a gap between the

shrinking tube and the sintered glass may have been present. If a ring-shaped volume of liquid with a thickness of 0.1 mm was assumed to be present between the sintered glass and the shrinking tube, the porosity of the sample with deionized water would be $\phi = 0.35 \pm 0.005$ and the porosity of the sample saturated with MgSO_4 solution would be $\phi = 0.36 \pm 0.005$. All estimates are close to the void fraction provided by the manufacturer ($\phi \approx 0.36$, VitraPOR P2, Robu, Hattert, Germany).

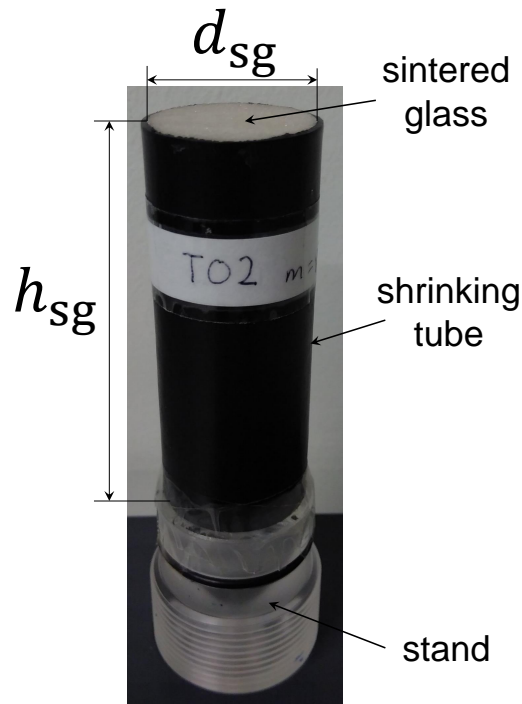


Figure 5.1: Photo of sintered glass sample (VitraPOR P2, Robu, Hattert, Germany) covered at the lateral surface with a shrinking tube. The height of the sintered glass sample h_{sg} was $80 \text{ mm} \pm 0.5 \text{ mm}$ and the diameter d_{sg} $30 \text{ mm} \pm 0.1 \text{ mm}$. The bottom of the sample was covered to prevent evaporation.

To initiate evaporation, the top cover was removed and the sintered glass samples were placed below a fan (WFB1212H-F00, Delta Electronics Inc., Bangwua, Thailand). The mass loss of both samples was determined every 12 h for the first two days, and then every 24 h until day 7. After day 7, the mass loss was measured every 72 h. These time intervals ensured a reliable determination of the evaporation rate. The saturation at each measurement time was obtained from the mass loss and the initial water content of the respective sample. Temperature (21°C - 27°C) and relative humidity (40% - 54%) were recorded with a data logger (FHAD 46-C2, ALMEMO[®] D06, Ahlborn, Holzkirchen, Germany). During evaporation of both the sand and the sintered glass sample, μXRCT and NMR measurements were performed. This is described in detail below.

5.2.2. Micro-X-ray computed tomography during evaporation

In the case of the sand sample with MgSO_4 solution, μXRCT measurements were made with a FOV in the center of the top 6 mm of the sample using the same settings and procedures described in Chapter 4. Only the number of clusters during segmentation (i.e., the number of phases assumed to be present in the FOV) was changed to four (i.e., void, liquid, salt, and sand) whenever necessary (see Table 4.5). The μXRCT measurements were made at a sample saturation of 90%, 81%, 72%, and 61%. During these measurements, the sample was covered with a flexible wax film cover (parafilm) to prevent further evaporation. The reference sample with deionized water was also covered for comparability, although no μXRCT measurements were made. The evaporation of the sample with MgSO_4 solution was stopped when 61% saturation was reached (i.e., after 15.3 days).

In the case of the sintered glass sample with MgSO_4 solution, the same procedures for acquiring 3D μXRCT data and basic post-processing described in detail in Chapter 4 were used, except for a few changes of the parameters. The exposure time for all scans of the sintered glass sample was increased to 3000 ms, which resulted in a total scan time of 15 h. Additionally, the tilt of the vertical rotation axis of the scan (center of rotation) was corrected during reconstruction by determining the center of rotation of three axial slices at the top, center, and bottom of the 3D image stack with the help of Octopus Reconstruction software (Table 4.2). The tilt angle was determined using simple linear regression and trigonometry of the deviations with respect to the center of rotation of the center slice.

In a first step, μXRCT measurements of the dry sintered glass sample without liquid were made. Then, the sample was saturated with MgSO_4 solution as described above. After this, the saturated sample was covered with a flexible wax film cover (parafilm) to prevent evaporation and μXRCT measurements were made again (i.e., at 100% saturation). Then, evaporation was initiated by removing the wax film cover and placing the sample below the fan. μXRCT measurements were obtained again at 90%, 80%, 70%, 60%, and 21% saturation. The sample with MgSO_4 solution as well as the reference sample with deionized water were covered with a flexible wax film cover (parafilm) to prevent further evaporation during the μXRCT measurements. It was only possible to reinstall the sample with an estimated positional accuracy between 50 μm to 100 μm in both vertical direction and axial rotation. Thus, in order to compare time-lapse μXRCT data, the measurements at different times needed to be registered. Registration of a 3D image is computationally expensive and not easy to achieve, as multiple parameters have to be adjusted on a subvolume of the data set. Therefore, a simplified and less computationally intensive registration was performed in three steps for the entire data set. In the first step, the intensity of all axial slices in the 3D image stack was adjusted to grey values between 0 and 65 536 by saturating the top 1% and the bottom 1% of the voxels of each axial (2D) slice using the

Table 5.1: Registration steps for vertical and horizontal correction during the simplified 2D registration, including methods and settings used for filtered μ XRCT data of the sintered glass sample using MATLAB[®] (Image processing toolbox, Version 2019b, The Mathworks Inc., Natick, MA, USA).

Step	Method	Parameter	Setting	Value	Details
1.	Imadjust	Image intensity	Contrast limits	1%	Both top and bottom
2.	Vertical correction	Vertical offset	Slices	-5 – 14	Visually obtained
	Imregconfig	Modality	Multimodal	-	Output: Optimizer, metric
3.	Imregtform	Optimizer	InitialRadius	0.0001 – 0.02	0.005 ^a
			Epsilon	$1e^{-6}$ – $1e^{-4}$	$1.5e^{-5}$, ^a
			GrowthFactor	1.01 – 1.2	1.05 ^a
			MaximumIterations	100 – 400	200 ^a
	Metric	UseAllPixels		1	All pixels used
	TransformType		Rigid	-	Translation, Rotation
	InitialTransformation		Matrix	-	Estimated translation

^a Starting value

MATLAB[®]-function "imadjust" (Table 5.1). This reduced the intensity of outlier voxels associated with dense impurities in the sintered glass and allowed the comparison of the intensity values of different images. In the second step, a correction in vertical direction of the 3D image stack was obtained by visually comparing one filtered axial slice of each (moving) data set after different times of evaporation with a filtered axial slice of the initially dry reference data set. This resulted in an offset in vertical direction between -5 and 14 slices (i.e., slice thickness of 1 voxel $\hat{=}$ 4 μ m), which was used to move the entire 3D image stack (Table 5.1). In the third step, a selected horizontal slice in the vertical center of the moving 3D image stack was registered to the corresponding slice of the reference (dry) 3D image stack. The initial settings for the registration were obtained from the MATLAB[®]-function "imregconfig" (Table 5.1). Then, the registration was performed using the two-dimensional MATLAB[®]-function "imregtform" (Mattes *et al.*, 2001, 2003; Thevenaz and Unser, 2000; Styner *et al.*, 2000) (Table 5.1). This intensity-based registration algorithm maximizes the mutual information of the difference in the intensity of all voxels between the moving and the reference image. Only translation and rotation of the moving image was considered with the settings shown in Table 5.1. First, the

algorithm was applied to a subarea with a size of 1000×1000 voxels (computational time: 1 min – 2 min), which provided an initial geometric transformation matrix. This transformation matrix was used to obtain a transformed 2D image, which was visually compared with the reference image. If the transformation matrix did not provide accurate results, the registration was repeated using adjusted settings (see Table 5.1). When the registration was sufficiently accurate for the subarea, the obtained transformation matrix served as a starting point for the registration of the entire slice (computational time: 2 min – 3 min). If necessary, the registration of the entire slice was also repeated using adjusted settings (see Table 5.1). Finally, the obtained 2D geometric transformation matrix was applied to all axial (horizontal) slices in the moving 3D image stack. The registration procedure was performed for each 3D image stack individually. Table 5.1 summarizes the used methods and parameters for the registration.

The μ XRCT data obtained for the dry reference sample was segmented slice-by-slice into void and glass phase using the MATLAB[®]-function "imquantize" (see Table 4.5). The required threshold for segmentation was obtained using Otsu's method (*Otsu, 1979*). The segmented data of the glass phase from the reference measurements were then used as a mask for all registered image data obtained at different times of evaporation. After the use of the mask, the remaining area of each registered horizontal slice was again segmented into void and non-void phase using the MATLAB[®]-function "imquantize" with an appropriate threshold (Table 4.5).

5.2.3. Water content profiles from unilateral nuclear magnetic resonance

The near-surface water content profile was measured using unilateral NMR after each μ XRCT measurement for both the sand and the sintered glass sample. To increase the temporal resolution, additional water content profiles were determined with NMR measurements in between the μ XRCT measurements. The unilateral single-sided NMR system used in this study is the MOBILE Universal Surface Explorer (NMR-MOUSE, Magritek, Aachen, Germany). The set-up of this system is shown in Figure 5.2a. The U-shaped permanent magnet has a field strength of 0.31 T, which gradually reduces with increasing distance. The sensitive region of the magnet lies at about 25 mm distance from the surface of the magnet. The use of a spacer allows the vertical adjustment of the rf-coil, which changes the length h_{sens} and thus the distance of the plane that is excited by pulses relative to the fixed magnetic field. A thicker spacer brings the rf-coil closer to the sample surface, which results in a higher signal intensity. At the same time, the thicker spacer leads to a smaller h_{sens} , which results in reduced measurement depths. Therefore, there is a trade-off between measurement depth and signal intensity, which should be considered for each specific application (*Blumich et al., 2014*). By moving the entire NMR-MOUSE with a lift, the position of the sensitive volume relative to the sample can be changed (i.e., lift position h_{lift}). It should be noted that the position of the sample was fixed for all

measurements and only the NMR-MOUSE was moved.

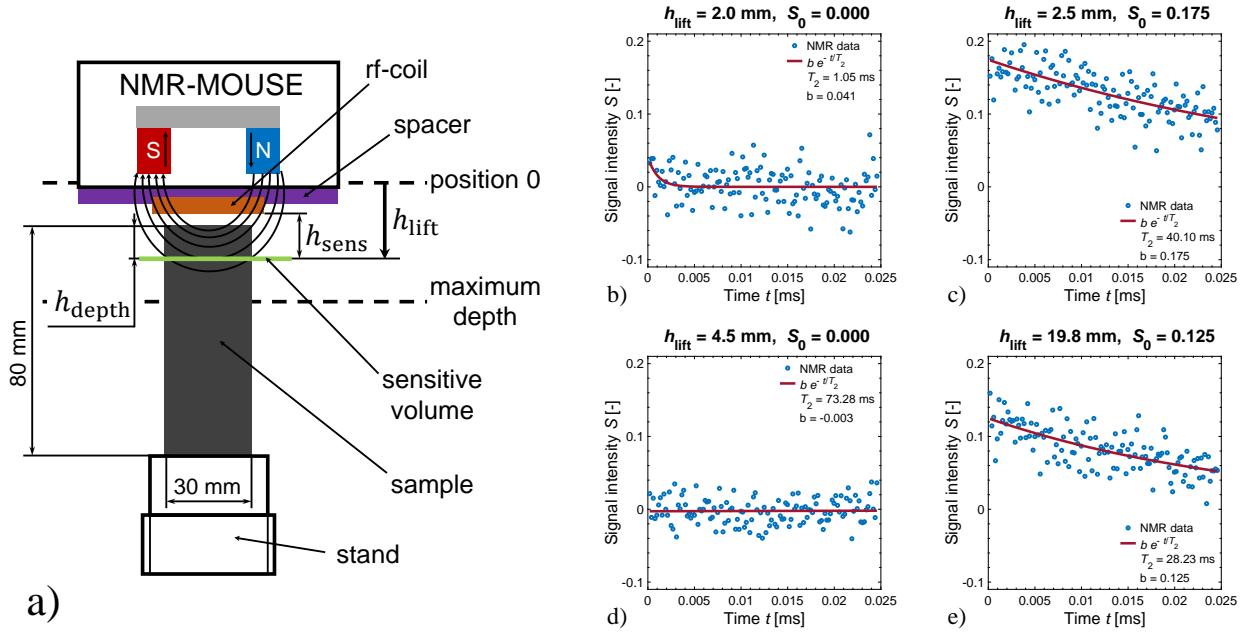


Figure 5.2: (a) Schematic set-up of the unilateral single-sided NMR-MOUSE. The measurement depth h_{depth} was adjusted by moving the entire NMR-MOUSE within the range of $h_{\text{lift}} = [0 \text{ mm}, 19.8 \text{ mm}]$ for the sintered glass sample. "position 0" indicates the highest possible position of the sensitive volume. (b) Measurement and exponential fit of data in the air above the sample, $h_{\text{lift}} = 2.0 \text{ mm}$, day 0. (c) Measurement and exponential fit of data inside the sample at 100% saturation, $h_{\text{lift}} = 2.5 \text{ mm}$, day 0. (d) Measurement and exponential fit of data inside the sample at 39% saturation, $h_{\text{lift}} = 4.5 \text{ mm}$, day 21. There was no detectable water (i.e., the sample was dry at $h_{\text{depth}} = 2 \text{ mm}$). (e) Calibration measurement and exponential fit on sample holder with marker solution, $h_{\text{lift}} = 19.8 \text{ mm}$, day 0. The parameter b indicates the fitted value of the signal intensity S_0 using Equation (2.34) (see text for details).

In the case of the sintered glass sample, the spacer with 5 mm thickness was used, which resulted in a maximum measurement depth of $h_{\text{depth}} = 17.3 \text{ mm}$. The thickness of the sensitive volume s_{sens} (i.e., the resolution) was 0.2 mm. All settings that were used to obtain the NMR data are provided in Table 5.2. A CPMG pulse sequence with 128 echos and an echo time of $192 \mu\text{s}$ was used (see Table 5.2 and Chapter 2 for a detailed description). The obtained signal intensity data were fitted using Equation (2.34) and the Trust-Region-Reflective Least Squares Algorithm (*More and Sorensen, 1983*) implemented in the MATLAB[®]-function "fit". This provided the fitted parameters b and T_2 (Figure 5.2b-e). The signal intensity at time 0 (S_0) was determined from this fit and is equal to b . For some measurements, the fitted T_2 was smaller than 5 ms or the fitted b was negative (Figure 5.2b,d). This is physically implausible and can be attributed to the scattering of the data. For these measurements, S_0 was set to 0.

Since the distance of the sensitive volume relative to the surface of the sample was unknown,

Table 5.2: Settings for NMR measurements on sintered glass and sand samples using the NMR-MOUSE. The settings for the calibration measurements were identical to the settings for the respective sample.

Parameter	Symbol	Value		Unit
		Sintered glass	Sand	
transmitter frequency	ν_{rf}	13.39	13.39	MHz
repetition time	t_R	4000	4000	ms
number of scans	n_S	64	64	-
echo time 0	t_E	200	200	μs
echo time	t_E	192	206	μs
number of echos	n_E	128	512	-
probe head/spacer	PM25-x mm	5	15	mm
resolution/slice thickness	s_{sens}	200	200	μm
transmitter attenuation for 90° pulse amplitude	-	-6	-9	dB
180° amplitude	-	0	-3	dB
acquisition time	t_{acq}	0.018	0.018	s
number of complex points	n_{acq}	36	36	-
receiver gain	-	31	31	dB
pulse length	t_P	12	12	ms
gradient	-	7	7	T/m
echo shift	-	0.5	0.5	μs
rxPhase	-	60	61	°
bandwidth	-	2000	2000	kHz

the NMR measurements at day 0 (100% saturation) made with different lift positions were used to determine the position of the sample surface. The measurements in Figure 5.2b and 5.2c were performed at the same time (day 0) at $h_{\text{lift}} = 2\text{ mm}$ and 2.5 mm , respectively, on the sintered glass sample containing MgSO_4 solution. At 2 mm , the sensitive volume was in the air above the sample and the detected signal was low and scattered around 0 (Figure 5.2b). The fitted T_2 was smaller than 5 ms and thus S_0 was defined to be 0. The measurement at 2.5 mm showed a higher signal intensity that decreased with time, which indicates that this is a measurement within the porous media (Figure 5.2c). Therefore, it is assumed that the NMR position of 2.5 mm indicated the surface of the sample ($h_{\text{depth}} = 0$). A list of all measurement depths can be found in Table C.1 in Appendix C.

The repetition time $t_R = 4000\text{ ms}$ was chosen to reduce the measurement time at one depth to 4.5 min (i.e., measurement time of $\approx 1\text{ h}$ for one water content profile). As described in Chapter 2, the longitudinal relaxation time constant T_1 should be three to five times lower than the repetition time t_R . T_1 of the porous medium filled with MgSO_4 solution was determined by fitting Equation (2.33) to multiple signal intensities obtained from measurements with different

repetition times (i.e., $t = t_R$). It was found that T_1 was 1400 ms for the porous medium filled with MgSO_4 solution, which was only 2.86 times lower than t_R . This resulted in a small but systematic underestimation of the signal intensity determined from the CPMG-echo sequence (see Chapter 2). Therefore, the signal intensity of each measurement with $t_R = 4000$ ms was corrected using Equation (2.33), which resulted in a correction by 6% towards higher signal intensity for each measurement.

To determine the water content at each measurement depth of the sintered glass sample, a calibration of the obtained signal intensity S_0 was necessary. For this, the PMMA sample holder described in Chapter 3 was filled with a marker solution, which consisted of 25 vol% deionized water ($^1\text{H}_2\text{O}$), 75 vol% deuterium ($^2\text{H}_2\text{O} = \text{D}_2\text{O}$), and 0.1 weight% copper sulfate (CuSO_4). The copper sulfate reduced the T_1 relaxation of the marker solution to about 1500 ms to match the T_1 of the sintered glass sample. The signal intensity S_{ref} of the marker solution was determined using the same settings listed in Table 5.2 (i.e., S_0 in Figure 5.2e). This calibration measurement was performed daily until day 18 after the NMR measurements on the sintered glass sample. The average signal intensity S_{ref} of all calibration measurements was 0.128. This value was corrected for the difference in the cross-sectional area of the sintered glass sample and the PMMA sample holder using Equation (2.36). The resulting corrected signal intensity $S_{\text{ref,corr}}$ was 0.120, which was then used in Equation (2.35) to determine the water content at each depth of all measurements in the sintered glass sample.

In the case of the sand sample with MgSO_4 solution, slightly different settings were used for the NMR measurements (Table 5.2). The use of the 15 mm spacer allowed a maximum measurement depth inside of the sample of 5.5 mm and a maximum range h_{lift} of 9.8 mm. Measurements were conducted at eleven positions with a separation of 0.5 mm. The surface of the sample was determined at $h_{\text{depth}} = 3.5$ mm as described above. The same reference marker solution as above was used to obtain the S_{ref} of 0.547 using the NMR settings listed in Table 5.2. This reference value was higher than the calibration value of the sintered glass sample because of the thicker spacer and the associated higher signal intensity.

5.3. Results and discussion

5.3.1. Evaporation from sand and from sintered glass

Figure 5.3a shows the cumulative mass loss of sand and sintered glass samples with deionized water and MgSO_4 solution with 0.96 mol/L initial concentration. It can be seen that evaporation of deionized water from both porous media proceeded in a similar way (Figure 5.3a,b). The slightly higher cumulative mass loss for sand is due to the higher porosity. The evaporation rate of deionized water from sand seems to decrease slightly faster than the evaporation rate

of deionized water from sintered glass, but this is likely related to the different measurement intervals for the two samples. The similar evaporation rate can at least partly be attributed to the similar intrinsic permeability of the sintered glass samples ($2.90 \cdot 10^{-11} \text{ m}^2$) and sand samples ($2.10 \cdot 10^{-11} \text{ m}^2$, Chapter 4). Additionally, the porosity (0.36) and the internal surface area ($0.13 \text{ m}^2/\text{g}$) of the sintered glass sample were similar to the porosity (0.37) and the internal surface area ($0.11 \text{ m}^2/\text{g}$ (Duschl *et al.*, 2016)) of the sand. Although the mean grain size differed for both porous media ($145 \mu\text{m}$ for the sintered glass samples and $240 \mu\text{m}$ for the sand samples), this seemed to have a minor impact on evaporation. This suggests that the amount and connectivity of active pores was similar for both porous media.

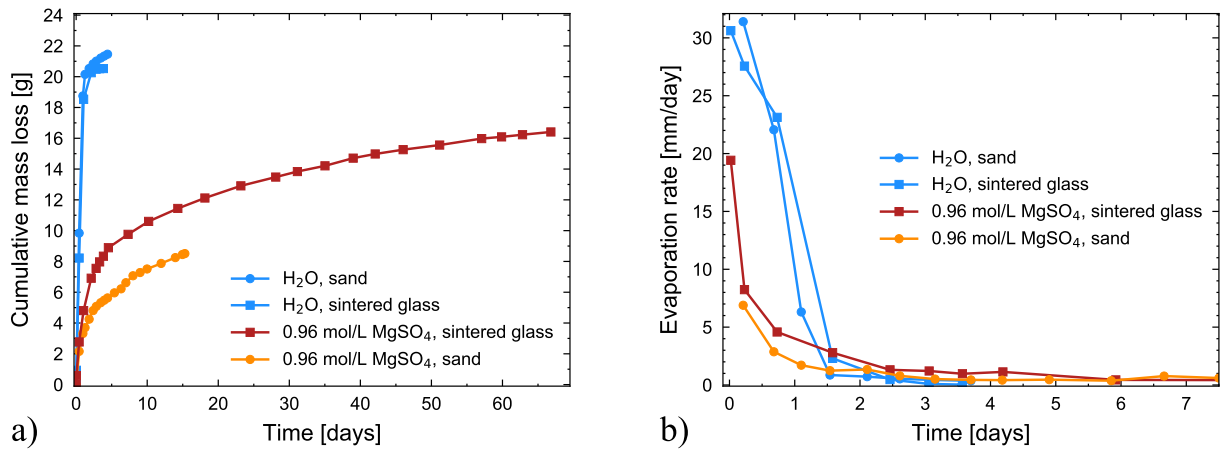


Figure 5.3: (a) Cumulative mass loss as a function of time for sintered glass and sand samples saturated with deionized water and 0.96 mol/L MgSO₄ solution. The evaporation of the sand sample with MgSO₄ solution was stopped after 15.3 days at 61% saturation and the sintered glass sample with MgSO₄ solution evaporated until 21% saturation (67 days). (b) Evaporation rate as a function of time for sintered glass and sand samples saturated with deionized water and 0.96 mol/L MgSO₄ solution. The evaporation rate of both samples with MgSO₄ solution stayed below 0.05 mm/day after day 7.

In the case of the samples with MgSO₄ solution, the cumulative mass loss also showed a similar shape for both porous media (Figure 5.3a). The initial evaporation rate from sintered glass was higher than the initial evaporation rate from sand and remained at a higher level until day 5 (see Figure 5.3b), which resulted in a higher cumulative loss. This may be related to the earlier crust development on the sand sample, which was already observed visually after the first day of evaporation (Figure 5.4a,b). In contrast, the sintered glass sample showed no visual signs of salt precipitation in the first day (Figure 5.4,c,d). The observed brown discoloration of the sintered glass sample (Figure 5.4,c,d) is attributed to the X-ray exposure of the borosilicate glass, which needs to be investigated in future studies. The results suggest that the formation of MgSO₄ crusts depends on the surface properties of the porous medium, which was also reported

in previous studies (*Espinosa-Marzal and Scherer, 2010, 2013*).

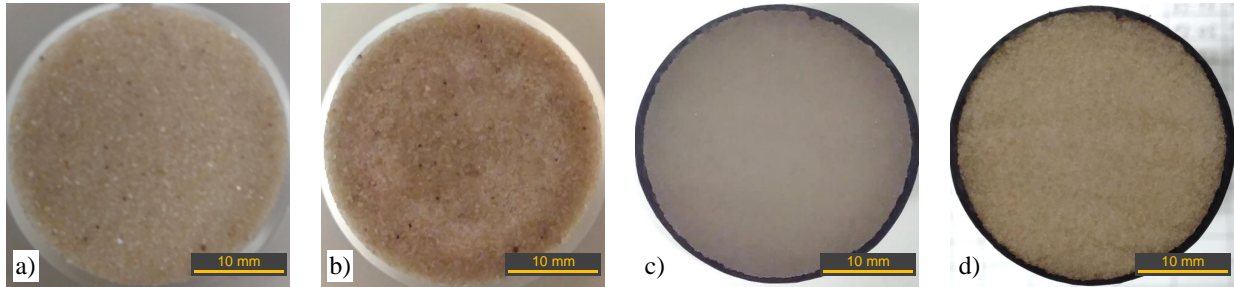


Figure 5.4: Surface pictures of sand and sintered glass sample with 0.96 mol/L MgSO_4 solution. (a) Sand at 100% saturation at day 0. (b) Sand at 85% saturation at day 1. (c) Sintered glass at 100% saturation at day 0. (d) Sintered glass at 85% saturation at day 0.5. The brown discoloration results from X-ray exposure of borosilicate glass, which needs to be investigated in future studies.

In the case of the sintered glass sample, it is important to note that the evaporation rate of the sample with MgSO_4 solution was substantially higher than the evaporation rate of the sample with deionized water between day 2 and 4. This suggests that a capillary connection still provided liquid to the surface and allowed the higher evaporation rate for the sample with MgSO_4 solution. The low evaporation rate of the sintered glass sample with deionized water after day 2 is characteristic of stage II of evaporation. A detailed discussion of the differences in evaporation between sand and sintered glass samples is provided after all results have been presented.

5.3.2. Water content profiles in sand and sintered glass samples

Water content profiles during evaporation were obtained using NMR measurements to investigate the water distribution in the porous medium during salt precipitation. In Figure 5.5a, water content profiles for the top 4 mm are shown for the sand sample prepared with 0.96 mol/L MgSO_4 solution during evaporation. The initial water content profile at day 0 was $0.40 \text{ cm}^3/\text{cm}^3$ and increased at the top. A thin layer of liquid was observed at the top of the sample during the initial measurements, and it seems likely that this liquid film affected the water content determination. The water content that was determined gravimetrically ($0.37 \text{ cm}^3/\text{cm}^3$) was smaller than the initial water content obtained from NMR ($0.40 \text{ cm}^3/\text{cm}^3$). This can be attributed to the heterogeneity of the sample and to the gravimetric water content determination, which is valid for the entire sample and not limited to the surface only. After 1.8 days of evaporation, the water content was $0.04 \text{ cm}^3/\text{cm}^3$ near the surface and $0.1 \text{ cm}^3/\text{cm}^3$ below a depth of -1.5 mm. This shows the formation of an evaporation front. At day 15.3, the evaporation front moved down to -2 mm and the water content above -1 mm was $0 \text{ cm}^3/\text{cm}^3$. Below -2 mm, the water content was still close to $0.1 \text{ cm}^3/\text{cm}^3$. Since evaporation was stopped after 15.3 days, there is

no information on the further development of the evaporation front after this time. It seems plausible that the crust dried out and built a barrier for vapor flow, which is also reflected in the low evaporation rate after day 2 (Figure 5.3b). The reduction of the water content near the surface was also observed during the evaporation of sand samples with deionized water (*Merz et al.*, 2014). However, the disconnection of the liquid in the capillaries at the surface (i.e., water content close to $0 \text{ cm}^3/\text{cm}^3$) reached deeper into the sand in *Merz et al.* (2014) than in this study. This illustrates the different evaporation of deionized water and of saline water from sand in the presence of a salt crust.

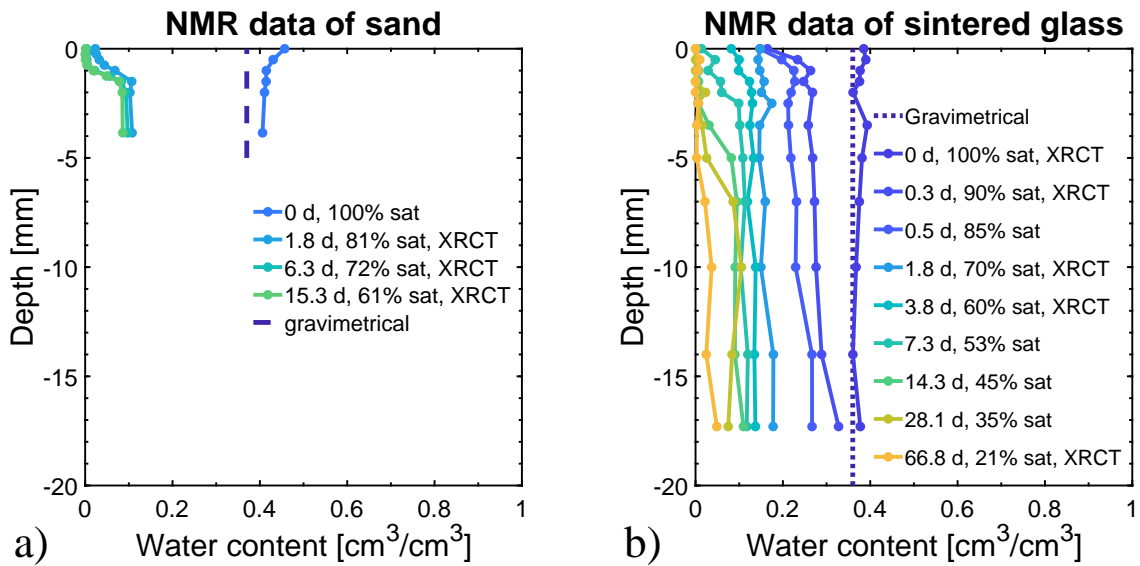


Figure 5.5: Water content profiles from NMR for (a) the sand and (b) the sintered glass sample with MgSO_4 solution. The percentage "sat" indicates the liquid saturation in the entire sample that was determined gravimetrically. The measurements marked with "XRCT" indicate days where μXRCT scans were also performed. The dashed line depicts the initial reference water content that was determined gravimetrically.

Figure 5.5b shows the water content profiles obtained from NMR measurements of the sintered glass sample prepared with $0.96 \text{ mol/L MgSO}_4$ solution during evaporation. For the initial state at day 0, an almost constant water content profile with a mean value of $0.37 \text{ cm}^3/\text{cm}^3$ was obtained. This profile slightly overestimated the initial water content of $0.36 \text{ cm}^3/\text{cm}^3$ that was determined gravimetrically for the entire sample, which can most likely be attributed to the uncertainty introduced by the gap between the shrinking tube and the sintered glass sample. After 3.8 days, the saturation in the entire sintered glass sample reached 60% (i.e., $0.22 \text{ cm}^3/\text{cm}^3$) and the water content at the surface was $0.09 \text{ cm}^3/\text{cm}^3$. This suggests that there was a liquid connection to the surface. A water content close to $0 \text{ cm}^3/\text{cm}^3$ appeared at the sample surface after 14.3 days at 45% saturation in the entire sample (i.e., $0.17 \text{ cm}^3/\text{cm}^3$). This

indicates the establishment of an evaporation front inside the sintered glass sample. It should be noted that after 66.8 days of evaporation, the water content in the top 5 mm of the sintered glass was close to $0 \text{ cm}^3/\text{cm}^3$. In contrast, the water content at the surface of the sand sample was close to $0 \text{ cm}^3/\text{cm}^3$ already after 6.3 days of evaporation (Figure 5.11a). Furthermore, it is important to note that the water content at the surface of the sintered glass sample was $0.19 \text{ cm}^3/\text{cm}^3$ after 1.8 days, while the water content at the surface of the sand sample was $0.04 \text{ cm}^3/\text{cm}^3$. This suggests that the water content distribution in sand and in sintered glass was different despite similar evaporative demand (Figure 5.3), which will be discussed in more detail after the results obtained from μXRCT data have been presented.

5.3.3. Pore-scale imaging of the salt crust developed in sand

The different evaporation and water content distribution in the sand and sintered glass sample indicated that salt precipitation most likely occurred differently in both types of porous media. Thus, it is interesting to investigate the change in volume fractions on the pore-scale. Figure 5.6a shows a side view of μXRCT imaging data of the sand sample with MgSO_4 solution after 0.4 days of evaporation (90% saturation in the entire sample). A homogeneous sand packing can be observed with a flat surface, where pores in the upper left are filled with liquid, while some pores are already invaded by air at the center and bottom of the FOV. Unfortunately, no matching NMR measurements are available for day 0.4 (90% saturation). Figure 5.6c shows the histogram data of an axial slice at the depth indicated in Figure 5.6a and Figure 5.6b. The three phases present in this axial slice correspond to the peak at 2.2×10^4 (void), the shoulder at 4.2×10^4 (liquid) and the peak at 5.8×10^4 (sand), which were segmented using k-means clustering (Table 4.5). Figure 5.6b shows the depth profiles of the segmented phases from μXRCT . Below -0.7 mm , the profile of the sand phase was almost constant and matched the reference sand volume fraction obtained gravimetrically. This suggests that the segmentation into void, liquid, and sand provided reliable results. The high void fraction above -0.7 mm is attributed to the pores that were already invaded by air. Additionally, since the volume fractions were obtained from each axial slice of the 3D image stack, the reduced sand fraction can most likely be related to the uneven surface of the sample and to a looser packing of the sand particles. This is consistent with the NMR measurements that showed a near-surface increase of the liquid phase fraction at 100% saturation (Figure 5.11a).

Figure 5.6d shows μXRCT imaging data of the same sample after 15.3 days of evaporation (61% saturation). It can clearly be seen that a gap formed at $\approx 1.4 \text{ mm}$ below the surface, which resulted in a high void fraction in the depth profile (0.34, Figure 5.6e). This was associated with an upward movement of the upper sand grains above the position of the surface at 90% saturation (see Figure 5.6a). The gap formation and the movement of the sand grains was

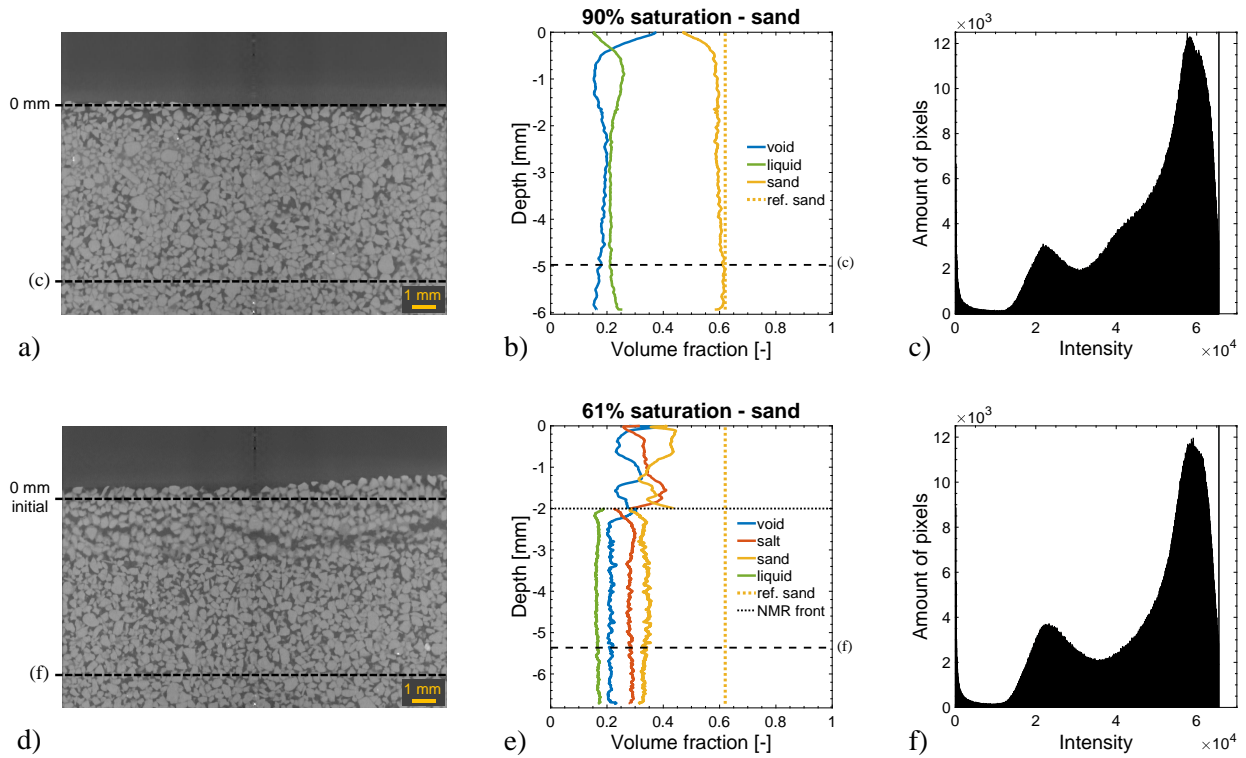


Figure 5.6: (a) Side view, (b) depth profile of phases, and (c) histogram from 3D μ XRCT image data obtained for the sand sample with MgSO_4 solution after 0.4 days at 90% saturation. The dashed yellow line marked "ref. sand" indicates the reference sand fraction that was determined gravimetrically. The histogram corresponds to the axial slice indicated in panel (a) and (b). The intensity below 1.1×10^4 depicts the area outside the FOV (Figure 4.8). The vertical line at 6.5536×10^4 indicates high intensity voxels (i.e., impurities) that were mapped during image adjustment (Table 5.1). (d) Side view, (e) depth profile of phases, and (f) histogram from 3D μ XRCT data after 15.3 days at 61% saturation. "0 mm initial" indicates the position of the surface at 90% saturation. NMR measurements showed liquid below the "NMR front" indicated in panel (e) so that four phases were segmented.

already expected from the μ XRCT data analysis presented in Chapter 4, and is attributed to the deforming effects of salt precipitation. Below a depth of 2 mm to 3 mm, the sand packing seemed to be unaffected by salt precipitation (Figure 5.6d). In Figure 5.6e, the depth profiles of the volume fraction of void, salt, sand, and liquid are shown at 61% saturation. As the water content from NMR was $0 \text{ cm}^3/\text{cm}^3$ above -2 mm (Figure 5.5a), three phases (i.e., void, salt, and sand) were segmented in this region. It was found that the sand fraction (0.45) was reduced considerably compared to the reference sand fraction (0.63) due to salt precipitation and the resulting deformation (Figure 5.6e). Below -2 mm, the water content from NMR ($0.1 \text{ cm}^3/\text{cm}^3$) indicated the presence of liquid. Thus, it was attempted to distinguish four phases (i.e., void, salt, sand, and liquid) using k-means clustering (Table 4.5). It was found that the sand fraction

(0.33) was significantly lower than the reference sand fraction (0.63) determined gravimetrically for the entire sample during preparation (Figure 5.6e), although no major deformation was observed below -2 mm (Figure 5.6d). This clearly suggests that the segmentation into four phases was not possible using the segmentation approach from Chapter 4. This is further supported by the histogram in Figure 5.6f, which shows that only two peaks and no shoulder were present. The left peak represents the void phase, whereas the right peak contains bulk information on the salt, sand, and liquid phase. Clearly, the contrast between the latter three phases is small and it is no surprise that the k-means clustering algorithm does not provide meaningful results. Thus, it is not known to which extent salt precipitation occurred below the consolidated crust. The physical reasons for this low contrast between the phases should be analyzed in future studies.

5.3.4. Registration of time-dependent imaging data

To overcome the deformation of the porous medium from subflorescent salt precipitation, the crust formation during evaporation was additionally monitored in the sintered glass sample. Since the solid sintered glass phase did not change during salt precipitation, the 3D distribution of the glass phase obtained for a dry sample was used as a mask to improve the interpretation of μ XRCT imaging data during evaporation. In particular, this mask allowed to distinguish between the solid glass phase (mask) and the non-glass phases. To apply this mask, the μ XRCT data at different times were matched to the initial dry reference μ XRCT data using image registration. Figure 5.7 shows the registration of a subarea from one 2D slice of the dry reference 3D image stack overlaid with the corresponding subarea from the 2D slice of the moving 3D image stack after 3.8 days (60% saturation). The glass phase has the highest density (2.23 g/cm^3), and is thus associated with the brightest part of the images. The density of the liquid phase at 60% saturation ($1.30 \text{ g/cm}^3 - 2.01 \text{ g/cm}^3$) was higher than the density of the air-filled voids ($1.162 \cdot 10^{-3} \text{ g/cm}^3$) in the reference measurement. Thus, the voxels of the liquid phase were brighter than the voxels of the void phase. Since it is not known if salt crystals were present after 3.8 days, this phase is called brine-crystal phase from now on.

In Figure 5.7a, six types of voxels can be distinguished in the subarea of the horizontal axial slice. First, the white voxels in the overlay area show the same intensity in the reference and the moving image, which represents the matching glass phase voxels. Second, the dark grey voxels in the overlay area indicate the same intensity of reference and moving image at that position, which represents the matching void voxels. Third, the green voxels at the left indicate the reference image without overlay of the moving image. The bright green shows the glass grains and the dark green are the voids according to the intensity of the filtered image data (i.e., the grey value was converted into a "green" value). Fourth, the purple voxels at the

right show the moving image without overlay of the reference image. Again, the bright purple depicts the glass grains and the darker purple shows the voids or liquid (i.e., grey value to "purple" value). Fifth, the pale green voxels in the overlay area indicate that the intensity of the reference image was higher than the intensity of the moving image at this position (i.e., a glass grain voxel of the reference image was at the same position as a void/liquid voxel of the moving image). Sixth, the pale pink voxels in the overlay area indicate positions where the intensity of the moving image was higher than the intensity of the reference image (i.e., a glass/liquid voxel of the moving image was at the same position as a void voxel of the reference image). With these definitions, the presence of (pale) green voxels in the overlay area indicates a poor registration.

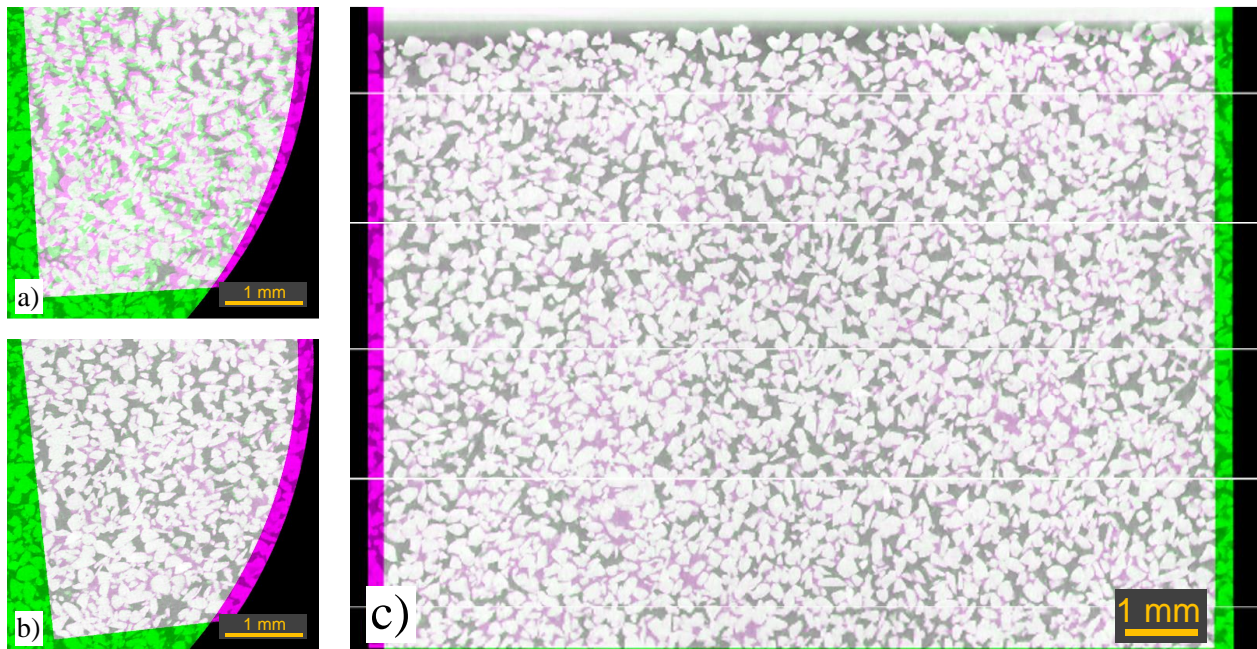


Figure 5.7: Registered μ XRCT data from sintered glass sample at the initial dry state and after 3.8 days (60% saturation). (a) Subarea of horizontal axial slice in case of poor registration. The purple "half moon" at the right side represents the part of the moving image (60% saturation) that does not overlap with the reference image (dry). The green "L" at the left side and at the bottom shows the reference image (dry) with no overlap of the moving image (60% saturation). The black area indicates the outside of the respective FOV of the reference image and of the moving image (see Figure 4.8). (b) Subarea of horizontal axial slice in case of a good registration. The glass grains are white, the void is dark grey, and the pale pink between the grains depicts the brine-crystal phase. (c) Vertical side view of entire stack. The white horizontal lines are not real and result from stitching subimages together to obtain the side view.

Figure 5.7b shows the same subarea after registration (see Table 5.1). The glass grains look focussed now, which indicates that the position of the grains and the void space matched for the reference and the moving image. The pale pink regions between the glass grains indicate

the brine-crystal phase of the moving image after 3.8 days (60% saturation). There are almost no green voxels in the overlapping region, which suggests a successful registration. To test the quality of the 2D registration procedure, Figure 5.7c shows an exemplary vertical overlay of the μ XRCT image data at the initial dry state and at day 3.8 (60% saturation). It can be seen that the 2D registration procedure in the horizontal plane was successful, as the top and the bottom of this vertical side view showed practically no deviation between the glass and the void phase of the reference and moving image. In addition, the brine-crystal phase at day 3.8 (60% saturation) can clearly be recognized as a pale pink phase between the bright glass grains. If the sample would have been tilted away from the vertical axis due to the removal and re-installation of the sample in the μ XRCT device, the glass grains and the void phase of the moving 3D image would not overlap with the reference 3D image. This mismatch would be visible as pale green voxels between the glass grains (see Figure 5.7a) at the top and the bottom of the vertical side view, which is clearly not the case. Despite the success of the 2D registration, future work should provide a comparison between the quality of 2D and 3D registration methods (e.g. using AVIZO[®] software).

5.3.5. Segmentation using the sintered glass phase mask

After registration of the time-dependent μ XRCT measurements made during evaporation from the sintered glass sample, the next step was to segment the different phases. The segmentation procedure is described in the following. Figure 5.8 shows a subarea of the axial slice at a depth of -0.8 mm for the initial dry state and at 21% saturation. The filtered data of the dry sample clearly shows that glass grains can be distinguished from the void space (Figure 5.8a), which is also reflected in the two distinct peaks in the corresponding histogram (Figure 5.8c). Threshold segmentation provided a separation of the glass phase from the void space. The segmented glass phase was used to mask the filtered data at the initial dry state (Figure 5.8b), which provided the grey value distribution of the void phase (Figure 5.8d).

Figure 5.8e and Figure 5.8g show the filtered μ XRCT data at 21% saturation and the associated histogram, respectively. The two peaks in the histogram (Figure 5.8g) before application of the mask suggest that only two phases can be distinguished. Since the NMR measurements at 21% saturation showed that no mobile water was present in the FOV of the μ XRCT data, it is suggested that the two peaks in the histogram represent the void phase (left peak) and the solid phase (right peak). Since the solid phase peak contains information on both the glass phase and the salt phase, it is clear that threshold segmentation cannot be used to distinguish between the glass and the precipitated solid salt phase. However, the mask obtained from the initial dry state represents the glass phase and can thus be used to separate the precipitated salt phase and the glass phase (Figure 5.8f). After masking the glass phase, the precipitated salt phase

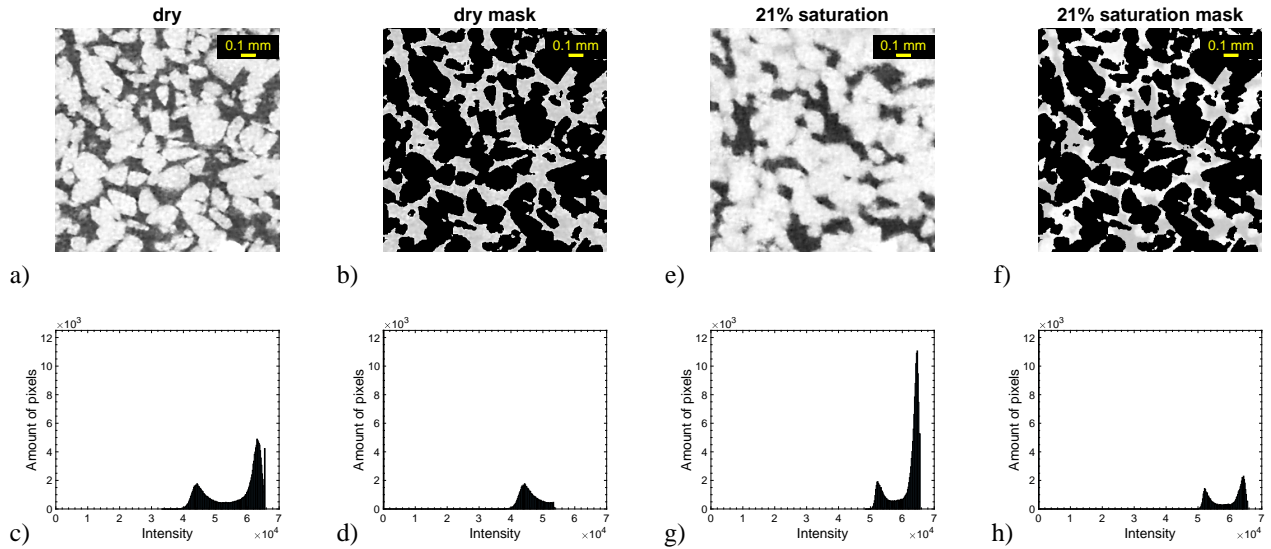


Figure 5.8: (a) Filtered data, (b) mask data, and (c,d) corresponding histograms of a subarea of an axial slice at initial dry state at -0.8 mm from the top of the sample. (e) Filtered data, (f) mask data, and (g,h) corresponding histograms of the same subarea after 66.8 days of evaporation (21% saturation). In panel (a) and (e), dark grey represents void space and bright areas show glass grains (and/or solid salt at 21% saturation). The glass phase (black) obtained from threshold segmentation of the dry image in panel (b) was used to mask all registered data.

(right peak, Figure 5.8h) can be distinguished from the void phase (left peak, Figure 5.8h). It is important to note that the high density of the solid salt phase after 66.8 days led to more X-ray attenuation than in the case of the dry sample. Thus, a lower beam intensity was detected for the measurement at day 66.8. Since the intensity was inverted during the reconstruction process, a higher mean intensity/brightness of the image with precipitates (Figure 5.8e) compared to the reference image (Figure 5.8a) was obtained. This difference can also be seen as a shift of the entire histogram to the right (Figure 5.8g) compared to the reference histogram (Figure 5.8c). This indicates that a simple segmentation using a subtraction of the two intensity distributions is not feasible.

5.3.6. Phase volume fractions from μ XRCT measurements

To understand salt crust formation, it is important to investigate the development of the volume fractions of different phases during evaporation. Figure 5.9a shows masked and segmented data for the same subarea shown in Figure 5.8 after 3.8 days (60% saturation). After masking, only two additional phases were segmented in the original void phase. These two phases represent the current void phase (grey) and the so-called brine-crystal phase (white). It is not clear to which extent the brine-crystal phase consisted of liquid or of precipitated salt for the measurement

at 60% saturation. However, the brine-crystal phase often seems to build menisci between glass grains, which suggests that at least a part of the brine-crystal phase was liquid. This was supported by the NMR measurements, which showed a relatively high water content of $0.09 \text{ cm}^3/\text{cm}^3$ at -0.8 mm (Figure 5.5b). At the same time, the brine-crystal phase was also present as a coating at the border of some glass grains, which might be a liquid film or a thin layer of salt precipitation. Since the apparent thickness of this thin layer is almost identical to the resolution ($4 \mu\text{m}$), artifacts due to the registration or segmentation can also not be excluded.

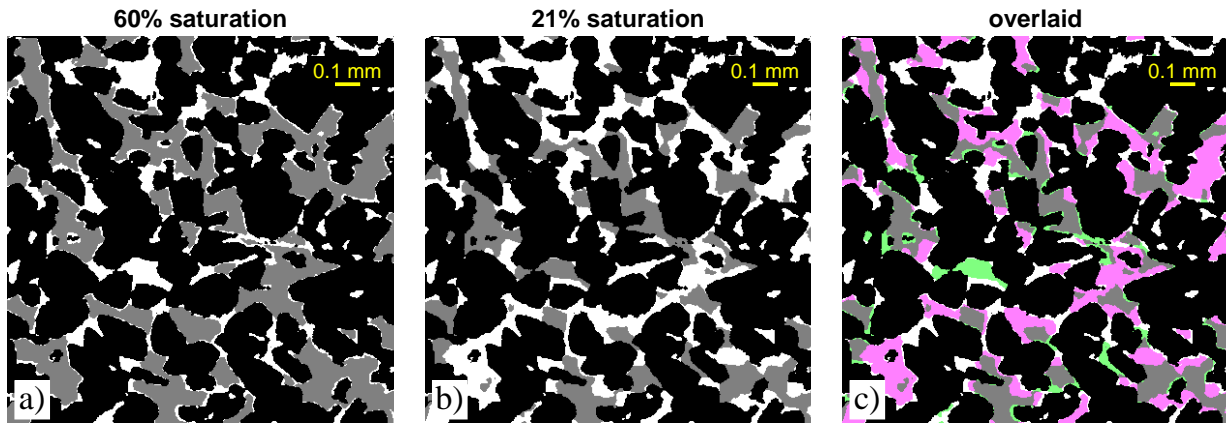


Figure 5.9: Segmented subarea at -0.8 mm from the surface at (a) 60% saturation and (b) 21% saturation. Black represents the masked glass phase, grey is the void space, and white is the brine-crystal phase (60% saturation) or the solid salt phase (21% saturation). (c) Overlay of both segmented images with a colored classification of the voxels. Green shows the brine-crystal phase at 60% saturation that turned into void at 21% saturation (i.e., indicating evaporated liquid). Pink is the solid salt phase at 21% saturation that was void phase at 60% saturation. White represents the area where brine-crystal phase was present at 60% saturation and solid salt phase remained at 21% saturation.

Figure 5.9b shows the segmented data of the same subarea after 66.8 days (21% saturation) (i.e., segmented result of Figure 5.8f). As argued above, the three segmented phases now represent the glass phase, the void phase, and the precipitated salt, since the NMR measurements indicated that no liquid was present anymore. To analyze the development of the phases between these two measurements, both segmented images were superimposed and classified (Figure 5.9c). Four classes of voxels can be distinguished besides the solid glass phase (Figure 5.9c, black). The first class consists of voxels that were void phase at both levels of saturation (Figure 5.9c, grey). The second class indicates voxels that belonged to the brine-crystal space at 60% saturation and turned into void at 21% saturation (Figure 5.9c, green). If it is assumed that salt is not removed again after precipitation, these areas can be interpreted as brine that was removed by evaporation between the two levels of saturation. This area thus represents the minimum liquid phase at 60% saturation. The third class of voxels indicates areas that belonged to the void space at 60% saturation and to the solid salt phase at 21%

saturation (Figure 5.9c, pink). These areas thus indicate the growth of salt precipitates into the pore space. It was found that the salt phase grew into void space over a considerable distance in the order of the glass grain size. This suggests that liquid supply to the surface was present during the evaporation from 60% to 21% saturation, which is supported by the NMR measurements (Figure 5.11b). The fourth class of voxels indicates regions that were brine-crystal phase at 60% saturation and solid salt at 21% saturation (Figure 5.9c, white). Since it was shown that the white areas were solid salt at 21% saturation (day 66.8), it might be assumed that these white areas were already solid salt at 60% saturation (day 3.8). Thus, these areas can be interpreted as the maximum possible volume fraction of solid salt that could have already precipitated at 60% saturation.

The presented results suggest that the minimum volume fraction of the liquid phase and the maximum possible volume fraction of solid salt at 60% saturation can be determined using a combination of μ XRCT and NMR data. However, solid salt and brine could not be consistently distinguished with the current work flow. This may be related to the small difference in the density of the supersaturated MgSO_4 solution and the crystal phase. The density of MgSO_4 solution at the solubility limit is 1.30 g/cm^3 , but it can be substantially higher for supersaturated solutions. The salt phase likely consists of a mixture of $\text{MgSO}_4 \cdot 7\text{H}_2\text{O}$ (1.68 g/cm^3 , (*Lide*, 2004)) and $\text{MgSO}_4 \cdot 4\text{H}_2\text{O}$ (2.01 g/cm^3 , (*Baur*, 1964)). It is therefore not clear, if and how much solid salt was present at 60% saturation. Another important result is the observation that the solid crystal phase grew into the void space during evaporation from 60% to 21% saturation. This suggests that liquid filled pores are not essential for crystal growth. It is possible that liquid film flow might provide the supply of ions for precipitation. Future studies should focus on the liquid transport of MgSO_4 solution in porous media to understand the role of film flow during subflorescent salt precipitation.

5.3.7. Depth profiles of segmented phases in sintered glass

In a next step, the variation of the phases with depth was analyzed after different amounts of evaporation to obtain insights on the liquid distribution and on the salt precipitation processes. Figure 5.10 shows the depth profiles of different volume fractions at 100%, 90%, 60%, and 21% saturation derived from the μ XRCT imaging results. The glass phase was determined for the dry initial state and showed a constant depth profile with a mean value of 0.65, which is within the uncertainty range of the gravimetrically determined glass phase fraction (0.64). Accordingly, the void space from μ XRCT (0.35) was almost equal to the porosity determined gravimetrically (0.36). Since this segmented glass phase was used as a mask to analyze all other μ XRCT measurements, the depth profiles of the glass phase are identical for all levels of saturation. At 100% saturation, all pores were filled with liquid so that the void fraction

was 0 and the mean liquid fraction was 0.35 for all depths (Figure 5.10a). This confirms the efficiency of the saturation procedure. In this context, Figure 5.11 compares the liquid fraction from μ XRCT with the water content profiles obtained using NMR. For the initial state (100% saturation, day 0), the measured quantities from NMR, μ XRCT, and the water content determined gravimetrically matched well and showed an averaged volume fraction of about $0.36 \text{ cm}^3/\text{cm}^3$. The slight deviation of the averaged volume fraction was attributed to the different FOVs of each measurement method.

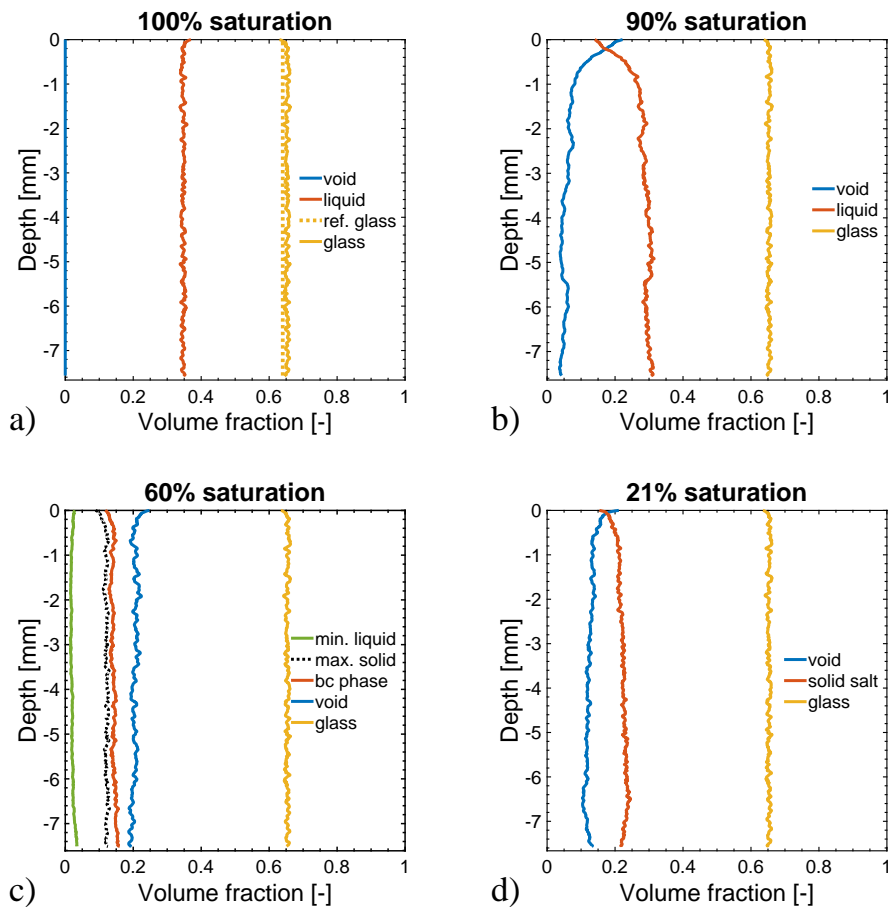


Figure 5.10: Depth profiles of segmented phases obtained from μ XRCT data of the sintered glass sample at (a) 100% saturation, day 0, (b) 90% saturation, day 0.3, (c) 60% saturation, day 3.8, and (d) 21% saturation, day 66.8.

As expected, the liquid fraction from μ XRCT decreased more quickly near the surface (0.13) than deeper in the sample (0.30) with increasing time of evaporation (0.3 days, 90% saturation, Figure 5.10b). The NMR measurements at day 0.3 (90% saturation) showed a similar decrease of the water content at the surface (Figure 5.11), which was also reported in the context of deionized water evaporation from porous media (*Merz et al.*, 2014). This suggests that there was liquid at the surface, which allowed a relatively high evaporation rate (8 mm/day). Between

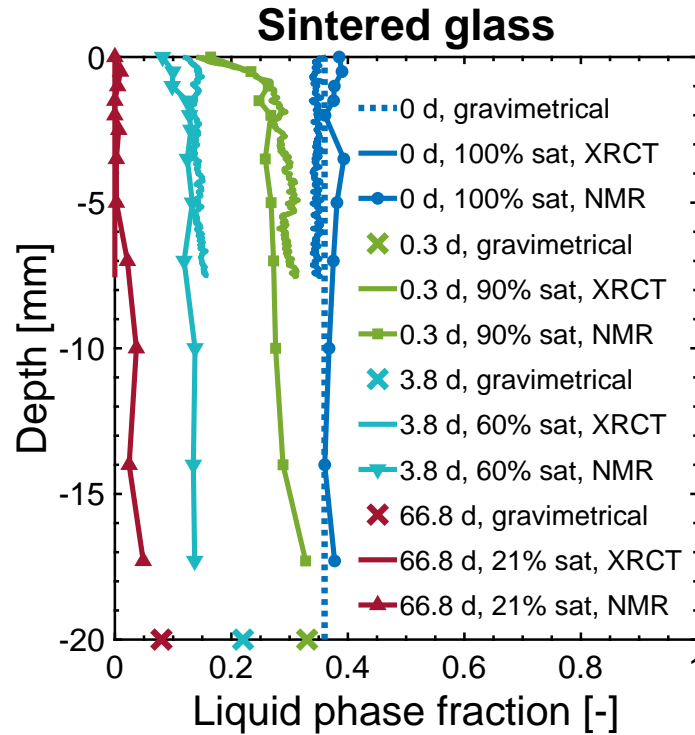


Figure 5.11: Depth profiles of the water/brine-crystal phase fraction from NMR data and μ XRCT data in the sintered glass sample and gravimetrical reference of the entire sample.

-1 mm and -7 mm, the brine-crystal phase fraction from μ XRCT was higher than the water content from NMR (Figure 5.11). This may be related to the difference in the FOV of both non-invasive measurement methods.

Figure 5.10c presents the depth profiles of the μ XRCT data at day 3.8 (60% saturation). As discussed above, the brine-crystal phase can be divided into the minimum liquid fraction (Figure 5.9c, green) and the maximum possible solid salt fraction (Figure 5.9c, white). The maximum possible solid salt fraction showed a mean value of 0.12 and was almost constant with depth. The minimum liquid fraction (Figure 5.9c, green) was much lower and also almost constant with depth (0.02). Nevertheless, this suggests that a liquid connection to the surface was present, which is consistent with the NMR measurements (i.e., day 3.8, Figure 5.11). However, the water content from NMR was above $0.10 \text{ cm}^3/\text{cm}^3$ for all depths at day 3.8, which suggests that the segmented brine-crystal phase from μ XRCT consisted mostly of liquid. It can be concluded that the minimum liquid fraction from μ XRCT underestimated the liquid content from NMR at day 3.8 (60% saturation) significantly. It is therefore possible that salt did not yet precipitate.

As already discussed, the water content from NMR was close to $0 \text{ cm}^3/\text{cm}^3$ in the topmost 5 mm at day 66.8 (21% saturation, Figure 5.11). Thus, the segmented brine-crystal phase

from μ XRCT data was assumed to be solid salt. Figure 5.10d shows the volume fractions at 21% saturation. It can be seen that the volume of the solid salt phase was higher than the brine-crystal phase at 60% saturation (Figure 5.10c). This suggests growth of the crystal phase into the void space, which was already shown in Figure 5.9c. The lack of μ XRCT data between day 3.8 (60% saturation) and day 66.8 (21% saturation) does not allow an unambiguous interpretation of the precipitation process. However, a possible explanation is provided in the following. It is reasonable to assume that salt precipitation started at the surface of the sample. Once the nuclei were formed, crystal growth was possible as long as supersaturated liquid was supplied. The movement of the evaporation front into the porous medium implies the disconnection of the liquid supply, as illustrated by NMR measurements (day 14.3 and day 28.1, Figure 5.5). Since the salt crystals could not grow without liquid supply, it seems plausible that the void space at a certain depth did not change due to precipitation after the evaporation front passed this depth. If the downward movement of the evaporation front occurred with a constant speed, a homogeneous subflorescent salt precipitation similar to the observation in Figure 5.10d could be expected. However, it is possible that a liquid film was present that could not be detected using NMR and μ XRCT. Therefore, future studies should compare the depth of the evaporation front and the location of salt precipitation with a focus on possible liquid film flow.

A slight decrease of the solid salt fraction can be observed at day 66.8 (21% saturation) in a depth of -7 mm (Figure 5.10d), whereas the void fraction increases at the same time. Since it was assumed that only three phases were present (i.e., void, solid salt, and glass), the slight decrease of the salt fraction may be related to an incomplete segmentation. Further, NMR measurements at -7 mm showed a water content of $0.03 \text{ cm}^3/\text{cm}^3$, suggesting the presence of liquid (Figure 5.11). However, this water content measurement with NMR is also affected by uncertainty due to scattering of the echo amplitude associated with the low signal intensity.

5.3.8. Differences in crust formation in sintered glass and sand

The presented results suggested that the evaporation of deionized water from sand and from sintered glass was similar. In contrast, the salt crust formation due to evaporation of 0.96 mol/L MgSO_4 solution from sintered glass samples was considerably delayed compared to the crust formation in sand samples. Possible explanations are discussed in the following.

The first explanation is related to salt crust formation in sand. At the beginning, liquid is provided to the surface by capillarity and is supersaturated by evaporation. It is plausible that the rough surface of the sand grains promote the formation of salt nuclei (*Scherer*, 2004). After nucleation, the salt crystals grow while the capillary liquid connection continuously provides dissolved ions and supersaturation is maintained by evaporation. The growing precipitates

reduce the pore radius, which results in an increase of the capillary pressure that enhances capillary flow to the surface. This positive feedback leads to an increased salt precipitation. On the other hand, more and larger precipitates deform the porous structure of the sand, which may disconnect the consolidated crust from the liquid supply. The near-surface water content of $0.0 \text{ cm}^3/\text{cm}^3$ at day 6.3 (71% saturation, Figure 5.5a) suggests the downward movement of the evaporation front, which most likely appeared at least partly due to the disconnected crust. As a result of the complex interplay of the deformation, the disconnection of the crust, and the pore blocking due to continuous precipitation, evaporation was reduced.

The second explanation is related to salt precipitation in sintered glass samples. It is reasonable to assume that the surface of the glass grains has become smooth during the sintering process. Such smooth surfaces provide less nuclei for salt crystallization than the (rougher) surface of untreated (sand) grains (*Scherer*, 2004). This may result in a higher supersaturation due to evaporation in the sintered glass compared to sand because less salt crystals formed and grew in the brine present in the sintered glass sample. Additionally, since it is known that higher supersaturation reduces the nucleation of MgSO_4 (*Espinosa-Marzal and Scherer*, 2010), less nucleation can be expected for the sintered glass sample, which leads to delayed crust formation and different hydraulic properties in sintered glass compared to sand. This provides a liquid capillary connection that is maintained for a longer time in the case of the sintered glass sample than in the case of sand. The higher water content of the sintered glass sample ($0.19 \text{ cm}^3/\text{cm}^3$) was observed with the NMR measurements near the surface after 1.8 days. At that time, a salt crust was already formed in the sand sample and the water content was $0.04 \text{ cm}^3/\text{cm}^3$. In contrast to the water content at the surface, it was found that the water content of the entire sintered glass sample ($0.25 \text{ cm}^3/\text{cm}^3$) was lower than the water content of the entire sand sample ($0.30 \text{ cm}^3/\text{cm}^3$) after 1.8 days (Figure 5.5). This may be attributed to the fact that salt did not yet precipitate in the sintered glass sample, which allowed a higher evaporation rate (Figure 5.3). This high evaporation rate was maintained by capillary liquid supply to the surface of the sintered glass sample, which was also confirmed by NMR measurements (Figure 5.5b). At some point, the very high supersaturation in the sintered glass sample resulted in nucleation and in crystal growth. The salt crystals grew as long as liquid was supplied. After the downward movement of the evaporation front, the salt volume fraction above the front stopped growing. It is possible that the evaporation front moved down with a relatively constant speed so that the homogeneous precipitation profile is obtained as observed by μXRCT . It can be concluded that the delayed precipitation in the sintered glass sample affected evaporation less than the early nucleation in sand, which resulted in deformation. This can partly be related to the delayed positive feedback of pore radius reduction due to precipitation on capillarity in the case of the sintered glass sample.

It is interesting to note that in contrast to subflorescent MgSO_4 precipitation, efflorescent NaCl

crusts from low initial concentration formed earlier on regular packed glass beads than on irregular sand grains of similar mean grain size (*Rad and Shokri, 2014*). This was attributed to the lower amount of active pores on the packed glass beads and seems to be in contrast to the findings of this study at first sight. It is plausible that the different type of salt (i.e., efflorescent NaCl precipitation in *Rad and Shokri (2014)* and subflorescent MgSO₄ precipitation in this study) has a major impact on the initial nucleation and the crust formation. In the case of efflorescent NaCl precipitation, the lower viscosity of the supersaturated solution (≈ 1.99 mPa s, *Lide (2004)*) may allow capillary liquid flow to the surface more quickly than the high viscosity of supersaturated MgSO₄ solution (> 8.07 mPa s). This may lead to earlier NaCl crystal formation, which in turn promotes further crystal growth of the efflorescent salt crust. Additionally, the glass beads were not sintered (*Rad and Shokri, 2014*), so the surface of the beads most likely was more rough than the surface of the sintered glass sample in this study. Another finding by *Rad and Shokri (2014)* is that the impact of the porous medium on evaporation and crust formation was reflected in the very steep gradient of the water content in the sand and in the glass beads during evaporation of the NaCl solution. As the gradient of the water content profile in this study was less steep, it can be concluded that the properties of the porous medium affect crust formation to a different extent for different salt types, which needs to be investigated in future studies. In particular, future experiments should investigate NaCl precipitation on porous media with smooth (grain) surface to compare efflorescent and subflorescent crust formation and to reveal the impact of the hydraulic properties of the porous medium on the water content profile.

The considerations above show that the complex interaction between nucleation, precipitation, capillarity, deformation, and evaporation strongly depends on the porous medium. More research with other types of salts is needed to understand the impact of the properties of the porous medium on salt crust formation.

5.4. Conclusions

In the case of MgSO₄ precipitation in sand, the NMR data showed the downward movement of the evaporation front that was associated with salt precipitation monitored with μ XRCT measurements. The segmentation of the μ XRCT data into void, liquid, salt, and sand was found to be challenging. The sand phase fraction obtained from μ XRCT data did not match the expected sand phase fraction determined gravimetrically and the sand was deformed during salt precipitation. Thus, sintered glass samples with similar porosity, intrinsic permeability, and internal surface area were prepared with MgSO₄ solution.

Time-lapse NMR measurements showed that the downward movement of the evaporation front

into the sintered glass was significantly delayed compared to sand. Additionally, salt crust formation in the sintered glass was slowed down. The difference in evaporation and crust formation in both porous media can be attributed to the combined effect of smoother surfaces (i.e., reduced nucleation) and higher level of supersaturation (i.e., higher solution viscosity and reduced nucleation), which was also mentioned in previous studies (*Scherer*, 2004; *Espinosa-Marzal and Scherer*, 2010, 2013). Additionally, it was shown in this study that the deformation of the unconsolidated sand after only one cycle of drying plays a significant role by (partly) disconnecting the liquid supply and thus, affecting subflorescent salt crust formation. It can be concluded that the subflorescent precipitation of MgSO_4 strongly depends on the particle surface properties and the structure of the porous medium, which led to a delayed downward movement of the evaporation front in case of the sintered glass samples. More research is needed to understand how the complex interaction of evaporation, precipitation, and liquid transport controls the crust formation in porous media.

The μXRCT data of the sintered glass sample showed that the segmentation into solid salt and glass after 66.8 days (21% saturation) was only possible by masking the glass phase from the initial dry μXRCT data, as the low contrast between glass and solid salt prevented the use of conventional algorithms. Further, solid salt that precipitated during evaporation from 60% saturation to 21% saturation could be identified. It is important to note that these salt crystals also grew into the void space that was not occupied with liquid before. This suggests that liquid supply needed for crystal growth may have been provided by film flow, since liquid was not transported with the help of capillarity. Future studies should test this hypothesis using the 3D data of the liquid phase provided in this study.

Chapter 6

Conclusions and outlook

In this chapter, the overall conclusions of the thesis will be presented and possible future research directions will be discussed in an outlook.

6.1. Conclusions

The impact of salt crusts on evaporation has been investigated in previous studies both on the micro- and macro-scale with a focus on efflorescent salt crusts. The contribution of the permeability and porosity of a salt crust to evaporation was linked to the flow of water and vapor only for samples with salt solution at the solubility limit (*Nachshon and Weisbrod, 2015*) or for the accessible part of a crust (*Weisbrod et al., 2014*). In addition, knowledge of the temporal development of salt crusts, which is important to understand evaporation and crust formation, was available for efflorescent salt crusts only (*Rad and Shokri, 2014*). The location of the salt crust (efflorescent or subflorescent) is affected by the evaporation rate, the supersaturation properties of the solution, and the properties of the porous medium (*Espinosa-Marzal et al., 2008; Espinosa-Marzal and Scherer, 2010, 2013*). Subflorescent precipitation was mainly investigated with respect to the destructive crystallization during multiple cycles of saturation and evaporation on the macro-scale (*Espinosa-Marzal and Scherer, 2013; Flatt et al., 2014*). Increasingly more complex REV-scale models that simultaneously describe salt precipitation and evaporation are being developed (*Jambhekar et al., 2015, 2016; Mejri et al., 2017*), and help to understand how single transport and precipitation mechanisms affect the entire process. However, the formation of a new porous medium during efflorescent precipitation is challenging to describe in such models due to the spatial change of the interface between the porous and the free flow domain (*Jambhekar et al., 2015; Shokri-Kuehni et al., 2020*). Additionally, the use of common porosity-permeability relationships to model the impact of precipitation on evaporation was found to be only partly suitable (*Jambhekar, 2017*), which is not unexpected in case of efflorescent precipitation. In this context, the overall aim of this thesis was to

improve understanding of the impact of salt crusts on evaporation with a focus on the porosity, the intrinsic permeability, and the spatial and temporal development of salt crusts. Three sub-objectives were formulated to address this overall aim.

The first sub-objective was to compare the impact of different salt solutions on the evaporation from sand and to analyse the role of the permeability of efflorescent and subflorescent salt crusts. This was addressed in two steps in Chapter 3. First, the permeability of subflorescent crusts from MgSO_4 solution was determined using liquid flow after resaturation. It was shown that liquid flow measurements of the permeability were prone to air entrapment during resaturation. Additionally, the resaturation resulted in unknown liquid properties (i.e., viscosity) due to mixing, and the anticipated solute concentrations below the solubility limit may also have led to partial dissolution of the salt crusts. Thus, it was concluded that the use of liquid flow measurements was not suitable for salt crusts formed from low initial concentration. To avoid the uncertainties associated with permeability determination using liquid flow, a novel gas permeameter was developed in this thesis to determine the permeability of salt crusts formed from low initial concentration. In a second step, evaporation and the associated salt crust formation of NaCl , MgSO_4 , and Na_2SO_4 solutions at 33% of the corresponding solubility limit was investigated. It was shown that the evaporation rate of the different salt solutions varied at the beginning of evaporation, which was attributed to the variation of the vapor pressure directly over the surface due to the presence of different solutes. The reduction of evaporation in the case of NaCl was related to the formation of an efflorescent barrier, which was also reported in previous studies (*Nachshon and Weisbrod, 2015*) that showed a similar intrinsic crust permeability despite different initial concentration and porous medium properties. The similar evaporation of the samples with Na_2SO_4 compared to the samples with NaCl indicated a similar impact of the intrinsic crust permeability on evaporation although subflorescent precipitation was observed. The relatively high permeability of the subflorescent MgSO_4 crusts was not consistent with the low evaporation rate of the samples with MgSO_4 solution. It was concluded that the properties of the porous medium and the initial solute concentration only slightly affect evaporation and the crust permeability of NaCl solution from porous media. In contrast, since a similar permeability of the dried crusts from the different salts was obtained using gas flow measurements, it was concluded that the type of salt and the properties of the porous medium are key factors for the intrinsic permeability of subflorescent crusts that affect evaporation to a different extent.

The second sub-objective was to establish a porosity-permeability relationship for subflorescent precipitation formed from evaporation of solutions with varying initial concentration. This was addressed in Chapter 4, where the permeability of separated MgSO_4 crusts from varying initial concentration in sand was determined using the gas permeameter set-up developed in Chapter 3. The crust thickness and the geometry of the pore space were obtained using μXRCT

measurements. It was found that the crust permeability decreased with increasing initial salt concentration and increasing time of evaporation (i.e., lower saturation), which was expected because both factors are associated with more salt precipitation. This was partly also confirmed by thicker crusts. However, the thickness of the crusts from high initial concentration remained relatively constant for longer evaporation time despite a significant reduction in permeability. The permeability determined in this chapter was one order magnitude lower than in Chapter 3, although the initial conditions were identical. This was attributed to the higher evaporation rate due to a higher air flow velocity in this chapter. This underlines the importance of the evaporation rate for subflorescent salt crust formation, which was already reported by *Espinosa-Marzal and Scherer (2010)*. The analysis of μ XRCT measurements showed a deformation of the porous matrix of at least 20% for all crusts. This deformation occurred after only one cycle of saturation and drying, which has not been reported before. Since the crusts were deformed, a rigid porous matrix could not be assumed. Thus, the porosity and the intrinsic permeability for the sand– MgSO_4 system were not related. It was concluded that the deformation during salt precipitation has to be considered to understand the impact of subflorescent crust formation on evaporation from unconsolidated porous media.

The third sub-objective was to monitor the time-dependent development of subflorescent salt crust formation to improve understanding of how pore-scale processes affect evaporation. This was addressed in Chapter 5, where the time-lapse crust formation from MgSO_4 solution was monitored using μ XRCT and single-sided unilateral NMR. In the case of a sand sample affected by MgSO_4 precipitation, limited contrast between the four phases void, liquid, salt, and sand as well as the expected deformation caused a substantial deviation of the segmented sand fraction compared to the reference sand fraction determined gravimetrically. However, qualitative side views from μ XRCT and NMR measurements suggested that the evaporation front moved into the sand, which involved salt precipitation and crust formation. Thus, to avoid deformation from precipitation and to improve the segmentation, sintered glass samples were prepared with MgSO_4 solution, which showed a similar porosity, intrinsic permeability, and internal surface area as the sand samples. It was found that evaporation of deionized water was similar for both types of porous media, which was attributed to the similar porous media properties (e.g. porosity, permeability, internal surface area) and evaporation conditions. In contrast, the evaporation of saline water and the resulting salt crust formation was different. In particular, salt crust formation was delayed for the sintered glass sample. This was attributed to the decreased nucleation due to both the smooth surface of sintered glass (*Scherer, 2004*) and the reduced nucleation rate from the highly supersaturated MgSO_4 solution (*Espinosa-Marzal and Scherer, 2010*). The imaging results for the sintered glass samples showed that a plausible determination of the water content and phase volume fractions could only be obtained when μ XRCT and NMR data were combined for interpretation. Analysis of the registered μ XRCT

data of the sintered glass samples after 3.8 and 66.8 days revealed that the salt crystals grew into the void space that was not occupied with liquid before. This suggests that film flow may have provided liquid for crystal growth. It was concluded that subflorescent MgSO_4 precipitation strongly depends on the surface properties and structure of the porous medium and on the properties (i.e., viscosity and nucleation properties) of the supersaturated solution, which resulted in a delayed downward movement of the evaporation front.

Overall, the results provided in this thesis suggest that efflorescent and subflorescent salt crust affect evaporation to a different extent. The intrinsic permeability of efflorescent NaCl crusts presented a barrier for evaporation so that the crust permeability was mostly independent from the supporting porous medium. In contrast, the intrinsic permeability of subflorescent MgSO_4 crusts strongly depended on the porous medium and on the initial solute concentration. This was reflected in an increasing evaporation rate of the samples with decreasing initial concentration, which resulted in an increasing intrinsic crust permeability. The surface properties of the porous medium and the properties of the supersaturated solution (i.e., viscosity and nucleation properties) are additional key factors that affect subflorescent salt precipitation and the downward movement of the evaporation front. Additionally, the deformation of unconsolidated porous media needs to be taken into account, which significantly affects subflorescent crust formation and thus evaporation.

6.2. Outlook

The results presented in this thesis improved understanding of evaporation and salt crust formation. A range of experimental methods have been established that may form the basis for future research on salt crust formation associated with evaporation. In this thesis, only the intrinsic permeability of the consolidated part of the salt crusts formed in sand was determined. It is not known to which extent precipitated salt was removed in the unconsolidated sand below the consolidated part of the crust because μXRCT measurements before and after crust separation were not available. Additionally, the deformation of the unconsolidated sand changed the initial structure of the packing, which obviously affected the intrinsic permeability. Therefore, it would be of interest to investigate the change of permeability due to salt precipitation in rigid sintered glass samples. For this, two sintered glass cylinders of different length and with a known intrinsic permeability could be fixed on top of each other using a shrinking tube. After saturation with a salt solution, the sample could be allowed to evaporate until unilateral NMR measurements indicate that the evaporation front passed below the shorter top cylinder. The permeability of the top cylinder containing precipitated salt could then be determined using the gas permeameter presented in this thesis. This would allow to investigate the impact of

subflorescent salt precipitation during evaporation on the intrinsic permeability in the absence of deformation.

Single-sided unilateral NMR was used in this thesis to determine water content profiles during evaporation. The settings were selected to obtain a large penetration depth into the sintered glass samples to investigate the development of the near-surface water content profiles as deep as possible. This resulted in a higher uncertainty in the soil water content measurements obtained with unilateral NMR. However, it was found that the water content was reduced relatively uniformly along the depth for the sintered glass samples, which suggests that NMR measurements in deeper regions of the sample may not provide much additional information. Thus, the trade-off between NMR signal intensity and measurement depth should be reconsidered and future experiments on the development of the water content profile during salt precipitation should focus on the top centimeter of the porous medium, in order to obtain more accurate water content measurements.

An interesting opportunity is to compare the intrinsic crust permeability obtained experimentally in this thesis to the intrinsic permeability estimated from Stokes flow simulations using the segmented solid (salt + sand) and void phase from μ XRCT imaging data (*Gueven et al.*, 2017). This may provide insights on the difference in connectivity of the pore space between salt crusts formed from different initial conditions and time of evaporation, which is of particular interest because crusts with similar thickness showed significant differences in intrinsic permeability. Figure 6.1 shows the 3D void space of a separated crust from Chapter 4, where the connectivity of the pores seems to allow gas flow through the crust. However, the determination of the intrinsic permeability of such a complex void space structure using Stokes flow simulations requires advanced modelling strategies, such as continuous boundary conditions and powerful computational hardware. In addition to Stokes flow simulations on the 3D structure obtained

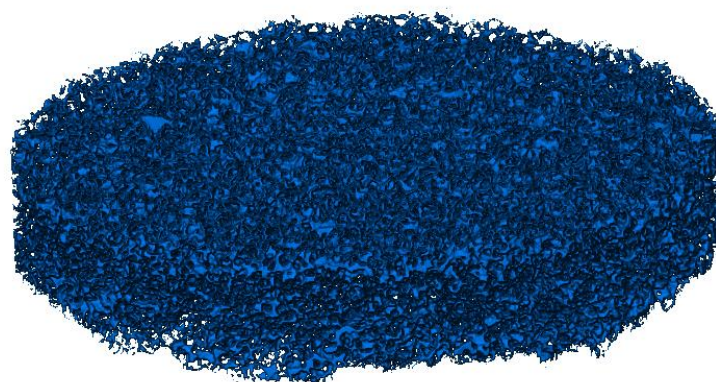


Figure 6.1: Segmented 3D void space from μ XRCT data of the separated crust from 0.64 mol/L initial concentration at 20% saturation in sand. The diameter of the volume is 11.76 mm.

from μ XRCT measurements, it is also interesting to explore the use of pore network models to estimate the intrinsic permeability of the salt crusts. For the data presented in this thesis, there is a difference in investigated volume between the intrinsic permeability determined using gas flow (the entire separated salt crusts) and the FOV of the μ XRCT measurements (center region of each crust). To better evaluate the accuracy of the intrinsic permeability estimates obtained from Stokes flow and pore network modelling, future studies should compare the estimated crust permeability to a measured intrinsic permeability determined experimentally for the same volume. For this, evaporation experiments should be performed with smaller samples (e.g., diameter ≈ 12 mm). However, wall effects during evaporation may need to be considered for smaller samples.

The registration of the μ XRCT imaging data allowed the segmentation of the sintered glass sample with MgSO_4 after 66.8 days of evaporation, which was not possible using conventional threshold segmentation. However, the registration procedure relied on vertical and axial 2D registration in two steps, which may have introduced additional uncertainty. Thus, future studies should validate the registration procedure developed in this thesis against 3D registration using e.g. AVIZO[®]. Only rotation and translation of the moving subvolume should be permitted. The 3D image could then be segmented into glass, voids, and solid salt and the volume fractions could be compared to the results obtained from 2D registration. Further, the validated registered imaging data could be used to analyse the presence of liquid films or thin layers of salt or brine-crystal phase during evaporation. This could improve understanding of how salt crystals grow into a void space that was not occupied with liquid before. Since the thin layers were in the order of the image resolution in this thesis ($4 \mu\text{m}^3$ per voxel), time-lapse μ XRCT measurements at higher resolution (e.g., $2 \mu\text{m}^3$ per voxel) may provide more insight in future evaporation experiments using sintered glass columns.

The segmentation of the μ XRCT imaging data of the dry separated crusts into void, salt, and sand provided plausible results and revealed the deformation of the sand. The use of sintered glass samples allowed to avoid deformation. Again, it was possible to separate the precipitated salt phase from the glass phase in the absence of the brine phase (i.e. a dry crust). However, it was not possible to segment the μ XRCT data into the four phases void, brine, salt, and sand with the used approaches. The reason for this is most likely related to the low contrast between the brine and the solid salt phase. Thus, future experiments should include strategies to enhance the contrast, which could be done by doping the liquid brine with dissolved components of higher (or lower) X-ray attenuation than the precipitated salt. Here, it is necessary that the added component does not alter the precipitation process, which should be investigated in pre-experiments. Another possibility to enhance the contrast between brine and solid salt may be the use of smaller samples. This would result in less inherent noise, since the X-ray beam would not have to pass the "thick" sample (diameter 30 mm) that was used

in this thesis. Additionally, the observation of the evaporation process over the entire cross section of the smaller sample would lead to a more reliable comparison of NMR and μ XRCT data due to the matched FOVs. However, as mentioned above, wall effects during evaporation may play an important role for smaller samples.

In this thesis, the deformation of the porous sand matrix during salt precipitation was observed using μ XRCT imaging data. NMR measurements on the deformed samples suggest that the deformed region was dry, which means that that image segmentation using the approaches presented in this thesis most likely provides accurate results. The μ XRCT imaging data showed that sand particles were dislocated and that gaps were formed near the surface of the samples. Tracking the movement of the particles may provide insights on the mechanical properties of the precipitating salt crystals such as stress or the crystallization pressure. The crystallization pressure of MgSO_4 has been determined in limestone on the REV-scale (*Espinosa-Marzal and Scherer, 2013*). However, this has not yet been investigated on the pore-scale and in the context of deformation of unconsolidated sand.

The results of the evaporation experiments performed in this thesis can obviously also be used to improve and validate REV-scale models that describe evaporation and associated salt precipitation (*Jambhekar et al., 2015; Mejri et al., 2020*). NaCl is known to form an efflorescent layer on top of the porous medium, which is challenging to include in numerical REV-scale simulations, since a new efflorescent porous structure is formed. Thus, the experimental results on the evaporation and subflorescent crust formation of MgSO_4 solution may provide a more suitable starting point to validate REV-scale evaporation models. The modelling of the presented experiments with unconsolidated sand is hampered by the need to consider the deformation of the subflorescent MgSO_4 crust. However, deformation did not occur in the evaporation experiments with the porous sintered glass samples, and therefore these experiments form an excellent basis for model validation. In particular, reproducing the water content profiles using REV-scale models may support the explanations provided in this thesis on the evolution of the evaporation front. Additionally, the amount and the location of the precipitated salt obtained from REV-scale modelling and experimental results in this thesis may be compared. In this context, the initial salt precipitation based on equilibrium chemistry may be predicted by REV-scale modelling and may be compared to the experimental results in this thesis, which may help to better understand the importance of nucleation, crystal growth during liquid supply, and the downward movement of the evaporation front.

Simulations that include reactive species transport at the pore-scale (e.g., phase field models (*von Wolff et al., 2021*)) may also provide insights on how the void, liquid, and solid fractions evolve before and during precipitation. The results provided in this thesis could be used to validate phase field models that describe the evaporation and precipitation process at the pore-scale. In the case of subflorescent salt precipitation, the viscosity of the supersaturated

MgSO₄ solution significantly affects liquid transport and thus evaporation and crust formation (*Espinosa-Marzal and Scherer, 2010, 2013*). Thus, it is important to understand how the liquid will distribute in the pore space during evaporation, which was monitored at discrete time steps in sintered glass samples in the thesis. Modelling the dynamic process on the pore-scale using validated models with a focus on the change of viscosity and salt accumulation may allow to better understand the delayed start of the precipitation in sintered glass. Furthermore, the impact of changing surface properties (i.e., roughness, charge, geometry) of the porous medium could be studied using phase field models at the pore-scale to predict evaporation and/or salt precipitation. The findings could then be used to design future evaporation experiment using sintered quartz glass or other rigid porous media.

In addition to the suggested improvements of the experiments presented in this thesis, additional experimental investigations focused on salt crust formation should be performed to obtain further insights on the precipitation of efflorescent and subflorescent salt crusts. For example, *Rad and Shokri (2014)* found that efflorescent crusts formed earlier on glass beads than on sand, while in this thesis it was found that subflorescent MgSO₄ crusts developed later in sintered glass than in sand. As discussed before, this may be attributed to the smoother surface properties of the sintered glass grains compared to non-sintered glass beads and to the different type of salt used in the experiments. In a first step, it is thus of interest to investigate if the formation of efflorescent NaCl crust on sintered glass would be delayed compared to the crust formation on quartz sand. If the efflorescent crust formation is similar for both porous media, this would suggest that the surface properties of the porous medium are less important for efflorescent NaCl precipitation than for subflorescent MgSO₄ precipitation.

In general, the evaporation of saline solutions from porous media occurs in a wide range of soil and engineering applications, some of which also involve consolidated porous media. Therefore, it is important to study the precipitation of different salt types in rigid porous media, as was done for MgSO₄ in this thesis. In the case of Na₂SO₄ precipitation, it is not entirely clear under which experimental conditions (i.e., evaporation rate and properties of the porous medium) an efflorescent or subflorescent crust is formed (*Espinosa-Marzal and Scherer, 2010, 2013*). Since the subflorescent precipitation of this salt is known to have a highly destructive impact on porous construction materials during multiple cycles of drying and rewetting, it is of interest to better understand the factors that promote subflorescence or efflorescence for this salt type. As MgSO₄ is known to precipitate subflorescently and since the same anion (SO₄²⁻) is present, the comparison of the crust formation of both salt solutions at different evaporation rates seems to be a good start to investigate the characteristics of efflorescent and subflorescent precipitation. In addition, the evaporation of NaCl solution at the same conditions could serve as a reference for efflorescent crust formation. The comparison between the three types of salt could shed light on what determines subflorescent or efflorescent precipitation of Na₂SO₄.

In another type of experiment with a continuous supply of liquid during evaporation (i.e., so-called wicking experiments), the accumulation of sodium ions during evaporation was monitored using magnetic resonance imaging (MRI) (*Perelman et al.*, 2020). It was shown that plumes of liquid with high sodium content moved downwards against the upward flux due to evaporation. This was attributed to the density difference of the (lighter) supply liquid and the (denser) liquid at the surface that contained more dissolved ions. It is anticipated that salt crust formation will be significantly delayed due to this downward redistribution of solutes. It has not yet been experimentally investigated if such downward redistribution also occurs during the evaporation from porous samples without constant liquid supply. Additionally, it is not clear if other salt types (e.g., MgSO_4 or Na_2SO_4) also show such downward redistribution. In the case of MgSO_4 , the high viscosity of the saturated solution may decrease such downward movement of denser solution. This suggests that crust formation from wicking experiments will be different than that of common evaporation experiments from packed columns without liquid supply, but this needs to be confirmed by additional experiments.

In this thesis, evaporation and salt precipitation were investigated for homogeneous porous media. However, most natural and man-made porous media are heterogeneous so that understanding the impact of such porous media on evaporation and salt precipitation is necessary. Evaporation from heterogeneous porous media was investigated for efflorescent NaCl precipitation from solutions initially below the solubility limit (*Bergstad et al.*, 2017). It was found that crusts formed earlier on the coarse region of sand columns with a sharp vertical textural interface with a fine region, which was related to a lower amount of active pores and the associated earlier supersaturation during evaporation. Numerical simulations with REV-scale models have predicted salt precipitation at the vertical interface between the coarse and fine sand region (*Mejri et al.*, 2017). However, this has not yet been validated experimentally. It should be noted that NaCl is known to preferably precipitate on top of the porous medium (*Nachshon et al.*, 2011a; *Veran-Tissoires and Prat*, 2014; *Eloukabi et al.*, 2013). Therefore, it is not clear if precipitation at the vertical textural interface occurs. Thus, it is of interest to monitor the precipitation of NaCl during evaporation of solutions from heterogeneous porous media with a sharp vertical interface in texture. Subflorescent salt crust formation in heterogeneous porous media is also a relevant research topic for protection of cultural heritage and a range of civil engineering applications such as building materials preservation. However, it has not yet been investigated whether subflorescent precipitation would preferably form in fine or coarse regions of a heterogeneous medium. Thus, additional evaporation experiments should be made to clarify whether preferential subflorescent precipitation occurs. The approach of *Bergstad et al.* (2017) using a sample with a sharp textural vertical interface can be used for this. The use of μXRCT measurements of the dried samples could show, whether precipitation occurred at the vertical interface. Furthermore, heterogeneous sintered glass cores could be used to avoid the

deformation from subflorescent salt precipitation in unconsolidated sand. This could provide a better understanding of subflorescent salt crust formation in heterogeneous porous media and may allow the design of materials with heterogeneous porous subdomains that promote or diminish subflorescent salt precipitation.

References

- An, N., C.-S. Tang, S.-K. Xu, X.-P. Gong, B. Shi, and H. I. Inyang (2018), Effects of soil characteristics on moisture evaporation, *Engineering Geology*, 239, 126–135, doi:10.1016/j.enggeo.2018.03.028.
- Artiola, J., J. Walworth, S. Musil, and M. Crimmins (2019), Soil and land pollution, in *Environmental and Pollution Science*, edited by M. L. Brusseau, I. L. Pepper, and C. P. Gerba, 3 ed., book section 14, pp. 219 – 235, Academic Press, London, United Kingdom, doi:10.1016/B978-0-12-814719-1.00014-8.
- Assouline, S., S. W. Tyler, J. S. Selker, I. Lunati, C. W. Higgins, and M. B. Parlange (2013), Evaporation from a shallow water table: Diurnal dynamics of water and heat at the surface of drying sand, *Water Resources Research*, 49(7), 4022–4034, doi:10.1002/wrcr.20293.
- Balboni, E., R. M. Espinosa-Marzal, E. Doehne, and G. W. Scherer (2011), Can drying and re-wetting of magnesium sulfate salts lead to damage of stone?, *Environmental Earth Sciences*, 63(7-8), 1463–1473, doi:10.1007/s12665-010-0774-1.
- Ball, B., and P. Schjønning (2002), Air permeability, in *Methods in Soil Analysis: Part 4 Physical Methods*, edited by J. H. Dane and G. C. Topp, SSSA Book Series, pp. 1141–1158, Soil Science Society of America, Madison, Wisconsin, United States, doi:10.2136/sssabookser5.4.frontmatter.
- Baur, W. (1964), On the crystal chemistry of salt hydrates. II. A neutron diffraction study of $\text{MgSO}_4 \cdot 4\text{H}_2\text{O}$, *Acta Crystallographica*, 17(7), 863–869.
- Bear, J. (1972), *Dynamics of fluids in porous media*, American Elsevier Publishing Company, New York, United States.
- Beavers, G. S., and D. D. Joseph (1967), Boundary conditions at a naturally permeable wall, *Journal of Fluid Mechanics*, 30, 197–207, doi:10.1017/s0022112067001375.
- Bechtold, M., S. Haber-Pohlmeier, J. Vanderborght, A. Pohlmeier, T. P. A. Ferre, and H. Vereecken (2011), Near-surface solute redistribution during evaporation, *Geophysical Research Letters*, 38, 6, doi:10.1029/2011gl048147.
- Bechtold, M., J. Vanderborght, L. Weihermuller, M. Herbst, T. Gunther, O. Ippisch, R. Kasteel, and H. Vereecken (2012), Upward transport in a three-dimensional heterogeneous laboratory soil under evaporation conditions, *Vadose Zone Journal*, 11(2), 21, doi:10.2136/vzj2011.0066.
- Bergstad, M., D. Or, P. J. Withers, and N. Shokri (2017), The influence of NaCl concentration on salt precipitation in heterogeneous porous media, *Water Resources Research*, 53(2), 1702–1712, doi:10.1002/2016wr020060.
- Bertolin, C. (2019), Preservation of cultural heritage and resources threatened by climate change, *Geosciences*, 9(6), 250, doi:10.3390/geosciences9060250.

- Blumich, B., S. HaberPohlmeier, and W. Zia (2014), *Compact NMR*, Compact NMR, 1-276 pp., Walter De Gruyter GmbH, Berlin, Germany.
- Bortolini, L., C. Maucieri, and M. Borin (2018), A tool for the evaluation of irrigation water quality in the arid and semi-arid regions, *Agronomy*, 8(2), 23, doi:10.3390/agronomy8020023.
- Butler, D. L. (2008), Surface roughness measurement, in *Encyclopedia of Microfluidics and Nanofluidics*, edited by D. Li, pp. 1945–1949, Springer US, Boston, Massachusetts, United States, doi:10.1007/978-0-387-48998-8_1506.
- Böcker, N., M. Grahl, A. Tota, P. Häussinger, P. Leitgeb, and B. Schmücker (2013), *Nitrogen*, pp. 1–27, American Cancer Society, New York, USA, doi:10.1002/14356007.a17_457.pub2.
- Carman, P. C. (1937), Fluid flow through granular beds, *Chemical Engineering Research and Design*, 75, S32–S48, doi:10.1016/S0263-8762(97)80003-2.
- Chan, T. F., and L. A. Vese (2001), Active contours without edges, *IEEE Transactions on Image Processing*, 10(2), 266–277, doi:10.1109/83.902291.
- Chaves, M. M., J. Flexas, and C. Pinheiro (2009), Photosynthesis under drought and salt stress: Regulation mechanisms from whole plant to cell, *Annals of Botany*, 103(4), 551–560, doi:10.1093/aob/mcn125.
- Chilton, T. H., and A. P. Colburn (1931), Pressure drop in packed tubes, *Industrial and Engineering Chemistry*, 23, 913–919, doi:10.1021/ie50260a016.
- Clarke, E. C. W. (1985), Evaluation of the thermodynamic functions for aqueous sodium chloride from equilibrium and calorimetric measurements below 154°C, *Journal of Physical and Chemical Reference Data*, 14(2), 489–610, doi:10.1063/1.555730.
- Class, H. (2001), Theorie und numerische Modellierung nichtisothermer Mehrphasenprozesse in NAPL-kontaminierten porösen Medien, Dissertation, University of Stuttgart, Stuttgart, Germany, doi:10.18419/opus-223.
- Cnudde, V., and M. N. Boone (2013), High-resolution X-ray computed tomography in geosciences: A review of the current technology and applications, *Earth-Science Reviews*, 123, 1–17, doi:10.1016/j.earscirev.2013.04.003.
- Daliakopoulos, I. N., I. K. Tsanis, A. Koutroulis, N. N. Kourgialas, A. E. Varouchakis, G. P. Karatzas, and C. J. Ritsema (2016), The threat of soil salinity: A European scale review, *Science of The Total Environment*, 573, 727–739, doi:10.1016/j.scitotenv.2016.08.177.
- Darcy, H. P. G. (1856), *Les Fontaines publiques de la ville de Dijon. Exposition et application des principes à suivre et des formules à employer dans les questions de distribution d'eau*, Victor Dalmont, Paris, France.
- Davis, J. C. (1986), *Statistics and data analysis in geology*, 2 ed., 74-77 pp., John Wiley & Sons, New York, United States.
- Dowuona, G., A. Mermut, and H. Krouse (1992), Isotopic composition of salt crusts in Saskatchewan, Canada, *Chemical Geology: Isotope Geoscience Section*, 94(3), 205–213.
- Driessen, P. M., and R. Schoorl (1973), Mineralogy and morphology of salt efflorescences on saline

- soils in the Great Konya Basin, Turkey, *Journal of Soil Science*, *24*(4), 436–442, doi:10.1111/j.1365-2389.1973.tb02310.x.
- Duschl, M., A. Pohlmeier, T. I. Brox, P. Galvosas, and H. Vereecken (2016), Effect of magnetic pore surface coating on the NMR relaxation and diffusion signal in quartz sand, *Magnetic Resonance in Chemistry*, *54*(12), 975–984, doi:10.1002/mrc.4486.
- Eggenweiler, E., and I. Rybak (2021), Effective coupling conditions for arbitrary flows in Stokes-Darcy systems, *Multiscale Modeling & Simulation*, *19*(2), 731–757, doi:10.1137/20m1346638.
- Eloukabi, H., N. Sghaier, S. Ben Nasrallah, and M. Prat (2013), Experimental study of the effect of sodium chloride on drying of porous media: The crusty-patchy efflorescence transition, *International Journal of Heat and Mass Transfer*, *56*(1-2), 80–93, doi:10.1016/j.ijheatmasstransfer.2012.09.045.
- Espinosa-Marzal, R. M., and G. W. Scherer (2010), Advances in understanding damage by salt crystallization, *Accounts of Chemical Research*, *43*(6), 897–905, doi:10.1021/ar9002224.
- Espinosa-Marzal, R. M., and G. W. Scherer (2013), Impact of in-pore salt crystallization on transport properties, *Environmental Earth Sciences*, *69*(8), 2657–2669, doi:10.1007/s12665-012-2087-z.
- Espinosa-Marzal, R. M., L. Franke, and G. Deckelmann (2008), Predicting efflorescence and subflorescences of salts, in *8th Symposium on Materials Issues in Art and Archaeology held at the 2007 MRS Fall Meeting, Materials Research Society Symposium Proceedings*, vol. 1047, p. 105.
- Faure, P., and P. Coussot (2010), Drying of a model soil, *Physical Review E*, *82*(3), 036,303.
- Fetzer, T., J. Vanderborght, K. Mosthaf, K. M. Smits, and R. Helmig (2017), Heat and water transport in soils and across the soil-atmosphere interface: 2. Numerical analysis, *Water Resources Research*, *53*(2), 1080–1100, doi:10.1002/2016wr019983.
- Flatt, R. J., and G. W. Scherer (2002), Hydration and crystallization pressure of sodium sulfate: A critical review, in *Materials Issues in Art and Archaeology VI, Materials Research Society Symposium Proceedings*, vol. 712, edited by P. B. Vandiver, M. Goodway, and J. L. Mass, pp. 29–34, Materials Research Society, Boston, Massachusetts, USA.
- Flatt, R. J., F. Caruso, A. M. A. Sanchez, and G. W. Scherer (2014), Chemomechanics of salt damage in stone, *Nature Communications*, *5*, 5, doi:10.1038/ncomms5823.
- Forchheimer, P. (1901), Water movement through the ground, *Zeitschrift des Vereines Deutscher Ingenieure*, *45*, 1781–1788.
- Fukushima, E., and B. Roeder, Stephen (1981), *Experimental pulse NMR - a nuts and bolts approach*, 1st ed., 556 pp., Perseus Publishing, Boca Raton, Massachusetts, USA, doi:10.1201/9780429493867.
- Ghezzehei, T. A. (2012), Linking sub-pore scale heterogeneity of biological and geochemical deposits with changes in permeability, *Advances in Water Resources*, *39*, 1–6, doi:10.1016/j.advwatres.2011.12.015.
- Glover, P. W. J., and E. Walker (2009), Grain-size to effective pore-size transformation derived from electrokinetic theory, *Geophysics*, *74*(1), E17–E29, doi:10.1190/1.3033217.
- Green, D., and R. Perry (2008a), *Agglomeration rate processes and mechanics*, pp. 21–83, 8 ed., McGraw-Hill Education, New York, doi:10.1036/0071511431.

- Green, D., and R. Perry (2008b), *Membrane separation processes*, pp. 20–55, 8 ed., McGraw-Hill Education, New York, USA, doi:10.1036/0071511431.
- Green, D., and R. Perry (2008c), *Liquid-solid operations and equipment*, pp. 18–42, 8 ed., McGraw-Hill Education, New York, USA, doi:10.1036/0071511431.
- Grünberger, O., P. Macaigne, J.-L. Michelot, C. Hartmann, and S. Sukchan (2008), Salt crust development in paddy fields owing to soil evaporation and drainage: Contribution of chloride and deuterium profile analysis, *Journal of Hydrology*, *348*(1), 110–123, doi:10.1016/j.jhydrol.2007.09.039.
- Guendouzi, M. E., A. Mounir, and A. Dinane (2003), Water activity, osmotic and activity coefficients of aqueous solutions of Li_2SO_4 , Na_2SO_4 , K_2SO_4 , $(\text{NH}_4)_2\text{SO}_4$, MgSO_4 , MnSO_4 , NiSO_4 , CuSO_4 , and ZnSO_4 at $T=298.15\text{K}$, *The Journal of Chemical Thermodynamics*, *35*(2), 209 – 220, doi: [https://doi.org/10.1016/S0021-9614\(02\)00315-4](https://doi.org/10.1016/S0021-9614(02)00315-4).
- Gueven, I., S. Frijters, J. Harting, S. Luding, and H. Steeb (2017), Hydraulic properties of porous sintered glass bead systems, *Granular Matter*, *19*(2), 28, doi:10.1007/s10035-017-0705-x.
- Gupta, R. K., I. P. Abrol, C. W. Finkl, M. B. Kirkham, M. C. Arbestain, F. Macías, W. Chesworth, J. J. Germida, R. H. Loeppert, M. G. Cook, G. O. Schwab, K. Konstankiewicz, J. Pytka, J. J. Oertli, A. Singer, W. J. Edmonds, Y. Feng, S. B. Feldman, C. Shang, L. W. Zelazny, P. W. Ford, B. E. Clothier, and M. A. Arshad (2008), *Soil salinity and salinization*, pp. 699–704, Springer Netherlands, Dordrecht, The Netherlands, doi:10.1007/978-1-4020-3995-9_552.
- Hahn, E. L. (1950), Spin echoes, *Physical Review*, *80*(4), 580, doi:10.1103/PhysRev.80.580.
- Hall, L. D., M. H. Gao Amin, E. Dougherty, M. Sanda, J. Votrubova, K. S. Richards, R. J. Chorley, and M. Cislerova (1997), MR properties of water in saturated soils and resulting loss of MRI signal in water content detection at 2 Tesla, *Geoderma*, *80*(3), 431–448, doi:10.1016/S0016-7061(97)00065-7.
- Helmig, R. (1997), *Multiphase flow and transport processes in the subsurface: A contribution to the modeling of hydrosystems*, Springer-Verlag, Heidelberg, Germany.
- Hillel, D. (2003), Water flow in saturated soil, in *Introduction to Environmental Soil Physics*, edited by D. Hillel, chap. 7, pp. 127–148, Academic Press, San Diego, California, doi:10.1016/B978-012348655-4/50008-3.
- Hommel, J., E. Coltman, and H. Class (2018), Porosity-permeability relations for evolving pore space: A review with a focus on (bio-)geochemically altered porous media, *Transport in Porous Media*, *124*(2), 589–629, doi:10.1007/s11242-018-1086-2.
- Icekson-Tal, N., O. Avraham, J. Sack, and H. Cikurel (2003), Water reuse in Israel - the Dan Region Project: Evaluation of water quality and reliability of plant's operation, *Water Supply*, *3*(4), 231–237, doi:10.2166/ws.2003.0067.
- Jambhekar, V. A. (2017), Numerical modeling and analysis of evaporative salinization in a coupled free-flow porous-media system, Dissertation, University of Stuttgart, Stuttgart, Germany, doi:10.18419/opus-8979.
- Jambhekar, V. A., R. Helmig, N. Schroder, and N. Shokri (2015), Free-flow-porous-media coupling for evaporation-driven transport and precipitation of salt in soil, *Transport in Porous Media*, *110*(2), 251–280, doi:10.1007/s11242-015-0516-7.

- Jambhekar, V. A., E. Mejri, N. Schroder, R. Helmig, and N. Shokri (2016), Kinetic approach to model reactive transport and mixed salt precipitation in a coupled free-flow-porous-media system, *Transport in Porous Media*, 114(2), 341–369, doi:10.1007/s11242-016-0665-3.
- Jelinkova, V., M. Snehota, A. Pohlmeier, D. van Dusschoten, and M. Cislserova (2011), Effects of entrapped residual air bubbles on tracer transport in heterogeneous soil: Magnetic resonance imaging study, *Organic Geochemistry*, 42(8), 991–998, doi:10.1016/j.orggeochem.2011.03.020.
- Kasenow, M. (2002), *Determination of hydraulic conductivity from grain size analysis*, 18 pp., Water Resources Publications, LLC, Denver, Colorado, USA.
- Kozeny, J. (1927), Über kapillare Leitung des Wassers im Boden, *Royal Academy of Science, Vienna, Proc. Class I*, 136, 271–306.
- Lehmann, P., and D. Or (2009), Evaporation and capillary coupling across vertical textural contrasts in porous media, *Physical Review E*, 80(4), 046,318, doi:10.1103/PhysRevE.80.046318.
- Lehmann, P., S. Assouline, and D. Or (2008), Characteristic lengths affecting evaporative drying of porous media, *Physical Review E*, 77(5), 16, doi:10.1103/PhysRevE.77.056309.
- Liao, R. K., H. L. Yu, H. Lin, and P. L. Yang (2019), A quantitative study on three-dimensional pore parameters and physical properties of sodic soils restored by FGD gypsum and leaching water, *Journal of Environmental Management*, 248, 10, doi:10.1016/j.jenvman.2019.109303.
- Licsandru, G., C. Noiriél, P. Duru, S. Geoffroy, A. Abou Chakra, and M. Prat (2019), Dissolution-precipitation-driven upward migration of a salt crust, *Physical Review E*, 100(3), 9, doi:10.1103/PhysRevE.100.032802.
- Lide, D. (Ed.) (2004), *Physical constants of inorganic compounds*, book section 4, pp. 4–68, 84 ed., CRC Press/Taylor & Francis, Boca Raton, Florida, USA.
- MacQuarrie, K. T. B., and K. U. Mayer (2005), Reactive transport modeling in fractured rock: A state-of-the-science review, *Earth-Science Reviews*, 72(3), 189–227, doi:10.1016/j.earscirev.2005.07.003.
- MacQueen, J. (1967), Some methods for classification and analysis of multivariate observations, in *Proceedings of the fifth Berkeley symposium on mathematical statistics and probability*, vol. 1, edited by L. Le Cam and J. Neyman, pp. 281–297, University California Press, California, USA.
- Mattes, D., D. Haynor, H. Vesselle, T. Lewellyn, and W. Eubank (2001), *Nonrigid multimodality image registration*, *Medical Imaging 2001*, vol. 4322, SPIE, San Diego, California, USA, doi:10.1117/12.431046.
- Mattes, D., D. R. Haynor, H. Vesselle, T. K. Lewellen, and W. Eubank (2003), PET-CT image registration in the chest using free-form deformations, *IEEE Transactions on Medical Imaging*, 22(1), 120–128, doi:10.1109/tmi.2003.809072.
- Mayer, K. U., E. O. Frind, and D. W. Blowes (2002), Multicomponent reactive transport modeling in variably saturated porous media using a generalized formulation for kinetically controlled reactions, *Water Resources Research*, 38(9), doi:10.1029/2001wr000862.
- McRobbie, D. W., E. A. Moore, and M. J. Graves (2017), *MRI from picture to proton*, 3rd edition, 1-383 pp., Cambridge Univ Press, Cambridge, United Kingdom, doi:10.1017/9781107706958.

- Mejri, E., R. Bouhlila, and R. Helmig (2017), Heterogeneity effects on evaporation-induced halite and gypsum co-precipitation in porous media, *Transport in Porous Media*, 118(1), 39–64, doi:10.1007/s11242-017-0846-8.
- Mejri, E., R. Helmig, and R. Bouhlila (2020), Modeling of evaporation-driven multiple salt precipitation in porous media with a real field application, *Geosciences*, 10(10), 19, doi:10.3390/geosciences10100395.
- Merz, S., A. Pohlmeier, J. Vanderborght, D. van Dusschoten, and H. Vereecken (2014), Moisture profiles of the upper soil layer during evaporation monitored by NMR, *Water Resources Research*, 50(6), 5184–5195, doi:10.1002/2013WR014809.
- More, J. J., and D. C. Sorensen (1983), Computing a trust region step, *Siam Journal on Scientific and Statistical Computing*, 4(3), 553–572, doi:10.1137/0904038.
- Mualem, Y. (1976), Hysteretical models for prediction of the hydraulic conductivity of unsaturated porous media, *Water Resources Research*, 12(6), 1248–1254, doi:10.1029/WR012i006p01248.
- Müller, E. (1939), Magnesium - Teil B, Die Verbindungen des Magnesium, in *Gmelins Handbuch der anorganischen Chemie*, edited by E. Pietsch, 8. Auflage, pp. 243–249, Deutsche Chemische Gesellschaft. Verlag Chemie, GmbH.
- Nachshon, U., and N. Weisbrod (2015), Beyond the salt crust: On combined evaporation and sub-florescent salt precipitation in porous media, *Transport in Porous Media*, 110(2), 295–310, doi:10.1007/s11242-015-0514-9.
- Nachshon, U., E. Shahraeeni, D. Or, M. Dragila, and N. Weisbrod (2011a), Infrared thermography of evaporative fluxes and dynamics of salt deposition on heterogeneous porous surfaces, *Water Resources Research*, 47, 16, doi:10.1029/2011wr010776.
- Nachshon, U., N. Weisbrod, M. I. Dragila, and A. Grader (2011b), Combined evaporation and salt precipitation in homogeneous and heterogeneous porous media, *Water Resources Research*, 47, 16, doi:10.1029/2010wr009677.
- Nachshon, U., N. Weisbrod, R. Katzir, and A. Nasser (2018), NaCl crust architecture and its impact on evaporation: Three-dimensional insights, *Geophysical Research Letters*, 45(12), 6100–6108, doi:10.1029/2018gl078363.
- Nield, J. M., C. M. Neuman, P. O'Brien, R. G. Bryant, and G. F. S. Wiggs (2016), Evaporative sodium salt crust development and its wind tunnel derived transport dynamics under variable climatic conditions, *Aeolian Research*, 23, 51–62, doi:10.1016/j.aeolia.2016.09.003.
- Nkonya, E., and W. Anderson (2015), Exploiting provisions of land economic productivity without degrading its natural capital, *Journal of Arid Environments*, 112, 33–43, doi:10.1016/j.jaridenv.2014.05.012.
- Or, D., P. Lehmann, E. Shahraeeni, and N. Shokri (2013), Advances in soil evaporation physics – a review, *Vadose Zone Journal*, 12(4), 16, doi:10.2136/vzj2012.0163.
- Oster, J. D. (1994), Irrigation with poor quality water, *Agricultural Water Management*, 25(3), 271–297, doi:10.1016/0378-3774(94)90064-7.

- Otsu, N. (1979), Threshold selection method from gray-level histograms, *IEEE Transactions on Systems Man and Cybernetics*, 9(1), 62–66, doi:10.1109/tsmc.1979.4310076.
- Perelman, A., N. Lazarovitch, J. Vanderborght, and A. Pohlmeier (2020), Quantitative imaging of sodium concentrations in soil-root systems using magnetic resonance imaging (MRI), *Plant and Soil*, 454(1), 171–185.
- [dataset] Piotrowski, J., and J. A. Huisman (2021), Sample, evaporation, and crust data of NaCl, MgSO₄, and Na₂SO₄ solutions from F32 quartz sand, doi:10.18419/darus-1642.
- Pitman, M. G., and A. Läuchli (2002), Global impact of salinity and agricultural ecosystems, in *Salinity: Environment - Plants - Molecules*, edited by A. Läuchli and U. Lüttge, book section 1, pp. 3–20, Springer Netherlands, Dordrecht, The Netherlands, doi:10.1007/0-306-48155-3_1.
- Plessen, H. v. (2000), *Sodium sulfates*, pp. 383–385, American Cancer Society, New York, USA, doi:10.1002/14356007.a24_355.
- Pohlmeier, A., S. Haber-Pohlmeier, and S. Stapf (2009), A fast field cycling nuclear magnetic resonance relaxometry study of natural soils, *Vadose Zone Journal*, 8(3), 735–742, doi:10.2136/vzj2008.0030.
- Rad, M. N., and N. Shokri (2012), Nonlinear effects of salt concentrations on evaporation from porous media, *Geophysical Research Letters*, 39, doi:10.1029/2011gl050763.
- Rad, M. N., and N. Shokri (2014), Effects of grain angularity on NaCl precipitation in porous media during evaporation, *Water Resources Research*, 50(11), 9020–9030, doi:10.1002/2014wr016125.
- Rad, M. N., N. Shokri, A. Keshmiri, and P. J. Withers (2015), Effects of grain and pore size on salt precipitation during evaporation from porous media, *Transport in Porous Media*, 110(2), 281–294, doi:10.1007/s11242-015-0515-8.
- Reynolds, O. (1894), II. On the dynamical theory of incompressible viscous fluids and the determination of the criterion, *Proceedings of the Royal Society of London*, 56(336-339), 40–45, doi:doi:10.1098/rspl.1894.0075.
- Reynolds, W. D., and D. E. Elrick (2002a), Constant head soil core (tank) method, in *Methods in Soil Analysis: Part 4 Physical Methods*, edited by J. H. Dane and G. C. Topp, SSSA Book Series, pp. 804–808, Soil Science Society of America, Madison, Wisconsin, United States, doi:10.2136/sssabookser5.4.frontmatter.
- Reynolds, W. D., and D. E. Elrick (2002b), Falling head soil core (tank) method, in *Methods in Soil Analysis: Part 4 Physical Methods*, edited by J. H. Dane and G. C. Topp, SSSA Book Series, pp. 809–812, Soil Science Society of America, Madison, Wisconsin, United States, doi:10.2136/sssabookser5.4.frontmatter.
- Rodriguez-Navarro, C., and E. Doehne (1999), Salt weathering: Influence of evaporation rate, supersaturation and crystallization pattern, *Earth Surface Processes and Landforms*, 24(3), 191–209, doi:10.1002/(sici)1096-9837(199903)24:3<191::Aid-esp942>3.0.Co;2-g.
- Rodriguez-Navarro, C., E. Doehne, and E. Sebastian (2000), How does sodium sulfate crystallize? Implications for the decay and testing of building materials, *Cement and Concrete Research*, 30(10), 1527–1534, doi:10.1016/s0008-8846(00)00381-1.

- Ruf, M., and H. Steeb (2020), An open, modular, and flexible micro X-ray computed tomography system for research, *Review of Scientific Instruments*, 91(11), 113,102, doi:10.1063/5.0019541.
- [dataset] Ruf, M., D. Lee, J. Piotrowski, J. A. Huisman, and H. Steeb (2021a), micro-XRCT and segmented data sets of subflorescent salt crusts from evaporation of MgSO₄ solution with 0.32 mol/L initial concentration, doi:10.18419/darus-2002.
- [dataset] Ruf, M., D. Lee, J. Piotrowski, J. A. Huisman, and H. Steeb (2021b), micro-XRCT and segmented data sets of subflorescent salt crusts from evaporation of MgSO₄ solution with 0.64 mol/L initial concentration, doi:10.18419/darus-1848.
- [dataset] Ruf, M., D. Lee, J. Piotrowski, J. A. Huisman, and H. Steeb (2021c), micro-XRCT and segmented data sets of subflorescent salt crusts from evaporation of MgSO₄ solution with 0.96 mol/L initial concentration, doi:10.18419/darus-2003.
- Rumble, J. R. (Ed.) (2019), *Concentrative properties of aqueous solutions: Density, refractive index, freezing point depression, and viscosity*, book section 5, 100 ed., CRC Press/Taylor & Francis, Boca Raton, Florida, USA, (Internet Version 2019).
- Rust, A. C., and K. V. Cashman (2004), Permeability of vesicular silicic magma: Inertial and hysteresis effects, *Earth and Planetary Science Letters*, 228(1-2), 93–107, doi:10.1016/j.epsl.2004.09.025.
- Scherer, G. W. (1990), Theory of drying, *Journal of the American Ceramic Society*, 73(1), 3–14, doi:10.1111/j.1151-2916.1990.tb05082.x.
- Scherer, G. W. (2004), Stress from crystallization of salt, *Cement and Concrete Research*, 34(9), 1613–1624, doi:10.1016/j.cemconres.2003.12.034.
- Schlichting, H., and K. Gersten (2017), *Boundary-layer theory*, chap. 1, p. 12, 9 ed., Springer-Verlag, Heidelberg, Germany, doi:10.1007/978-3-662-52919-5.
- Schlüter, S., A. Sheppard, K. Brown, and D. Wildenschild (2014), Image processing of multiphase images obtained via X-ray microtomography: A review, *Water Resources Research*, 50(4), 3615–3639, doi:10.1002/2014WR015256.
- Schofield, R. V., and M. J. Kirkby (2003), Application of salinization indicators and initial development of potential global soil salinization scenario under climatic change, *Global Biogeochemical Cycles*, 17(3), doi:10.1029/2002GB001935.
- Shahraeeni, E., and D. Or (2012a), Pore scale mechanisms for enhanced vapor transport through partially saturated porous media, *Water Resources Research*, 48(5), doi:10.1029/2011WR011036.
- Shahraeeni, E., and D. Or (2012b), Pore-scale evaporation-condensation dynamics resolved by synchrotron X-ray tomography, *Physical Review E*, 85(1), doi:10.1103/PhysRevE.85.016317.
- Shokri, N., and D. Or (2011), What determines drying rates at the onset of diffusion controlled stage-2 evaporation from porous media?, *Water Resources Research*, 47(9), doi:10.1029/2010WR010284.
- Shokri, N., P. Lehmann, P. Vontobel, and D. Or (2008), Drying front and water content dynamics during evaporation from sand delineated by neutron radiography, *Water Resources Research*, 44(6), doi:10.1029/2007WR006385.
- Shokri, N., P. Lehmann, and D. Or (2010), Evaporation from layered porous media, *Journal of Geophysical Research: Solid Earth*, 115(B6), doi:10.1029/2009JB006743.

- Shokri-Kuehni, S. M. S., T. Vetter, C. Webb, and N. Shokri (2017), New insights into saline water evaporation from porous media: Complex interaction between evaporation rates, precipitation, and surface temperature, *Geophysical Research Letters*, *44*(11), 5504–5510, doi:10.1002/2017gl073337.
- Shokri-Kuehni, S. S., B. Raaijmakers, T. Kurz, D. Or, R. Helmig, and N. Shokri (2020), Water table depth and soil salinization: From pore-scale processes to field-scale responses, *Water Resources Research*, *56*(2), e2019WR026,707, doi:10.1029/2019wr026707.
- Smoot, J. P., B. Castens-Seidell, R. W. Renaut, and W. M. Last (1994), *Sedimentary features produced by efflorescent salt crusts, Saline Valley and Death Valley, California*, vol. 50, book section 1, pp. 73 – 90, SEPM Society for Sedimentary Geology, Tulsa, Oklahoma, USA, doi:10.2110/pec.94.50.0073.
- Steiger, M., and S. Asmussen (2008), Crystallization of sodium sulfate phases in porous materials: The phase diagram Na₂SO₄-H₂O and the generation of stress, *Geochimica Et Cosmochimica Acta*, *72*(17), 4291–4306, doi:10.1016/j.gca.2008.05.053, <https://creativecommons.org/licenses/by-nc-nd/3.0/de/>.
- Steiger, M., J. Kiekbusch, and A. Nicolai (2008), An improved model incorporating Pitzer’s equations for calculation of thermodynamic properties of pore solutions implemented into an efficient program code, *Construction and Building Materials*, *22*(8), 1841–1850, doi:10.1016/j.conbuildmat.2007.04.020, <https://creativecommons.org/licenses/by-nc-nd/3.0/de/>.
- Steiger, M., A. E. Charola, and K. Sterflinger (2011a), Weathering and deterioration, in *Stone in Architecture: Properties, Durability*, edited by S. Siegesmund and R. Snethlage, pp. 227–316, Springer-Verlag, Heidelberg, Germany, doi:10.1007/978-3-642-14475-2_4.
- Steiger, M., K. Linnow, D. Ehrhardt, and M. Rohde (2011b), Decomposition reactions of magnesium sulfate hydrates and phase equilibria in the MgSO₄-H₂O and Na⁺-Mg²⁺-Cl-SO₄²⁻-H₂O systems with implications for Mars, *Geochimica Et Cosmochimica Acta*, *75*(12), 3600–3626, doi:10.1016/j.gca.2011.03.038, <https://creativecommons.org/licenses/by-nc-nd/3.0/de/>.
- Styner, M., C. Brechbuhler, G. Szekely, and G. Gerig (2000), Parametric estimate of intensity inhomogeneities applied to MRI, *IEEE Transactions on Medical Imaging*, *19*(3), 153–165, doi:10.1109/42.845174.
- Takeuchi, S., S. Nakashima, and A. Tomiya (2008), Permeability measurements of natural and experimental volcanic materials with a simple permeameter: Toward an understanding of magmatic degassing processes, *Journal of Volcanology and Geothermal Research*, *177*(2), 329–339, doi:10.1016/j.jvolgeores.2008.05.010.
- Thevenaz, P., and M. Unser (2000), Optimization of mutual information for multiresolution image registration, *IEEE Transactions on Image Processing*, *9*(12), 2083–2099, doi:10.1109/83.887976.
- Tsui, N., R. J. Flatt, and G. W. Scherer (2003), Crystallization damage by sodium sulfate, *Journal of Cultural Heritage*, *4*(2), 109–115, doi:10.1016/s1296-2074(03)00022-0.
- Van der Heijden, G., H. Huinink, L. Pel, and K. Kopinga (2009), Non-isothermal drying of fired-clay brick - an NMR study, *Chemical Engineering Science*, *64*(12), 3010–3018.
- van Duijn, C. J., and I. S. Pop (2004), Crystal dissolution and precipitation in porous media: Pore

- scale analysis, *Journal für die reine und angewandte Mathematik*, 2004(577), 171–211, doi:10.1515/crll.2004.2004.577.171.
- Van Genuchten, M. T. (1980), A closed-form equation for predicting the hydraulic conductivity of unsaturated soils, *Soil Science Society of America Journal*, 44(5), 892–898, doi:10.2136/sssaj1980.03615995004400050002x.
- Vanderborght, J., T. Fetzner, K. Mosthaf, K. M. Smits, and R. Helmig (2017), Heat and water transport in soils and across the soil-atmosphere interface: 1. Theory and different model concepts, *Water Resources Research*, 53(2), 1057–1079, doi:10.1002/2016wr019982.
- Veran-Tissoires, S., and M. Prat (2014), Evaporation of a sodium chloride solution from a saturated porous medium with efflorescence formation, *Journal of Fluid Mechanics*, 749, 701–749, doi:10.1017/jfm.2014.247.
- Vereecken, H., P. Burauel, J. Groeneweg, E. Klumpp, W. Mittelstaedt, H. D. Narres, T. Putz, J. van der Kruk, J. Vanderborght, and F. Wendland (2009), Research at the Agrosphere Institute: From the process scale to the catchment scale, *Vadose Zone Journal*, 8(3), 664–669, doi:10.2136/vzj2008.0143.
- Vlassenbroeck, J., M. Dierick, B. Masschaele, V. Cnudde, L. Hoorebeke, and P. Jacobs (2007), Software tools for quantification of X-ray microtomography, *Nuclear Instruments & Methods in Physics Research Section A: Accelerators Spectrometers Detectors and Associated Equipment*, 580(1), 442–445, doi:10.1016/j.nima.2007.05.073.
- von Wolff, L., F. Weinhardt, H. Class, J. Hommel, and C. Rohde (2021), Investigation of crystal growth in enzymatically induced calcite precipitation by micro-fluidic experimental methods and comparison with mathematical modeling, *Transport in Porous Media*, 137(2), 327–343.
- Weingärtner, H., I. Teermann, U. Borchers, P. Balsaa, H. V. Lutze, T. C. Schmidt, E. U. Franck, G. Wiegand, N. Dahmen, G. Schwedt, F. H. Frimmel, and B. C. Gordalla (2016), Water, 1. Properties, analysis, and hydrological cycle, in *Ullmann's Encyclopedia of Industrial Chemistry*, chap. 1, pp. 1–40, American Cancer Society, New York, USA, doi:10.1002/14356007.a28_001.pub3.
- Weisbrod, N., U. Nachshon, M. Dragila, and A. Grader (2014), Micro-CT analysis to explore salt precipitation impact on porous media permeability, in *Transport and Reactivity of Solutions in Confined Hydrosystems*, NATO Science for Peace and Security Series C: Environmental Security, pp. 231–241, Springer Netherlands, Dordrecht, The Netherlands.
- Westphal, G., G. Kristen, W. Wegener, P. Ambatiello, H. Geyer, B. Epron, C. Bonal, G. Steinhauser, and F. Götzfried (2010), Sodium chloride, in *Ullmann's Encyclopedia of Industrial Chemistry*, pp. 320–322, American Cancer Society, New York, USA, doi:10.1002/14356007.a24_317.pub4.
- Whitaker, S. (1986), Flow in porous media I: A theoretical derivation of Darcy's law, *Transport in Porous Media*, 1(1), 3–25, doi:10.1007/BF01036523.
- Wildenschild, D., and A. P. Sheppard (2013), X-ray imaging and analysis techniques for quantifying pore-scale structure and processes in subsurface porous medium systems, *Advances in Water Resources*, 51, 217–246, doi:10.1016/j.advwatres.2012.07.018.

- Withers, P. J., C. Bouman, S. Carmignato, V. Cnudde, D. Grimaldi, C. K. Hagen, E. Maire, M. Manley, A. Du Plessis, and S. R. Stock (2021), X-ray computed tomography, *Nature Reviews Methods Primers*, 1(1), 18, doi:10.1038/s43586-021-00015-4.
- Yiotis, A. G., A. G. Boudouvis, A. K. Stubos, I. N. Tsimpanogiannis, and Y. C. Yortsos (2004), Effect of liquid films on the drying of porous media, *AIChE Journal*, 50(11), 2721–2737, doi:10.1002/aic.10265.
- Zeng, Z. W., and R. Grigg (2006), A criterion for non-Darcy flow in porous media, *Transport in Porous Media*, 63(1), 57–69, doi:10.1007/s11242-005-2720-3.

Appendix A

Supplementary material Chapter 3

A.1. Thickness of crusts from different salts

Table A.1: Measured distance from top and bottom of the sample holder to the crust and resulting thickness for each crust. The measurements were distributed along the perimeter of the crust close to the wall at the equidistant position 1 to 4. Subtracting the top and bottom distance from the length of the sample holder $l = 140$ mm (see Figure 3.4) provided the crust thickness at each measurement position and the mean crust thickness was obtained. The mean crust thickness deviated from each measurement position 26% for the NaCl crusts, 12% for the MgSO₄ crusts, and 17% for the Na₂SO₄ crusts. Drying did not change the crust thickness within the accuracy of the caliper (± 0.05 mm).

Crust	Measured	Measured at position				Mean crust thickness s [mm]
		1 [mm]	2 [mm]	3 [mm]	4 [mm]	
NaCl	top	16.6	17.4	17.0	17.1	
	bottom	120.9	120.8	121.1	121.4	1.9
	thickness	2.5	1.8	1.9	1.5	
NaCl	top	17.5	17.8	18.3	17.9	
	bottom	119.8	119.6	119.9	119.9	2.3
	thickness	2.7	2.6	1.8	2.2	
NaCl	top	17.8	17.9	17.3	17.2	
	bottom	120.9	120.8	121.1	120.9	1.5
	thickness	1.3	1.3	1.6	1.8	

Table A.1: Continued.

Crust	Measured	Measured at position				Mean crust thickness s [mm]
		1 [mm]	2 [mm]	3 [mm]	4 [mm]	
MgSO ₄	top	18.5	18.4	18.6	18.5	2.5
	bottom	118.8	119.0	118.9	119.2	
	thickness	2.7	2.6	2.5	2.3	
MgSO ₄	top	18.7	18.8	18.9	18.9	2.6
	bottom	118.8	118.5	118.4	118.7	
	thickness	2.5	2.7	2.7	2.4	
MgSO ₄	top	18.7	18.7	18.5	18.7	1.7
	bottom	119.5	119.4	119.9	119.8	
	thickness	1.8	1.9	1.6	1.5	
Na ₂ SO ₄	top	18.4	18.4	18.6	18.3	1.2
	bottom	120.2	120.5	120.3	120.4	
	thickness	1.4	1.1	1.1	1.3	
Na ₂ SO ₄	top	17.9	18.0	18.3	17.9	1.4
	bottom	120.5	120.7	120.5	120.5	
	thickness	1.6	1.3	1.2	1.6	
Na ₂ SO ₄	top	17.8	17.9	17.6	18.2	1.9
	bottom	120.1	120.4	120.3	120.0	
	thickness	2.1	1.7	2.1	1.8	

Sand

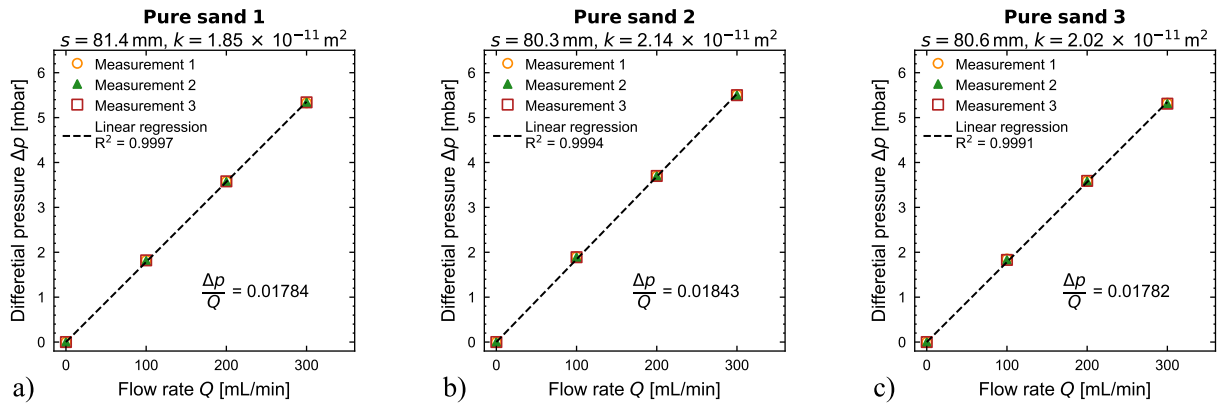


Figure A.1: Pressure difference over gas flow rate of all sand samples.

A.2. Pressure measurements of crusts from different salts

Dry crusts

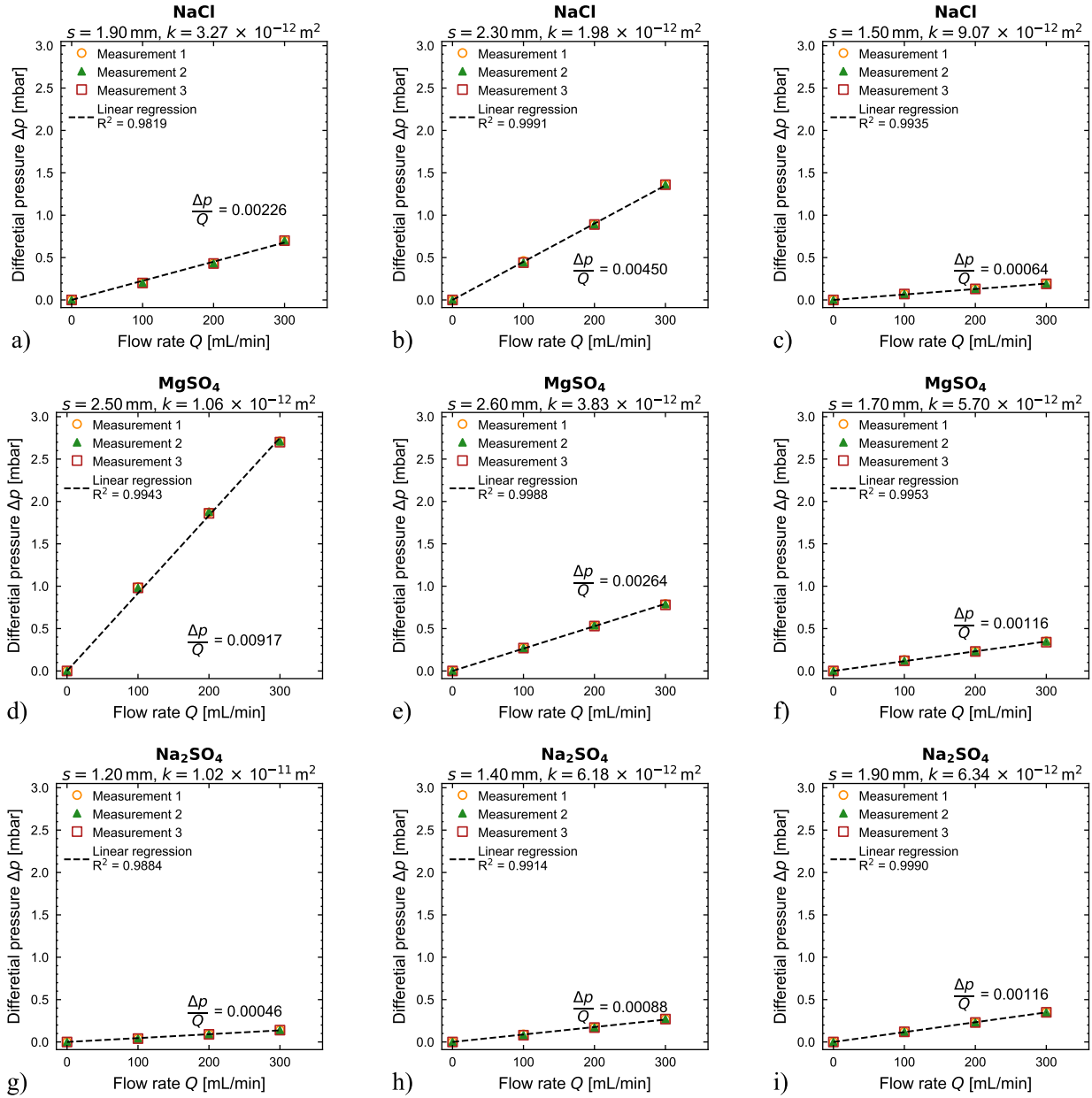


Figure A.2: Pressure difference over gas flow rate of all dried salt crusts.

Wet crusts

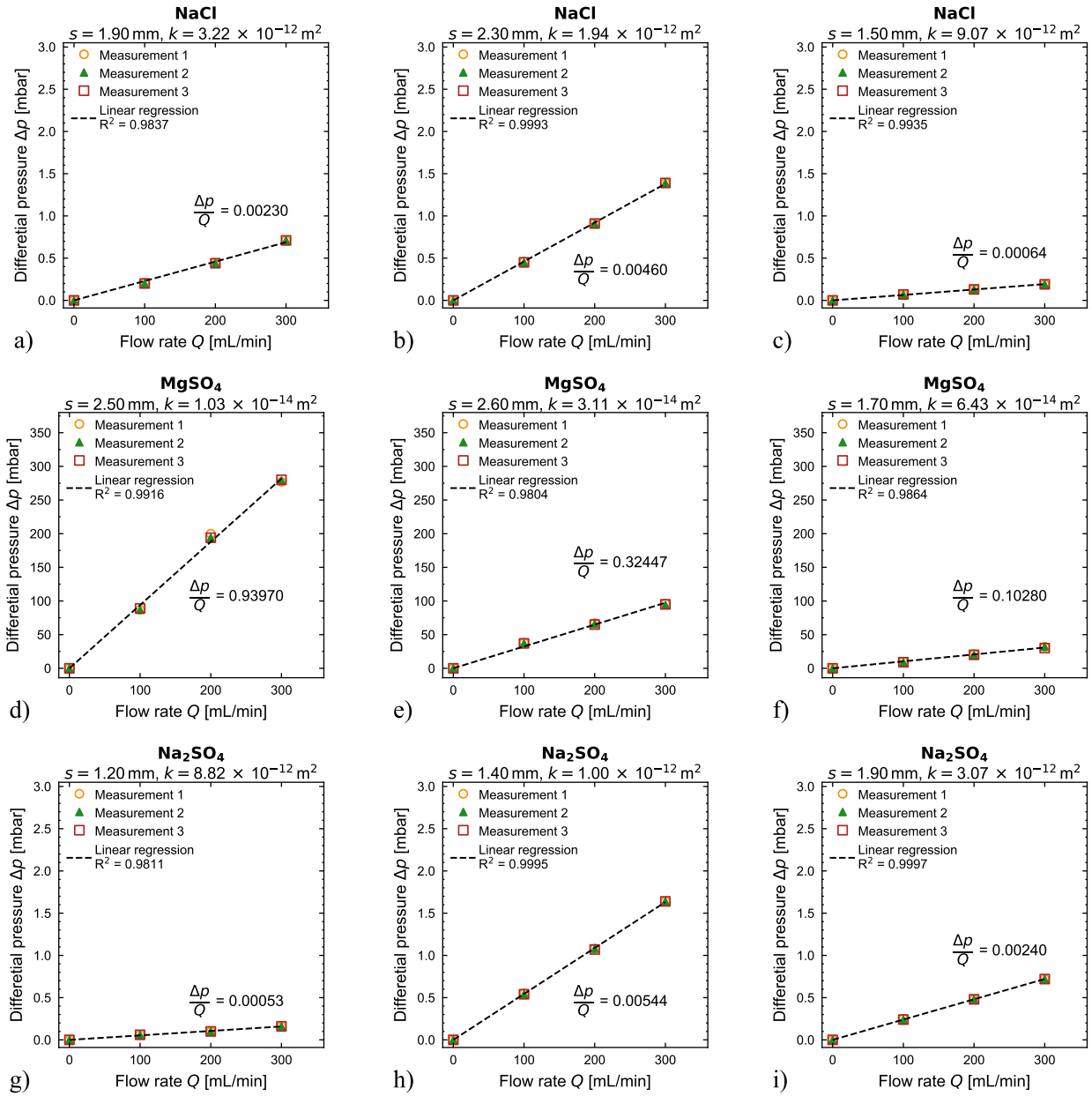


Figure A.3: Pressure difference over gas flow rate of all wet salt crusts.

Appendix B

Supplementary material Chapter 4

B.1. Surface data and thickness distribution of separated crusts

Table B.1: Arithmetic and harmonic mean of the thickness distribution of the crust segments obtained from μ XRCT data. The deviation is related to the arithmetic mean.

Concentration	Saturation	Arithmetic	Harmonic	Deviation
[mol/L]	[%]	[mm]	[mm]	[%]
0.32	40	0.46	0.42	8.7
0.32	30	1.17	1.07	8.5
0.32	20	1.92	1,86	3.1
0.64	40	1.35	1.31	3.0
0.64	30	2.04	2.04	0
0.64	20	1.90	1.87	1.6
0.96	40	2.20	2.17	1.3
0.96	30	2.13	1.96	8.1
0.96	25	2.33	1.92	17.8

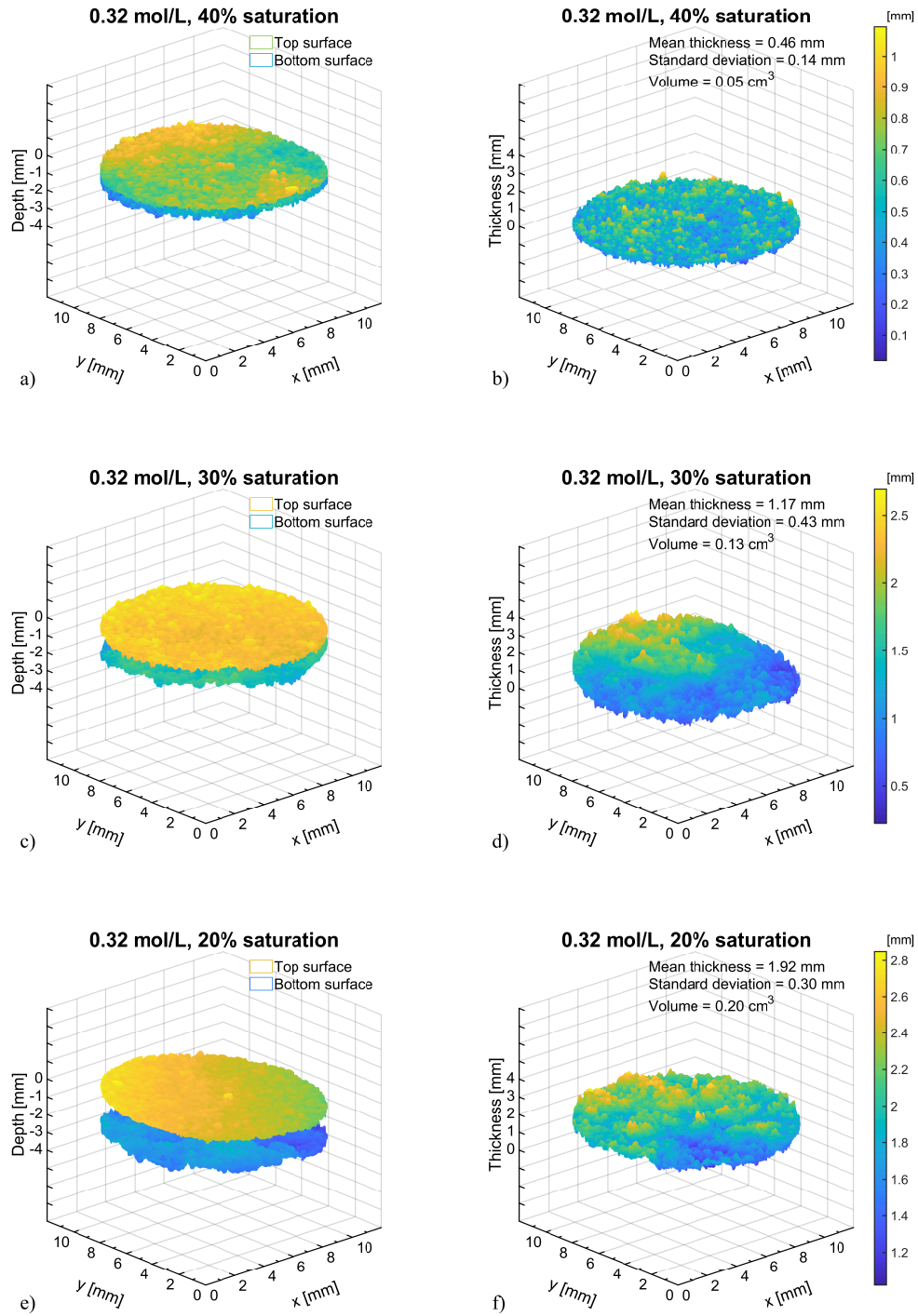


Figure B.1: Surface data and thickness distribution of separated and dried crusts from 0.32 mol/L initial concentration.

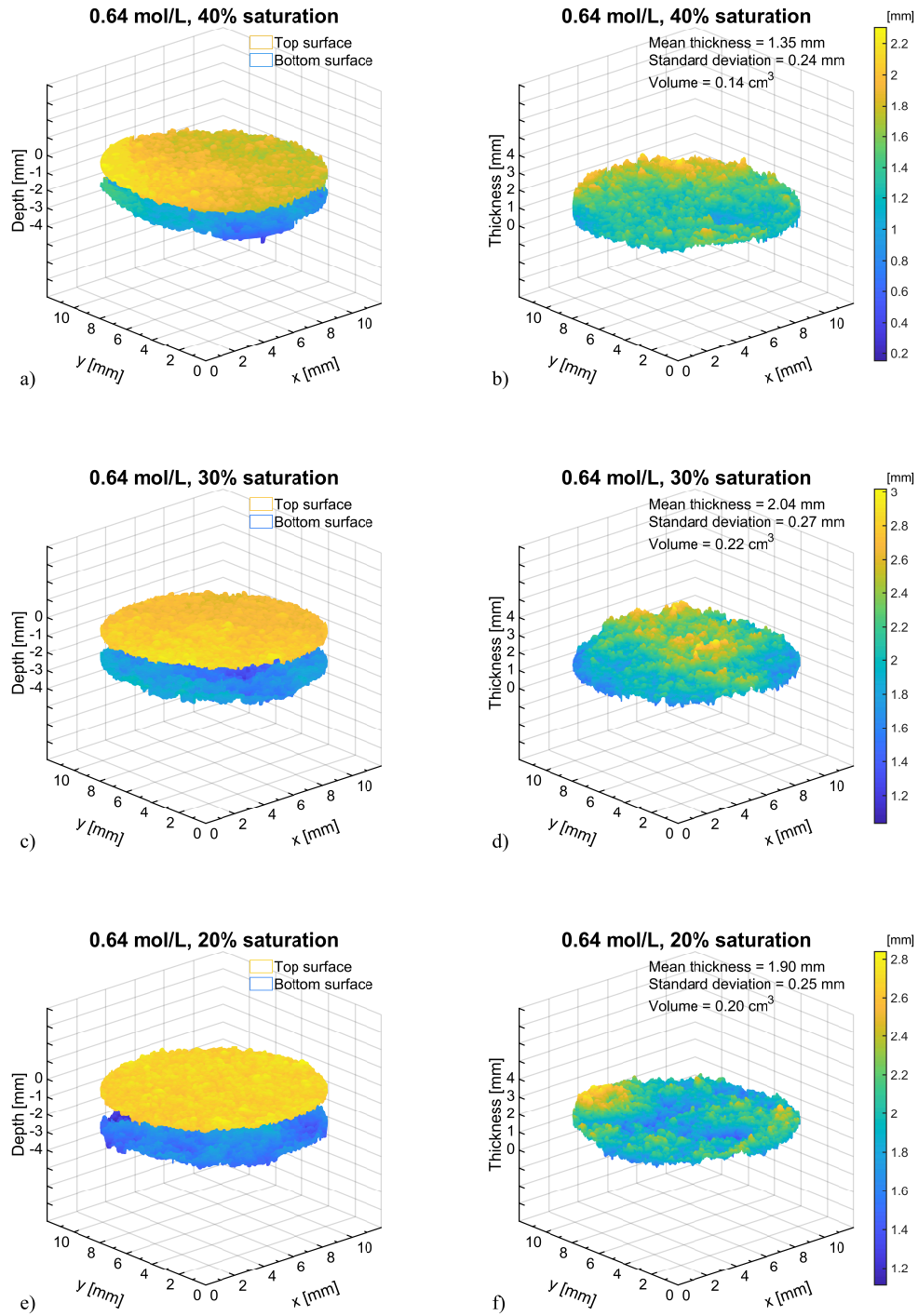


Figure B.2: Surface data and thickness distribution of separated and dried crusts from 0.64 mol/L initial concentration.

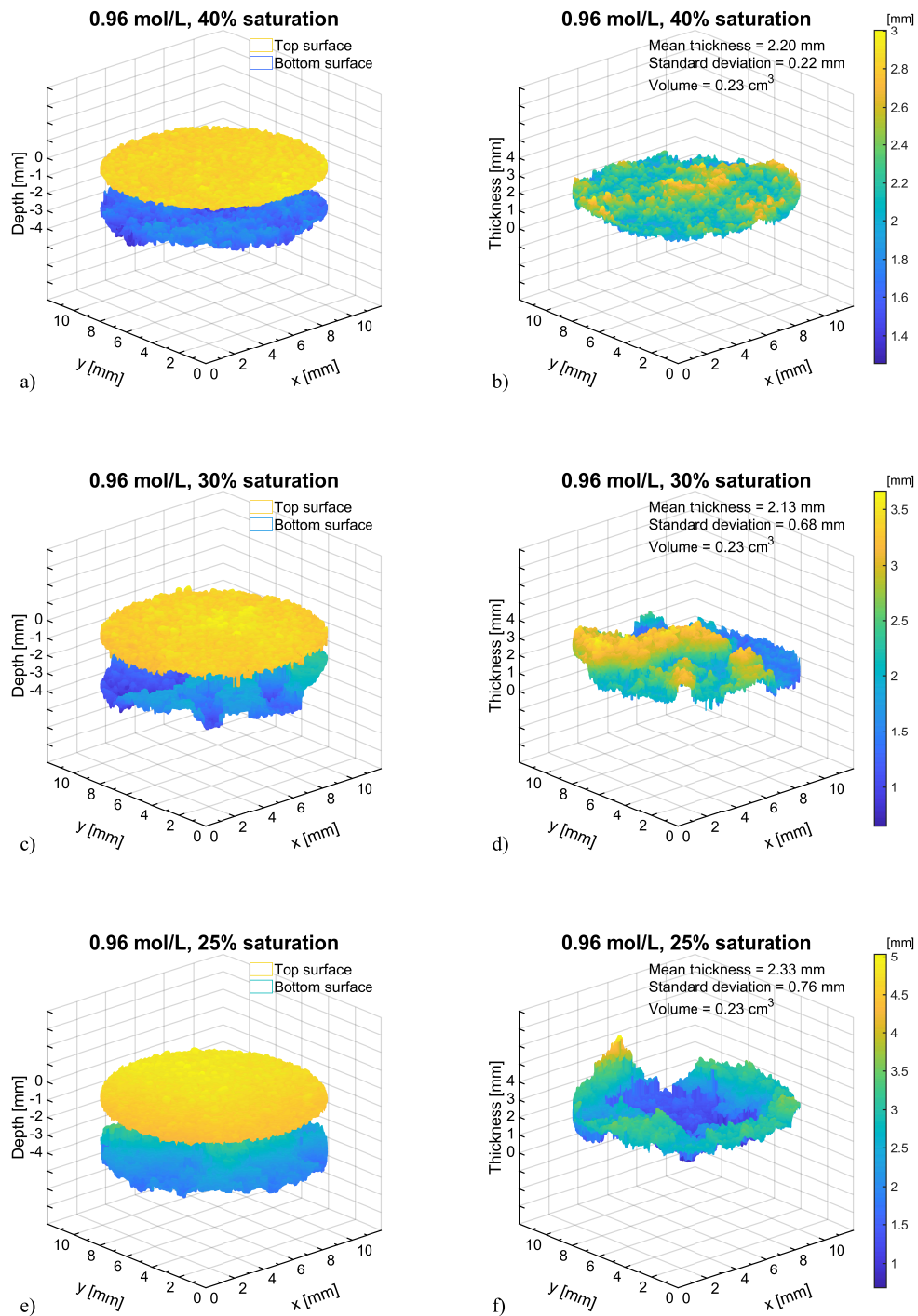


Figure B.3: Surface data and thickness distribution of separated and dried crusts from 0.96 mol/L initial concentration.

B.2. Pressure measurements of separated crusts

Dry crusts

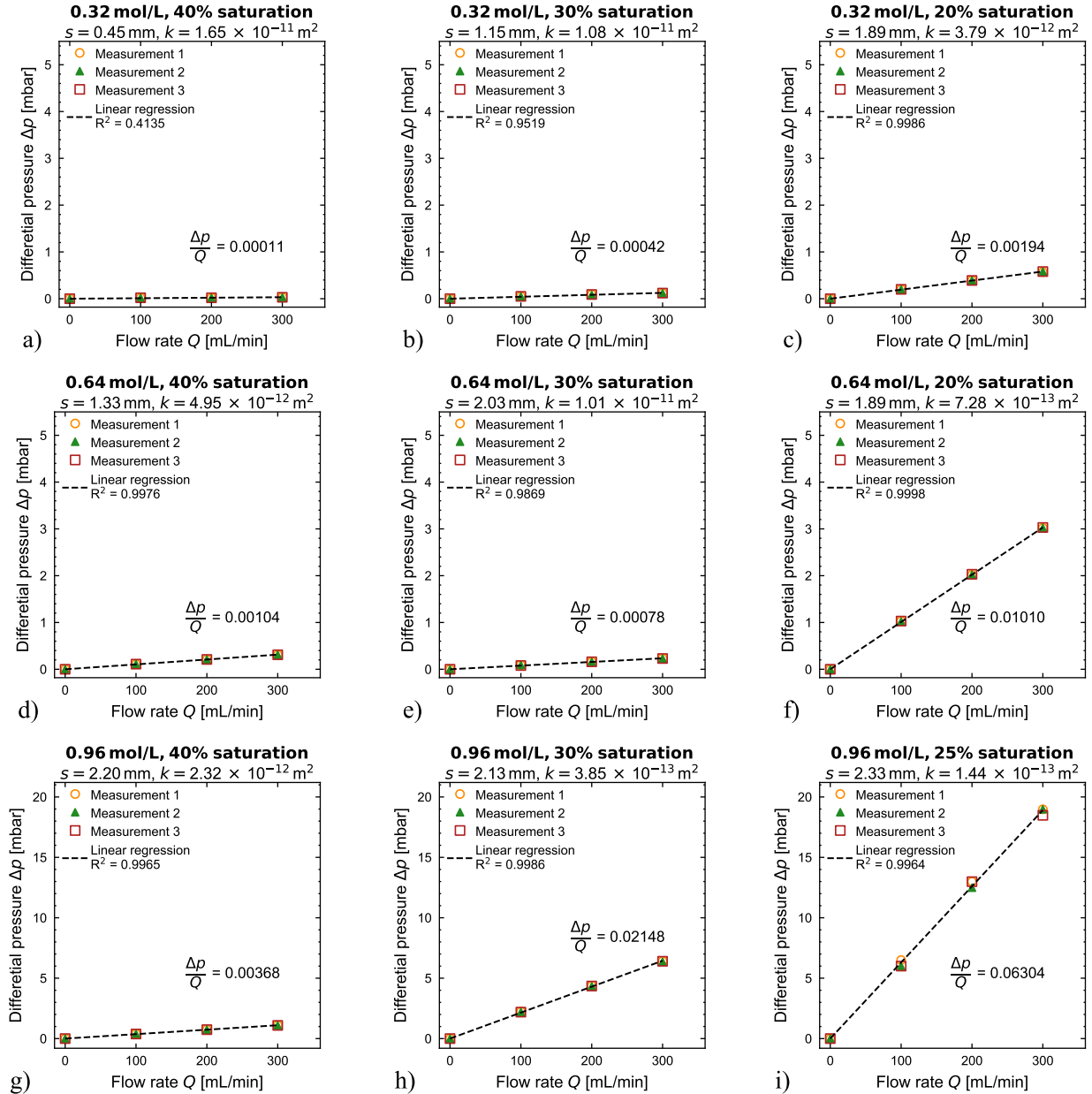


Figure B.4: Pressure measurements of separated and dried crusts from 0.32 mol/L, 0.96 mol/L, and 0.96 mol/L initial concentration.

Wet crusts

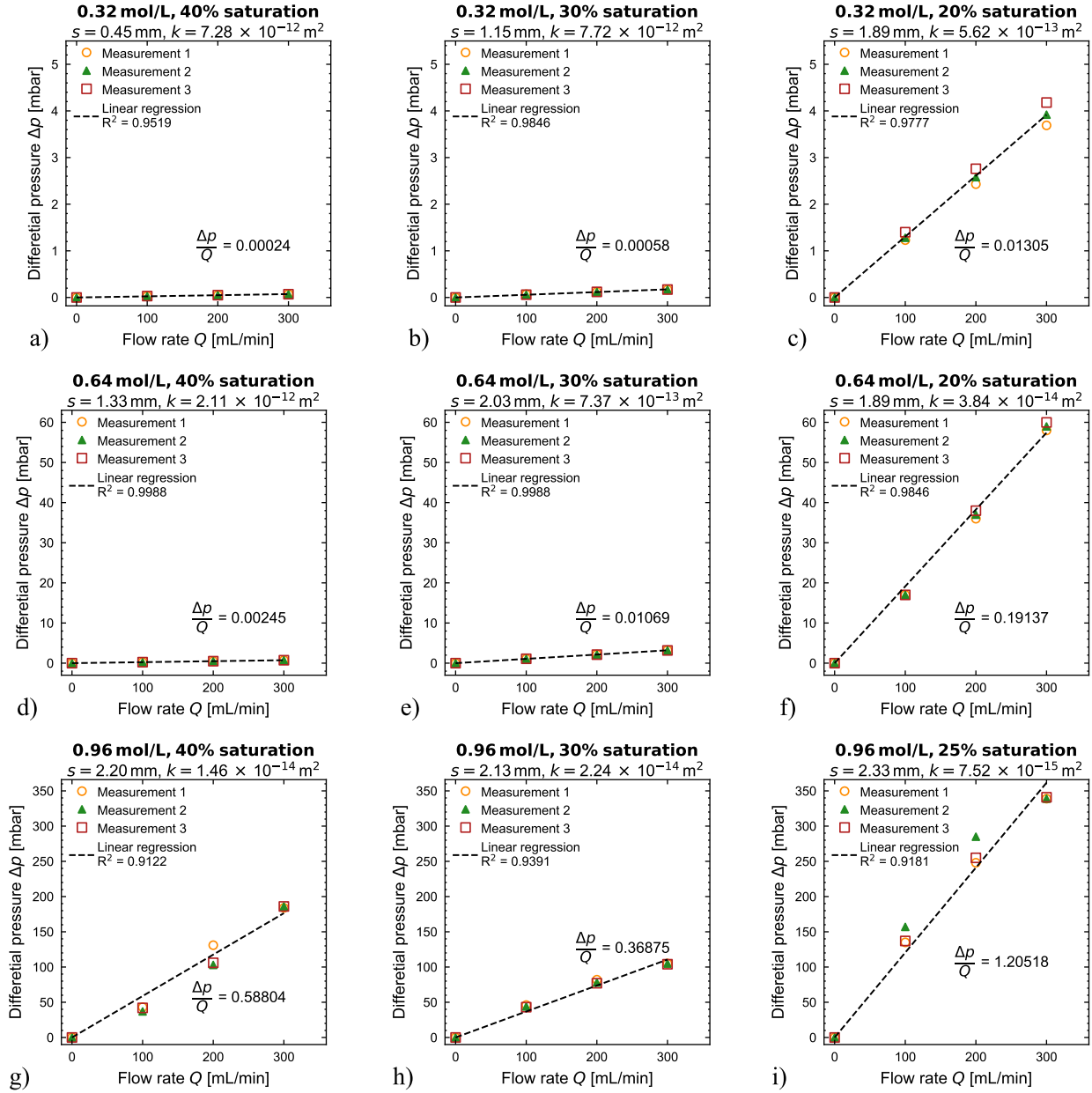


Figure B.5: Pressure measurements of separated, wet crusts from 0.32 mol/L, 0.96 mol/L, and 0.96 mol/L initial concentration.

Sand

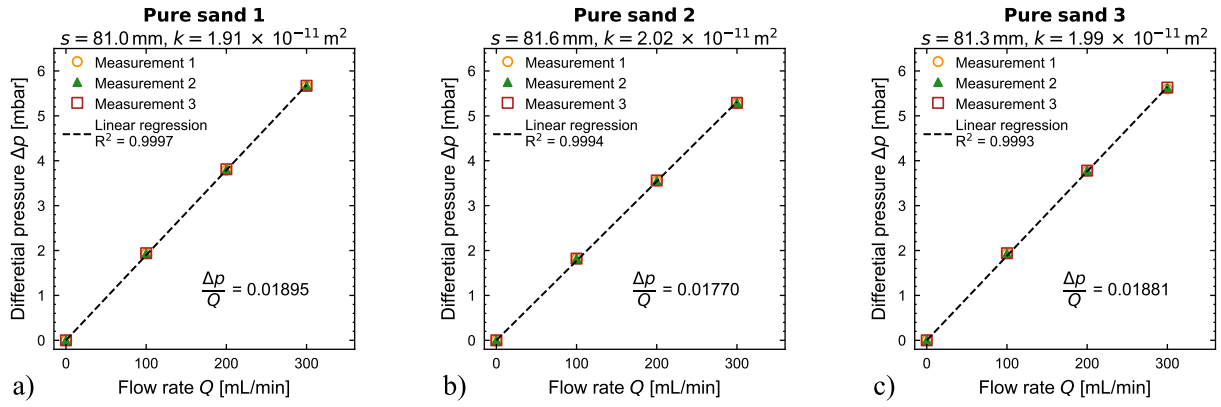


Figure B.6: Pressure measurements of sand samples.

Appendix C

Supplementary material Chapter 5

Table C.1: Measurement depths on sintered glass and marker solution using the NMR-MOUSE. The surface position of the sample was determined from the signal intensity S_0 of the fully saturated sample at different depths (see text for details). The marker solution was measured at 19.8 mm (position NMR-MOUSE).

Position NMR-MOUSE	Depth sample
h_{lift} [mm]	h_{depth} [mm]
1	1.5
1.5	1
2	0.5
2.5	0 (surface)
3	-0.5
3.5	-1
4	-1.5
4.5	-2
6	-3.5
7.5	-5
9.5	-7
12.5	-10
16.5	-14
19.8	-17.3